



ARISTOTLE UNIVERSITY OF THESSALONIKI
DEPARTMENT OF GEOPHYSICS

EVANGELIA TSAKIROUDI

Graduate Geologist

**SOURCE PARAMETERS OF THE 24 MAY 2014
NORTH AEGEAN EARTHQUAKE**

MSc Thesis

Thessaloniki
2015

EVANGELIA TSAKIROUDI

Graduate Geologist

SOURCE PARAMETERS OF THE 24 MAY 2014
NORTH AEGEAN EARTHQUAKE

Submitted to the School of Geology within the
framework of the Postgraduate Programme
“Applied and Environmental Geology”
Specialization: Geophysics

Date of Oral Examination: 11/09/2015

Supervising Committee:

Anastasia Kiratzi.....Professor of Seismology (Supervisor)

George Karakaisis..... Professor of Seismology (Member)

Nikolaos TheodoulidisResearch Director -I.T.S.A.K (Member)

Reference Number of Scientific Annals of the School of Geology No:

© Evangelia Tsakiroudi, 2015

All Rights Reserved

SOURCE PARAMETERS OF THE 24 MAY 2014 NORTH AEGEAN EARTHQUAKE

No part of this publication may be reproduced, stored or distributed for commercial purposes. Reproduction, storage and distribution for non-profitable educational or scientific purposes are permitted with the limitation of reference to the source and the preservation of the current message. Queries regarding non profitable permission requests must be appended to the author.

Opinions and conclusions included in this document express the author and do not correspond to the official attitude of A.U.Th.

Preface

This thesis was elaborated in the framework of the Postgraduate Programme "Applied and Environmental Geology" of the School of Geology of the Aristotle University of Thessaloniki, in the specialization field of Seismology. The scope of this thesis is the determination of the source parameters and of a finite fault slip model of the 24 May 2014 North Aegean earthquake, using spectral analysis, body wave modeling and slip inversion of broadband teleseismic data.

In the first chapter, the seismotectonic properties of the North Aegean region are discussed, along with the spatiotemporal characteristics of the aftershock sequence, as derived from other studies. The data retrieval and station features are presented in the second chapter. Next, in the third chapter, an analysis of P and S wave spectra is carried out, to calculate seismic moment and corner frequency. The resulted values are then used as input parameters in various empirical relations in order to derive the source dimensions, stress drop and maximum dislocation. In the following chapters, the MT5 program (Zwick et al., 1995) is used to derive the focal mechanism and scalar moment of the source. The software of Kikuchi and Kanamori (1982, 1991) and Kikuchi et al. (1993) is also employed, firstly, for the focal mechanism estimation and, secondly, for the finite fault slip model determination. A comparison between the results of this study and other published solutions is, finally, attempted.

At this point, I would like to express my sincere gratitude to my supervisor, Professor Anastasia Kiratzi, for her substantial support to my MSc study and related research, for her patience, cooperation and motivation to improve my general skills. I, also, feel grateful for her moral and financial support through the THALES PROJECT with acronym SITE-CLASSIFICATION (MIS 7377335).

I would like to thank my thesis committee, Dr. George Karakaisis, Professor of Seismology, and Dr. Nikolaos Theodoulidis, Research Director of I.T.S.A.K, for their productive comments and attempt to broaden my perspectives, as well as PhD Candidate Harris Kkallas, for his significant scientific assistance and encouragement, and Dr. Christos Evangelidis for sharing data and information of his personal work, required for the accomplishment of this research.

I am, also, grateful to Dr. Mohammad Raeesi and Professor Jens Havskov from the Department of Earth Sciences of University of Bergen, for their kindness to share their knowledge and scientific opinions with me, as well as to Dr. Alex Copley from the Department of Earth Sciences of University of Cambridge.

My sincere thanks also go to all the members of the Geophysics Department, particularly my MSc colleagues and friends Chris Kourouklas, Io Ioannidi and Antonia Michailidou for their encouragement and knowledge exchange. Last, I would like to mostly thank my dear family and friends for their vital and irreplaceable support.

Acknowledgments

This research has been in part co-financed by the European Union (European Social Fund – ESF) and Greek national funds through the Operational Program "Education and Lifelong Learning" (Project THALES: MIS 377335 SITE-CLASSIFICATION- Characterization of site conditions in Greece for realistic seismic ground motion simulations: pilot application in urban areas; Coordinator- Anastasia A. Kiratzi).

Contents

1	The 24 May 2014 North Aegean Earthquake	1
1.1	Tectonic setting	1
1.2	The location of the mainshock.....	3
1.3	Reported source parameters for the mainshock.....	5
1.4	Reported damage.....	7
2	Data retrieval and processing.....	10
3	Spectral Analysis	16
3.1	The source spectrum	16
3.2	Brune model and seismic moment.....	18
3.3	Attenuation	20
3.4	Geometrical spreading	21
3.5	Source parameters derived from spectral analysis	23
3.6	Spectral analysis application	24
3.6.1	Signal-to-noise analysis and data preparation.....	24
3.6.2	Application procedure	28
3.7	Spectral analysis results.....	33
4	Teleseismic Body Wave Inversion	41
4.1	Waveform modeling - Basic model.....	41
4.1.1	Source time function and directivity.....	42
4.1.2	Body wave modeling	45
4.1.3	Earthquake moment tensors.....	48
4.1.4	Moment tensor inversion.....	51
4.2	Waveform modeling of the mainshock.....	52
4.2.1	Method 1 – MT5	52
4.2.2	Method - 2	58
4.2.3	Application and results.....	61
5	Finite-Fault Slip Inversion.....	67
5.1	Fault slip determination	67
5.2	Method adopted	68
5.3	Preferred slip model of the mainshock	69
6	Summary and Discussion	76

7	References	82
	Appendix A: Signal-to-noise Fourier spectrums	88
	Appendix B: Fourier spectrums of vertical and horizontal components.....	115

List of Figures

Figure 1.1. The plate motions of Arabian, Anatolian and Aegean microplates (modified from Papazachos et al., 1998).	1
Figure 1.2. Historical and current seismicity ($M \geq 6.0$) of the North Aegean region (data from Seismological Station of Aristotle University of Thessaloniki).	3
Figure 1.3. The Saros and North Aegean basins. Focal mechanisms of $M < 5.9$ earthquakes and GPS vector arrows mainly indicate right-lateral shearing (Kiritzi et. al., 2015 and references therein).	4
Figure 1.4. Aftershock distribution ($M \geq 1.8$) of the 24/05/2014 earthquake. The three largest aftershocks are marked by stars. A and B denote the clusters of Saros basin and NAB, respectively (Kiritzi et al., 2015).	5
Figure 1.5. Focal mechanism solutions provided by various agencies (Table 1.1), as presented in European-Mediterranean Seismological Centre (EMSC).	6
Figure 1.6. PGA distribution by ELER (Earthquake Loss Estimation Routine) with information from ITSAK, KOERI and AFAD seismic networks (picture by KOERI Earthquake Report).	7
Figure 1.7. Shake map of 24/05/2014 North Aegean earthquake (picture from U.S. Geological Survey (U.S.G.S.) Earthquake Report).	8
Figure 1.8. Damaged buildings in the regions of Imbros (top) and Canakkale (bottom) (after KOERI Institute's Earthquake Report).	9
Figure 1.9. Suspended ceiling damage at Lemnos Airport (after KOERI Institute's Earthquake Report).	9
Figure 2.1. Stations of Global Seismographic Network (GDSN).	10
Figure 2.2. Frequency response of broadband and long-period seismometers such as STS-2 and DWWSSN, respectively (Stein and Wysession, 2003).	11
Figure 2.3. Stations in epicentral distances between 30° and 90° from the 24/05/2014 North Aegean earthquake epicenter (yellow star), as provided by 'Wilber 3' tool of IRIS.	12
Figure 3.1. The earthquake source spectrum (Shearer, 2009).	17
Figure 3.2. Amplitude spectra for different earthquake magnitudes. Earthquakes of different magnitudes reflect energy release at difference frequencies (Geller, 1976).	18
Figure 3.3. Far field displacement and velocity in time and frequency domain (Shearer, 2009).	19
Figure 3.4. Geometrical spreading functions for teleseismic distances.	22

Figure 3.5. Noise and P-wave amplitude spectrums for the Kurchatov station in Kazakhstan.	25
Figure 3.6. Typical corner frequencies for earthquakes of different magnitudes (Aki and Richards, 2002).	26
Figure 3.7. Data Preparation of Borovoye station record in Kazakhstan (vertical component). Top: raw waveform in counts, Medium: Instrument corrected and bandpass filtered in 0.01-2 Hz in m/s , Bottom: Integrated to displacement in meters. T8 and T9 markers represent the P and S arrivals, respectively.....	27
Figure 3.8. P-wave Fourier amplitude spectrum of displacement of the Borovoye station record in Kazakhstan (vertical component). .	27
Figure 3.9. Brief presentation of SAC commands, used for the data preparation in spectral analysis.	28
Figure 3.10. Anelastic attenuation models proposed by Houston and Kanamori (1986), Futterman (1962) (followed by Lay and Wallace, 1995) and Choy and Cormier (1986), for teleseismic distances. ...	29
Figure 3.11. P-wave Fourier amplitude spectrum of displacement of Kurchatov station record in Kazakhstan (vertical component). Blue color: Attenuation corrected spectrum, used for moment magnitude (M_w) and corner frequency (f_c) determination. Black color: Uncorrected spectrum. Red color: Linear fitting of the flat and descending part. The cross-section of the fitting lines represents the corner frequency f_c	30
Figure 3.12. Ambiguous S-wave displacement spectrum of Nilore station record in Pakistan (E-W component). Blue color: Attenuation corrected S-wave spectrum. The ω^{-1} part is not visually separated from flat level part. Black color: Uncorrected spectrum. Red color: Problematic linear fitting.	31
Figure 3.13. S-wave displacement spectrum of Nilore station in Pakistan (E-W component). The flat part is defined from the attenuation corrected spectrum (cyan color) and the corner frequency from the observed spectrum (black color). Blue color: Linear fitting. Red color: Corner frequency (f_c).....	32
Figure 3.14. Azimuthal coverage of stations used in P-wave spectral analysis. The center of the circle represents the earthquake epicenter. The epicentral distances are presented in meters.	33
Figure 3.15. Azimuthal coverage of stations used in S-wave (E-W component) spectral analysis. The center of the circle represents the earthquake epicenter. The epicentral distances are presented in meters.	35

Figure 3.16. Azimuthal coverage of stations used in S-wave (N-S component) spectral analysis. The center of the circle represents the earthquake epicenter. The epicentral distances are presented in meters.	35
Figure 4.1. Inversion and forward modeling schemes for the estimation of source parameters.	41
Figure 4.2. Seismogram as the convolution product of source, structure and instrument responses (Stein and Wysession, 2003).	42
Figure 4.3. For a fault of finite length, the duration of the source time function depends on azimuth, rupture velocity and wave-velocity (Stein and Wysession, 2003).	43
Figure 4.4. The derivation of a trapezoidal source time function from rise and rupture time, according to Stein and Wysession (2003) (described in the text).	44
Figure 4.5. Effects of rupture directivity on the source time function (Stein and Wysession, 2003).	45
Figure 4.6. P-wave arrival for a shallow earthquake at epicentral distances between 30° and 90° is modeled as the sum of direct P, pP and sP waves (free surface reflections of P wave)(Stein and Wysession, 2003).	46
Figure 4.7. Relative polarities and amplitudes of direct P, pP and sP waves for different focal mechanisms (Stein and Wysession, 2003).	47
Figure 4.8. Polarity of P-wave first arrival in relation to fault strike and station azimuth (Stein and Wysession, 2003).	47
Figure 4.9. Equivalent body force descriptions for a single force, a single couple and a double couple (Stein and Wysession, 2003). ..	49
Figure 4.10. The nine force couples which compose the seismic moment tensor (Stein and Wysession, 2003).	50
Figure 4.11. Example of source time function as a sum of overlapping triangles with different amplitudes.	53
Figure 4.12. Brief presentation of the SAC commands used in MT5 data preparation.	55
Figure 4.13. P-wave data preparation of the Kabul station (vertical component) in Afghanistan for the MT5 program. Black color (top): Raw waveform in counts. Blue color: Instrument correction (m/s). Red color: Bandpass filtering. Green color: Integration to displacement (meters). Black color (Bottom): Convolution with the WWLPBN response.	55
Figure 4.14. Waveform fit of the MT5 solution for the 24/05/2014 North Aegean earthquake (Kiratzis et al., 2015).	57

Figure 4.15. Elementary moment tensors as described in Equation 4.17 (Kikuchi and Kanamori, 1991).	59
Figure 4.16. Fault geometry pattern used in 'green' and 'inversion' algorithms (Kikuchi and Kanamori, 1982).	60
Figure 4.17. Source time function shapes (impulse, trapezoid, cosine tapered trapezoid and triangular) (Kikuchi and Kanamori, 1982).	61
Figure 4.18. Waveform fit of the minimum misfit solution for a double couple source, described by 4 subevents and a fault length of 100 km ($T_0=5$ s).	64
Figure 4.19. Waveform fit of higher-frequency data for a pure strike-slip source, described by 3 subevents and an impulse-shaped source time function ($T_0=20$ s).	66
Figure 5.1. Fault grid pattern used in 'MOM3' algorithm (Kikuchi et al and Kanamori, 1982).	69
Figure 5.2. Variance of V_r (rupture velocity) values. The minimum misfit value is for $V_r=3$ km/s.	71
Figure 5.3. Final fault slip model and waveform fit of the 24/05/2014 North Aegean earthquake, as derived from 'MOM3' algorithm.	72
Figure 6.1. Aftershock spatial distribution (cross-section at 73°) of 2014 North Aegean sequence, using the relocated catalog of C. Evangelidis (personal communication). A lack of aftershocks on the asperity areas is noticeable.	80

List of Tables

Table 1.1. Typical parameters of the North Aegean strike-slip faulting (Papazachos et al., 1997).	2
Table 1.2. Focal mechanism solutions of different institutes, as reported to European-Mediterranean Seismological Centre (EMSC). 6	
Table 2.1. Sampling properties of digital seismometer channels. ..	11
Table 2.2. Features of stations derived by 'Wilber 3' tool of IRIS. .	13
Table 3.1. Seismic moment (M_0) and corner frequency (f_c) values derived from P-wave spectral analysis for each station (vertical component *BHZ).	34
Table 3.2. Seismic moment (M_0) and corner frequency (f_c) values derived from S-wave spectral analysis for each station (horizontal E-W component *BHE).	36
Table 3.3. Seismic moment (M_0) and corner frequency (f_c) values derived from S-wave spectral analysis for each station (horizontal N-S component *BHN).	37
Table 3.4. Mean values of seismic moment (M_0), moment magnitude (M_w) and corner frequency (f_c) for P and S wave spectral analysis.....	38
Table 3.5. Source dimensions and stress drop derived from the circular models (for $V_s=3.8$ km/s) of Brune (1970) and Madariaga (1976), and rectangular strike-slip models of Wells and Coppersmith (1994) and Papazachos et al. (2004).	39
Table 4.1. Focal mechanism solution with MT5 program.	56
Table 4.2. Jeffreys-Bullen velocity model and density (data from Kikuchi and Kanamori, 2003).	62
Table 4.3. Focal mechanisms for different fault types and number of subevents, derived from the 'INVERSION' algorithm.	65
Table 6.1. The results of this study (MT5 and Slip Inversion) compared to the published solutions of various Institutes, as reported to the European-Mediterranean Seismological Centre (EMSC).	78

1 The 24 May 2014 North Aegean Earthquake

1.1 Tectonic setting

On 24 May 2014 (UTC 09:24), an Mw6.8 earthquake occurred in the North Aegean region, about ~20 km southwest of Samothraki Island and ~40 km northeast of Lemnos Island. The epicenter of this earthquake lies in North Greece, in the area of North Aegean.

The seismotectonic region of interest is the North Aegean Trough (NAT) mostly described by right-lateral strike-slip faulting. It has an ENE-WSW direction, starting from the west part of the North Anatolian Fault (NAF), in Marmara Sea, and extending up to the eastern coasts of central Greece.

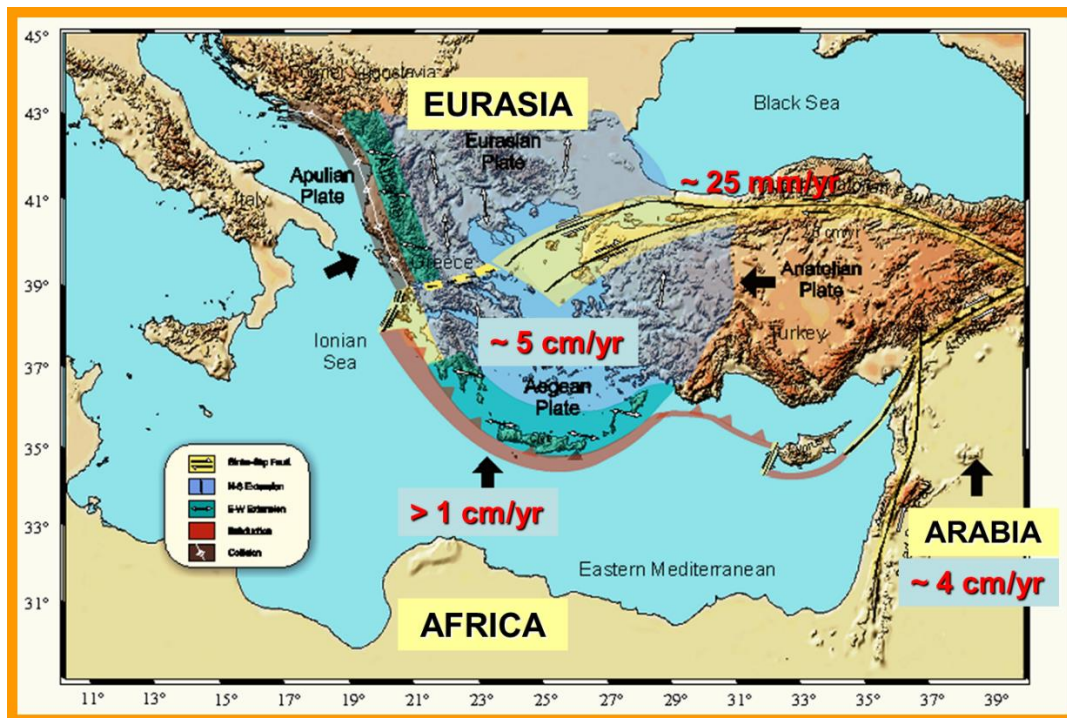


Figure 1.1. The plate motions of Arabian, Anatolian and Aegean microplates (modified from Papazachos et al., 1998).

The North Aegean Trough accommodates the westward motion of the Anatolian plate and the quick southwest motion of the Aegean (~5 cm/yr). The westward escape of Anatolia, is facilitated by the existence of the North Anatolian fault, a 1000 km right-lateral strike-slip fault, that defines the deforming zone between Eurasia and Turkey. What generates the westward motion of Anatolia, is the NNE

motion of the Arabian plate (Fig. 1.1), with a velocity of 2.5 cm/yr in the north part, which pushes Anatolia towards the Greek region. In further detail, Anatolia constitutes a compact plate which, in regard to Eurasia, rotates counterclockwise, around a pole, located in the Sinai peninsula, with an angular velocity of 1.5°/Myr (Oral et al. 1995; Papazachos, 1999). The westward Anatolian movement towards North Aegean does not create a compressional field, as it may have been expected. That is because of the quick SW movement of the Aegean plate, towards the South Aegean subduction zone, that causes an extensional regime in the North Aegean area.

The typical fault mechanism for the North Aegean seismic regime (Papazachos and Papazachou, 2003) is shown in Table 1.1. The NAT reaches an underwater level of 1500 m. This trough and the surrounding basins, such as the Marmara basin, constitute the southern part of the Eurasian plate.

Table 1.1. Typical parameters of the North Aegean strike-slip faulting (Papazachos and Papazachou, 2003).

Typical Fault	strike=238°	dip=88°	rake=-174°
Typical P-axis	azimuth=104°	plunge=6°	
Typical T-axis	azimuth=14°	plunge=3°	

The North Aegean region hosts fairly frequent moderate-to-large seismic events. Since 1900, there have been 21 earthquakes of magnitude $M > 6.0$ within 250 km of the 24 May 2014 earthquake. Several of these took place along the trend of the North Aegean Trough, including the $M=6.6$ 24/05/2014 event and the $M=6.7$ earthquake in 1975, ~55 km to the northeast (Fig. 1.2). The largest nearby earthquake was a $M=7.6$ event in August 1912 near the western end of the Sea of Marmara, which is thought to have caused approximately 200 fatalities. As for the nearby North Anatolian Fault, there had been a lot of $M > 6.0$ recorded earthquakes, with the 1939 Erzincan and 1999 Izmit earthquakes being the strongest, with respective magnitudes 7.9 and 7.6, causing thousands of casualties and huge damage (U.S.G.S. Earthquake Report).



Figure 1.2. Historical and current seismicity ($M \geq 6.0$) of the North Aegean region (data from Seismological Station of Aristotle University of Thessaloniki).

1.2 The location of the mainshock

The North Aegean Trough is constituted by various basins, and for the present study, the discussion will focus on the Saros and North Aegean basins (Fig. 1.3), following the classification of Papanikolaou and Papanikolaou (2007). The mainshock epicenter lies in the Saros basin. The North Aegean basin, located below the Athos peninsula, was also activated, as indicated by the aftershock distribution (Kiritzi et al. 2015).

According to Kurt et al. (2000) and McNeill et al. (2004), the Saros basin can be divided into two sub-basins, i.e. a western and an eastern. The mainshock epicenter is located in the junction of the two sub-basins. The interesting feature of this location is that a trending $N310^\circ$ fault crosses the sub-basins' junction, probably related to left-lateral movement (McNeill et al., 2004), confusing the local tectonic properties even more. However, the aftershock sequence clearly defines an ENE-WSW fault.

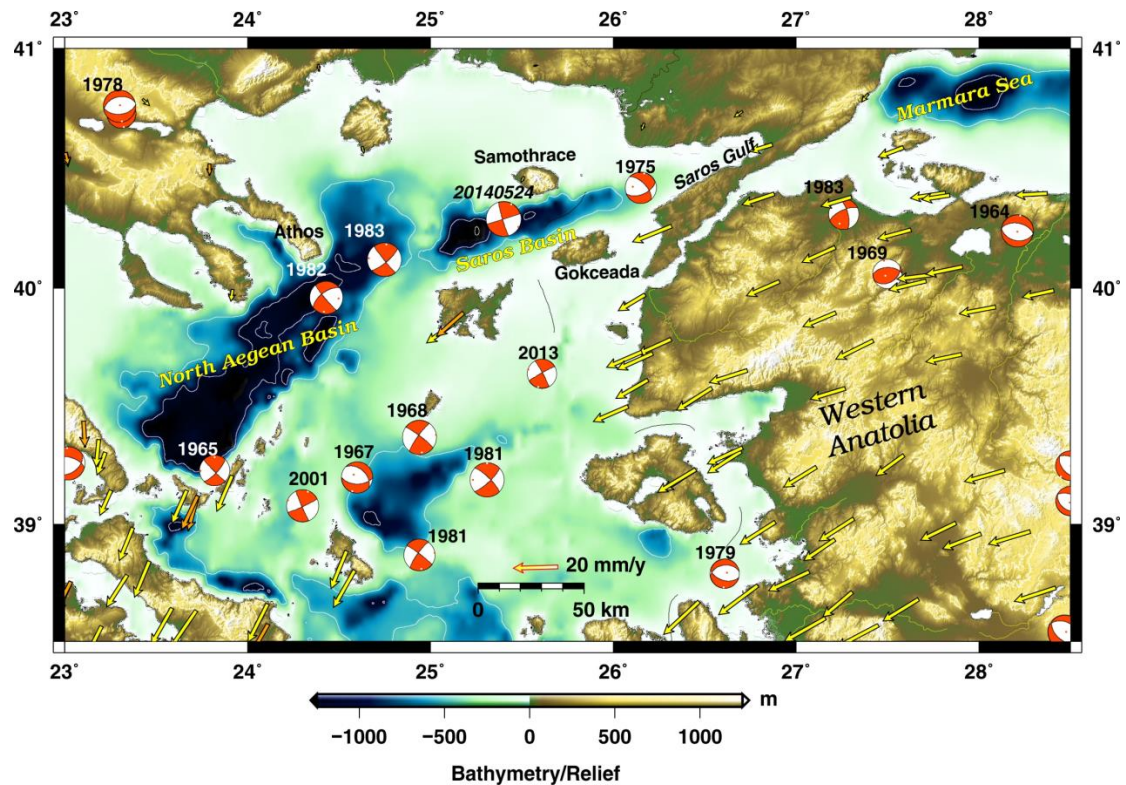


Figure 1.3. The Saros and North Aegean basins. Focal mechanisms of $M < 5.9$ earthquakes and GPS vector arrows mainly indicate right-lateral shearing (Kiritzi et. al., 2015 and references therein).

In general, the North Aegean Trough is described by highly complex seismotectonic and geometrical properties, and therefore, is regarded as a transitional zone, combining right-lateral and normal motions. According to Kiritzi et al. (2015), the 24/05/2014 North Aegean earthquake initiated at the junction of the Saros sub-basins and managed to activate a very wide zone of approximately 200 km length, constituted by almost the whole Saros basin (~100) km and the northern margin of the North Aegean Basin (NAB), below the Athos peninsula.

The estimation of the activated fault area is yielded by the aftershock distribution. The aftershock sequence, relocated by Evangelidis (2015), was rich in moderate size aftershocks and very poor in strong events. The two strongest aftershocks have magnitudes of $M=4.9$. The first occurred within some minutes at the far eastern end of Saros basin, immediately followed by an $M=4.6$ earthquake in the NAB region, and the second occurred three months later at the western end of Saros basin, which is the junction of North Aegean and Saros basins (Fig. 1.4).

The aftershock sequence is spatiotemporally evolved in two main clusters: the main cluster of the Saros basin related to a bilateral rupture of ~ 100 km, and the secondary cluster of North Aegean basin.

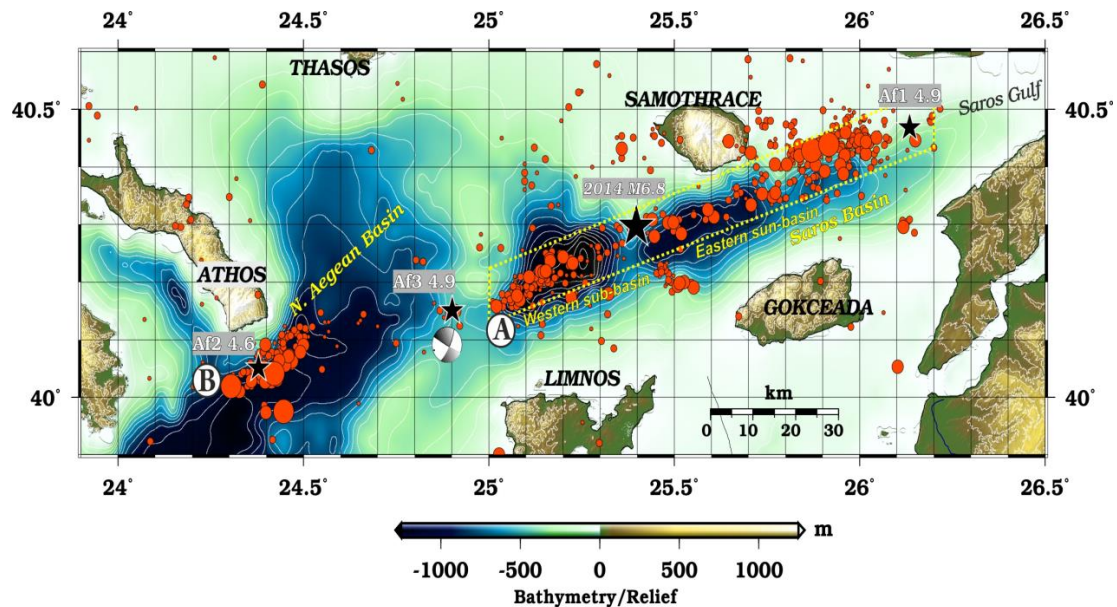


Figure 1.4. Aftershock distribution ($M \geq 1.8$) of the 24/05/2014 earthquake. The three largest aftershocks are marked by stars. A and B denote the clusters of Saros basin and NAB, respectively (Kiritzi et al., 2015).

1.3 Reported source parameters for the mainshock

The distribution of the aftershocks, as well as the focal mechanism solutions obtained from various institutes, are compatible with the seismotectonic regime, indicating a NE-SW dextral strike-slip source (Fig. 1.5).

Table 1.2 lists the earthquake parameters of the 24/05/14 event, in regard to time, hypocenter location, fault strike, dip and rake, as well as moment magnitude, as they were obtained by 13 institutes with the moment tensor inversion method. The values have large differences among them, with magnitudes varying from 6.3 to 7.1. The ML magnitude estimations from peak-to-peak measurements, mostly, yielded even smaller magnitudes reaching values below $ML=6.0$. The large divergence among magnitude estimations indicates a complicated seismic event, making it more difficult to be resolved.

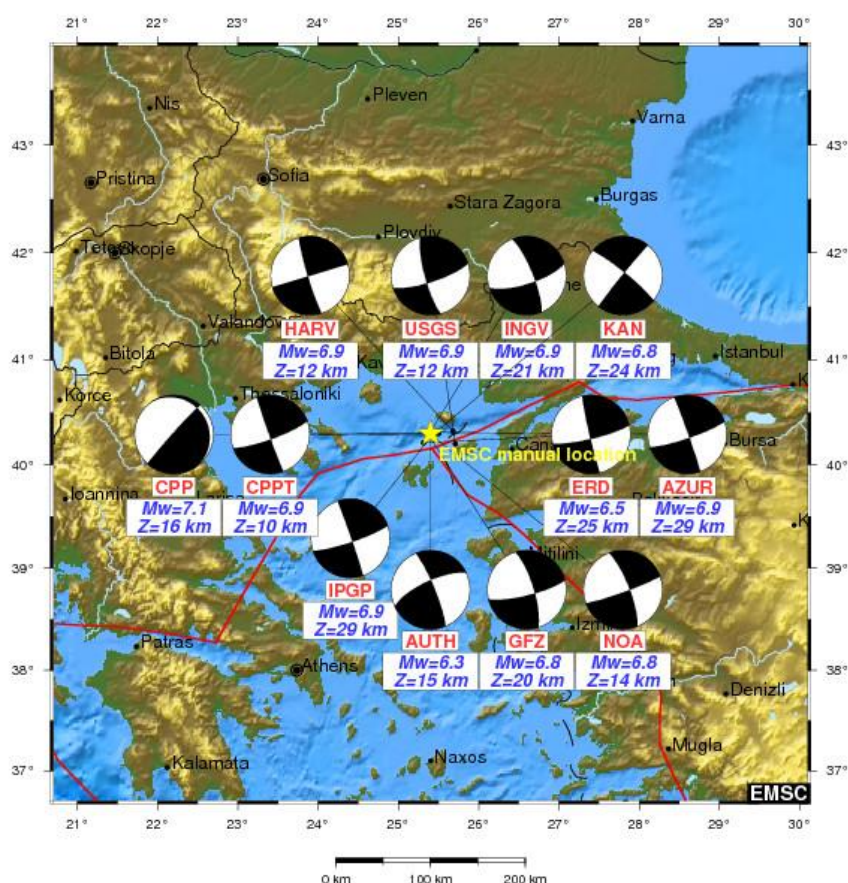


Figure 1.5. Focal mechanism solutions provided by various agencies (Table 1.1), as presented in European-Mediterranean Seismological Centre (EMSC).

Table 1.2. Focal mechanism solutions of different institutes, as reported to European-Mediterranean Seismological Centre (EMSC).

Time (UTC)	Lat (deg)	Lon (deg)	Depth (km)	Str1 (deg)	Dip1 (deg)	Rake1 (deg)	Str2 (deg)	Dip2 (deg)	Rake2 (deg)	M w	Agency
09:25:22.6	40.3	25.4	21	72	73	-167	-	-	-	6.9	INGV
09:25:19.2	40.3	25.7	12	163	85	0	253	90	-175	6.9	HARVARD
09:25:17.0	40.2	25.7	12	72	77	168	165	78	13	6.9	USGS
09:25:03.0	40.3	25.4	20	343	76	-12	76	77	-164	6.8	GFZ
09:25:03.0	40.3	25.5	16	222	87	102	325	13	12	7.1	CPP
09:25:03.0	40.3	25.5	29	71	82	-178	341	88	-8	6.9	GeoAzur
09:25:03.0	40.3	25.5	29	341	88	-8	71	82	-178	6.9	IPGP
09:25:02.0	40.3	25.4	15	245	72	171	-	-	-	6.3	AUTH
09:25:02.0	40.3	25.4	14	70	85	-167	338	77	-5	6.8	NOA
09:25:01.0	40.3	25.5	24	219	88	173	-	-	-	6.8	KOERI
09:25:00.0	40.2	25.3	25	167	87	9	76	81	177	6.5	ERD
09:25:00.0	40.3	25.4	10	70	80	178	160	88	10	6.9	CPPT
09:25:03.1	40.3	25.7	12	73	85	-177	343	87	-5	6.9	GCMT

1.4 Reported damage

The earthquake was widely felt across Greece, Turkey and Bulgaria. The major cities which felt the strong shaking were Çanakkale, Thessaloniki, Edirne, Plovdiv, Izmir and Istanbul. According to KOERI Institute, the maximum intensity of strong shaking felt on land was VI-VII on the EMS'98 scale. This level of shaking has the potential to cause light damage to buildings and moderate damage to vulnerable structures. This is the reason that no serious damage was reported in nearby regions. Figures 1.6 and 1.7 show the PGA distribution and ShakeMap of the 24/05/2014 earthquake.

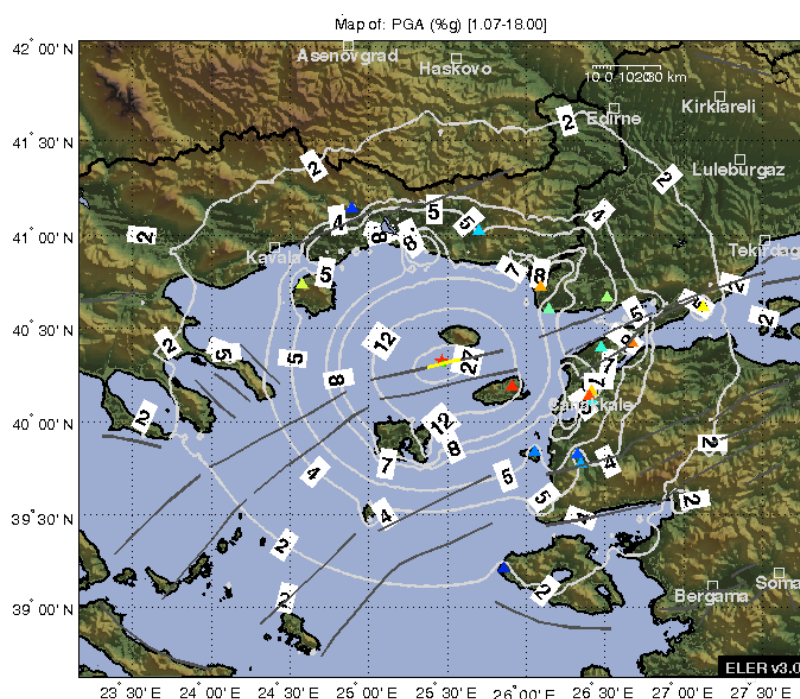


Figure 1.6. PGA distribution by ELER (Earthquake Loss Estimation Routine) with information from ITSAK, KOERI and AFAD seismic networks (picture by KOERI Earthquake Report).

In the Çanakkale province and Imbros Island, 300 buildings were damaged, along with 8 schools and a state hospital, which was followed by evacuation of the patients and construction of a field hospital. In regard to human injuries, several hundreds of people were slightly injured and temporarily hospitalized, mostly as a result of panic, as reported by Disaster and Emergency Management Presidency of Turkey (AFAD).



Figure 1.8. Damaged buildings in the regions of Imbros (top) and Canakkale (bottom) (after KOERI Institute's Earthquake Report).



Figure 1.9. Suspended ceiling damage at Lemnos Airport (after KOERI Institute's Earthquake Report).

2 Data retrieval and processing

Spectral analysis, body wave inversion and finite-fault slip inversion are performed to retrieve the source characteristics of the 24 May 2014 mainshock. These techniques can be executed in various ways, concerning various methodologies, software programs, input data and fixed constraints. In this study, these procedures are approached with teleseismic input data and are presented in detail in the next chapters.

The data were retrieved from the Data Management Center (DMC) of Incorporated Research Institutions for Seismology (IRIS). I used the 'Wilber 3' tool of IRIS, which is a web-based event explorer allowing the user to view earthquake waveforms and access data in various formats.



GLOBAL SEISMOGRAPHIC NETWORK

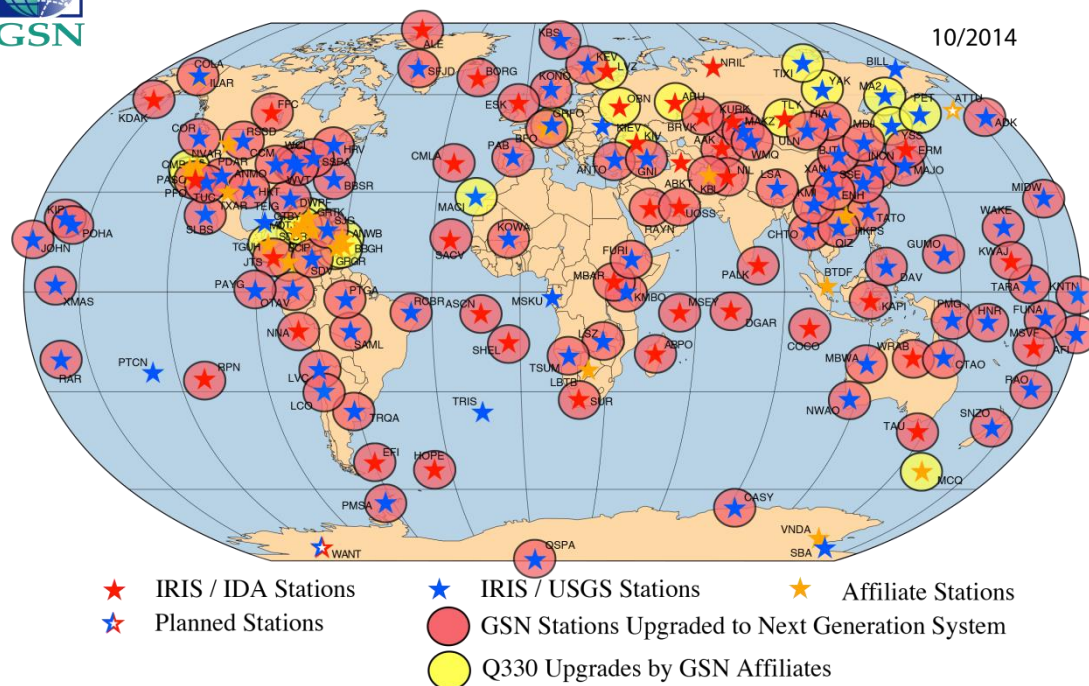


Figure 2.1. Stations of Global Seismographic Network (GDSN).

I selected broadband (20 sps) data of the Global Seismographic Network (GSN), from stations at an epicentral distance range of 30-90 degrees (Fig. 2.1 and 2.3). These are the recommended distance limits for the usage of teleseismic data, because in this range, mantle triplications and complexities due to core-mantle boundary are avoided. The long-period data (1sps) are not recommended for these

techniques, due to their limited frequency band (Fig. 2.2 and Table 2.1).

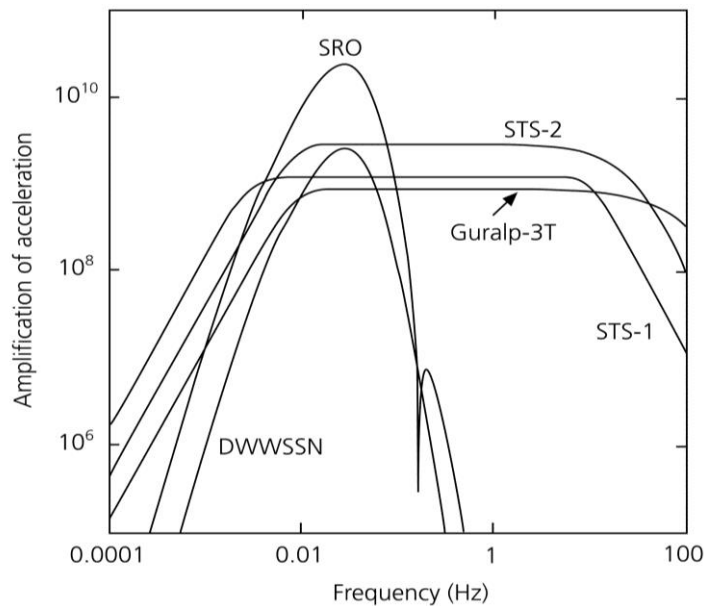


Figure 2.2. Frequency response of broadband and long-period seismometers such as STS-2 and DWWSSN, respectively (Stein and Wyssession, 2003).

Table 2.1. Sampling properties of digital seismometer channels.

Channel	Sampling rate (sample/s)	Time interval (s)
VH	1/10	10
LH	1/1	1
BH	20/1	0.05
HH-SH	50/1-100/1	0.02-0.01

Seventy nine stations were available for this query, responding to azimuths from -180 to 180 degrees (Fig. 2.3). The azimuthal coverage is adequate, with only one exception: the 180°-270° quadrant, where the stations are sparsely located. The stations belong to the following seismic networks:

- IU (Global Seismograph Network GSN-IRIS/USGS)
- II (IRIS/IDA Seismic Network)
- GT (Global Telemetered Seismograph Network USAF/USGS)
- HK (Hong Kong Seismograph Network)
- MS (Singapore Seismological Network)
- CU (Caribbean Network)
- IM (International Miscellaneous Stations).

The stations' name, geographical coordinates, distance, azimuth and region are presented in Table 2.2.

Both vertical (BHZ) and horizontal (BHE, BHN) components were retrieved, obtaining a total of 237 (79x3) seismic waveforms. The signals started 10 minutes before and 60 minutes after the P phase arrival.



Figure 2.3. Stations in epicentral distances between 30° and 90° from the 24/05/2014 North Aegean earthquake epicenter (yellow star), as provided by 'Wilber 3' tool of IRIS.

The data were downloaded in SEED format. Using the RDSEED program, which is available to download from IRIS (<http://ds.iris.edu/ds/nodes/dmc/forms/rdseed/>), the waveforms were extracted in SAC format, in order to be processed in the Seismic Analysis Code (SAC). The response (RESP*) and pole-zero (SAC_PZ*) files were extracted as well from RDSEED, in order to remove the instrument with the 'transfer' command and obtain the ground motion. The further data processing depends on each program's requirements and is described in detail in the following chapters.

Table 2.2. Features of stations derived by 'Wilber 3' tool of IRIS.

Name	Network	Latitude	Longitude	Distance	Azimuth	Name
BRVK	II	53.06°	70.28°	32.69°	51.76°	Borovoye, Kazakhstan
FURI	IU	8.90°	38.68°	33.55°	155.73°	Mt. Furi, Ethiopia
KBL	IU	34.54°	69.04°	34.79°	85.26°	Kabul, Afghanistan
BORG	II	64.75°	-21.33°	36.10°	-31.81°	Borgarfjordur, Asbjarnarstadir, Iceland
MACI	IU	28.25°	-16.51°	36.27°	-96.11°	Morro de la Arena, Canary Islands
AAK	II	42.64°	74.49°	36.35°	69.74°	Ala Archa, Kyrgyzstan
KOW A	IU	14.50°	-4.01°	36.37°	-126.71°	Kowa, Mali
KURK	II	50.72°	78.62°	37.85°	55.75°	Kurchatov, Kazakhstan
NIL	II	33.65°	73.27°	38.35°	84.30°	Nilore, Pakistan
KBS	IU	78.92°	11.94°	38.99°	-4.08°	Ny-Alesund, Spitzbergen, Norway
CMLA	II	37.76°	-25.52°	39.08°	-76.72°	Cha de Macela, Sao Miguel Island, Azores
MAKZ	IU	46.81°	81.98°	40.63°	61.33°	Makanchi, Kazakhstan
MBA R	II	-0.60°	30.74°	41.18°	171.86°	Mbarara, Uganda
KMB O	IU	-1.13°	37.25°	42.81°	162.39°	Kilima Mbogo, Kenya
WMQ	IC	43.81°	87.70°	45.30°	64.03°	Urumqi, Xinjiang Province, China
SFJD	IU	67.00°	-50.62°	48.14°	-30.61°	Sondre Stromfjord, Greenland
SACV	II	14.97°	-23.61°	49.42°	-106.27°	Santiago Island, Cape Verde
ALE	II	82.50°	-62.35°	49.83°	-9.82°	Alert, N.W.T., Canada
MSEY	II	-4.67°	55.48°	52.76°	141.12°	Mahe, Seychelles
TLY	II	51.68°	103.64°	52.87°	49.59°	Talaya, Russia
LSA	IC	29.70°	91.13°	53.65°	79.47°	Tibet, China
LSZ	IU	-15.28°	28.19°	55.63°	176.73°	Lusaka, Zambia
TIXI	IU	71.63°	128.87°	56.10°	21.66°	Tiksi, Russia
ULN	IU	47.87°	107.05°	56.38°	52.86°	Ulaanbaatar, Mongolia
PALK	II	7.27°	80.70°	59.17°	108.22°	Pallekele, Sri Lanka
TSUM	IU	-19.20°	17.58°	59.93°	-171.48°	Tsumeb, Namibia
ASCN	II	-7.93°	-14.36°	60.55°	-133.34°	Butt Crater, Ascension Island
YAK	IU	62.03°	129.68°	61.13°	31.26°	Yakutsk, Russia
ABPO	II	-19.02°	47.23°	62.70°	156.68°	Ambohimpanompo, Madagascar

HIA	IC	49.27°	119.74°	63.11°	46.84°	Hailar, Neimenggu Autonomous Region, China
SHEL	II	-15.96°	-5.75°	63.26°	-146.18°	Horse Pasture, St. Helena Island
XAN	IC	34.03°	108.92°	64.34°	66.00°	Xi'an, China
DGAR	II	-7.41°	72.45°	64.42°	126.40°	Diego Garcia, Chagos Islands, Indian Ocean
KMI	IC	25.12°	102.74°	64.80°	77.51°	Kunming, Yunnan Province, China
LBTB	GT	-25.02°	25.60°	65.30°	179.79°	Lobatse, Botswana, Africa
CHTO	IU	18.81°	98.94°	65.61°	85.42°	Chiang Mai, Thailand
BJT	IC	40.02°	116.17°	65.93°	57.00°	Baijiatuan, Beijing, China
ENH	IC	30.28°	109.49°	66.82°	69.15°	Enshi, Hubei Province, China
BILL	IU	68.07°	166.45°	67.78°	14.69°	Bilibino, Russia
HRV	IU	42.51°	-71.56°	68.35°	-51.94°	Adam Dziewonski Observatory, (Oak Ridge), Massachusetts, USA
BBSR	IU	32.37°	-64.70°	69.80°	-64.15°	Bermuda Institute of Ocean Studies, St George's Bermuda
MA2	IU	59.58°	150.77°	70.49°	25.98°	Magadan, Russia
MDJ	IC	44.62°	129.59°	71.28°	46.77°	Mudanjiang, Heilongjiang Province, China
RCBR	IU	-5.83°	-35.90°	72.61°	-113.89°	Riachuelo, Brazil
SUR	II	-32.38°	20.81°	72.79°	-175.95°	Sutherland, South Africa
SSPA	IU	40.64°	-77.89°	73.25°	-50.47°	Standing Stone, Pennsylvania
QIZ	IC	19.03°	109.84°	73.71°	78.60°	Qiongzong, Hainan Province, China
INCN	IU	37.48°	126.62°	74.01°	54.07°	Inchon, Republic of Korea
SSE	IC	31.09°	121.19°	74.46°	62.16°	Shanghai, China
COLA	IU	64.87°	-147.86°	74.70°	-2.97°	College Outpost, Alaska, USA
IL31	IM	64.77°	-146.89°	74.76°	-3.40°	ILAR Array, Eilson, AK, USA
FFC	II	54.73°	-101.98°	74.90°	-28.39°	Flin Flon, Canada
HKPS	HK	22.28°	114.14°	74.90°	73.38°	Po Shan, Hong Kong
YSS	IU	46.96°	142.76°	76.51°	38.56°	Yuzhno Sakhalinsk, Russia

ANWB	CU	17.67°	-61.79°	76.58°	-78.07°	Willy Bob, Antigua and Barbuda
BBGH	CU	13.14°	-59.56°	77.73°	-83.06°	Gun Hill, Barbados
PET	IU	53.02°	158.65°	78.34°	26.57°	Petropavlovsk, Russia
TATO	IU	24.97°	121.50°	78.50°	66.90°	Taipei, Taiwan
SJG	IU	18.11°	-66.15°	79.54°	-75.06°	San Juan, Puerto Rico
WCI	IU	38.23°	-86.29°	79.70°	-47.89°	Wyandotte Cave, Indiana, USA
GRGR	CU	12.13°	-61.65°	79.96°	-82.55°	Grenville, Grenada
BTDF	MS	1.36°	103.77°	80.28°	96.53°	Bukit Timah Dairy Farm, Singapore
ERM	II	42.02°	143.16°	80.28°	41.83°	Erimo, Hokkaido Island, Japan
GRTK	CU	21.51°	-71.13°	81.00°	-69.37°	Grand Turk, Turks and Caicos Islands
MAJO	IU	36.55°	138.20°	81.52°	48.48°	Matsushiro, Japan
KDAK	II	57.78°	-152.58°	81.91°	-1.09°	Kodiak Island, Alaska, USA
WVT	IU	36.13°	-87.83°	82.05°	-48.55°	Waverly, Tennessee, USA
CCM	IU	38.06°	-91.24°	82.57°	-45.22°	Cathedral Cave, Missouri, USA
SDDR	CU	18.98°	-71.29°	82.73°	-71.23°	Presa de Sabenta, Dominican Republic
DWPF	IU	28.11°	-81.43°	83.69°	-58.15°	Disney Wilderness Preserve, Florida, USA
RSSD	IU	44.12°	-104.04°	84.12°	-33.88°	Black Hills, South Dakota, USA
COCO	II	-12.19°	96.83°	84.22°	111.35°	West Island, Cocos (Keeling) Islands
TRIS	IU	-37.07°	-12.32°	84.73°	-150.66°	Tristan da Cunha
GTBY	CU	19.93°	-75.11°	84.85°	-68.15°	Guantanamo Bay, Cuba
ADK	IU	51.88°	-176.68°	85.85°	13.45°	Adak, Aleutian Islands, Alaska
PTGA	IU	-0.73°	-59.97°	86.93°	-93.56°	Pitinga, Brazil
PD31	IM	42.77°	-109.56°	87.51°	-31.34°	PDAR Array, Pinedale, WY, USA
MTDJ	CU	18.23°	-77.53°	87.70°	-67.90°	Mount Denham, Jamaica
SDV	IU	8.88°	-70.63°	88.81°	-79.35°	Santo Domingo, Venezuela

3 Spectral Analysis

3.1 The source spectrum

It is widely known that signals can be expressed in both time and frequency domain. Seismologists, nowadays, use both of them to determine a variety of features that are related with seismology, earthquake engineering and more. Spectra of seismic signals can obtain information about a variety of tasks. The most common is the calculation of seismic moment, source radius and stress drop using P or S waves. The theory behind earthquake spectra is presented below, based on the formulations of Stein and Wyssession (2003) and Havskov and Ottemöller (2010).

The relations between the seismic moment and various magnitudes arise from the spectrum of the radiated seismic signals. As shown in the following chapters, where we use a source time function (STF) yielded by the convolution of two boxcar time functions, in regard to the fault and rise time finiteness, the Fourier transform of the STF is the product of the Fourier transforms of the boxcar functions, since convolution in the time domain equals multiplication in the frequency domain. The Fourier transform of a boxcar of height $1/T$ and length T is

$$F(\omega) = \int_{-T/2}^{T/2} \frac{1}{T} e^{i\omega t} dt = \frac{\sin(\frac{\omega T}{2})}{\omega T/2} \quad (3.1)$$

This function, sometimes written as $\text{sinc } x = (\sin x)/x$, indicates that the source pulse has a finite duration. Thus, the source spectrum amplitude $A(\omega)$ is the product of the seismic moment M_0 and two sinc terms

$$|A(\omega)| = M_0 \left| \frac{\sin(\frac{\omega T r}{2})}{\omega T r/2} \right| \left| \frac{\sin(\frac{\omega T d}{2})}{\omega T d/2} \right| \quad (3.2)$$

where T_r is the rupture time and T_d is the rise time (Stein and Wyssession, 2003). In a logarithmic sense, this equation becomes

$$\log A(\omega) = \log M_0 + \log \left[\text{sinc} \left(\frac{\omega T r}{2} \right) \right] + \log \left[\text{sinc} \left(\frac{\omega T d}{2} \right) \right] \quad (3.3)$$

In this approximation, the logarithm of spectral amplitude versus the logarithm of ω , yields three segments that correspond to different frequency ranges.

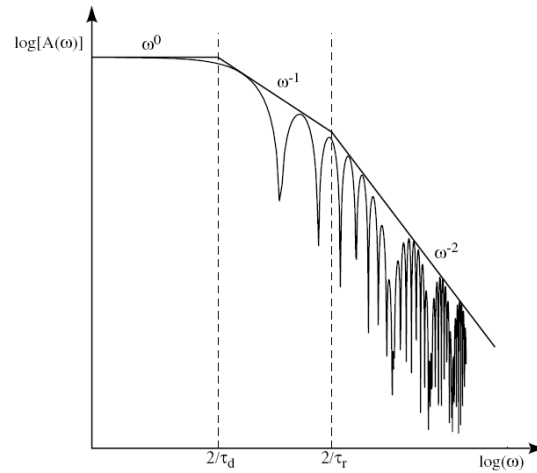


Figure 3.1. The earthquake source spectrum (Shearer, 2009).

Assuming that $T_r > T_d$, the final relation becomes

$$\log|A(\omega)| = \begin{cases} \log M_0 & \omega < 2/T_r \\ \log M_0 - \log\left(\frac{T_r}{2}\right) - \log \omega & 2/T_r < \omega < 2/T_d \\ \log M_0 - \log\left(\frac{T_r T_d}{4}\right) - 2 \log \omega & 2/T_d < \omega \end{cases} \quad (3.4)$$

(Stein and Wyssession, 2003).

As we see in Figure 3.1, there are three regions with slopes 1, ω^{-1} , ω^{-2} , that are separated by the frequencies $2/T_r$ and $2/T_d$, which are called corner frequencies, f_c . Before the first corner, the spectrum is flat, between the corners it goes as ω^{-1} , and in the third frequency region it decays as ω^{-2} . The spectrum depends on three parameters: seismic moment, rise time and rupture time. In most cases, the source spectrum is used to estimate a single corner frequency, that combines the results of rise and rupture time. This approximation of the corner frequency helps us define the frequency range, in which the major part of signal (flat level) is radiated. Also, the estimation and interpretation of the corner frequency are always in regard to the

source model used in each case, e.g. Haskell model, Brune model and others. Figure 3.2 shows the relation of corner frequency and earthquake magnitude for body and surface waves.

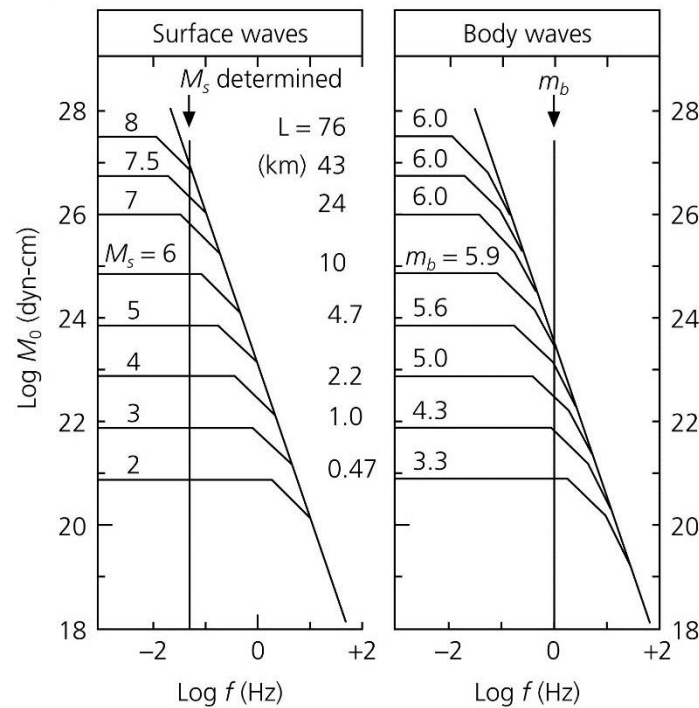


Figure 3.2. Amplitude spectra for different earthquake magnitudes. Earthquakes of different magnitudes reflect energy release at difference frequencies (Geller, 1976).

3.2 Brune model and seismic moment

The amplitude spectrum has different shapes for displacement, velocity and acceleration domains (Fig. 3.3). According to the Brune model, the source displacement spectrum is defined as

$$S(f) = \frac{M_0}{(1 + (\frac{f}{f_0})^2) 4\pi\rho v^3} \quad (3.5)$$

where M_0 is the seismic moment in Nm, ρ is the density in kg/m³, v is the velocity in m/s at the source (V_p or V_s depending on spectrum) and f_0 is the corner frequency. Radiation pattern is not included in this expression.

It is very useful to use a logarithmic scale to observe the spectrum. As we can see in Figures 3.1 and 3.3, the displacement spectrum is flat and proportional to M_0 at lower frequencies, while at higher

frequencies, the spectral level decays linearly with a slope of -2 (Havskov and Ottemöller, 2010). At the corner frequency, f_0 , the spectral amplitude is half the amplitude of the flat part.

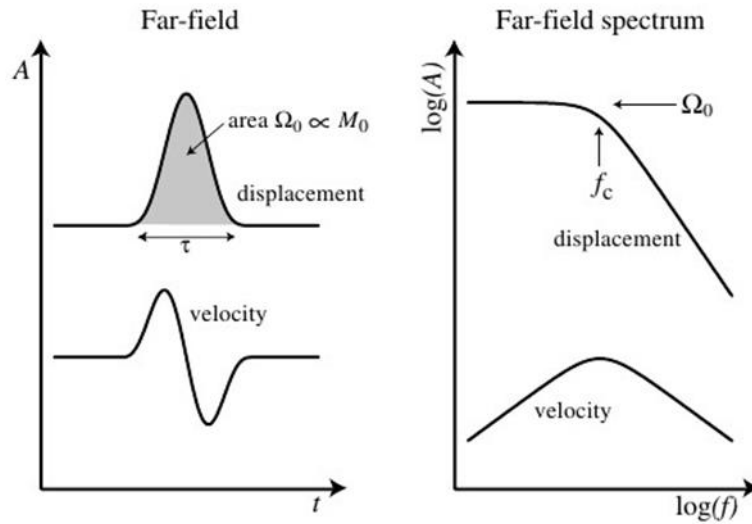


Figure 3.3. Far field displacement and velocity in time and frequency domain (Shearer, 2009).

The displacement spectrum at the receiver is the source spectrum affected by attenuation and geometrical spreading. If we correct for attenuation, then, at an epicentral distance Δ , and a hypocentral depth h , the observed displacement spectrum at the receiver is

$$D(f, t) = \frac{M_0 \times \Re_{\theta\phi} \times 2.0 \times G(\Delta, h)}{(1 + (\frac{f}{f_0})^2) 4\pi\rho v^3} \quad (3.6)$$

where $G(\Delta, h)$ is the geometrical spreading parameter, $\Re_{\theta\phi}$ is the radiation pattern effect and 2.0 responds to the free surface effect value assuming a vertical incident (Havskov and Ottemöller, 2010). The attenuation corrected spectrum is used to observe the corner frequency f_c and the spectral flat level Ω_0 . Thus, the seismic moment can be described as

$$M_0 = \frac{\Omega_0 4\pi\rho v^3}{\Re_{\theta\phi} \times 2.0 \times G(\Delta, h)} \quad (3.7)$$

It is always safest to perform spectral analysis in the vertical component, which, in general, corresponds to the P wave spectrum.

This is because of the near-surface site amplification, which mainly affects the horizontal components and therefore the S wave spectrum. Another important difference between P and S wave spectra is the difference in the corner frequency value (Madariaga, 1976).

3.3 Attenuation

In order to estimate the corner frequency, f_c , and the spectral flat level, Ω_0 , the seismic spectrum must be corrected for the attenuation. As presented in Havskov and Ottemöller (2010), the amplitude decay caused by anelastic attenuation and scattering is generally described by

$$A(f, t) = A_0 e^{\frac{-\pi f t}{Q(f)}} \quad (3.8)$$

where A_0 is the initial amplitude that corresponds to the source (thus not affected by attenuation effects), $A(t)$ is the amplitude after travelling for time t , f is the frequency and $Q(f)$ is the frequency depended quality factor described as

$$Q(f) = Q_0 f^a \quad (3.9)$$

Quality factor Q depends majorly on the velocity of the layers that the wave travels through. Also, it differs for P and S waves. Two mechanisms are responsible for the amplitude decay caused by Q : intrinsic Q due to heat loss (seismic absorption) and redistribution of energy due to scattering. The quality factor is estimated to strongly vary regionally in the lithosphere, while being more stable in the earth interior.

The signal spectrum is affected by attenuation in two ways: change of the shape, which is related with the corner frequency estimation, and change of the flat level, which is related with seismic moment calculation. There are a lot of proposed equations, both theoretical and empirical, that describe attenuation effects. In local studies, Q is considered constant along the ray path, although it may increase with depth. On the other hand, for a continuously changing Q , responding to travelling through a lot of layers, we can write

$$A(f, t) = A_0 e^{-\pi f \int_{path} \frac{dt}{Q(r, f)}} = A_0 e^{-\pi f t^*} \quad (3.10)$$

where t^* is defined as

$$t^* = \int_{path} \frac{dt}{Q(r, f)} = \frac{T}{Q_{av.}(f)} \quad (3.11)$$

where r is the hypocentral distance, T is the total travel time along the path and $Q_{av.}$ is the average Q value along the path, as presented in Havskov and Ottemöller (2010). That means, for teleseismic body waves, t^* is often nearly constant for different travel times, due to increasing Q with depth, counteracting the increase in ray path length (Lay and Wallace, 1995).

3.4 Geometrical spreading

The geometrical spreading effect depends mainly on the distance and the wave type. At local distances, this term can be simply expressed as

$$G(\Delta, h) = \frac{1}{\sqrt{\Delta^2 + h^2}} = \frac{1}{r} \quad (3.12)$$

This is the simple assumed geometrical spreading effect used for short distances. A lot of empirical and theoretical approximations are proposed, all yielded under the assumption that $G(\Delta, h)$ depends on distance, wave type and depth. It is also assumed to be regional independent.

As for the larger teleseismic distances, there is not a simple equation to describe the body wave spreading effects. According to Stein and Wyssession (2003) and Okal (1992), the geometrical spreading is proportional to the second derivative of the travel time curve and, accordingly, can be calculated by travel time curves and earth models. Similarly with the regional and local distances, we can describe the $G(\Delta, h)$ term for teleseismic distances as

$$G(\Delta, h) = \frac{1}{g_d} \quad (3.13)$$

where g_d is called geodistance, and refers, in general, to the travelled distance. The unit of this expression is km^{-1} . There are many

difficulties in trying to approach this parameter in a detailed manner for the teleseismic distances. The following empirical relation, which is proposed by Havskov and Ottemöller (2010), can be applied in distances 30°-90° and approximate the geometrical spreading effect, in accordance with the Bullen tables,

$$\frac{1}{g_d} = \frac{0.0048}{27.0 + \Delta} \quad (3.14)$$

where the left part is the $G(\Delta, h)$ term and Δ is the epicentral distance. Figure 3.4 shows the differences between the two aforementioned approaches. We can see that using the formula of Havskov and Ottemöller (2010), leads to larger seismic moment values, according to Equation 3.14.

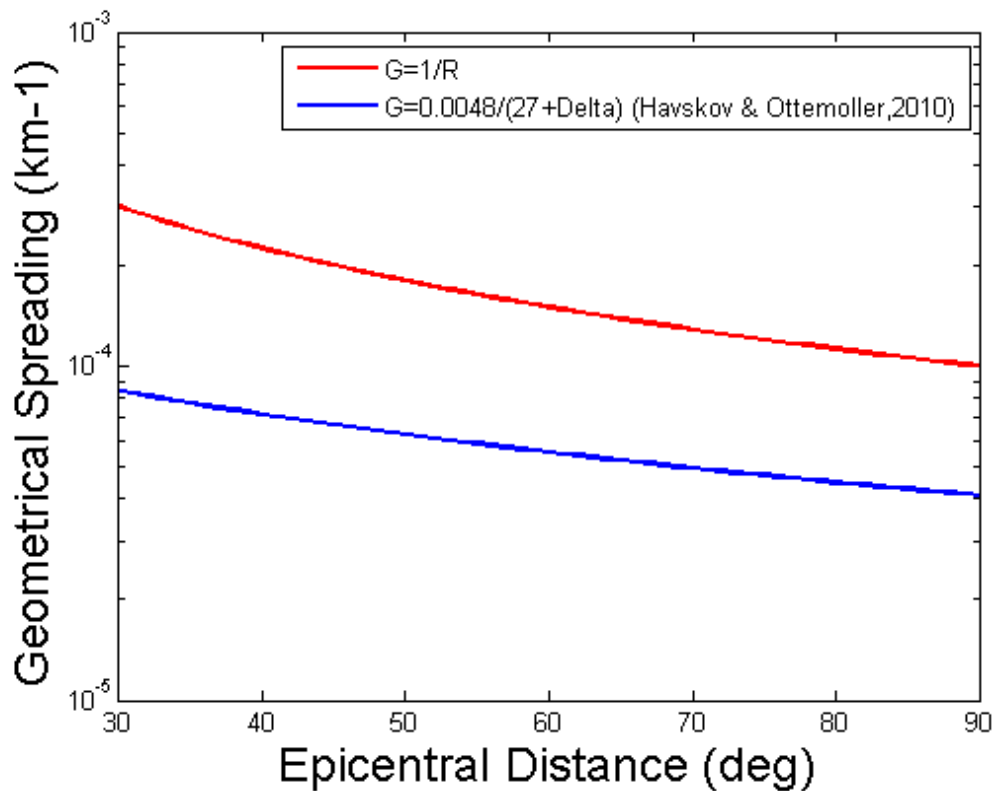


Figure 3.4. Geometrical spreading functions for teleseismic distances.

3.5 Source parameters derived from spectral analysis

The fault dimensions, the slip and the stress drop can easily be derived from the results of spectral analysis, in regard to seismic moment and corner frequency.

As for the fault dimensions, there are several models responding to different fault shapes, fault mechanisms, among others. Brune (1970) and Madariaga (1976) assume a circular fault model of radius R , related to corner frequency, f_c , and shear velocity, V_s , firstly as

$$R = \frac{0.50 V_s}{f_c} \quad (3.15)$$

according to Brune (1970), and secondly as

$$R = \frac{0.32 V_s}{f_c} \quad (3.16)$$

according to Madariaga (1976). Following Aki (1972), the stress drop, $\Delta\sigma$, is related to the fault area, S , and seismic moment, M_0 , as

$$\Delta\sigma = c \frac{M_0}{S^{3/2}} \quad (3.17)$$

where c is a constant related to the geometry of the crack. According to Eshelby (1952), for circular faults

$$c = \frac{7}{16} \pi^{3/2} \quad (3.18)$$

resulting in

$$\Delta\sigma = \frac{7}{16} \frac{M_0}{R^3} \quad (3.19)$$

As for the average slip on the fault, U , it can be computed in regard to seismic moment M_0 , fault area, S , and rigidity μ , following

$$M_0 = \mu S U \quad (3.20)$$

Since the 24/05/2014 North Aegean earthquake is mostly related to strike-slip conditions, the models of Wells and Coppersmith (1994) and Papazachos et al. (2004) are examined as well. These models assume a rectangular strike-slip fault, whose dimensions, length L

and width W , as well as the fault slip, U , are related to the moment magnitude M_w as

$$\begin{aligned} \log L &= 0.59M_w - 2.30 \\ \log W &= 0.23M_w - 0.49 \\ \log U &= 0.68M_w - 2.59 \end{aligned} \quad (3.21)$$

according to Papazachos et al. (2004) for the Greek region, and as

$$\begin{aligned} \log L &= 0.62M_w - 2.57 \\ \log W &= 0.27M_w - 0.76 \\ \log U &= 0.90M_w - 6.32 \end{aligned} \quad (3.22)$$

according to Wells and Coppersmith (1994) for global application. Following Knopoff (1957), the c parameter of Equation 3.17, for buried strike-slip faults, is

$$c = \frac{4}{\pi} \left(\frac{L}{W} \right)^{1/2} \quad (3.23)$$

resulting in

$$\Delta\sigma = \frac{4}{\pi} \frac{M_0}{W^2 L} \quad (3.24)$$

3.6 Spectral analysis application

3.6.1 Signal-to-noise analysis and data preparation

As previously stated, for the spectral analysis of the 24/05/2014 mainshock, broadband teleseismic records were used, from stations with epicentral distance between 30-90 degrees, both in vertical and horizontal components. The waveforms were edited and processed with the SAC software (Goldstein and Snoke, 2005). Using the SAC 'transfer' command and the pole-zero files of the stations, I deconvolved the instrument response, in order to obtain the ground motion.

Before further processing of the data, it is essential to perform a 'signal-to-noise' examination. The aim is to define the frequency range, in which the amplitude of the seismic signal is larger than the pre-event noise amplitude. The observed data can be used only in this specific frequency range. Otherwise, it is possible to confound the noise signal with the seismic signal, resulting in false estimations.

After the determination of the frequency range limits, it is essential to apply a band-pass, high-pass or low-pass filter with the respective corner frequencies, on the time-series data, in order to remove the noise. This is essential for every application and process that could be applied on signals. The most common convention for the definition of the seismic signal frequency band, is that the signal-to-noise ratio equals at least 3:1, which means that the signal spectrum must be 3 times larger than the noise spectrum. In this study, the determination of the frequency limits is performed visually on overlay signal-to-noise spectrum plots.

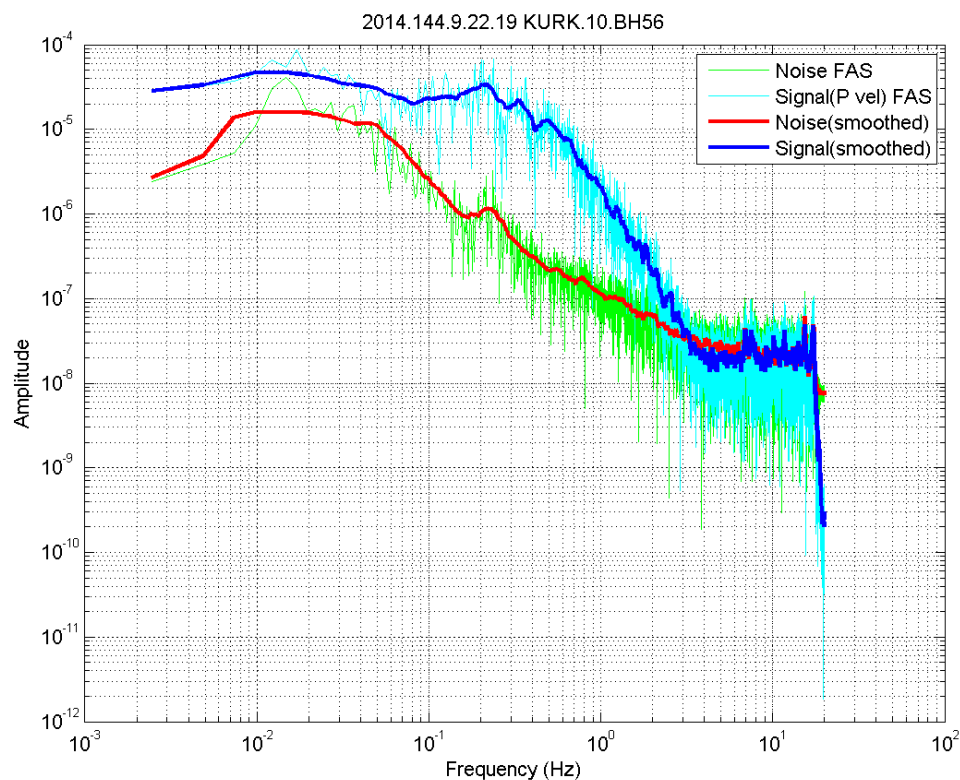


Figure 3.5. Noise and P-wave amplitude spectra for the Kurchatov station in Kazakhstan.

For the signal-to-noise analysis, I used pre-event noise and signal windows of equal time duration for each station record. Fast Fourier Transform was applied in both the signal and noise time windows. Finally, I created signal-to-noise overlay plots for each station component and visually estimated the earthquake frequency band, in which the signal was larger than the noise amplitude. The station components which had a very low or negative signal-to-noise ratio were removed and not further used. The overlay signal-to-noise plots are all presented in Appendix A.

The most common frequency band for the data of this study was from 0.01 to 2 Hz. Therefore, all the waveforms were band-pass filtered from 0.01 to 2 Hz, in order to remove the noise. The records, whose signal-to-noise ratio was not compatible with these limits, were rejected. This bandpass filter is commonly used at teleseismic records.

It is highly important to make sure that the expected corner frequency is not filtered. There are many proposed formulas to estimate the expected corner frequency, before it is actually calculated by spectral analysis. According to Havskov and Ottemöller (2010), assuming a stress drop of 30 bars and a V_s of 3.5 km/sec, the f_c - M_w relation is

$$\log(f_c) = 2.35 - 0.5M_w \quad . \quad (3.25)$$

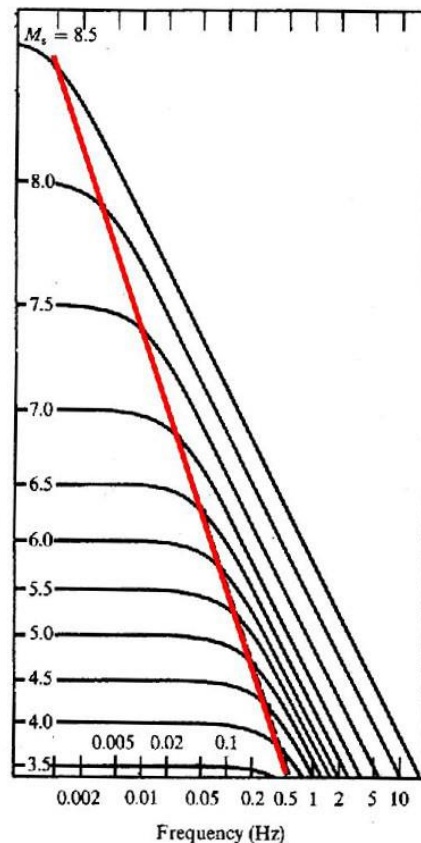


Figure 3.6. Typical corner frequencies for earthquakes of different magnitudes (Aki and Richards, 2002).

Once the expected f_c value is known, we need to make sure that is not beyond the filtering corner limits. Otherwise, f_c would be marked

at the point in which the spectrum starts to decrease due to the filter and not due to the signal.

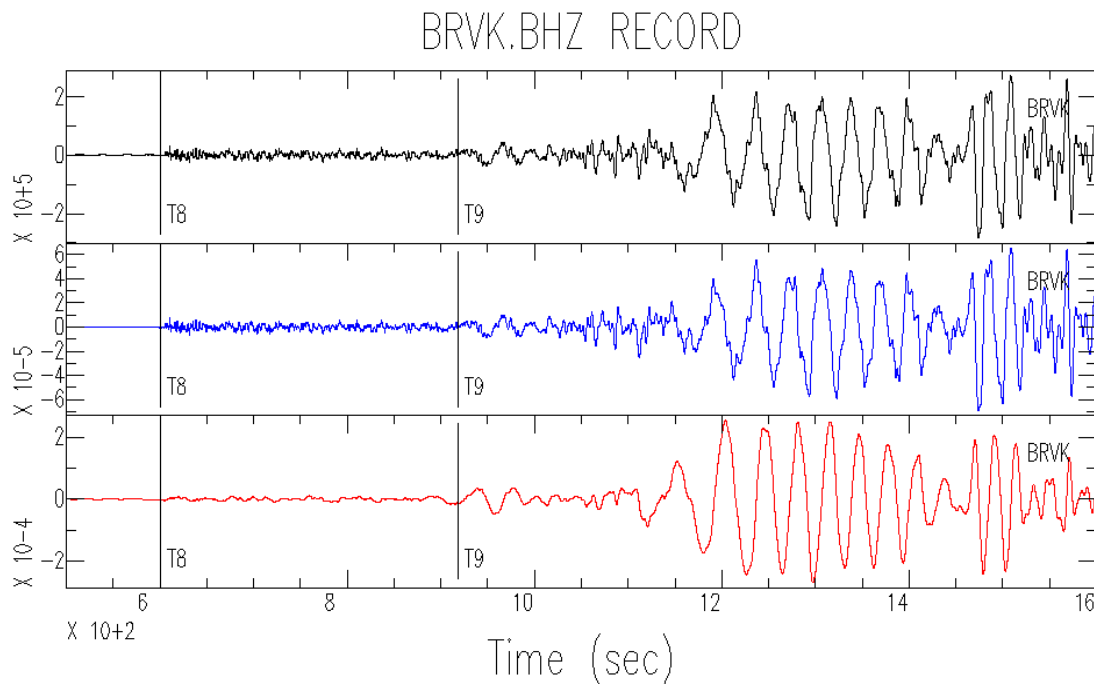


Figure 3.7. Data Preparation of Borovoye station record in Kazakhstan (vertical component). Top: raw waveform in counts, Medium: Instrument corrected and bandpass filtered in 0.01-2 Hz in m/s , Bottom: Integrated to displacement in meters. T8 and T9 markers represent the P and S arrivals, respectively.

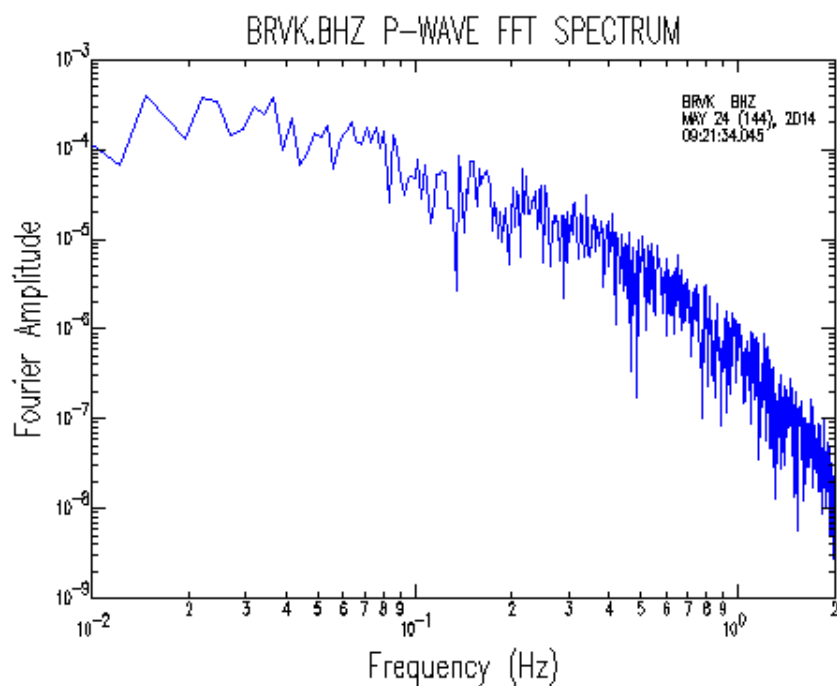


Figure 3.8. P-wave Fourier amplitude spectrum of displacement of the Borovoye station record in Kazakhstan (vertical component).

This analysis was made for both P and S wave trains. Using the 'cutim' command, the P-wave train signals were cut from the vertical (*BHZ) components. Similarly, the S-wave train signals were cut from E-W (*BHE) and N-S (*BHN) horizontal components. With the 'fft' SAC command, the Fourier spectrum of each waveform was obtained. These P and S spectrums were used for the process of spectral analysis. The final spectrums are, also, checked for providing a good azimuthal distribution.

- r *SAC
- setbb pzfile SAC_PZ*
- transfer from polezero subtype %pzfile to vel
- bp co 0.01 2 n 4 p 2
- rmean
- rtrend
- taper
- int
- ppk
- cuterr fillz
- cutim
- rmean
- rtrend
- taper
- fft

Figure 3.9. Brief presentation of SAC commands, used for the data preparation in spectral analysis.

3.6.2 Application procedure

The aim of the spectral analysis is to estimate the seismic moment and corner frequency of the 24/05/2014 North Aegean earthquake. The data preparation was carried out in SAC and the scalar moment and corner frequency determination was held in MATLAB.

In order to determine the seismic moment, the flat spectrum level, Ω_0 , of each waveform is measured. Next, using the following equation

$$M_0 = \frac{\Omega_0 4\pi\rho v^3}{\Re_{\theta\phi} \times 2.0 \times G(\Delta, h)} \quad (3.26)$$

where $\mathfrak{R}_{\theta\phi}$ is the radiation pattern effect, the scalar seismic moment is derived. In this equation, velocity, v , is 6.5 km/s for P waves and 3.6 km/s for S waves. The density value, ρ , is 2.8 g/cm³. As for the radiation pattern effect, R , it is 0.52 for P waves and 0.63 for S waves (Aki and Richards, 2002). The geometrical spreading term, $G(\Delta, h)$, is proportional to Δ and is derived from Equation 3.14.

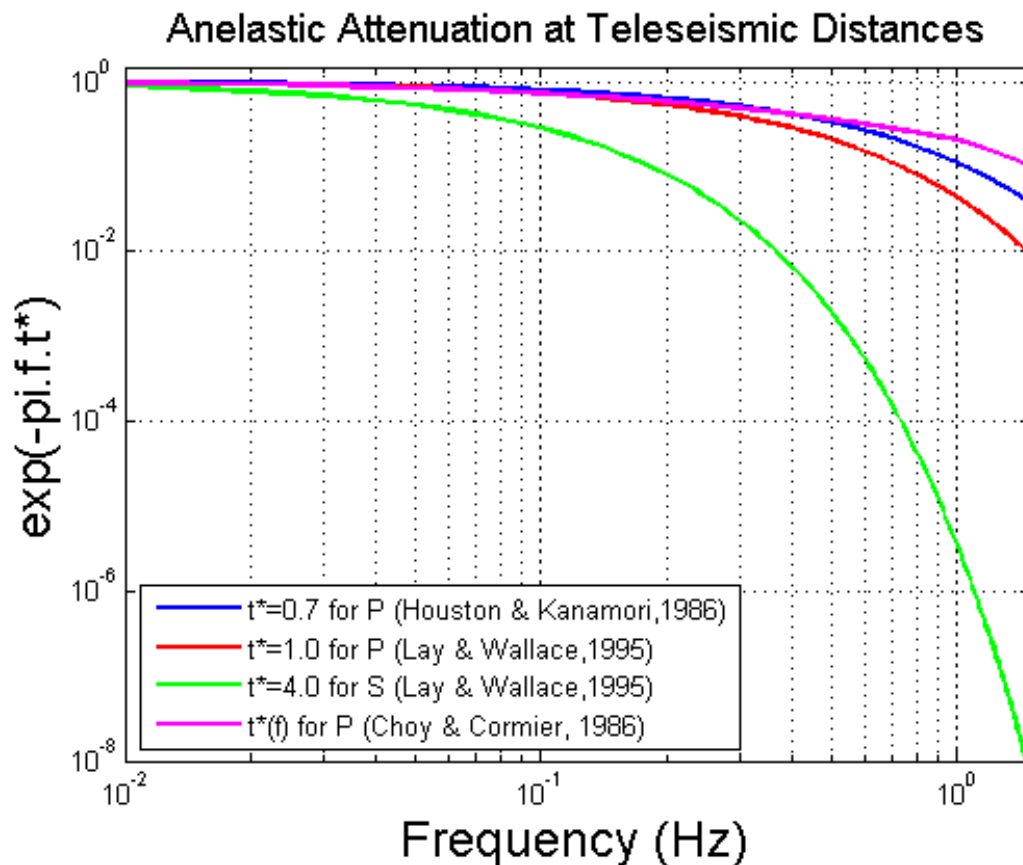


Figure 3.10. Anelastic attenuation models proposed by Houston and Kanamori (1986), Futterman (1962) (followed by Lay and Wallace, 1995) and Choy and Cormier (1986), for teleseismic distances.

For the corner frequency estimation, linear fitting is applied both in the flat part and the descending part. The frequency of the intersection point of the two lines is the corner frequency (Fig. 3.11).

As it was previously mentioned, attenuation effects are responsible for changes in both shape and amplitude of the source spectrum. Therefore, it is highly important that the spectrums are corrected for attenuation, before the Ω_0 and f_c estimation, as it is described in Chapter 3.1.3. In epicentral distances of 30-90 degrees, t^* is rather

constant. Various formulas have been proposed for this value and are presented in Figure 3.10. In this study, t^* is 1 for P waves and 4 for S waves, following Futterman (1962) and Lay and Wallace (1995). According to Stein and Wysession (2003), correction for t^* is valid for frequencies below 1 Hz.

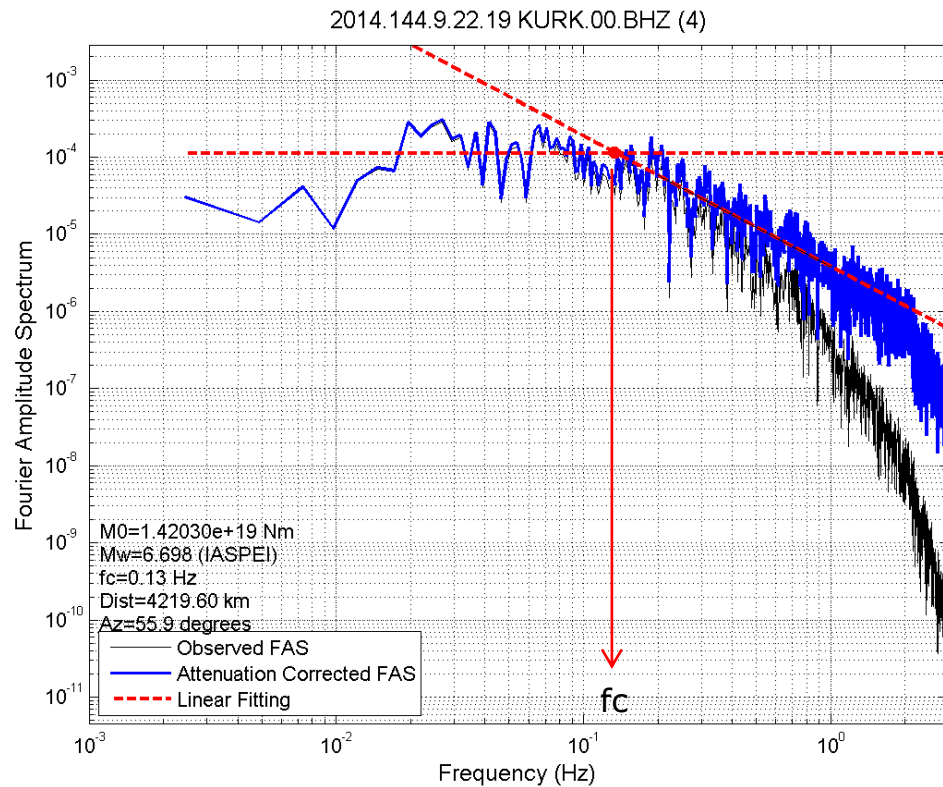


Figure 3.11. P-wave Fourier amplitude spectrum of displacement of Kurchatov station record in Kazakhstan (vertical component). Blue color: Attenuation corrected spectrum, used for moment magnitude (M_w) and corner frequency (f_c) determination. Black color: Uncorrected spectrum. Red color: Linear fitting of the flat and descending part. The cross-section of the fitting lines represents the corner frequency f_c .

In Figures 3.10 and 3.11, we can see that the attenuation correction for P waves does not result in big changes, since t^* factor is around unity in the valid frequency band. On the contrary, the t^* factor for S waves can reach values of nearly $1E-06$, near the frequency of 1 Hz. According to Equation 3.10, multiplication with such minor values results in a continuously ascending spectrum, which is not the familiar form of the seismic source spectrum, in which the amplitude decreases after the corner frequency. Figure 3.12 shows the overlay of the observed and the attenuation-corrected spectrums, as well as

a failed attempt of a linear fitting in flat and descending parts of the corrected spectrum. It is interesting to observe the difficulty of the f_c determination in the attenuation-corrected spectrum and compare it with the uncorrected spectrum, in which the f_c is much more obvious.

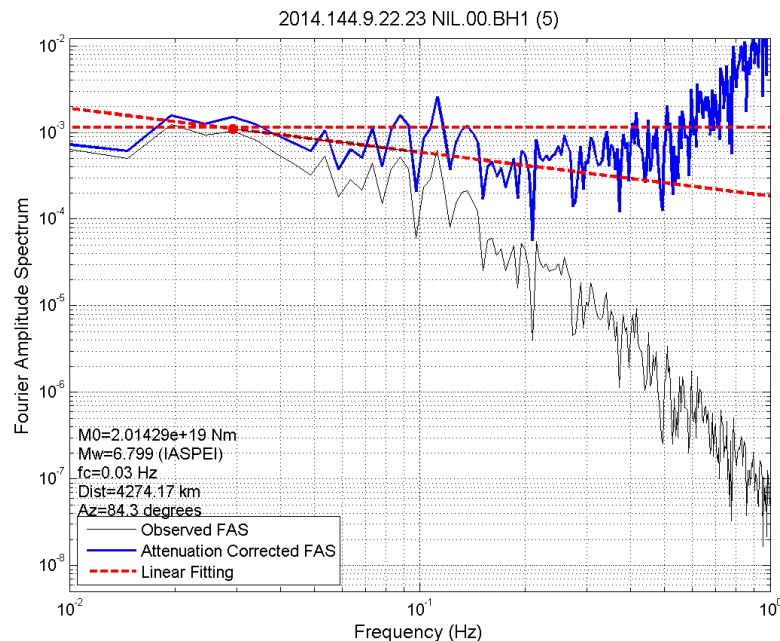


Figure 3.12. Ambiguous S-wave displacement spectrum of Nilore station record in Pakistan (E-W component). Blue color: Attenuation corrected S-wave spectrum. The ω^{-1} part is not visually separated from flat level part. Black color: Uncorrected spectrum. Red color: Problematic linear fitting.

This is the reason that S-wave teleseismic spectral analysis is not that common in scientific research. Despite all the difficulties and uncertainties, I attempted to perform spectral analysis on S waves, using the flat level of the attenuation corrected spectrum, and the corner frequency of the uncorrected spectrum, which, in most cases, happened to be similar to the f_c derived from P wave analysis. After all, the corner frequency represents the frequency, below which, the signal amplitude describes the major signal of the earthquake, and above which the amplitude decreases drastically, not representing the earthquake signal. In this case, f_c can be derived from the raw spectrum, as well (Fig. 3.13).

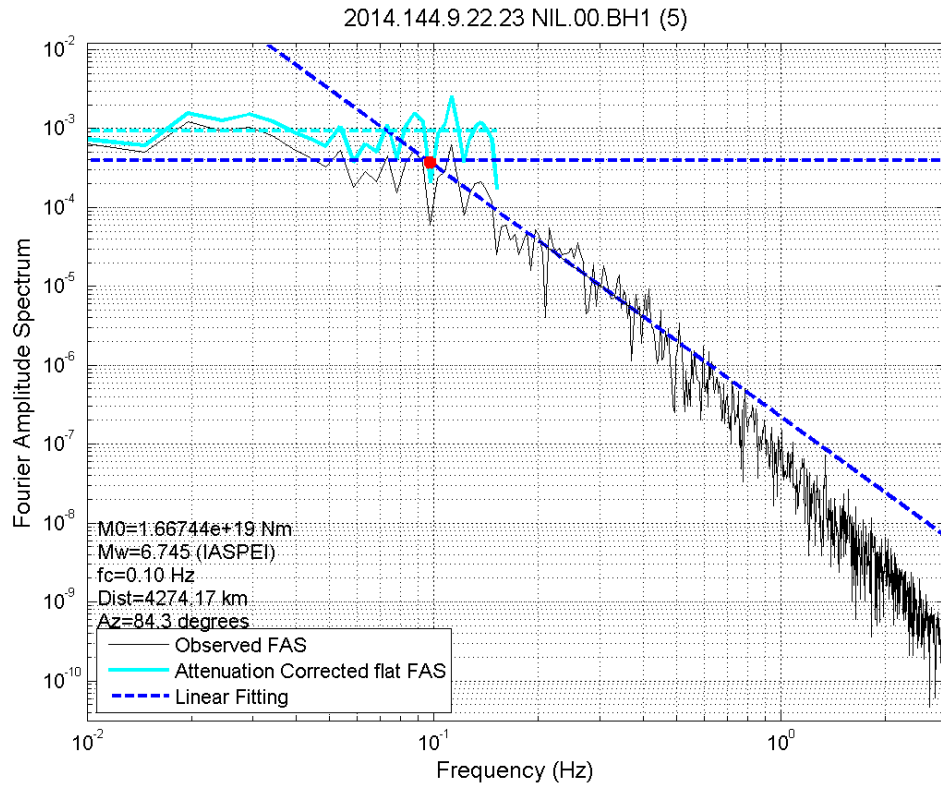


Figure 3.13. S-wave displacement spectrum of Nilore station in Pakistan (E-W component). The flat part is defined from the attenuation corrected spectrum (cyan color) and the corner frequency from the observed spectrum (black color). Blue color: Linear fitting. Red color: Corner frequency (f_c).

After the seismic moment and corner frequency determination, the moment magnitude M_w , developed by Kanamori (1977) and Hanks and Kanamori (1979), is calculated for each waveform, using the IASPEI recommended standard form as

$$M_w = \frac{2}{3} \log M_0 - 6.07 \quad (3.27)$$

where the moment M_0 is measured in Nm. The seismic moment is a direct measure of the tectonic size of the earthquake, and therefore does not saturate, provided that it is measured in frequencies higher than the corner frequency of the radiated source spectrum (Havskov and Ottemöller, 2010).

Finally, scalar moment (M_0), corner frequency (f_c) and moment magnitude (M_w) are calculated for each waveform. The waveform fittings along with the resulted seismic parameters are presented in Appendix B, for each one of the selected stations.

3.7 Spectral analysis results

The spectral analysis for the case of 24/05/2014 North Aegean earthquake was performed for P waves, using vertical (*BHZ) components, and for S waves using E-W (*BHE) and N-S (*BHN) components. The stations for each one of the BHZ, BHE and BHN groups were chosen based on azimuthal coverage and high signal-to-noise ratio. The results of M_0 and f_c for each record are shown in Tables 3.1, 3.2 and 3.3, for P, S (E-W) and S (N-S) components, respectively, along with the resulted mean values for each group.

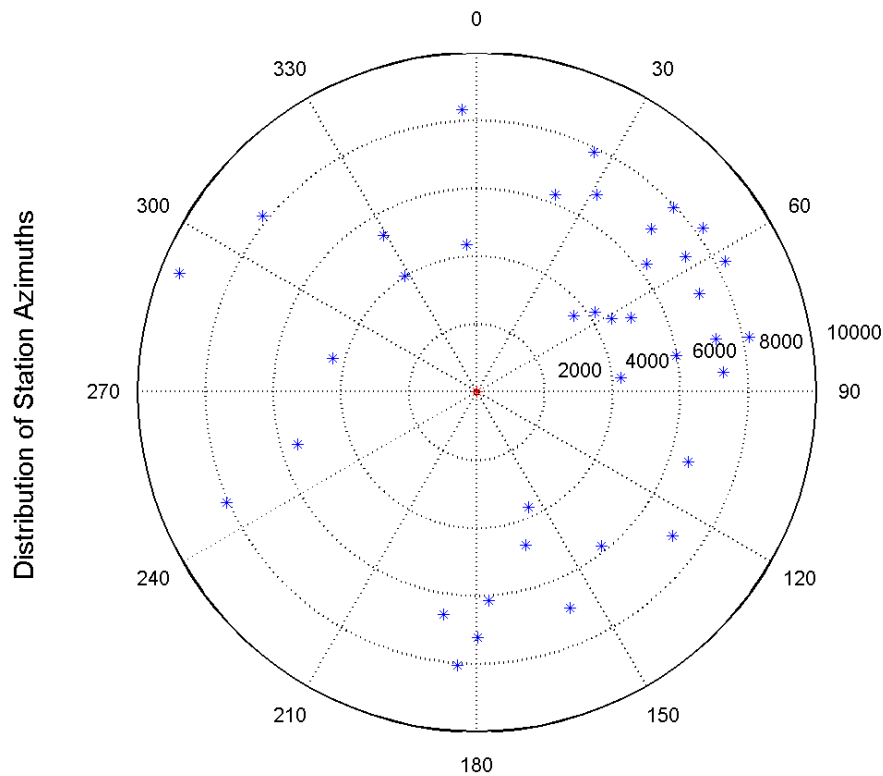


Figure 3.14. Azimuthal coverage of stations used in P-wave spectral analysis. The center of the circle represents the earthquake epicenter. The epicentral distances are presented in km.

Table 3.1. Seismic moment (M_0) and corner frequency (f_c) values derived from P-wave spectral analysis for each station (vertical component *BHZ).

Station (*BHZ)	Azimuth (degrees)	Distance (km)	Ω_0 (E-03 m)	f_c (Hz)	Moment (E+19 Nm)
BRVK	51.864	3643.8	0.1080	0.10	1.2497
FURI	155.649	3719.2	0.0712	0.14	0.8337
BORG	328.093	4022.6	0.0482	0.26	0.5899
KURK	55.856	4219.6	0.1129	0.13	1.4203
NIL	84.320	4274.2	0.0938	0.15	1.1891
KBS	355.909	4343.5	0.0840	0.08	1.075
CMLA	283.230	4356.6	0.0721	0.20	0.9237
MAKZ	61.424	4529.6	0.1349	0.13	1.7694
KMBO	162.329	4742.2	0.0511	0.14	0.6894
WMQ	64.114	5050.1	0.0964	0.17	1.3514
SFJD	329.295	5366.4	0.0518	0.11	0.7551
SACV	253.787	5497.9	0.0540	0.13	0.799
MSEY	141.013	5851.4	0.0616	0.10	0.9494
LSA	79.512	5978.2	0.0445	0.13	0.6966
LSZ	176.715	6158.2	0.0465	0.09	0.7426
TIXI	21.740	6254.8	0.0492	0.15	0.7937
ULN	52.967	6285.6	0.0688	0.13	1.1131
PALK	108.152	6579.6	0.0531	0.10	0.8857
TSUM	188.555	6635.3	0.0484	0.11	0.8129
YAK	31.363	6816.1	0.0498	0.13	0.8522
ABPO	156.602	6945.1	0.0424	0.14	0.7355
HIA	46.954	7036.6	0.0588	0.10	1.0286
DGAR	66.088	7170.3	0.0486	0.13	0.8617
XAN	126.291	7150.7	0.0482	0.15	0.8518
KMI	77.560	7218.6	0.0459	0.10	0.8166
LBTB	179.792	7229.4	0.0503	0.10	0.8962
CHTO	85.438	7305.7	0.0524	0.09	0.9404
BJT	57.106	7349.2	0.0473	0.14	0.8525
MA2	26.066	7860.2	0.0516	0.11	0.9759
MDJ	46.882	7946.4	0.0478	0.12	0.9123
RCBR	246.193	8067.3	0.0331	0.11	0.6374
SUR	184.062	8059.4	0.0460	0.21	0.8871
SSPA	309.418	8165.3	0.0344	0.11	0.6685
QIZ	78.648	8208.4	0.0407	0.11	0.7951
INCN	54.175	8249	0.0471	0.15	0.9234
SSE	62.253	8297.3	0.0447	0.11	0.8801
COLA	357.023	8330.2	0.0377	0.15	0.7451
GTBY	291.778	9450.6	0.0368	0.18	0.7974
Mean Values				0.14 ± 0.03	0.9074 ± 0.2

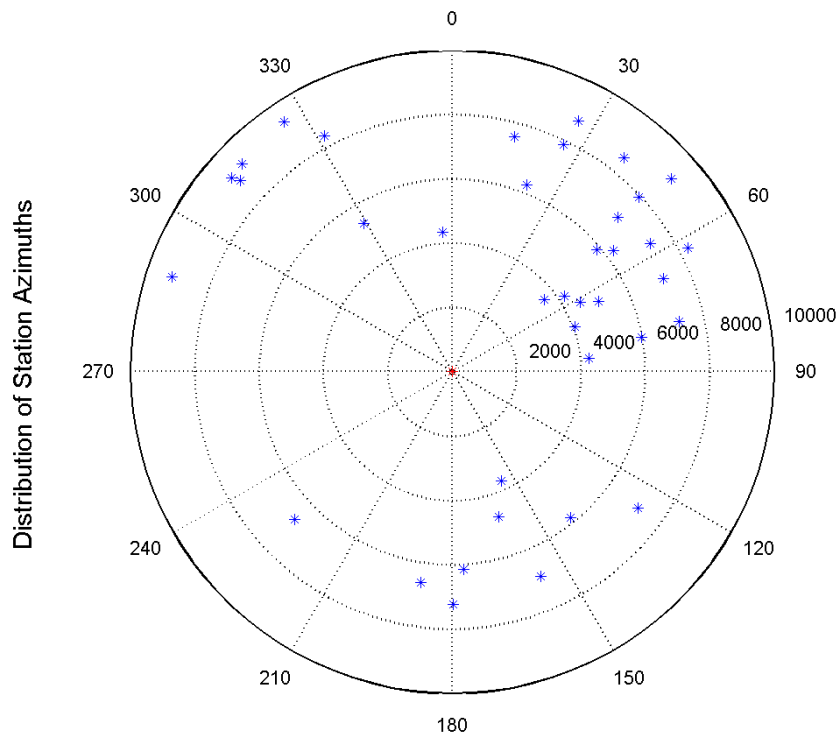


Figure 3.15. Azimuthal coverage of stations used in S-wave (E-W component) spectral analysis. The center of the circle represents the earthquake epicenter. The epicentral distances are presented in km.

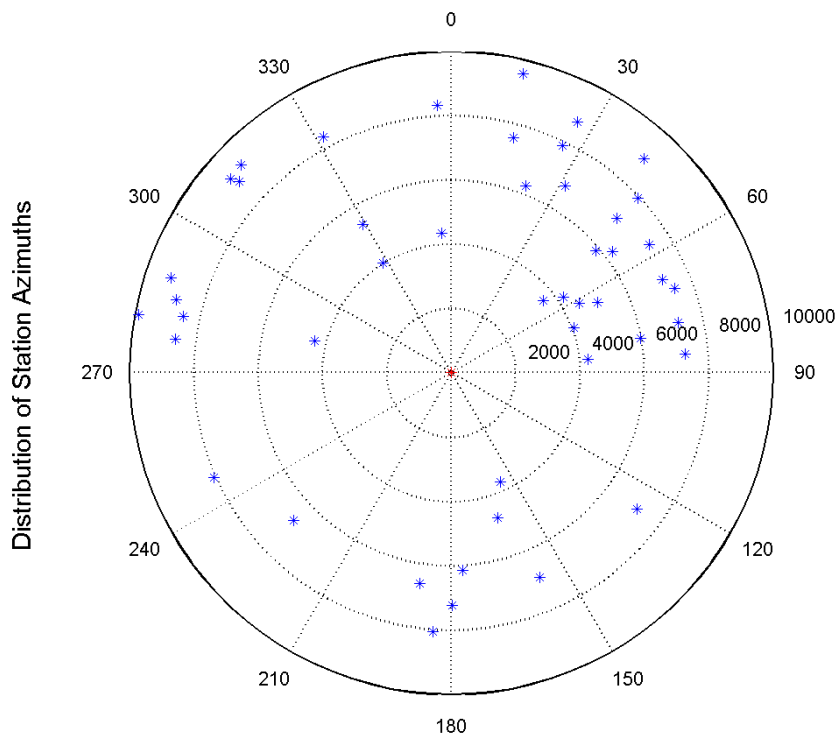


Figure 3.16. Azimuthal coverage of stations used in S-wave (N-S component) spectral analysis. The center of the circle represents the earthquake epicenter. The epicentral distances are presented in km.

Table 3.2. Seismic moment (M_0) and corner frequency (f_c) values derived from S-wave spectral analysis for each station (horizontal E-W component *BHE).

Station (*BHE)	Azimuth (degrees)	Distance (km)	Ω_0 (E-03 m)	f_c (Hz)	Moment (E+19 Nm)
BRVK	51.864	3643.8	0.1712	0.07	1.9812
FURI	155.649	3719.2	0.0959	0.08	1.1222
AAK	69.814	4052.7	0.0931	0.07	1.1444
KURK	55.856	4219.6	0.0583	0.10	0.7336
NIL	84.320	4274.2	0.1316	0.10	1.6674
KBS	355.909	4343.5	0.0760	0.10	0.9725
MAKZ	61.424	4529.6	0.0802	0.11	1.0525
KMBO	162.329	4742.2	0.0393	0.11	0.5299
WMQ	64.114	5050.1	0.0850	0.11	1.1920
SFJD	329.295	5366.4	0.0478	0.10	0.6973
MSEY	141.013	5851.4	0.0592	0.11	0.9137
TLY	49.700	5894.8	0.1098	0.11	1.7020
LSA	79.512	5978.2	0.1019	0.08	1.5944
LSZ	176.715	6158.2	0.0595	0.09	0.9499
TIXI	21.740	6254.8	0.0945	0.10	1.5240
ULN	52.967	6285.6	0.0889	0.09	1.4384
TSUM	188.555	6635.3	0.0536	0.09	0.8996
ASCN	226.769	6718.5	0.0509	0.10	0.8616
ABPO	156.602	6945.1	0.0359	0.10	0.6215
HIA	46.954	7036.6	0.0653	0.09	1.1420
DGAR	66.088	7170.3	0.0538	0.12	0.9530
XAN	126.291	7150.7	0.0760	0.08	1.3444
KMI	77.560	7218.6	0.0530	0.11	0.9442
LBTB	179.792	7229.4	0.0446	0.12	0.7950
BJT	57.106	7349.2	0.0745	0.11	1.3437
BILL	14.745	7557.7	0.0465	0.09	0.8545
MA2	26.066	7860.2	0.0939	0.10	1.7770
MDJ	46.882	7946.4	0.0713	0.09	1.3604
SSE	62.253	8297.3	0.0610	0.08	1.2000
FFC	331.521	8351.1	0.0298	0.12	0.5901
YSS	38.667	8530.1	0.0818	0.09	1.6427
PET	26.658	8734.4	0.0845	0.07	1.7277
WCI	311.994	8883.8	0.0407	0.10	0.8422
MAJO	48.590	9086.0	0.0504	0.08	1.0602
WVT	311.344	9144.3	0.0351	0.10	0.7434
CCM	314.667	9203.0	0.0376	0.10	0.8000
SDDR	288.703	9214.0	0.0458	0.08	0.9738
RSSD	326.016	9377.5	0.0335	0.10	0.7216
Mean Values				0.10 ± 0.01	1.116 ± 0.3

Table 3.3. Seismic moment (M_0) and corner frequency (f_c) values derived from S-wave spectral analysis for each station (horizontal N-S component *BHN).

Station (*BHN)	Azimuth (degrees)	Distance (km)	W0 (E-03 m)	f_c (Hz)	Moment (E+19 Nm)
BRVK	51.864	3643.8	0.1132	0.10	1.3099
FURI	155.649	3719.2	0.0637	0.08	0.7462
BORG	328.093	4022.6	0.0509	0.16	0.6226
AAK	69.814	4052.7	0.1305	0.07	1.6036
KURK	55.856	4219.6	0.1214	0.11	1.5270
NIL	84.320	4274.2	0.1094	0.09	1.3862
KBS	355.909	4343.5	0.1035	0.08	1.3236
CMLA	283.230	4356.6	0.0899	0.16	1.1517
MAKZ	61.424	4529.6	0.1119	0.09	1.4683
KMBO	162.329	4742.2	0.0476	0.09	0.6417
WMQ	64.114	5050.1	0.0648	0.10	0.9088
SFJD	329.295	5366.4	0.0483	0.11	0.7045
TLY	49.700	5894.8	0.1518	0.07	2.3524
LSA	79.512	5978.2	0.0844	0.09	1.3204
LSZ	176.715	6158.2	0.0405	0.10	0.6461
TIXI	21.740	6254.8	0.0939	0.09	1.5142
ULN	52.967	6285.6	0.1073	0.09	1.7353
TSUM	188.555	6635.3	0.0393	0.11	0.6591
ASCN	226.769	6718.5	0.0533	0.11	0.9025
YAK	31.363	6816.1	0.0780	0.07	1.3342
ABPO	156.602	6945.1	0.0389	0.09	0.6732
HIA	46.954	7036.6	0.0988	0.09	1.7273
DGAR	66.088	7170.3	0.0484	0.10	0.8573
XAN	126.291	7150.7	0.0707	0.09	1.2506
KMI	77.560	7218.6	0.0575	0.10	1.0230
LBTB	179.792	7229.4	0.0590	0.10	1.0511
CHTO	85.438	7305.7	0.0653	0.10	1.1729
BJT	57.106	7349.2	0.0758	0.11	1.3665
ENH	69.222	7445.4	0.0503	0.10	0.9154
BILL	14.745	7557.7	0.0705	0.10	1.2962
MA2	26.066	7860.2	0.0679	0.11	1.2839
MDJ	46.882	7946.4	0.0689	0.08	1.3132
RCBR	246.193	8067.3	0.0308	0.10	0.5940
SUR	184.062	8059.4	0.0431	0.12	0.8311
COLA	357.023	8330.2	0.0588	0.09	1.1616
FFC	331.521	8351.1	0.0321	0.11	0.6351
ANWB	281.889	8527.6	0.0379	0.07	0.7603
BBGH	276.909	8653.5	0.0825	0.08	1.6752
PET	26.658	8734.4	0.0617	0.07	1.2609
SJG	284.889	8857.8	0.0305	0.08	0.6296

WCI	311.994	8883.8	0.0440	0.10	0.9117
ERM	41.946	8949.4	0.0925	0.08	1.9263
WVT	311.344	9144.3	0.0381	0.09	0.8060
SSM	314.667	9203.0	0.0355	0.08	0.7551
SDDR	288.703	9214.0	0.0458	0.08	0.9736
ADK	13.500	9571.4	0.0391	0.09	0.8563
SDV	280.613	9885.1	0.0290	0.11	0.6499
Mean Values				0.10±0.01	1.110±0.4

In Table 3.4, we can see the mean M_0 , M_w and f_c for each group. The S wave groups yielded the same corner frequency of 0.10 Hz, while the P wave group yielded a slightly higher f_c , equal to 0.14 Hz. Additionally, P waves resulted in the moment magnitude of $M_w=6.56$, while S waves gave a slightly larger magnitude of $M_w=6.62$. These results are very common between P and S waves, due to differences in frequency band, attenuation effects etc. In most cases, P waves are related to higher corner frequencies, as theoretically predicted by Madariaga (1976) and observed by Abercrombie (1995), as well as smaller magnitudes, compared to S waves.

Table 3.4. Mean values of seismic moment (M_0), moment magnitude (M_w) and corner frequency (f_c) for P and S wave spectral analysis.

Group	M_0 (Nm)	M_w (IASPEI)	f_c (Hz)
P (Vertical)	0.9074E+19	6.56	0.14
S (E-W)	1.1160E+19	6.62	0.10
S (N-S)	1.1100E+19	6.62	0.10

Table 3.5 presents the source dimensions along with stress drop, as they are derived from the models of Brune (1970), Madariaga (1976), Wells and Coppersmith (1994) and Papazachos et al. (2004). The models of Brune and Madariaga assume a circular fault of radius R , whereas the models of Papazachos et al. and Wells and Coppersmith concern rectangular strike-slip faults, of length L and width W . The circular models are described by radius and length and the rectangular by length and width. The stress drop, $\Delta\sigma$, is calculated from Equation 3.19 for the circular models and from Equation 3.24 for the rectangular models. The fault slip of the circular models was computed from Equation 3.20. The M_0 and M_w values were taken as the mean values from P and S (EW+NS) results.

Table 3.5. Source dimensions and stress drop derived from the circular models (for $V_s=3.8$ km/s) of Brune (1970) and Madariaga (1976), and rectangular strike-slip models of Wells and Coppersmith (1994) and Papazachos et al. (2004).

Model	Fault Shape	Fault Type	Radius (km)	Length (km)	Width (km)	$\Delta\sigma$ (bars)	Slip (m)
Brune (1970)	circular	all	13.6	27.2	-	18	0.57
Madariaga (1976)	circular	all	8.7	17.4	-	67	1.41
<i>Mean Values (circular)</i>			<i>11.15</i>	<i>22.3</i>		<i>43</i>	<i>0.99</i>
Wells and Coppersmith (1994)	rectangular	strike-slip	-	33.2	10.5	35	0.42
Papazachos et al. (2004)	rectangular	strike-slip	-	39.3	10.7	29	0.79
<i>Mean Values (rectangular strike-slip)</i>				<i>36.3</i>	<i>10.6</i>	<i>32</i>	<i>0.60</i>

Spectral analysis of 24/05/2014 North Aegean earthquake yielded a mean magnitude of $M_w=6.6$ and a mean corner frequency of 0.12 Hz. The fault length of the circular models is ~ 22 km and the slip reaches ~ 1 m, while the rectangular strike-slip models give a bigger length of 36 km and a smaller slip of 0.6 m. The circular models have large differences among them. For this reason, as well as due to their strike-slip specialization, only the rectangular models of Wells and Coppersmith (1994) and Papazachos et al. (2004) are considered in this study.

At this point, it is of major importance to clarify that, when it comes to a multiple-source event, spectral analysis yields a corner frequency representing the strongest sub-source, and not the whole earthquake source. According to Bormann and Saul (2009), for large events which often consist of multiple ruptures, like this one, the corner frequency will not represent the whole length of the fault, but only the largest subevent. Therefore, spectral analysis would underestimate both the source dimension and seismic moment. On the contrary, in cases of single events, spectral analysis is much more reliable to describe the whole rupture.

The seismic moment and magnitude that resulted from spectral analysis is not that similar to the respective published values. The GCMT solution give a magnitude of $M_w=6.9$, obtained by centroid moment tensor inversion. The last mentioned procedure is more reliable than spectral analysis, due to the use of long period waves

with periods larger than the whole rupture time of the multiple event. In other words, the GCMT solutions represent the energy of the whole earthquake, and not just the biggest subevent.

It seems that this is the case for this study, as well. Spectral analysis yielded a fault length of 36 km, corresponding to a M_w of 6.6, while the aftershock distribution define a much bigger fault length of ~ 100 km (Evangelidis, 2015) and the bigger published magnitude is 6.9. Therefore, the results of 36 km length and magnitude of 6.6, might represent only the biggest subevent of this multiple earthquake. This is examined in Chapter 5.

The fault length of 100 km represents earthquakes of much larger magnitudes of $M_w \approx 7.4$, following the empirical relations of Wells and Coppersmith (1994) for strike-slip faults. The larger published magnitude for the 24/05/2014 North Aegean earthquake is $M_w = 6.9$ (GCMT, USGS, HRV, INGV etc) which is much smaller than the 7.4 magnitude, required for an 100 km fault length. The 6.9 magnitude is related to 51 km, according to the empirical relations of Wells and Coppersmith (1994). All these arguments indicate the source complexity of the 24/05/2014 North Aegean earthquake. It is obviously not compatible with most of the proposed empirical models, in regard to fault dimensions, as expected for such complex events.

Summing up, spectral analysis was executed in this chapter, in order to determine the seismic moment and geometrical properties of the source. The P and S broadband data were, firstly, filtered for the noise to be removed and, next, Fast Fourier Transform was applied in order to obtain the seismic spectrums. After correcting for attenuation, the M_0 and f_c were calculated by visual linear fitting, with geometrical spreading and radiation pattern effects taken into account as well. This procedure was not simple for S spectrums, due to complexities related with attenuation correction. Only slight differences existed between P and S results. The average M_0 ($\sim 1E+19$ Nm), M_w (~ 6.6) and f_{cP} (0.14 Hz) were, finally, used to estimate the source dimensions and stress drop, yielding an interestingly smaller fault length (~ 36 km) than the 100 km length derived from aftershock distribution, a value that possibly describes only the biggest subevent, and not the whole earthquake.

4 Teleseismic Body Wave Inversion

4.1 Waveform modeling - Basic model

One of the most important fields in Seismology is the determination of the focal mechanisms of the earthquakes. One way to accomplish that, is the use of the polarities of P-wave first motions. Unfortunately, this approach is often inadequate. Additional information about the earthquake parameters is obtained by forward modeling or by inversion (Fig. 4.1). The main idea is the minimization of the residuals between the observed and the calculated waveforms. These methods give, also, a good insight to the determination of the hypocenter depth and the rupture process. The theory of waveform modeling and inversion is presented below, based on the formulations of Stein and Wysession (2003) and references therein.

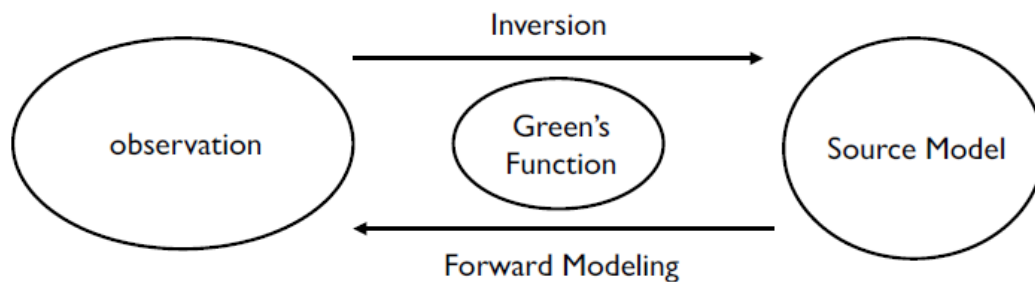


Figure 4.1. Inversion and forward modeling schemes for the estimation of source parameters.

In simple words, we regard the observed seismogram that is recorded at a station, as a convolution of three main factors: the source that generated the earthquake, the structure path that the seismic wave propagated through and the response of the seismometer that recorded the signal. Thus, a seismogram $u(t)$ can be written as

$$u(t) = x(t) * e(t) * q(t) * i(t) \quad (4.1)$$

where $x(t)$ is the source time function, $e(t)$ represents the elastic wave phenomena (geometrical spreading, reflections and conversions at interfaces along the ray path), $q(t)$ is the anelastic attenuation and $i(t)$ is the instrument response (Fig. 4.2).

Convolution in the time domain equals multiplication in the frequency domain, so a seismogram spectrum can be expressed as the product of the source, structure and instrument's response spectra.

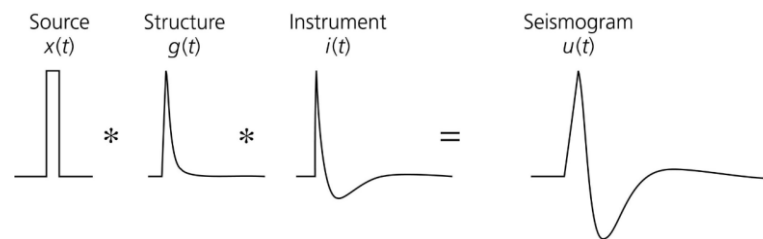


Figure 4.2. Seismogram as the convolution product of source, structure and instrument responses (Stein and Wyession, 2003).

4.1.1 Source time function and directivity

The source time function is, basically, the signal that the earthquake source puts into the ground. It is the source signal produced by the fault rupture and is indicated as the derivative $\dot{M}(t)$ of the seismic moment function $M(t)$

$$M(t) = \mu D(t) S(t) \quad (4.2)$$

where μ is rigidity, $D(t)$ is the history of slip and $S(t)$ is the fault area. In the simplest case where a small fault ruptures instantaneously, the seismic moment function is a step function, whose derivative, a delta function, constitutes the source time function. In reality, fault rupture is not instant and the resulting source time function is more complicated than a simple delta function.

In a more realistic case of a rectangular fault that the rupture takes some time to finish, the radiated signal is not impulsive, as waves arrive firstly from the initial point of rupture and later from points further along, as described in Figure 4.3.

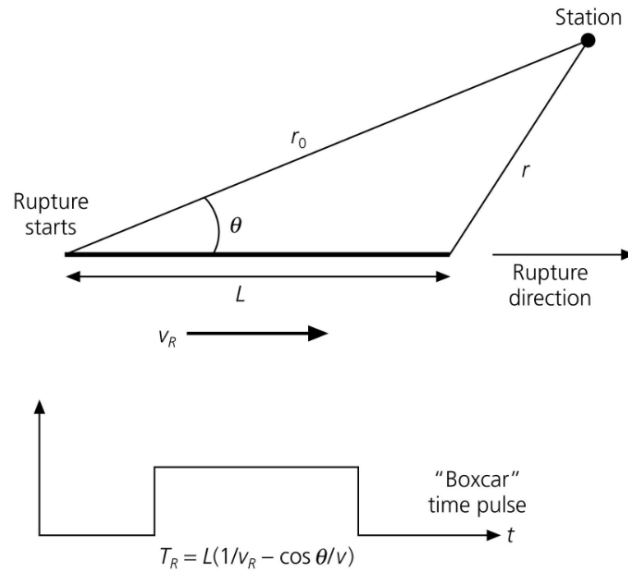


Figure 4.3. For a fault of finite length, the duration of the source time function depends on azimuth, rupture velocity and wave-velocity (Stein and Wyssession, 2003).

Assuming a rupture that propagates with velocity V_r along a fault of length L , and a receiver at distance R_0 and azimuth θ from the initial rupture point, the first wave arrives at time R_0/V , where V is the wave velocity, and the last wave from the last rupture point on the fault, arrives at $L/V_r + R/V$, where R is the distance from this point to the receiver (Fig. 4.3). The law of cosines shows that

$$R^2 = R_0^2 + L^2 - 2 R_0 L \cos \theta \quad (4.3)$$

which for $R \gg L$, is approximately

$$R \approx R_0 - L \cos \theta \quad (4.4)$$

and, as a result, the time pulse due to the fault length is a boxcar of duration

$$T_r = L \left(\frac{1}{V_r} - \cos \frac{\theta}{V} \right) = \left(\frac{L}{V} \right) \left(\frac{V}{V_r} - \cos \theta \right) \quad (4.5)$$

where T_r is the rupture time, as presented in Stein and Wyssession (2003). The maximum duration occurs at 180° from the rupture direction, and the minimum occurs at 0° from the rupture direction.

Of course, all the aforementioned expressions are modified according to the fault shape and rupture propagation directions.

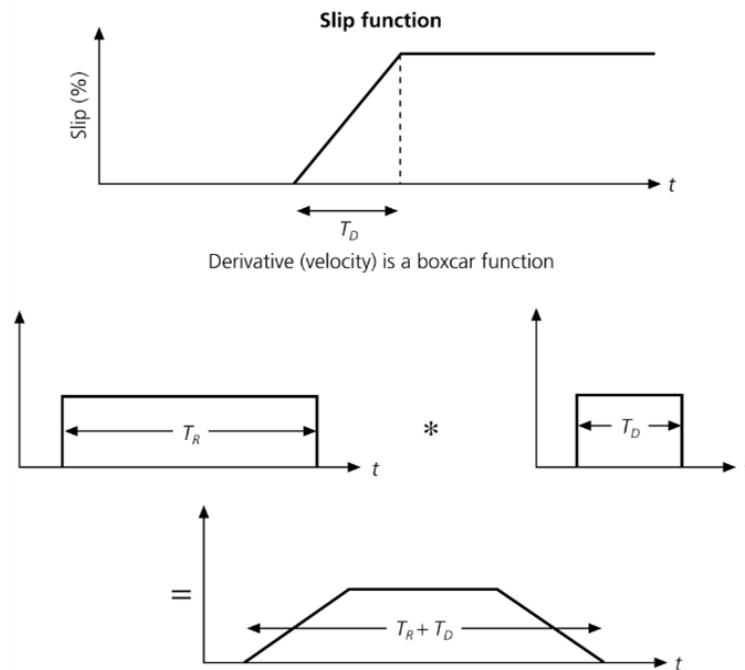


Figure 4.4. The derivation of a trapezoidal source time function from rise and rupture time, according to Stein and Wyssession (2003) (described in the text).

Apart from the source not being a point, but a fault with length L , there is also the fact that slip does not occur instantaneously. The most usual approach is for the slip history to be a ramp function that starts at time 0 and finishes at rise time T_D . The source time function depends on the derivative of the slip history (ramp function) which is a boxcar function, for this circumstance. Convolution of the finiteness and rise time effects yields a trapezoidal shape, that often describes the source time function (Stein and Wyssession, 2003). The length of the trapezoid is the sum of the rise and rupture times (Fig. 4.4). Source time functions could also be approached with other shapes such as triangles, cosine-tapered trapezoids etc. For large earthquakes, which are naturally more complex events, the source time function is more complicated, describing the complication of slip time and space distribution on the fault.

The source radiated pulse is also affected by the azimuth of the receiver in reference to the source. The integral area of the pulse, recorded at a station, has to be the same in all directions, as the Doppler effect does for sound. Thus, because the time duration changes with azimuth, the amplitude of the source time function

changes proportionally, in order to keep the area same in all directions (Fig. 4.5). This effect is called directivity and it is often used to distinguish the fault plane from the auxiliary plane.

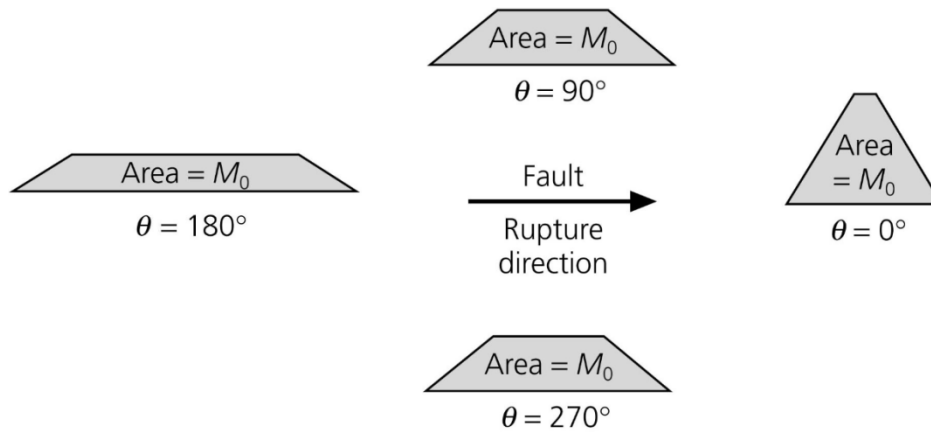


Figure 4.5. Effects of rupture directivity on the source time function (Stein and Wysession, 2003).

4.1.2 Body wave modeling

In the case of shallow earthquakes, we usually model the first few seconds of the P-wave arrival, as the sum of three waves (Fig. 4.6): the direct P-wave, the pP-wave (reflected from the surface) and the sP-wave (converted at the surface). It is wise to use epicentral distances $30^\circ < \Delta < 90^\circ$ from the source, for the effects of the mantle triplications and core-mantle boundary complications to be ignored.

Based on the four factors in Equation 4.1, the displacement u , as a function of time t , distance Δ and azimuth φ , for the three aforementioned wave phases at distances $30^\circ < \Delta < 90^\circ$, can be synthesized as

$$u(t, \Delta, \varphi) = i(t) * q(t) * \frac{M_0}{4\pi p_h a_h^3} \frac{g(\Delta)}{a_r} C(i_0) \times [Pterm + pPterm + sPterm] \quad (4.6)$$

where $i(t)$ is the instrument response, $q(t)$ is the anelastic attenuation term, the term $M_0 / 4\pi p_h a_h^3$ is the amplitude scale factor, which contains the seismic moment M_0 , the density p and the P-wave velocity a at depth h , the $g(\Delta)/a_r$ term is the geometrical spreading

term with a_r being the earth radius, and the $C(i_0)$ term corrects for the free surface effects, as approached in Stein and Wyssession (2003). The P-term, pP-term and sP-term are parameters that contain the source time function (lagged by the corresponding travel time), the radiation pattern, reflection coefficients and other values, for each one of the P, pP and sP waves. In a similar sense, we can construct the SH waves.

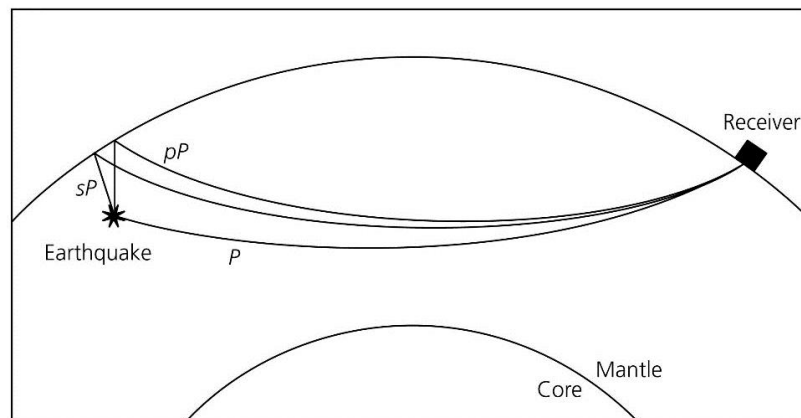


Figure 4.6. P-wave arrival for a shallow earthquake at epicentral distances between 30° and 90° is modeled as the sum of direct P, pP and sP waves (free surface reflections of P wave)(Stein and Wyssession, 2003).

We can see in Equation 4.6, that the synthetic waveforms depend on some assumed parameters. The assumed source depth controls the time distance between arrivals, the focal mechanism determines the relative amplitude and polarity of the arrivals in each azimuth, and the source time function affects the pulse shape. Figure 4.7 and 4.8 show an example of how the focal mechanism affects the polarity of the arrivals, making the seismogram a useful diagnostic in a trial and error (forward modeling) or an inversion procedure.

When it comes to large earthquakes, all the aforementioned procedures and assumptions get more complicated. It is shown that large events, occur on larger faults and, thus, yield longer duration source time functions. This makes it possible to resolve details of the complex slip process. The basic idea is to separate the large fault into subfaults or similarly put, to treat the seismic event as a sum of sub-events.

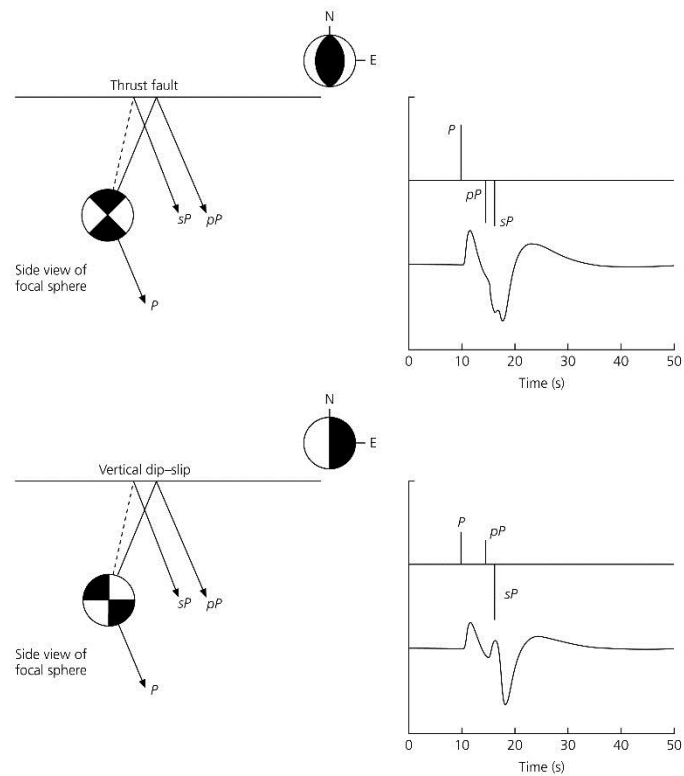


Figure 4.7. Relative polarities and amplitudes of direct P, pP and sP waves for different focal mechanisms (Stein and Wyssession, 2003).

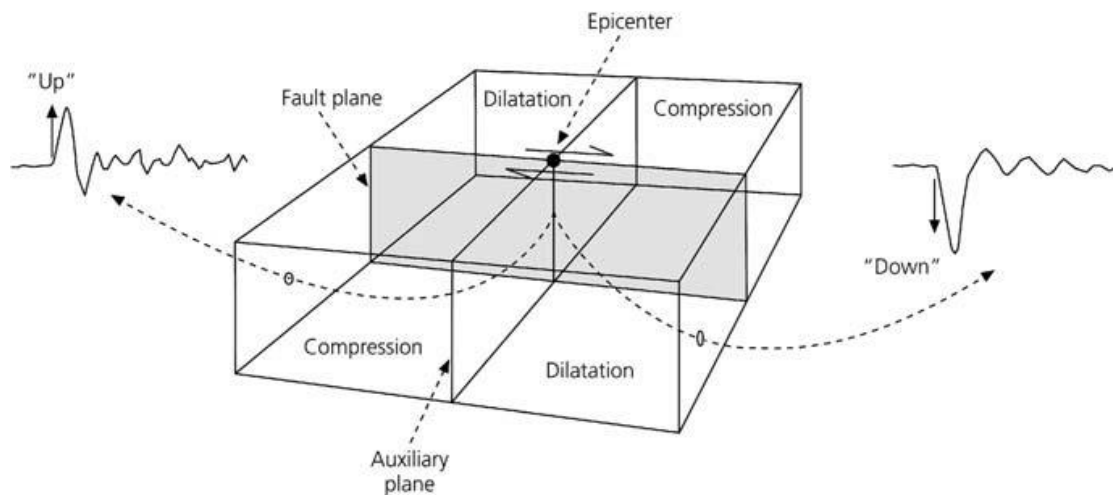


Figure 4.8. Polarity of P-wave first arrival in relation to fault strike and station azimuth (Stein and Wyssession, 2003).

A useful way to estimate the source time function is based on the Green's function

$$g(t) = e(t) * q(t) \quad (4.7)$$

which represent the elastic and anelastic effects of the raypath (attenuation, reflection etc) on the propagating wave. The Green's function describes the signal that would arrive at the seismometer, if the source time function were a delta function. That means that the source time function can be determined by deconvolving the Green's function and the instrument response from the seismogram, as expressed in the following relation

$$x(t) = u(t) * [g(t) * i(t)]^{-1} \quad (4.8)$$

Thus, large events can be modeled using Green's functions derived for a simple source in the fault region. The seismogram is treated as the sum of source time functions with different amplitudes C_j at different times τ_j

$$u(t) = \sum_{j=1}^K C_j [x(t - \tau_j) * g(t) * i(t)] \quad (4.9)$$

With high quality data, it is possible to estimate how the seismic moment release varied on the fault area, as a function of time.

4.1.3 Earthquake moment tensors

If we consider the forces acting on a fault surface and give rise to rupture and slip, the common approach to model this procedure is a double force couple, composed of four single equivalent forces. The relation between a single force, a force couple and a double couple is presented in Figure 4.9 (Stein and Wysession, 2003).

Combinations of differently oriented force couples can describe various seismic sources. The double sets of force couples are used to model earthquakes, and the triple sets of couples, which denote volume, are used to model explosions. Force couples like these, do not generate net torques. This is the reason that one force couple would be inadequate to model a seismic event. Also, this approach is related to the use of the auxiliary fault plane in the description of a focal mechanism. A real fault plane and an auxiliary plane yield the

same waveform field, because they are both represented by the same double couple of forces.

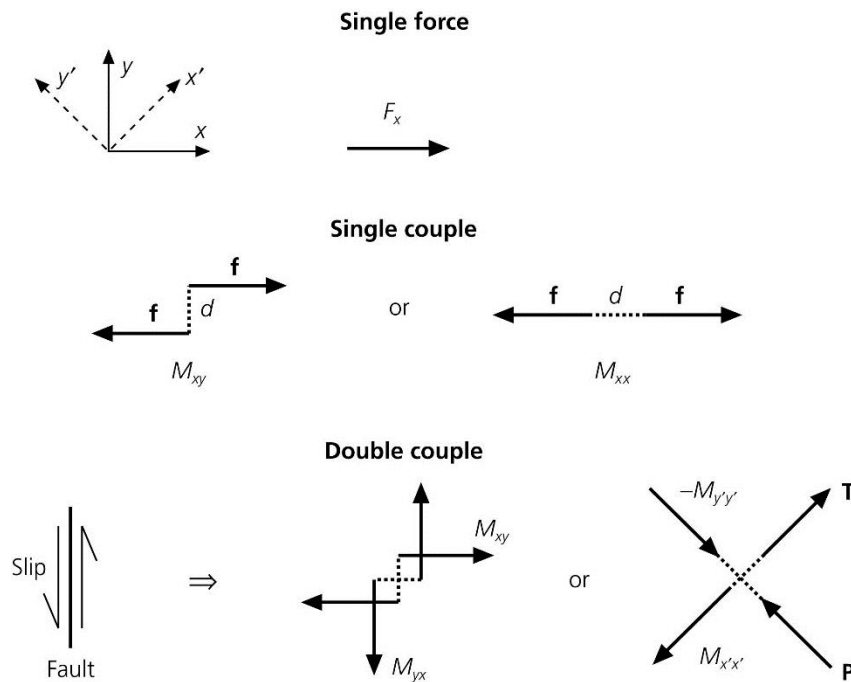


Figure 4.9. Equivalent body force descriptions for a single force, a single couple and a double couple (Stein and Wyssession, 2003).

The seismic source is generally represented by nine force couples, as shown in Figure 4.10 (Stein and Wyssession, 2003). These nine force couples are the nine components of a tensor, known as the seismic moment tensor **M**

$$\mathbf{M} = \begin{bmatrix} M_{xx} & M_{xy} & M_{xz} \\ M_{yx} & M_{yy} & M_{yz} \\ M_{zx} & M_{zy} & M_{zz} \end{bmatrix} \quad (4.10)$$

Using the double couple example of Figure 4.9, the earthquake is represented as

$$\mathbf{M} = \begin{bmatrix} 0 & Mo & 0 \\ Mo & 0 & 0 \\ 0 & 0 & 0 \end{bmatrix} = Mo \begin{bmatrix} 0 & 1 & 0 \\ 1 & 0 & 0 \\ 0 & 0 & 0 \end{bmatrix} \quad (4.11)$$

where M_0 is the released scalar moment. Hence, the seismic moment tensor represents the geometry of the fault via its components, and the earthquake magnitude via the scalar moment.

The moment tensor can be expressed in regard to any orthogonal coordinate system. Thus, we can describe it using the components of \hat{N} , the unit normal vector to the fault plane, and \hat{D} , the unit slip vector

$$M_{ij} = M_0 (N_i D_j + N_j D_i) \quad (4.12)$$

or

$$M = M_0 \begin{bmatrix} 2N_x D_x & N_x D_y + N_y D_x & N_x D_z + N_z D_x \\ N_y D_x + N_x D_y & 2N_y D_y & N_y D_z + N_z D_y \\ N_z D_x + N_x D_z & N_z D_y + N_y D_z & 2N_z D_z \end{bmatrix} \quad (4.13)$$

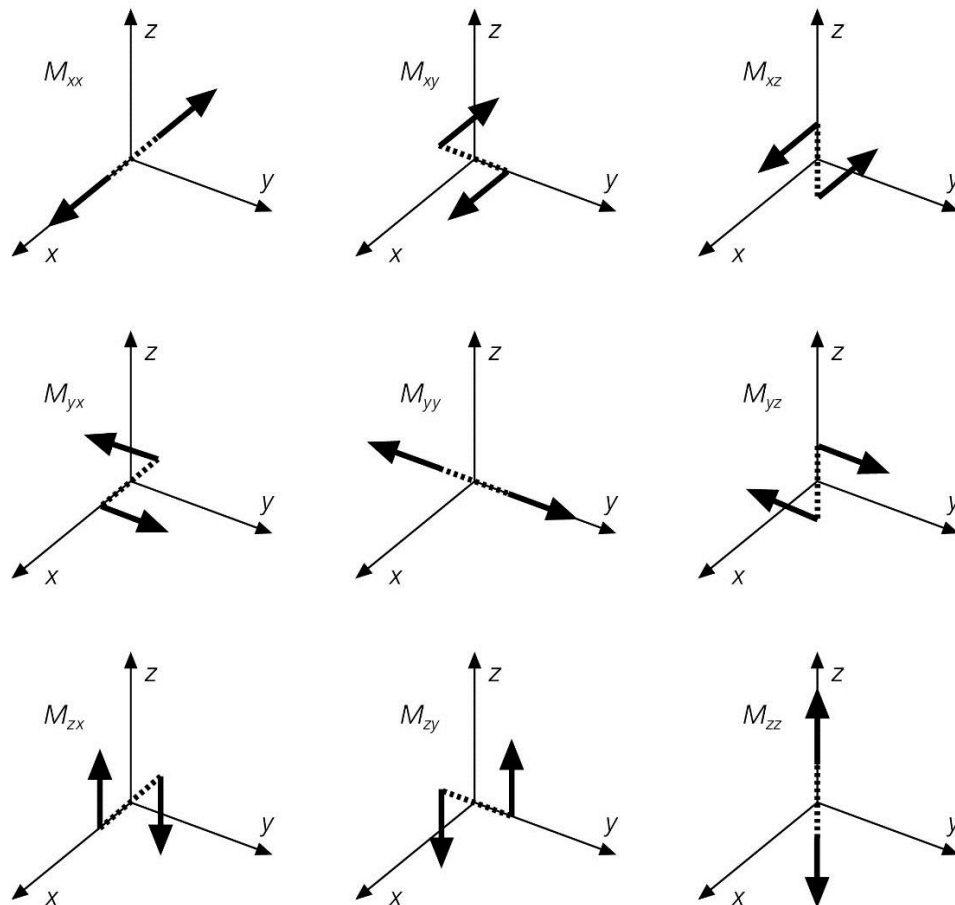


Figure 4.10. The nine force couples which compose the seismic moment tensor (Stein and Wyssession, 2003).

This is the basic idea behind the fault geometry estimation, as presented in Stein and Wysession (2003). Equation 4.13 shows that the tensor is symmetric ($M_{ij}=M_{ji}$). The physical interpretation of the moment tensor's symmetry is that slip on the either the real fault or the auxiliary plane yields the same radiation pattern. A second remark is that the tensor's trace is zero ($M_{xx}+M_{yy}+M_{zz}=0$). That refers to earthquake moment tensors, which describe slip on a plane. A non-zero trace indicates a volume change, as in the case of explosions.

4.1.4 Moment tensor inversion

In order to estimate the fault angles, we write the seismograms as linear functions of the seismic moment tensor's components. The source is described by a vector **m**, containing six independent components, which represent the nine symmetric ones. With the use of the Green's functions, we can also define $G_{ij}(t)$, as the recorded seismogram of the i^{th} seismometer due to the m_j tensor component. This term contains the effect of the earth structure and the instrument. Thus, the i^{th} seismogram can be expressed as

$$u_i(t) = \sum_{j=1}^6 G_{ij}(t)m_j \quad (4.14)$$

and all the recorded seismograms can be written in a vector-matrix form

$$\mathbf{u} = \mathbf{G} \mathbf{m} \quad (4.15)$$

This is an overdetermined system with more equations than unknowns. Since we can not invert the \mathbf{G} matrix because it's not square, according to the theory of linear systems, we can solve for the moment tensor **m** in a least square sense, using the generalised inverse of **G**

$$\mathbf{m} = (\mathbf{G}^T \mathbf{G})^{-1} \mathbf{G}^T \mathbf{u} \quad (4.16)$$

In order to match the observed seismograms in a least square sense, we can use Equation 4.16 to invert for **m**. The aim is to estimate the six values of **m** that are needed to construct the seismogram.

The accuracy of the Green's functions plays a very important role in procedures like this. At teleseismic distances, this is not a problem, since the P, pP and sP rays have simple structural interactions. At regional distances, the crust results to multiple reflections between the surface and Moho discontinuity, making it harder to accurately calculate the Green's functions. As for the source time function, we usually recast the problem as an iterative inversion, because of the lack of the a-priori estimation.

When a large seismic event takes place, there are several agencies which provide moment tensor solutions. One of the largest databases worldwide is the Global Centroid-Moment-Tensor (CMT) Project (www.globalcmt.org). The centroid-moment-tensor inversion process fits the very long period ($T > 40$ s) body wave train from the P arrival until the fundamental modes and mantle waves ($T > 135$ s). It is a fact that long period waves, such as surface waves, give a more accurate estimation of seismic moment and rupture duration, than shorter period waves.

4.2 Waveform modeling of the mainshock

4.2.1 Method 1 – MT5

In this approach, the MT5 software is used for the determination of the 24/05/2014 North Aegean earthquake. MT5 (Zwick et al., 1994) is an advanced version of SYN3 and SYN4 software created by McCaffrey and Abers (1998) and McCaffrey et al. (1991). Based on the methodology of Helmberger (1974), Langston and Helmberger (1975) and Nabelek (1984), MT5 provides earthquake moment tensor solutions and double-couple fault plane solutions based on inversion of teleseismic P and SH data.

Initially, the user is asked to obtain the observed teleseismic data and station headers in an ASCII file, as well as some parameters related to a starting source model, which could be based on published solutions or the seismotectonic regime of the earthquake, in order to facilitate the procedure. With this information, MT5 constructs Green's functions and synthetic seismograms for the stations of the observed data. Next, with an inversion procedure and after a number of iterations, the misfit between the observed and synthetic data is minimized, followed by changes in the initial model. Finally, the

minimum misfit solution is considered to be the best estimation of the focal mechanism of the earthquake, in regard to strike, dip, rake, depth, source time function and scalar moment of the seismic source.

In order to construct synthetic waveforms, it is essential to have a good estimation of the velocity and density model of the ray path. For this reason, it is highly recommended to use stations with epicentral distance between 30 and 90 degrees, in order to minimize the problem of lateral heterogeneities along the ray path. MT5 uses a simple one-dimensional structure of either a half-space, or a layer over a half-space. Each layer is characterized by its P and S velocities, density and depth of upper layer. The velocity structure above the seismic source affects the temporal distance between the direct and reflected phases. The structure below the source, controls the take-off angles.

The temporal evolution of the source slip is described by the source time function. In MT5, the source time function is considered to be a series of overlapping isosceles triangular shapes (Fig 4.11), with half width $\Delta\tau$, usually set to 1 sec. The number and half width of the triangles are given by the user, while the height of each triangular pulse is determined by the inversion. The time length of the source time function is proportional to the seismic moment release and therefore magnitude. The integral area under the source time function curve indicates the scalar moment. That's why earthquakes of smaller magnitude have a short and simple shaped source time function, mainly corresponding to an impulsive single rupture. On the contrary, stronger earthquakes have a long and complex shaped source time function, indicating a stronger complex rupture.

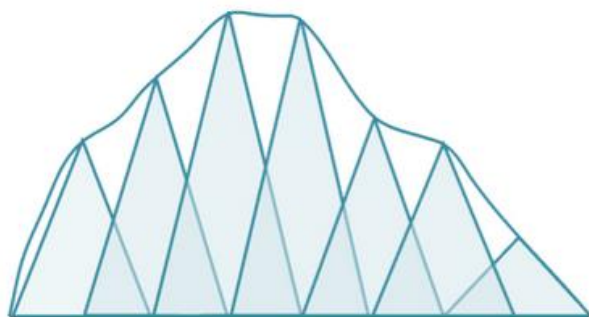


Figure 4.11. Example of source time function as a sum of overlapping triangles with different amplitudes.

One of the most useful features of this software is that it can perform inversion and obtain solution not only for one single event, but for multiple events as well. If the time, distance and azimuth separation of the subevents are well approximated, then MT5 provides a good focal mechanism estimation for each subevent. Another useful tool is the manual or automatic waveform realignment capability. With this tool, it is easy to realign the synthetic data in order to better fit the observed. This is a very important procedure for these techniques to be best performed, but it should be executed with caution.

4.2.1.1 Data preparation

For the body wave inversion with the MT5 software, we retrieved broadband teleseismic data from the Data Management Center (DMC) of Incorporated Research Institutions for Seismology (IRIS). Only stations with epicentral distance between 30-90 degrees were chosen. The waveforms were edited and processed with the SAC software (Goldstein and Snoke, 2005).

Firstly, we fixed some of the seismograms to have the same time interval with the others, with the 'decimate' or 'interpolate' commands. With this step, it is easier to handle all the seismograms at once. We, then, deconvolved the instrument response using the 'transfer' command and the corresponding polezero files. The output of the transfer command was set to be velocity in m/s.

Next, we applied a bandpass filter with corner frequencies of 0.01 and 0.1 in order to remove the noise. This filter was applied with the 'bandpass' command. After that, we removed the mean and the trend with the 'rmean' and 'rtrend' commands, respectively. We also applied a Hanning taper filter of 0.05 width with the 'taper' command. Then, we integrated the waveforms to displacement in meters, using the 'integrate' command. At this point, the horizontal E-W and N-S components were rotated with the 'rotate' command, in order to obtain the SH transverse component.

As a next step, we convolved the seismograms with the WWLPBN response, in order to reduce the sensitivity to the uncertainties of the local velocity model. After this, we cut 20 s before the P or S arrival and 80 s after, with a time interval of 1 s. Finally, the waveforms were multiplied by 1E+06, because MT5 requires the observed data in microns.

- r *SAC
- setbb pzfile SAC_PZ*
- transfer from polezero subtype %pzfile to vel
- bp co 0.01 0.1 n 4 p 2
- rmean
- rtrend
- taper
- int
- rot
- transfer to WWLPBN
- cuterr fillz
- cutim
- dec
- mul 1000000

Figure 4.12. Brief presentation of the SAC commands used in MT5 data preparation.

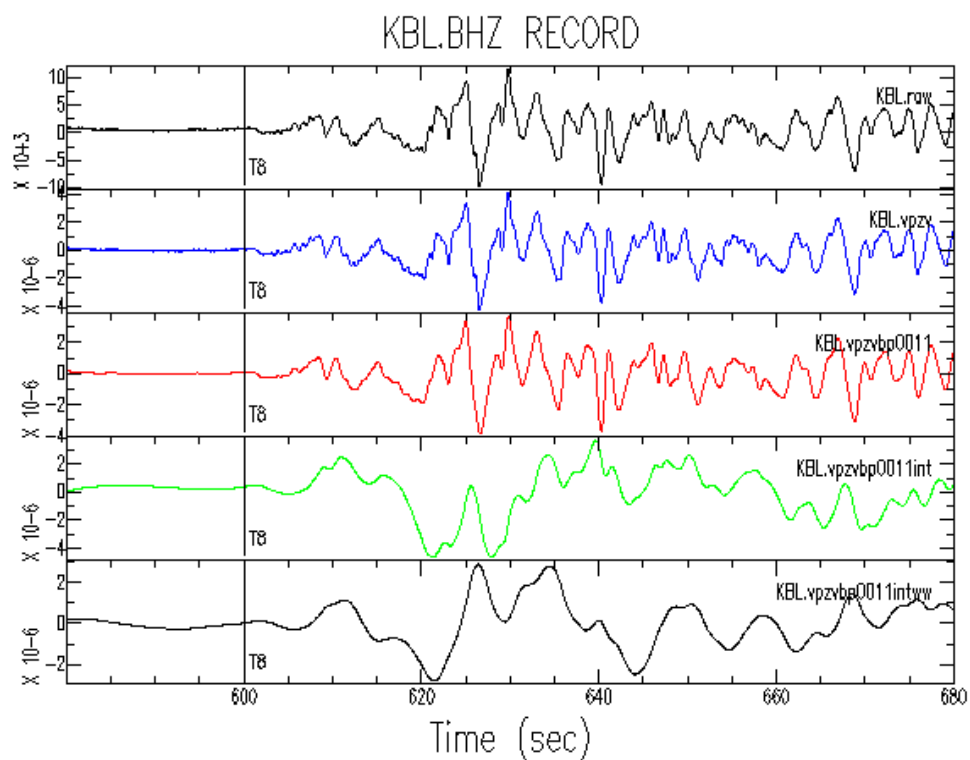


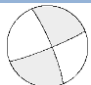
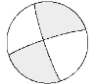
Figure 4.13. P-wave data preparation of the Kabul station (vertical component) in Afghanistan for the MT5 program. Black color (top): Raw waveform in counts. Blue color: Instrument correction (m/s). Red color: Bandpass filtering. Green color: Integration to displacement (meters). Black color (Bottom): Convolution with the WWLPBN response.

4.2.1.2 Application and results

The inversion adjusts the relative amplitudes of the source time function elements, the centroid depth, the seismic moment and the source orientation to obtain the minimum misfit match between the observed and synthetic seismograms. The employed data were teleseismic P and SH waveforms from stations with epicentral distances 30 – 90 degrees in order to avoid upper mantle triplications, providing a good azimuthal coverage at the same time. The data were bandpass filtered from 0.01 to 0.1 Hz, integrated to displacement and resampled at 1 Hz. The seismograms were also weighted according to azimuthal density.

The attenuation parameter t^* is 1 for P waves and 4 for SH waves (Futterman, 1962). For the synthetic seismograms, we used a halfspace with 6.5 and 3.7 km/s, for P and S waves respectively, and density 2.8 g/cm³. This model is adequate to explain the low-frequency content of the teleseismic records at distances between 30° and 90° due to the simplicity of the earth layer structure at the same distance range (Helmberger, 1974; Langston and Helmberger, 1975). As a starting model, we used the GCMT solution, i.e. strike=73°, dip=85°, rake=-177. The misfit was minimized when we inverted for two sources, with the second subevent occurring 13 s after the first, as proposed by Evangelidis (2015), and 30 km apart in the same azimuth. The results are presented in Table 4.1 and Figure 4.14.

Table 4.1. Focal mechanism solution with MT5 program.

Algorithm	Lat.°N	Long.°E	Strike°	Dip°	Rake°	Depth (km)	Moment (Nm)	Mw	Focal Sphere
MT5 (1 st subevent)	40.297	25.398	68	85	-172	8	9.98E+18	6.6	
MT5 (2 nd subevent)	40.409	25.729	252	83	-174	7	7.30E+18	6.6	

The minimum misfit solution was yielded for two seismic sources of the same M6.6 magnitude. Both sources indicate strike-slip ENE-WSW faulting, almost parallel to the Saros basin. This solution is accordant with the general seismotectonic properties of NAT, other published solutions, such as GCMT and USGS, and the aftershock distribution, as well. The source time function is approximately 30 s.

24 May 2014 Earthquake (North Aegean Sea)

Source 1: 68/85/-172/8/9.981E18

Source 2: 252/83/-174/7/7.308E18

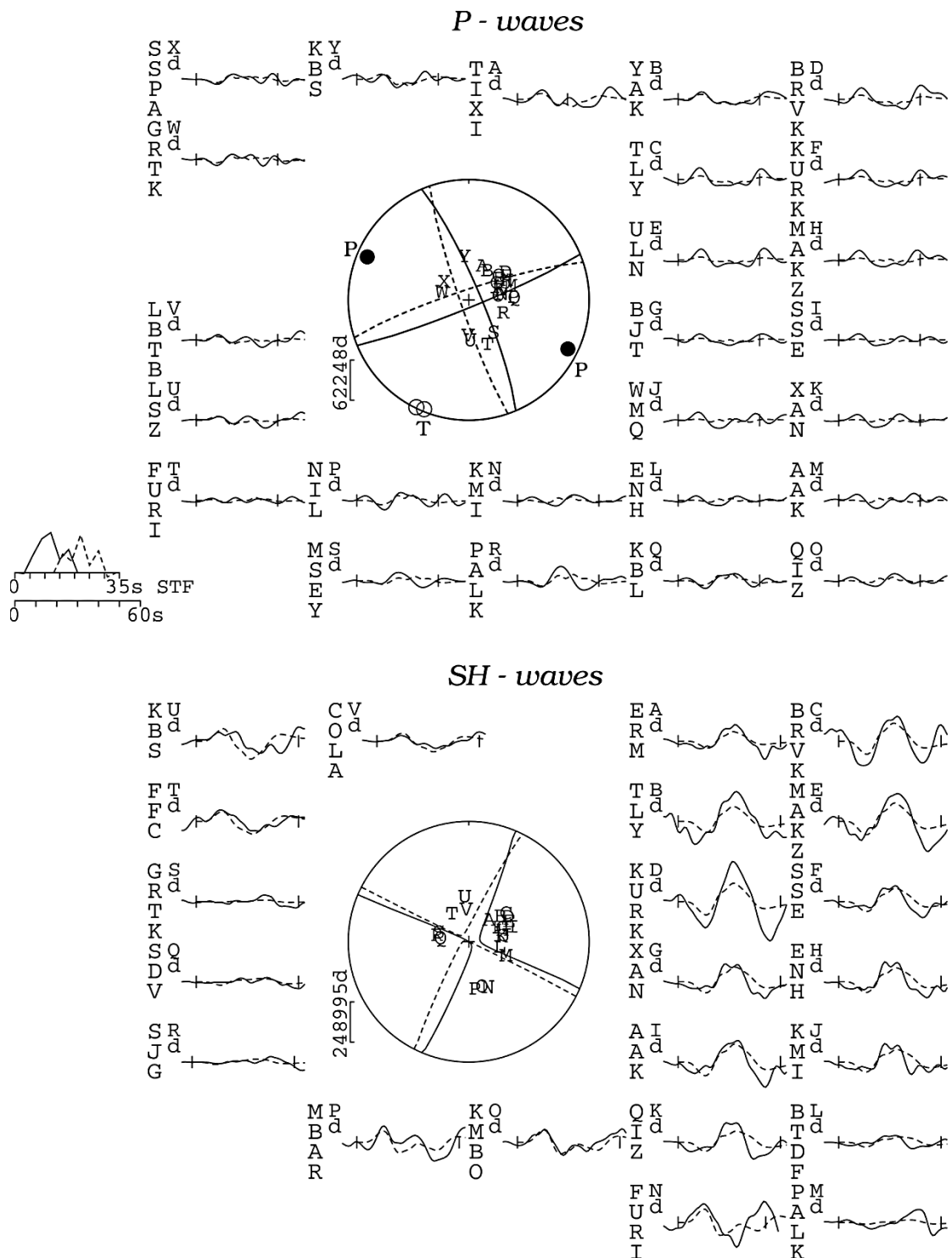


Figure 4.14. Waveform fit of the MT5 solution for the 24/05/2014 North Aegean earthquake (Kiritzi et al., 2015).

4.2.2 Method - 2

The second software that I used to perform a teleseismic inversion for the case of 24/05/2014 North Aegean earthquake is the teleseismic inversion software created by Kikuchi and Kanamori (1982, 1991) and Kikuchi et al. (1993). This software contains codes that are related to the focal mechanism and rupture pattern determination. I used the 'INVERSION' algorithm for the fault mechanism estimation and the 'MOM3' algorithm for the final fault slip distribution. 'MOM3' algorithm is described in the next chapter.

According to this method, a seismic source is characterized as a sequence of point sources with various focal mechanisms. The point sources are determined iteratively by matching the observed seismograms with the synthetic ones. Each point source is described by a moment tensor.

The methodology proposed by Kikuchi and Kanamori (1982, 1991) allows the use of P, SH, SV and PP phases, as well as the use of a multi-layer structure to compute the response of the source, station and PP bounce point structures. For this computation, the Haskell propagator matrix is used, as described in Bouchon (1976) and Haskell (1960, 1962).

For general moment tensor sources, six elementary moment tensors are the basic ones to represent a seismic source:

$$\begin{aligned} M1 &= \begin{bmatrix} 0 & 1 & 0 \\ 1 & 0 & 0 \\ 0 & 0 & 0 \end{bmatrix}; \quad M2 = \begin{bmatrix} 1 & 0 & 0 \\ 0 & -1 & 0 \\ 0 & 0 & 0 \end{bmatrix}; \quad M3 = \begin{bmatrix} 0 & 0 & 0 \\ 0 & 0 & 1 \\ 0 & 1 & 0 \end{bmatrix}; \\ M4 &= \begin{bmatrix} 0 & 0 & 1 \\ 0 & 0 & 0 \\ 1 & 0 & 0 \end{bmatrix}; \quad M5 = \begin{bmatrix} -1 & 0 & 0 \\ 0 & 0 & 0 \\ 0 & 0 & 1 \end{bmatrix}; \quad M6 = \begin{bmatrix} 1 & 0 & 0 \\ 0 & 1 & 0 \\ 0 & 0 & 1 \end{bmatrix}; \end{aligned} \quad (4.17)$$

where the coordinates x, y, z for M_{ij} correspond to north, east, vertical axis. Any moment tensor can be represented by a linear combination of M_n ($n=1,...,6$). In Figure 4.15, the respective area projection of the lower focal hemisphere is presented in six beachball shapes.

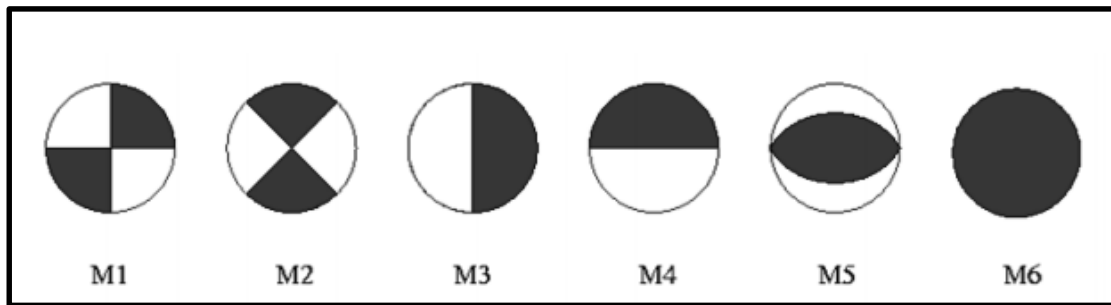


Figure 4.15. Elementary moment tensors as described in Equation 4.17 (Kikuchi and Kanamori, 1991).

The advantage of this method is that the inversion can be performed for five types of sources, represented by five respective subgroups of the basic tensor system, as follows :

- 1) M_1, \dots, M_6 = general moment tensor
- 2) M_1, \dots, M_5 = pure-deviatoric moment tensor
- 3) M_1, \dots, M_5 with zero $\det[M_{ij}]$ = general double couple
- 4) M_1, \dots, M_4 with zero $\det[M_{ij}]$ = double couple with a vertical nodal plane
- 5) M_1, M_2 = pure strike-slip.

As for the double-couple sources, a double-couple mechanism is represented by a moment tensor with zero trace and zero determinant. Therefore, the best-fit double-couple source is computed by imposing the constraint $\det[M_{ij}] = 0$, on a pure deviatoric moment tensor.

The subevents are successfully determined by minimizing the squared difference between the observed and synthetic waveforms with a grid search. This is done by an iterative technique. In general, the subevents are determined in the sense of decreasing scalar moment (Kikuchi and Kanamori, 1982). The mechanisms of the subevents are computed by the inversion, in contrast with the older techniques proposed by the authors, at which the mechanisms were fixed by the user.

In order to obtain a teleseismic body wave inversion, the programs 'GREEN' and 'INVERSION' must be used. These programs use the input data contained in the fort.1 file. Fort.1 file contains the observed seismogram windows, which are used for the inversion. Their duration, time step, high-pass and low-pass frequencies are set by the user. It is recommended that the data start some seconds before

the phase arrival, in case of realignment needs. The phase arrival is computed by the program, based on the given structure model.

The 'GREEN' program computes the Green's functions based on some input parameters such as the source depth, the fault grid along strike, the epicenter position along strike and the fault dip. The input parameters of the fault strike grid are shown in Figure 4.16, where h_0 is the hypocenter depth, n_k is the grid points along strike, dk is the length between two grid points with k_0 being the reference point.

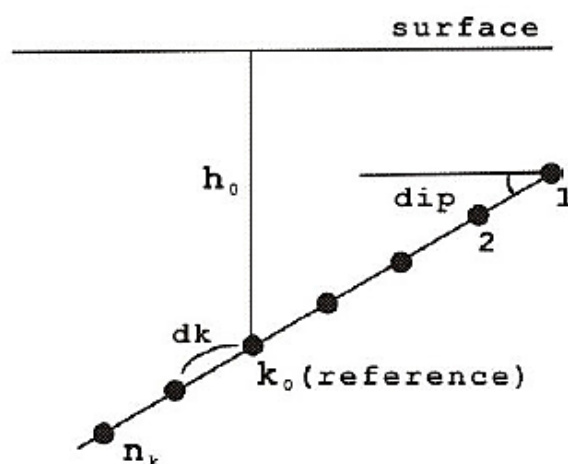


Figure 4.16. Fault geometry pattern used in 'green' and 'inversion' algorithms (Kikuchi and Kanamori, 1982).

The 'INVERSION' program performs an inversion for a given source time function, number of subevents, epicenter position along strike grid, type of source (as mentioned above), seismogram weighting, maximum rupture velocity and a starting value for strike, based on published solutions or seismotectonic regime. There are four basic shapes for the source time function: impulse, trapezoidal, cosine-tapered trapezoid and triangular. Figure 4.17 shows the source time function pattern that the user is supposed to adjust, in regard to shape and length. Another important factor is the attenuation effect, which is determined by $t^*=1$ for P waves and 4 for SH waves (Futterman, 1962).

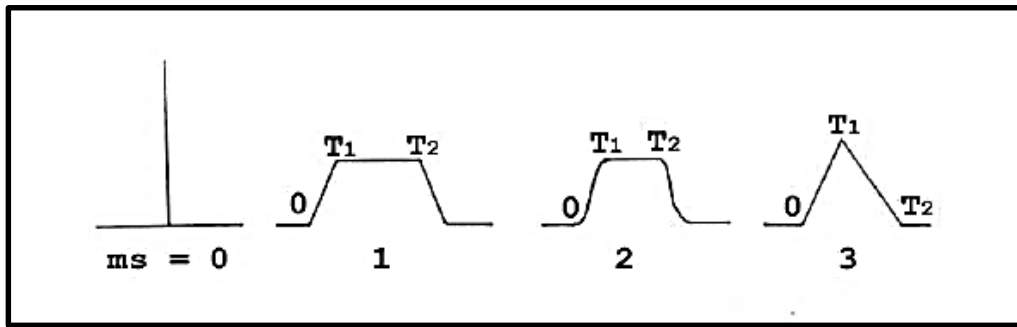


Figure 4.17. Source time function shapes (impulse, trapezoid, cosine tapered trapezoid and triangular) (Kikuchi and Kanamori, 1982).

It is a fact, that various solutions can describe the observed data equally well. For procedures like these, experience and judgment play an important role. Therefore, it is essential to perform a lot of trial inversions, in order to get a sense of each examined case, before accepting a final solution. The user should, also, examine all the possible trade-offs, e.g. the trade-off between the mechanism, timing and location of subevents.

4.2.3 Application and results

The methodology of Kikuchi and Kanamori (1982, 1991) and Kikuchi et al. (1993) was applied for the case of 24/05/2014 North Aegean earthquake. I used the 'GREEN' and 'INVERSION' algorithms in order to invert for strike, dip, rake, source time function and seismic moment.

I retrieved broadband teleseismic data in a SEED format from Data Management Center (DMC) of Incorporated Research Institutions for Seismology (IRIS). Only stations with epicentral distance between 30-90 degrees were chosen in order to avoid mantle triplications and complexities due to core-mantle boundary. The stations, also, provided a good azimuthal coverage. I used vertical components for P waves, and horizontal components, that were rotated to the SH transverse component. Using the RDSEED program, provided by IRIS Institution, I converted the seismograms into SAC format. The data were instrument corrected by the program, using the corresponding response files, obtained by RDSEED, and integrated to displacement. All waveforms start at $T_0=5$ s before the phase arrival. This delay is depicted in both the observed-to-synthetic seismograms' and the

STF's horizontal axis of time. I, also, applied a high-pass and a low-pass filter with frequencies 0.01 Hz and 0.1 Hz, respectively. The final input data, consisting of 32 seismograms, are presented in the fort.1 file, which is the input file for all the inversion programs of this software.

For the hypocenter, I used the longitude and latitude from the relocated catalog of Evangelidis (2015). The structure model is considered to be the Jeffreys-Bullen velocity model (Table 4.2)

Table 4.2. Jeffreys-Bullen velocity model and density (data from Kikuchi and Kanamori, 2003).

Depth (km)	Vs (km/s)	Vp (km/s)	Density (kg/m ³) *10 ³
Near Source Structure (J-B)			
0.00	4.68	8.10	3.30
15.00	3.36	5.57	2.65
18.00	3.74	6.50	2.87
Near Receiver Structure (J-B)			
0.00	4.68	8.10	3.30
15.00	3.36	5.57	2.65
18.00	3.74	6.50	2.87
PP Bounce Point Structure (J-B)			
0.00	3.74	6.50	2.87

As a starting strike and dip, I used the GCMT solution with strike=73° and dip=85°. For the source time function, I selected a trapezoidal shape. The weights of the seismograms were 1 for P waves and 0.2 for SH waves. The maximum rupture velocity was set to 4.0 km/s.

Following the pattern of Evangelidis (2015), I started with an inversion for a double couple and a pure strike-slip source, both characterized by 2 subevents on a 80 km fault ($n_k=9$, $dk=10$, $k_0=3$). The double-couple approach had a lower misfit of 0.22, against 0.29 for pure strike-slip. The fault length, strike and dip, as well as the hypocenter depth, reference point k_0 and STF basic shape were examined by trial and error. I also inverted for a single double-couple source, as an initial approach, resulting in a much larger variance of 0.32 (Table 4.3).

Both of the double-couple and pure strike-slip approaches, yield a total moment magnitude of $M_w=6.7$. According to two empirical

relations for strike-slip faults, proposed by Wells and Coppersmith (1994) and Papazachos et al. (2004), the dimensions of a fault related to a 6.7 earthquake are $39 \times 11 \text{ km}^2$ and $45 \times 11 \text{ km}^2$, respectively. I, also, tried to pursue the inversion problem for these smaller dimensions but the misfit was higher. As mentioned before, the dimensions of this fault are larger than the empirically predicted.

The aftershock distribution, using the relocated catalog of Evangelidis (2015), yields a fault length of nearly 100 km. Additionally, in regard to Evangelidis (2015), the total rupture is estimated to have a length of approximately 85 km. According to the aforementioned study, the rupture is supposed to have taken place in two subevents: the first one that propagated for 20 km westward of the epicenter and the second one that propagated for 65 km eastward of the epicenter. The inversion described above, also, yielded lower misfits for bigger fault length values than for smaller lengths. The same situation describes the fault width as well. These remarks are additional indicators of the complexity of the 24/05/2014 North Aegean earthquake, as well as the strike-slip faults in general.

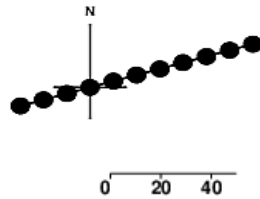
After a long trial-and-error process, the minimum misfit solution was yielded for a double-couple source type with 4 subevents at 5, 8.5, 19, 24.5 s, and a fault length of 100 km (Fig. 4.18), described by a total magnitude of 6.56. The first subevent is located near the hypocenter area, the next two are activated in the western part and the last one takes place in the eastern part. The variance is 0.17, against the 0.23 misfit of the previous approach, i.e. for a double-couple source with 2 subevents and 80 km fault length (Table 4.3). The big difference in the misfit value was, mainly, a result of the higher number of subevents, clearly reflecting the source complexity. The seismic moment decrease, when inverting for more subevents, is also worth noting.

In terms of strike, dip, rake, seismic moment and source time function, there are not big differences between the previous trials for 2 sources. These parameters are in a good agreement with the MT5 solution, Saros tectonic regime and the aftershock distribution, all capturing a $\sim 30\text{s}$ shallow multiple rupture on a $\sim \text{N}70$ right-lateral fault of approximately 100 km length. The results of the methodology of Kikuchi and Kanamori are shown in Table 4.3.

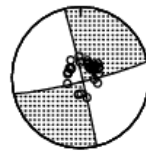
N.Aegean, 24/05/2014

1 6.00 12.00 0.1779

Mo[Nm]= 0.873E+19 Mw= 6.56



5.0 10.0 8.5 -10.0 19.0 70.0 24.5 -10.0
1 0 73.0 3 -30.0 73.0 4 -10.0 73.0 2 40.0 73.0



Total

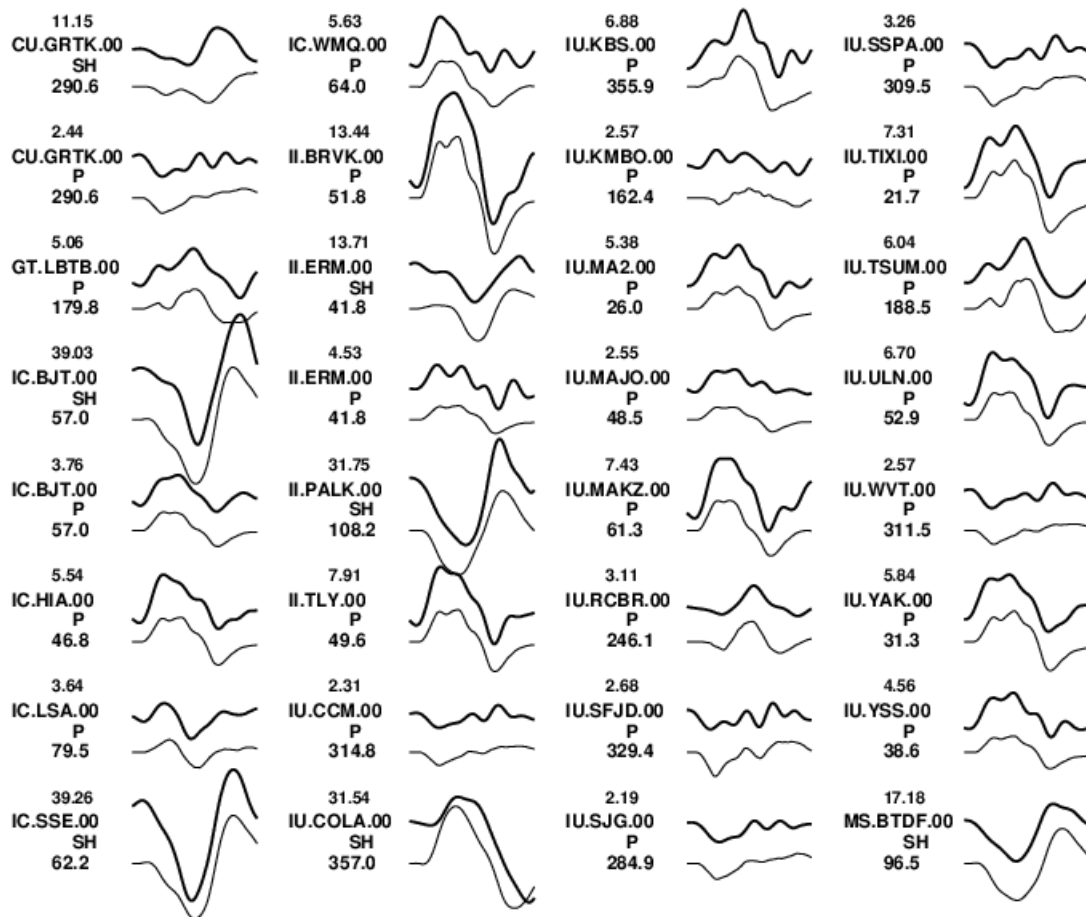
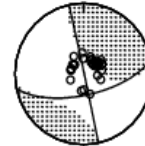
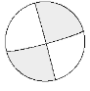
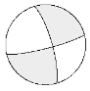
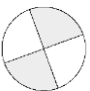



Figure 4.18. Waveform fit of the minimum misfit solution for a double couple source, described by 4 subevents and a fault length of 100 km ($T_0=5$ s).

Table 4.3. Focal mechanisms for different fault types and number of subevents, derived from the 'INVERSION' algorithm.

Algorithm	Type	Strike°	Dip°	Rake°	Moment (Nm)	Mw	Focal Sphere	Misfit
Kikuchi & Kanamori (single event)	Double Couple	345	89	-5	0.191E+20	6.79		0.32
Kikuchi & Kanamori (2 subevents)	Double Couple	344	77	-8	1.331E+19	6.68		0.23
Kikuchi & Kanamori (2 subevents)	Pure Strike-Slip	340	90	0	1.277E+19	6.67		0.29
Kikuchi & Kanamori (4 subevents)	Double Couple	348	89	-25	0.873E+19	6.56		0.17

It is worth noting, that during the initial processing trials, the data were filtered between 0.01 and 1 Hz in order to include a larger frequency band. The signal had a very 'high-frequency' appearance, that could only be matched with an inappropriate source time function of a very sharp and impulse shape. Additionally, the misfit was significantly higher. An example is presented in Figure 4.19, where the shape of the source time function is an impulse function. The data start $T_0=20$ s before the P arrival. The inversion is performed for three subevents and 23 seismograms. The misfit for this approach is 0.65, against 0.17 of the previously presented solution. It is interesting that apart from the large misfit value, the visual match is not bad at all and the mechanism solution is in agreement with the previous.

Summing up, we employed two methods of teleseismic waveform inversion, in order to obtain the focal mechanism and magnitude of 24 May 2014 earthquake. The MT5 method yielded a M6.6 earthquake on a $\sim N70^\circ$ dextral strike-slip fault, described by two sources separated by 13 s (Evangelidis, 2015) and 30 km. The method of Kikuchi and Kanamori resulted in a M6.6 event, described by four sources indicating a very multiple source, on a $\sim N75^\circ$ right lateral strike-slip fault of 100 km length, in accordance with the aftershock distribution. A source time function of approximately ~ 30 -40 s was derived by both methods.

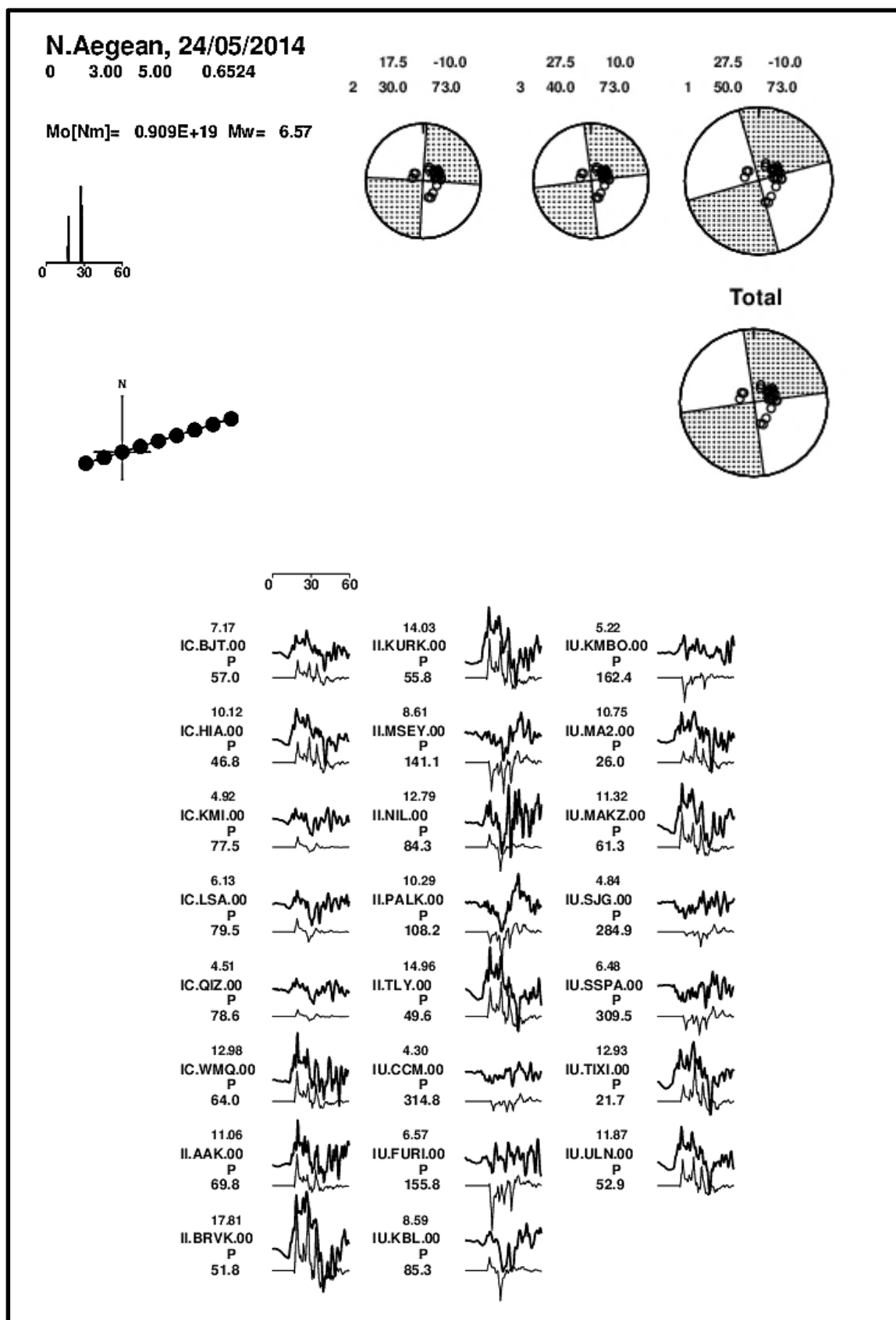


Figure 4.19. Waveform fit of higher-frequency data for a pure strike-slip source, described by 3 subevents and an impulse-shaped source time function ($T_0=20$ s).

5 Finite-Fault Slip Inversion

5.1 Fault slip determination

Up to the aforementioned procedures in Chapter 4.1, the rupture process is thought to be smooth. That refers to a simple trapezoid source time function and an average slip value responding to the whole fault. In reality, the slip is not equally distributed and the source time functions are not simple trapezoids. On the contrary, slip is heterogenous as a main result of the fault roughness with jogs and steps, that yield irregular and complex time functions. There are regions of high slip and low slip on the ruptured fault surface. The regions of very high slip, known as asperities, are connected with very large stress drop and are majorly responsible for the moment release. The regions of lower amounts of slip are regions strong enough to impede or terminate rupture. Known as strength barriers, these regions are important to hazard analysis, since they are indicators of possible future rupture. Similarly, the high slip regions may act as relaxation barriers for subsequent earthquakes.

The methods of estimating the fault slip distribution are all behind the concept of treating the seismic event as a sum of subevents. Large earthquakes are complex earthquakes that occur on large faults with large heterogeneities. This is particularly true for faults connected with strike-slip earthquakes. The concept is to think of the main source process as a series of moderate sized earthquakes. By fitting the observed waveforms recorded in stations providing azimuthal coverage, we can determine the duration and moment of each subevent. This process is repeated for a respective number of iterations, all resulting to the estimation the overall rupture process.

In general, the mathematical formulation of slip inversion considers a fault rupture as the spatiotemporal distribution of dislocation $\Delta u(x,t)$, across the fault planes, Σ . According to Aki and Richards (2002), in an elastic medium, the displacement at (x,t) produced by slip discontinuity $\Delta u(\xi,\tau)$ is

$$u_i(x,t) = \int_{-\infty}^{\infty} d\tau \int_{\Sigma} \Delta u_j(\xi,\tau) \times C_{j k p q} G_{i p, q}(x,t; \xi,\tau) v_k(\xi) d\Sigma(\xi) \quad (5.1)$$

where C_{jkpq} is the elastic constant, G_{ip} is a Green tensor function that is the i th component of displacement at (x,t) , due to an impulsive force at (ξ,τ) , in p th direction, and q is the derivative in (ξ_q) direction. The summation convention is used for index j, k, p, q . This approximation corresponds only to shear slip, so that the product of $\Delta u(x,t) \cdot v(x)$, where $v(x)$ is the fault normal, is everywhere equal to zero.

5.2 Method adopted

The program 'MOM3' of the software of Kikuchi and Kanamori (1982, 1991) and Kikuchi et al. (1993) is used to calculate the final fault slip model. According to the methodology proposed by the authors, the rupture pattern is characterized as a sequence of subevents distributed on the fault plane. The fault rupture pattern is usually very complex, and the slip distribution is often interpreted as a combination of asperities and barriers on the fault plane.

In the earlier software version, the fault mechanisms were fixed, in contrast with the newer method, in which the subevents' mechanisms are calculated by the data and they have the ability to vary during the sequence. This may result in the inversion to be unstable, due to complex trade-offs between the mechanisms, timing and location of subevents.

It is a fact that many combinations can describe the observed data equally well. That's why some constraints must be imposed in order to estimate a range of allowable solutions for the inversion to be stabilized. In this method, a network of grid points is constructed on the τ - l plane, where τ is the onset time and l the distance from the epicenter of the subevent. The best-fit subevent is determined at all grid points.

MOM3 program uses the data in the fort.1 file and some input parameters as well, in order to pursue the slip inversion problem. The strike, dip and depth values are fixed and the rake can vary at ± 45 degrees. The source time function is described by a number of overlapping triangular pulses of specified half width. The rupture velocity, rigidity and smoothing value are fixed and weighting of seismograms is, also, available.

The fault grid is presented in Figure 5.1. N_x and N_y are the grid points along strike and dip, respectively, as well as dx and dy are the distances between them. The (N_{x_0}, N_{y_0}) point represents the rupture initiation point.

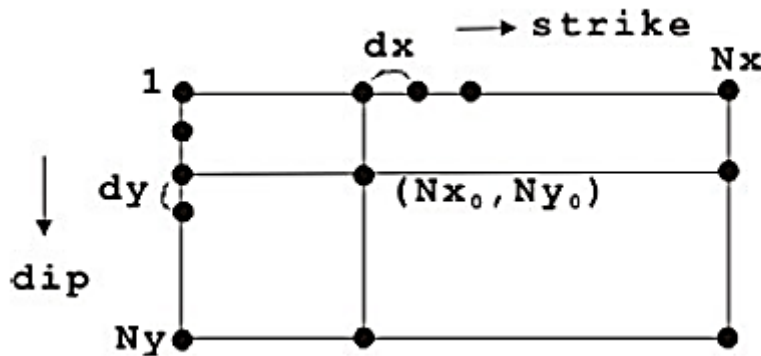


Figure 5.1. Fault grid pattern used in 'MOM3' algorithm (Kikuchi et al. and Kanamori, 1982).

The final output is the slip distribution on the fault plane, in terms of a slip value, a seismic moment value and a rake value for each grid point. The total source time function and total rake of the focal mechanism are estimated by the inversion.

5.3 Preferred slip model of the mainshock

I used the 'MOM3' program of Kikuchi and Kanamori (1982, 1991) and Kikuchi et al. (1993), in order to determine the final fault slip model of the 24/05/2014 North Aegean earthquake.

I used teleseismic broadband data of both P and S waves from the Data Management Center (DMC) of the Incorporated Research Institutions for Seismology (IRIS). These are the same data used in the 'INVERSION' program, described in Chapter 4.2.2. I selected 32 stations with epicentral distances between 30 and 90 degrees, to avoid complications of upper mantle triplications and diffractions of the core-mantle boundary. The stations were carefully chosen in order to give good azimuthal coverage. The data were band-pass filtered between 0.01 and 0.1 Hz, resampled at 2 Hz and integrated to displacement. The horizontal components were rotated in order to

obtain the SH component. All waveforms start at $T_0=5$ s before the phase arrival.

The grid points were 20 along strike and 8 along dip, corresponding to a 95km x 35 km fault area, and were determined by trial and error. The distance between the grid points is 5 km. These values are consistent with Evangelidis (2015), who proposes a total rupture of ~85 km, expressed in two subevents: the first one that propagated for 20 km westward of the epicenter and the second one that propagated for 65 km eastward of the epicenter. The grid point network values, also, agree with the aftershock distribution from the relocated catalog of Evangelidis (2015), which yields a fault length of nearly 100 km, corresponding to the Saros basin rupture.

The fault area was divided into 5 km x 5 km subfaults. As for the strike and dip, after I tested the misfit in a range of 60-80 and 80-90, respectively, I chose the values of 73, for strike, and 85, for dip, in accordance with the quick Global CMT solution. This mechanism is almost identical with the strike and dip angles of strike-slip faulting in the North Aegean region. The rupture was assumed to start at the grid point, which was closest to the hypocenter location.

The moment rate function was expressed by 3 basic triangular source time functions, with 3 s half duration overlapping by 3 s. The body-wave Green's functions were computed for the Jeffreys-Bullen model. No time realignments were made and the weights are 1 for P waves and 0.2 for SH waves.

In this search, a velocity of 3 km/s was determined, by trial and error, as an optimal maximum rupture velocity, minimizing the observed and synthetic residuals (Fig. 5.2).

The preferred slip model is presented in Figures 5.3 and 5.4. A moment magnitude of 6.76 with a seismic moment of $0.176E+20$ Nm was obtained by the source inversion. A source time function of ~30 s and an average rake of -171° , were also determined. The maximum dislocation was found at 0.67 m, with a fixed rigidity of 30 GPa. The variance between the observed and synthetic waveforms was 0.34.

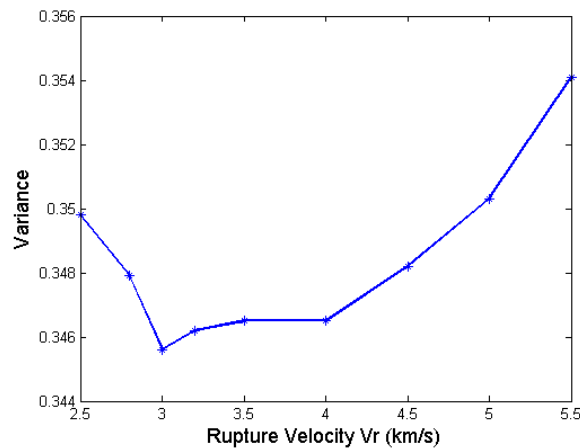


Figure 5.2. Variance of V_r (rupture velocity) values. The minimum misfit value is for $V_r=3$ km/s.

The slip distribution of the 24 May 2014 North Aegean earthquake (Figure 5.2) yielded two noticeable asperities. The first lies west and downwards from the hypocenter and is about 40 km long. The second patch lies east and upwards from the hypocenter, indicating a ~60 km long rupture, probably reaching the sea bottom surface.

This two-lobbed slip pattern could be a representation of the source process proposed by Evangelidis (2015), where an initial rupture, that was propagated westward from the hypocenter for about 20 km, was followed by a 13 s delayed second rupture, which was spread eastward from the hypocenter for about 65 km. A super shear rupture velocity of 5.5 km/s is also proposed by Evangelidis (2015). This value, which refers to the second eastward rupture, is neither validated nor excluded by this study.

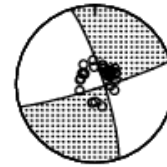
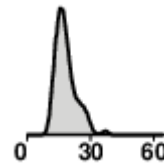
The maximum dislocation value of 0.67 m is consistent with empirical relations proposed by Wells and Coppersmith (1994) and Papazachos et al. (1989). The inversion is considered to be stable, since the main pattern is not majorly affected, when we use different or less stations. As for the rake, the earthquake is mainly a strike-slip event (Fig. 5.2). The west asperity has an obvious strike-slip rake, while the east asperity definitely has a normal component, as well. In the down-east fault region, there are two visible shapes, probably related to errors.

N.Aegean 24/05/2014

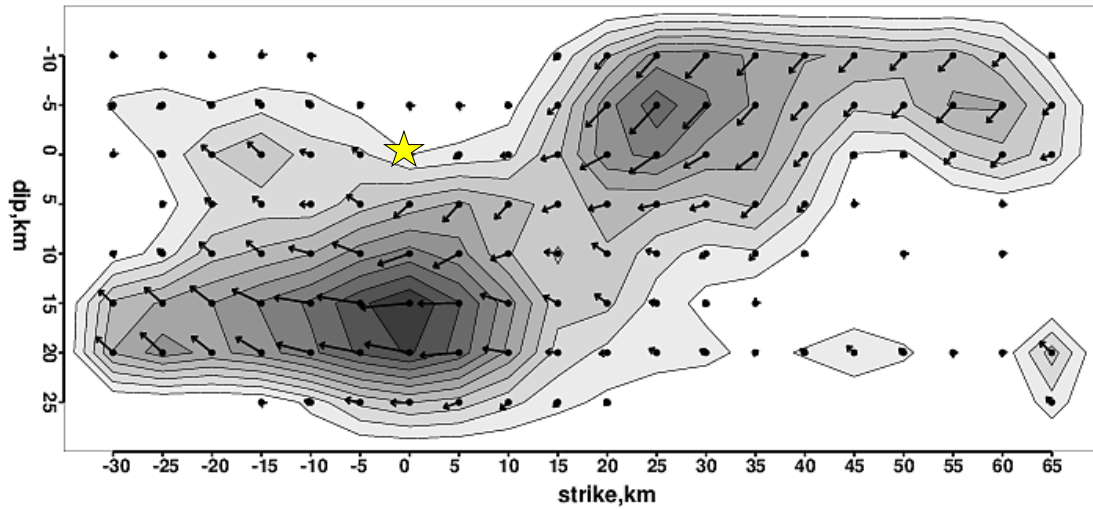
$M_o = 0.176E+20 \text{ Nm}$ $M_w = 6.76$

$H = 12.0 \text{ km}$

$\text{var.} = 0.3458$



(73.,85.,-171.)



0 30 60

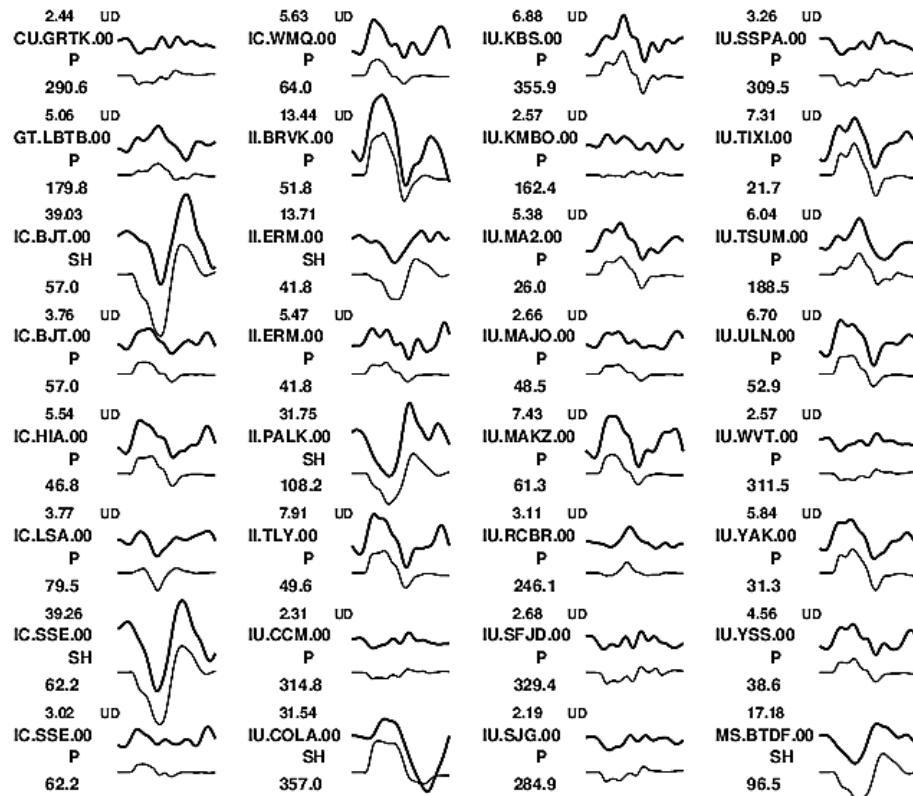


Figure 5.3. Preferred fault slip model and waveform fit of the 24/05/2014 North Aegean earthquake, as derived from 'MOM3' algorithm.

The main slip pattern was verified by the same data being filtered in a different band-pass range, from 0.01 to 1 Hz, yielding a similar variance. The observed data could be matched only with a very sharp source time function basic pulse of 3 triangular pulses with 1 s halfwidth and 2 s overlapping. Figure 5.5 shows the fault slip distribution that resulted from this approach. As we can see, the main pattern is similar and the main asperities are yielded again with this approach. The westward slip pattern is described by clear strike-slip motion, while the eastward has a significant normal component, as well.

Due to program discretization limitations, the subfault length could not be less than 10 km, in this approach, while in the previous trials it was 5 km. Despite the lower fault discretization, the inversion yielded a more detailed slip pattern, with more and smaller asperities (Fig. 5.5). In general, higher frequency bands produce more detailed outputs. This is the reason that inversion of strong motion records gives a 'higher resolution' view of the fault slip. But, concerning teleseismic records, the higher resolution could produce more visible errors, too. Consequently, it is not sure if all the dark-colored shapes, in Figure 5.5, are asperities or errors. This is the reason that I chose the previous model as the final one and used this approach only for validation reasons. When using teleseismic data for the inversion of a multiple-source event, such as the 24/05/2014 North Aegean earthquake, I believe it may be safer to keep a macroscopic view of the fault slip distribution, recognizing the few main big asperities, rather than a lot of smaller ambiguous ones. This means that, in cases of such complex event, inverting teleseismic data of a lower frequency band could be a safer technique, than using a higher frequency band. On the contrary, for a single event it is better to use a frequency band of 0.002 to 2 Hz.

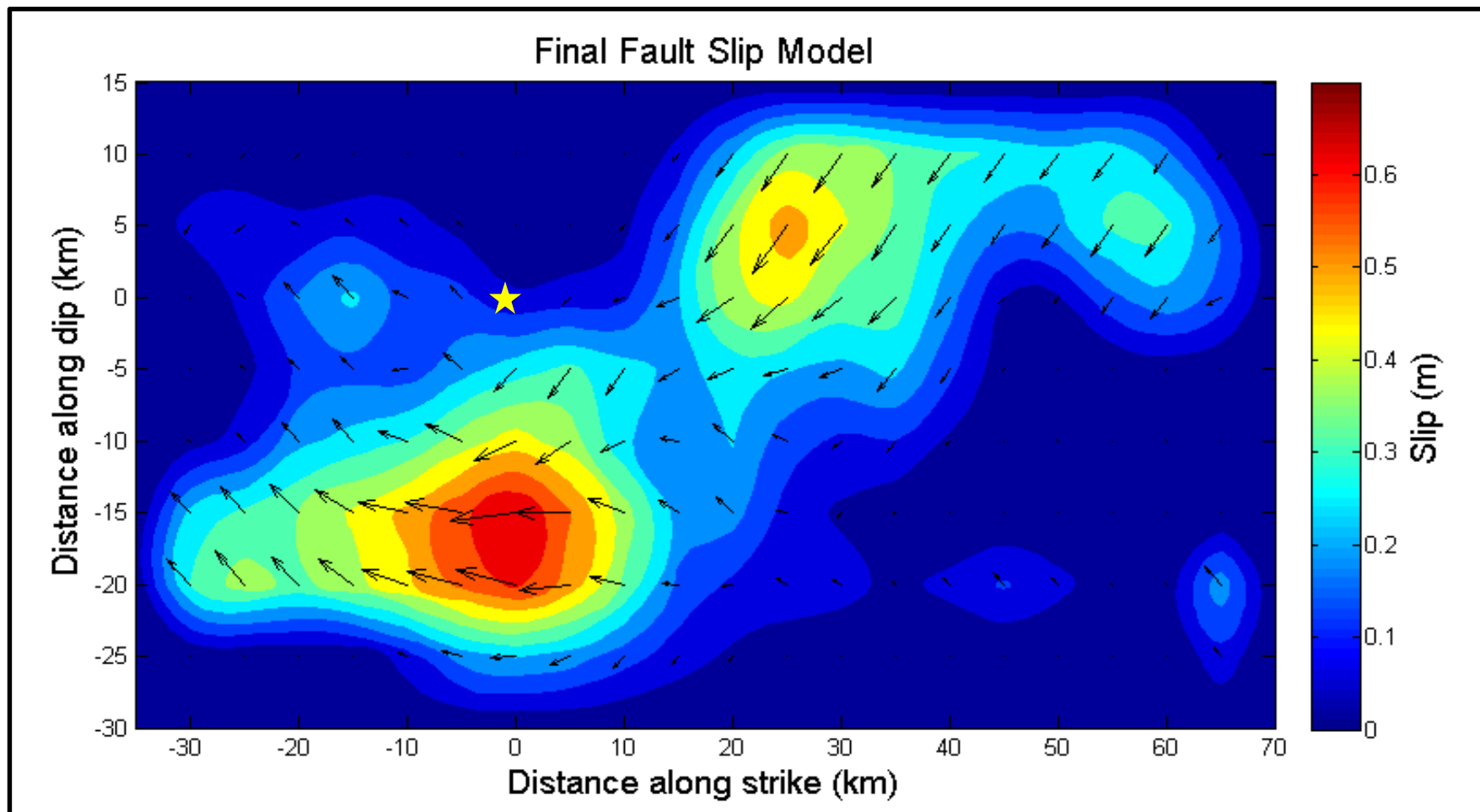


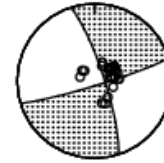
Figure 5.4. Preferred fault slip model for the 24 May 2014 North Aegean Earthquake (Matlab graphics). The yellow star represents the rupture initiation point.

N.Aegean 24/05/2014

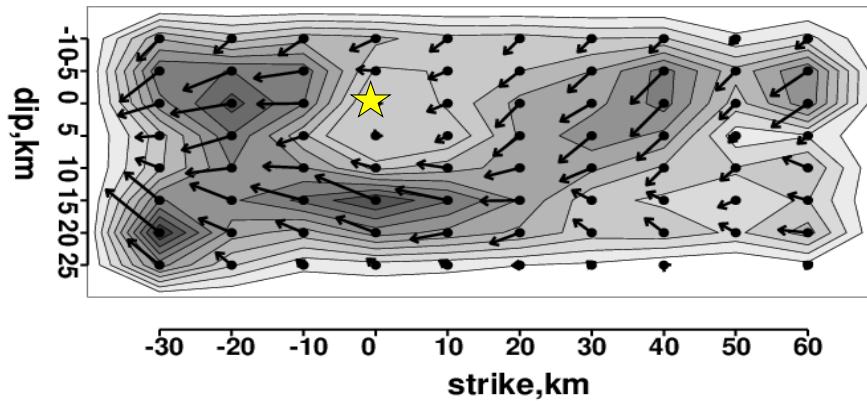
$M_o = 0.200E+20 \text{ Nm}$ $M_w = 6.80$

$H = 12.0 \text{ km}$

var. = 0.3425



(73.,85.,-170.)



0 30

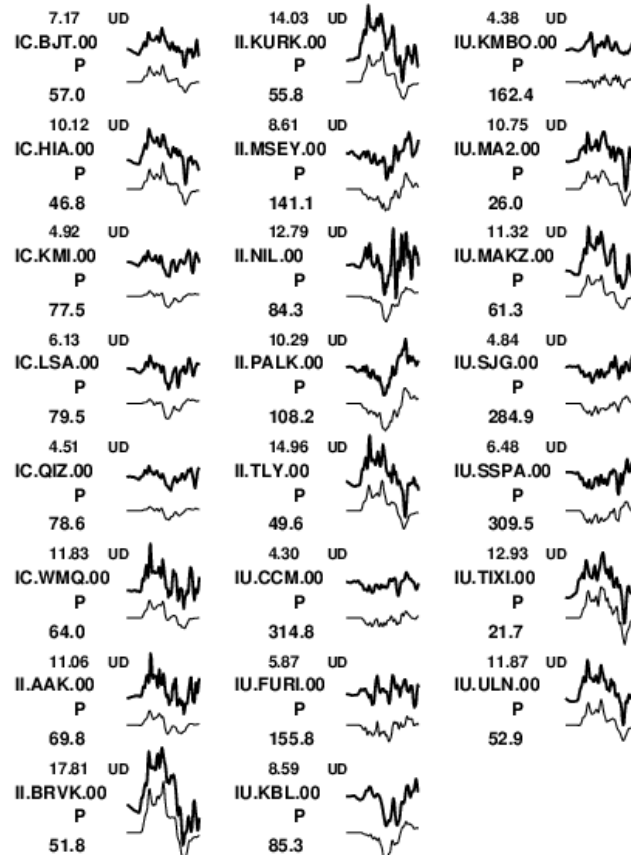


Figure 5.5. Fault slip model derived using higher-frequency data and different stations.

6 Summary and Discussion

The aim of this study was the determination of the source parameters and the finite fault slip model of the 24/05/2014 North Aegean earthquake, with the application of three methods: spectral analysis, moment tensor inversion and slip inversion of teleseismic data. This earthquake was selected to be investigated due to its source complexity and its magnitude, one of the largest and most ambiguous magnitudes of the past few years in the Greek region.

Initially, the seismic parameters were investigated through spectral analysis of teleseismic data. After noise filtering and attenuation correction of the data, I estimated the seismic moment and corner frequency, by linear fitting on the flat and descending spectrum parts, for each one of P and S wave spectrums. Corrections for radiation pattern and geometrical spreading were also applied. The spectral analysis yielded a mean moment magnitude of 6.6 and a mean f_c of 0.12 Hz. I used these results on empirical relations for circular and rectangular strike-slip models, which predict source dimensions, stress drop and maximum dislocation. For a mean magnitude of 6.6 and f_{cP} of 0.14, a $36 \times 11 \text{ km}^2$ fault was yielded, along with a $\Delta\sigma$ of 32 bars and a maximum dislocation of 0.6 m.

Next, after selecting the proper waveforms based on azimuthal coverage and signal-to-noise ratio, teleseismic body wave inversion was carried out. With the codes of McCaffrey et al. (1991) (i.e. MT5 software) and Kikuchi & Kanamori (1982, 1981), a dextral EWE-WSW multiple strike-slip source was obtained. The MT5 minimum misfit solution was provided for two subevents of M6.6, 13 s and 30 km apart in time and distance. In the method of Kikuchi and Kanamori, the minimum misfit solution appeared for 4 subevents with a total magnitude of M6.6, on a 100 km fault. The first subevent is located near the hypocenter area, the next two are activated in the western part and the last one takes place in the eastern part.

Finally, the finite fault slip model is determined using the software of Kikuchi and Kanamori (1982, 1991). Two main asperities were revealed, east and west of the hypocenter, in consistence with the double-source process proposed by Evangelidis (2015), where an initial 20 km westward rupture is followed, after 13 s, by a second eastward rupture. The slip inversion yielded a magnitude of Mw6.8, $\sim 100 \text{ km}$ fault length, 30 s source duration and 0.68 m maximum dislocation. The rupture velocity was estimated at 3.0 km/s by trial

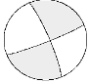
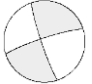
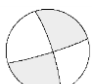
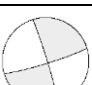
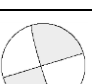
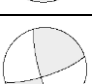
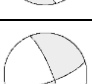
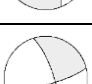
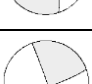
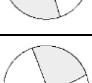
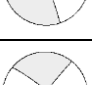
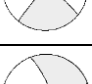
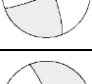
and error. The final fault slip model is considered stable, since the jack-knifing of the data does not result in significant changes of the main two-lobbed fault slip pattern, and is, also, consistent with the other results presented so far. The results of body wave modeling and slip inversion, transacted in this study, are presented in Table 6.1.

The 6.6 magnitude of the body wave modeling (MT5 and 'INVERSION' codes) is a lot smaller than the $M_w6.8$, obtained by the slip inversion. This is an expected result, due to the differences of the methodologies. The slip inversion technique determines seismic moment and slip values for every grid point, and thus slip is allowed to vary spatially. On the contrary, the moment tensor inversion method considers a constant slip value. For complex earthquakes, characterized by a number of subevents, the slip inversion could possibly obtain a more reliable magnitude. The centroid-moment-tensor published solutions, such as the GCMT solution, mostly agree in a 6.9 magnitude. The CMT inversion is a technique that captures the energy of all subevents and therefore provides better magnitude estimation. As for the significantly lower ML magnitudes, calculated by peak-to-peak measurements, they mainly reflect the biggest subevent and thus underestimate the total magnitude, just like the case of spectral analysis, which revealed a moment magnitude of 6.6.

As for the focal mechanism, a right-lateral strike-slip source is clearly yielded both from slip and body-wave inversion, by the software of MT5 and Kikuchi & Kanamori. With a strike of $\sim N70$, the source is almost parallel to the Saros basin. This estimation is accordant with the seismotectonic regime of North Aegean Trough, which has a dominant NE-SW dextral strike-slip component, reflected in GPS measurements (Kreemer et al., 2004; Chousianitis et al., 2015 and references therein). The aftershock distribution of the relocated catalog of Evangelidis (2015) clearly defines an ENE-WSW faulting, as well. Additionally, all the published solutions mostly agree on a dextral strike-slip shallow source, as shown in Table 6.1.

The source dip estimations mostly vary between 80° - 90° , indicating vertical faulting. As for the slip angle, Table 6.1 shows a rake of approximately -170° , mainly corresponding to a right-lateral strike-

Table 6.1. The results of this study (MT5 and Slip Inversion) compared to the published solutions of various Institutes, as reported to the European-Mediterranean Seismological Centre (EMSC).

Lat.°N	Long.°E	Strike°	Dip°	Rake°	Depth h (km)	Mw	Focal Sphere	Reference
40.29	25.398	68	85	-172	8	6.6		MT5 (1 st subevent)
40.40	25.729	252	83	-174	7	6.6		MT5 (2 nd subevent)
40.29	25.398	73	85	-171	12	6.8		Kikuchi & Kanamori Slip Inversion
40.30	25.70	73	85	-177	12	6.9		GCMT
40.30	25.70	253	90	-175	12	6.9		HRV
40.20	25.70	72	77	168	12	6.9		USGS
40.30	25.40	72	73	-167	21	6.9		INGV
40.30	25.40	76	77	-164	20	6.8		GFZ
40.30	25.50	71	82	-178	29	6.9		IPGP
40.30	25.50	71	82	-178	29	6.9		GeoAzur
40.30	25.50	219	88	173	24	6.8		KOERI
40.30	25.40	70	85	-167	14	6.8		NOA
40.30	25.40	245	72	171	15	6.3		AUTH

slip source with a small normal component. This estimation is reflected in the final fault-slip model, where the large western patch

is dominated by a strike-slip rake angle, while the eastern has a dip-slip component as well.

The final slip model corresponds to an approximately 95 km x 35 km fault, in accordance with the aftershock distribution. The relocated aftershock catalog of Evangelidis (2015) shows almost the whole activation of the ~100 km long Saros basin, as the main cluster, accompanied by the secondary triggered northern NAB cluster, reaching a really wide seismic zone (Kiratzi et al., 2015). Body wave inversion with the software of Kikuchi and Kanamori also yielded an 100 km fault length. Apart from the aftershock sequence, Evangelidis (2015) estimates a total fault length of ~85 km, from the backprojection of strong motion envelopes technique.

There is an obvious mismatch between the magnitude and fault length estimations. According to the empirical relations of Wells and Coppersmith (1994) and Papazachos et al. (2004) for rectangular strike-slip sources, an Mw6.8 earthquake is related with a ~50 km fault and an 100 km fault corresponds to a Mw7.4 earthquake, a lot larger even than the biggest published solutions of Mw6.9. The empirically-unexpected activation of such long seismic zones, even with earthquakes of smaller magnitudes, appears to be a seismological characteristic of the North Aegean Trough, considering that it has been repeated in the past. However, using the empirical relations of Wells and Coppersmith (1994) for an Mw6.8 event, a maximum dislocation of 0.63 m is yielded, pretty close to 0.68 m of the final fault slip model.

Both slip and moment tensor inversion, revealed a source duration of ~30 s. A rupture velocity of 3.0 km/s was also determined by trial and error, a lot smaller than the supershear 5.5 km/s value of Evangelidis (2015). In a simple approach, these values yield a ~90 km rupture, in consistence with the 95 km fault length of slip inversion and aftershock distribution.

The preferred fault slip model (Fig. 5.4) reveals a bilateral rupture, gathered in two main asperities, west and east of the relocated epicenter. The maximum dislocation appears in the deeper western asperity of 40 km length x 20 km width. The eastern shallower rupture indicates a length of up to ~60 km. This pattern fits the N73° cross-section of aftershock spatial distribution (Fig. 6.1). As expected, the asperity areas are poor in aftershock hypocenters.

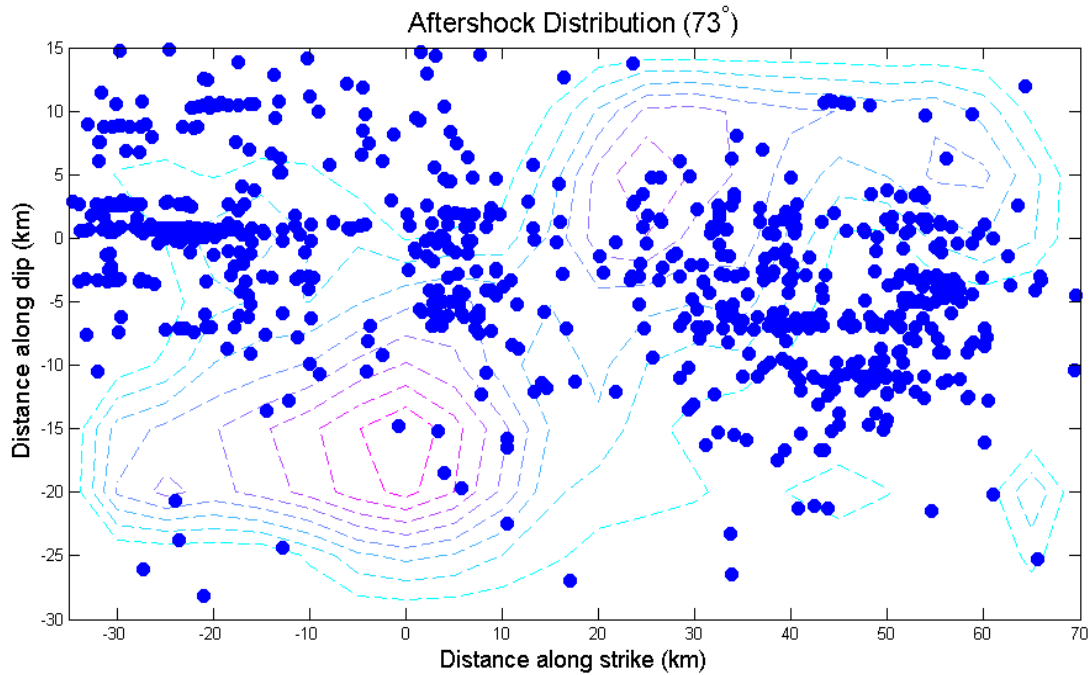


Figure 6.1. Aftershock spatial distribution (cross-section at 73°) of 2014 North Aegean sequence, using the relocated catalog of C. Evangelidis (personal communication). A lack of aftershocks on the asperity areas is noticeable.

The slip model of two lobes, east and west of the hypocenter, is accordant to the source process proposed by Evangelidis (2015). According to the last, there was an initial 20 km rupture westward of the epicenter, followed by 65 km rupture that spread eastward of it, delayed by 13 s. The 13 s time lagging was also used in the MT5 inversion. The moment tensor inversion with the software of Kikuchi and Kanamori, revealed that the western part was activated first, as well, with the three first subevents occurring west of the hypocenter.

The two main asperities possibly represent the two sub-events of the MT5 solution, indicating a multiple-source event, which is, anyway, observed in some of the strong motion records. The source complexity is, also, reflected at the source time function yielded by the higher-frequency data inversion.

Last, the spectral analysis resulted in an Mw6.6 earthquake, probably representing the biggest subevent. The empirical relations of Wells and Coppersmith (1994) and Papazachos et al. (2004), yield a corresponding fault length of 36 km. If the biggest asperity is regarded as the biggest subevent, then the ~40 km length of the western asperity is a value consistent with the 36 km empirically-predicted length.

Apart from the seismic parameter quantification and the determination of slip distribution of the 2014 North Aegean earthquake, the scientific contribution of this MSc thesis is the investigation on how the aforementioned three different techniques could be combined in order to best resolve such complex cases. The source parameters and the fault slip model, yielded from this study, although being consistent with the complicated seismotectonic characteristics of the dextral strike-slip North Aegean faulting, reveal the significant related source complexities and therefore inspire for further research.

7 References

- Abercrombie, R. E. (1995). Earthquake source scaling relationships from -1 to 5 ML using seismograms recorded at 2.5 km depth. *J. Geophys. Res.* 100, 24015-24036.
- Aki, K. (1972). The upper mantle techtonophysics, *Techtonophysics*, 13, 1-4, 423-446.
- Aki, K. and P. G. Richards (2002). *Quantitative seismology*. Second Edition, ISBN 0-935702-96-2, University Science Books, Sausalito, 704 pp.
- Bormann, P. and J. Saul (2009). Earthquake magnitude. In: Meyers, A. (Ed.) *Encyclopedia of complexity and systems science*, Vol. 3, Springer, Heidelberg - New York, 2473-2496.
- Bouchon, M. (1976). Teleseismic body wave radiation from a seismic source in a layered medium, *Geophys. J. R. Astr. Soc.* 47, 515-530.
- Brune, J. (1970). Tectonic stress and seismic shear waves from earthquakes. *J. Geophys. Res.* 75, 4997-5009.
- Chousianitis, K., Ganas, A., & Evangelidis, C. P. (2015). Strain and rotation rate patterns of mainland Greece from continuous GPS data and comparison between seismic and geodetic moment release. *Journal of Geophysical Research: Solid Earth*.
- Choy, G. L., & Cormier, V. F. (1986). Direct measurement of the mantle attenuation operator from broadband P and S waveforms. *Journal of Geophysical Research: Solid Earth* (1978-2012), 91(B7), 7326-7342.
- Eshelby, J. D. (1957). The determination of the elastic field of an ellipsoidal inclusion and related problems, *Proceedings of the Royal Society of London, Series A*, 241, 376-396.
- Evangelidis, C. P. (2015). Imaging supershear rupture for the 2014 Mw 6.9 Northern Aegean earthquake by backprojection of strong motion waveforms. *Geophysical Research Letters*, 42, 307-315.
- Futterman, W.I. (1962). Dispersive body waves, *J. Geophys. Res.*, 67, 5279-5291.
- Geller, R. J. (1976). Scaling relations for earthquake source parameters and magnitudes. *Bulletin of the Seismological Society of America*, 66(5), 1501-1523.
- Goldstein, P., D. Dodge, M. Firpo, Lee Minner (2003). SAC2000: Signal processing and analysis tools for seismologists and engineers. In: Lee, W. H. K., H. Kanamori, P. C. Jennings and C. Kisslinger (Eds.) *Invited contribution to, The IASPEI international handbook of earthquake and engineering seismology*. Academic Press, London.
- Goldstein, P., A. Snoke, (2005). "SAC Availability for the IRIS Community", *Incorporated Institutions for Seismology Data Management Center Electronic Newsletter*.

- Hanks, M. and H. Kanamori (1979). A moment magnitude scale. *J. Geophys. Res.* 84, 2348–2340.
- Haskell, N. A. (1960). Crustal reflection of plane SH waves. *Journal of Geophysical Research*, 65(12), 4147-4150.
- Haskell, N. A. (1962). Crustal reflection of plane P and SV waves. *Journal of Geophysical Research*, 67(12), 4751-4768.
- Havskov, J. and L. Ottemöller, *Routine Data Processing in Earthquake Seismology*, DOI 10.1007/978-90-481-8697-6, © Springer Science+Business Media B.V. 2010.
- Helmberger, D.V., (1974). Generalized ray theory for shear dislocation, *Bull. Seism. Soc. Am.*, 64, 45-64.
- Houston, H. and H. Kanamori (1986). Source spectra of great earthquakes: Teleseismic constraints on rupture process and strong motion. *Bull. Seism. Soc. Am.* 76, 19–42..
- IASPEI (2005). Summary of magnitude working group recommendations on standard procedures for determining earthquake magnitudes from digital data. <http://www.iaspei.org/commissions/CSOI.html>
- Jeffreys, H. and K. E. Bullen (1940). *Seismological tables*. British Association for the Advancement of Science, Burlington House, London.
- Kanamori, H. (1977). The energy release in great earthquakes, *JGR*, 82, No. 20, 2981-2987.
- Kikuchi, M. and H. Kanamori (1982). Inversion of complex body waves, *Bull. Seism. Soc. Am.* 72, 491-506.
- Kikuchi, M. and H. Kanamori (1991). Inversion of complex body waves – III. *Bull. Seism. Soc. Am.* 81, 2335–2350.
- Kikuchi, M., Kanamori, H., & Satake, K. (1993). Source complexity of the 1988 Armenian Earthquake: Evidence for a slow after-slip event. *Journal of Geophysical Research: Solid Earth* (1978–2012), 98(B9), 15797-15808.
- Kiratzí, A., Tsakiroudi, E. and G. Karakaisis (2015). The May 24, 2014 (Mw6.8) earthquake in North Aegean Trough: spatiotemporal evolution, source and slip model from teleseismic data, *Physics and Chemistry of the Earth*, under review.
- Knopoff, L. (1957). Energy release in great earthquakes, *Geophysical Journal*, 1, 44-52.
- Kreemer, C., & Chamot-Rooke, N. (2004). Contemporary kinematics of the southern Aegean and the Mediterranean Ridge. *Geophysical Journal International*, 157(3), 1377-1392.
- Kurt, H., Demirbaşı, E., & Kuşçu, İ. (2000). Active submarine tectonism and formation of the Gulf of Saros, Northeast Aegean Sea, inferred from multi-channel seismic reflection data. *Marine Geology*, 165(1), 13-26.

Langston, C. A. and D. V. Helmberger (1975). A procedure for modeling shallow dislocation sources. *Geophys. J. R. Astr. Soc.* 42, 117–130.

Lay, T. and T. C. Wallace (1995). *Modern global seismology*. Academic Press, San Diego, 521 pp.

Madariaga, R. (1976). Dynamics of an expanding circular fault. *Bull. Seism. Soc. Am.* 66, 639–666.

McCaffrey, R., and G. Abers, (1988). SYN3: A program for inversion of teleseismic body wave form on microcomputers, Air Force Geophysics Laboratory Technical Report, AFGL-TR-88-0099.

McCaffrey, R., Zwick, P., and Abers, G. (1991). "SYN4 Program", IASPEI Software Library, 3, 81-166.

McCaffrey, R., G. Abers, and P. Zwick (1991). Inversion of Teleseismic Body Waves, IASPEI Software Library, Volume 3, Chapter 3.

McNeill, L. C., Mille, A., Minshull, T. A., Bull, J. M., Kenyon, N. H., & Ivanov, M. (2004). Extension of the North Anatolian Fault into the North Aegean Trough: Evidence for transtension, strain partitioning, and analogues for Sea of Marmara basin models. *Tectonics*, 23(2).

Nabelek, J. L. (1984). Determination of earthquake source parameters from inversion of body waves, Ph.D. Thesis, MIT, Cambridge, Massachusetts.

Okal, E. A. (1992). A student's guide to teleseismic body wave amplitudes. *Seismological Research Letters*, 63(2), 169-180.

Oral, M., Reilinger, R. E., Nafi Toksöz, M., King, R. W., Aykut Barka, A., Kinik, I., & Lenk, O. (1995). Global positioning system offers evidence of plate motions in eastern Mediterranean. *EOS, Transactions American Geophysical Union*, 76(2), 9-11.

Papanikolaou, I. D., & Papanikolaou, D. I. (2007). Seismic hazard scenarios from the longest geologically constrained active fault of the Aegean. *Quaternary international*, 171, 31-44.

Papazachos, B. C. (1989). A time-predictable model for earthquake generation in Greece. *Bulletin of the Seismological Society of America*, 79(1), 77-84.

Papazachos, B. C. and Papazachou, C. (1997). *The Earthquakes of Greece*, Editions Ziti, Thessaloniki, pp. 286 (in greek).

Papazachos, B. C., Papadimitriou, E. E., Kiratzi, A. A., Papazachos, C. B., & Louvari, E. K. (1998). Fault plane solutions in the Aegean Sea and the surrounding area and their tectonic implications. *Boll. Geof. Teor. Appl*, 39(3), 199-218.

Papazachos, C. B. (1999). Seismological and GPS evidence for the Aegean-Anatolia Interaction. *Geophysical Research Letters*, 26(17), 2653-2656.

Papazachos, B. C., Savvaidis, A. S., Karakaisis, G. F., & Papazachos, C. B. (2002). Precursory accelerating seismic crustal deformation in the Northwestern Anatolia Fault Zone. *Tectonophysics*, 347(4), 217-230.

Papazachos, B., Scordilis, E., Panagiotopoulos, D., Papazachos, C. and Karakaisis, G. (2004). Global relations between seismic fault parameters and moment magnitude of earthquakes. 10th International Congress of Geological Society of Greece, Thessaloniki, 15- 17 April 2004, 539-540.

SEED (2007). SEED reference manual. Standard for the exchange of earthquake data, SEED format version 2.4. International Federation of Digital Seismograph Networks Incorporated Research Institutions for Seismology (IRIS), USGS. www.iris.edu

Shearer, P. M. (2009). *Introduction to seismology*. Cambridge University Press.

Stein, S. and M. Wysession (2003). *Introduction to seismology, earthquakes and earth structure*. Blackwell Publishing, Oxford, 498 pp.

Wells, D. L., and K. J. Coppersmith (1994). New empirical relationships among magnitude, rupture length, rupture width, rupture area, and surface displacement, *Bull. Seism. Soc. Am.* 84, 974-1002.

Zwick, P., McCaffery, R., and Abers, G. (1994). "MT5 Program", IASPEI Software Library, 4.

Data and Resources

The facilities of IRIS Data Services, and specifically the IRIS Data Management Center, were used for access to waveforms, related metadata, and/or derived products used in this study. IRIS Data Services are funded through the Seismological Facilities for the Advancement of Geoscience and EarthScope (SAGE) Proposal of the National Science Foundation under Cooperative Agreement EAR-1261681.

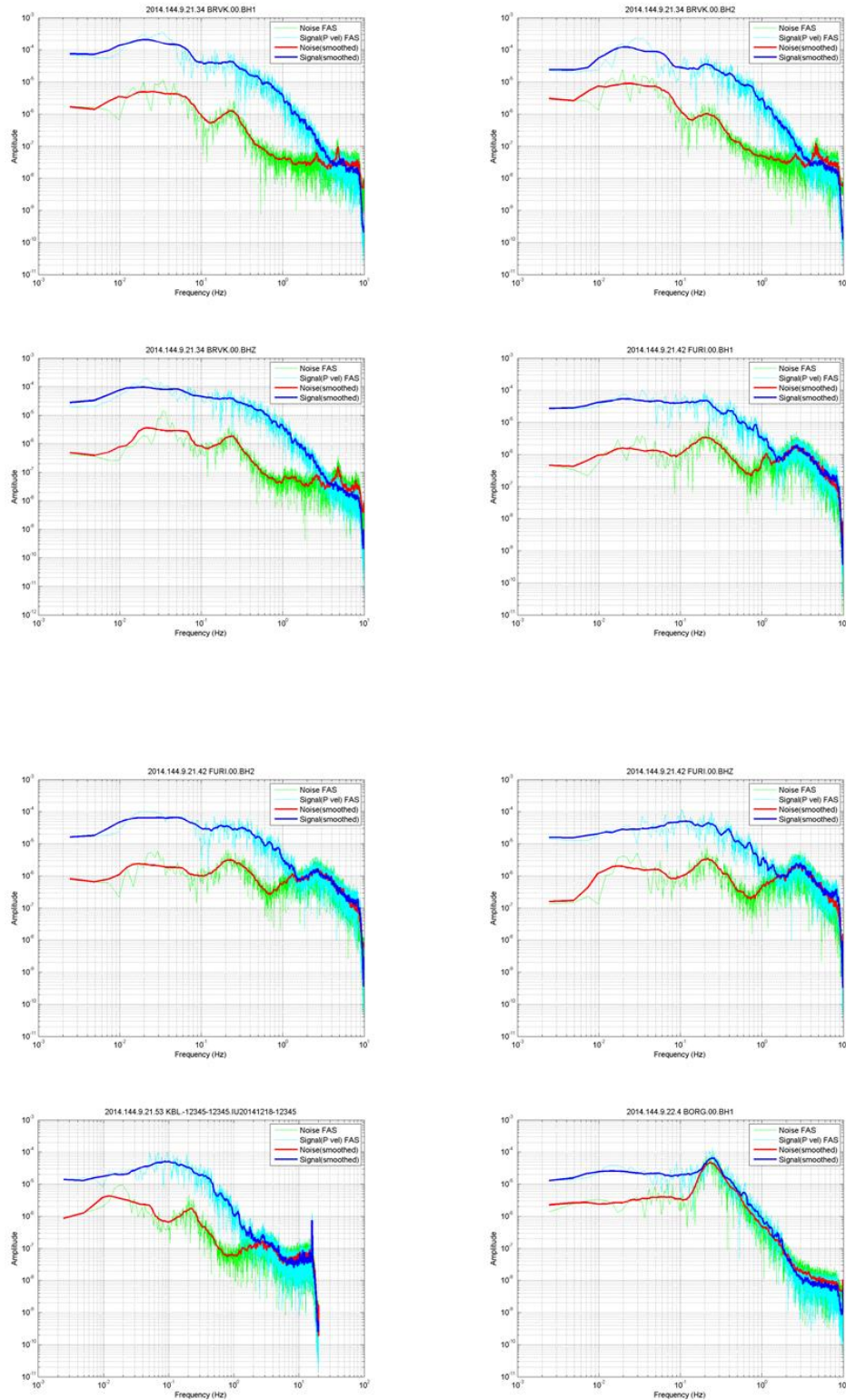
The seismic stations, used in this study, belong to the GSN network. Global Seismographic Network (GSN) is a cooperative scientific facility operated jointly by the Incorporated Research Institutions for Seismology (IRIS), the United States Geological Survey (USGS), and the National Science Foundation (NSF), under Cooperative Agreement EAR-1261681. The networks of the retrieved station records are:

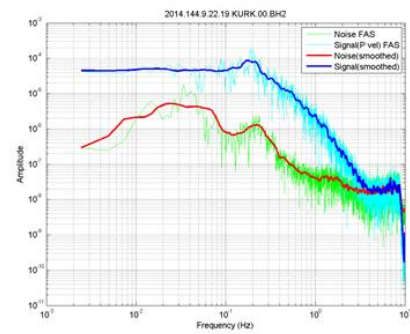
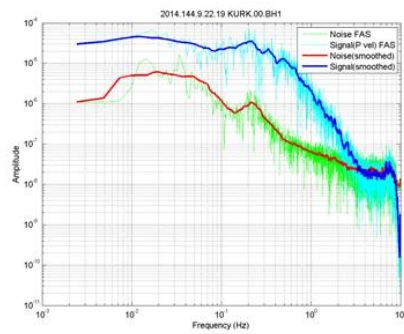
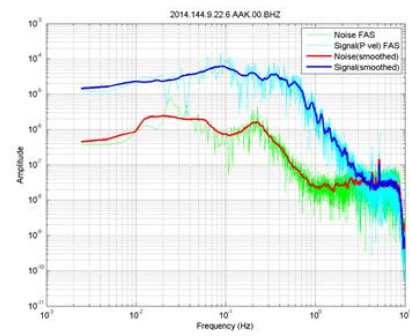
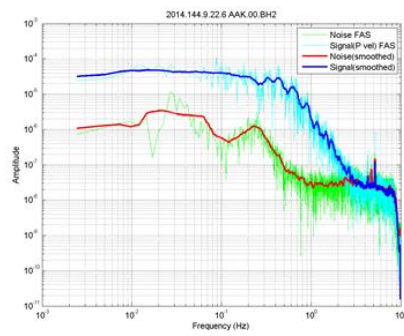
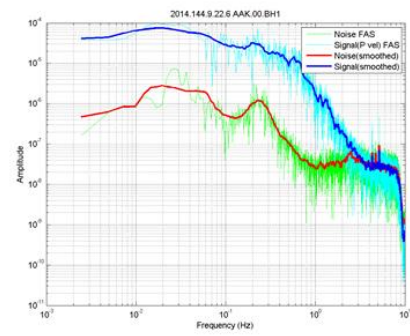
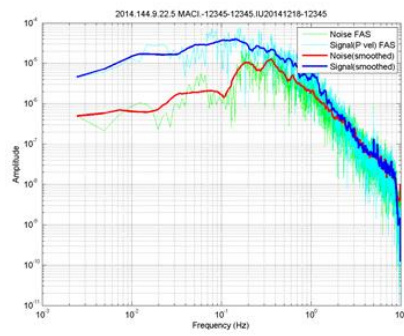
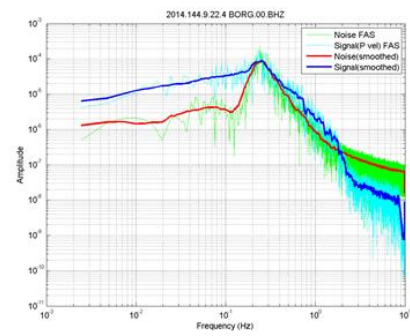
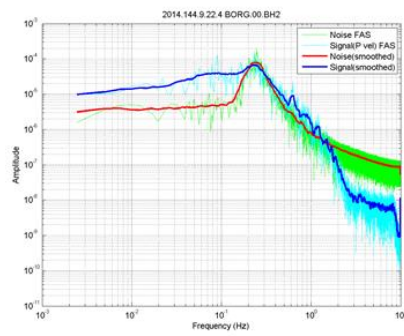
- Northern California Earthquake Data Center. (2014). Berkeley Digital Seismic Network (BDSN). Northern California Earthquake Data Center. <http://doi.org/10.7932/BDSN>
- California Institute of Technology (Caltech) (1926): Southern California Seismic Network. International Federation of Digital Seismograph Networks. Other/Seismic Network. doi:10.7914/SN/CI
- Albuquerque Seismological Laboratory (ASL)/USGS (1993): Global Telemetered Seismograph Network (USAF/USGS). International Federation of Digital Seismograph Networks. Other/Seismic Network. doi:10.7914/SN/GT
- Albuquerque Seismological Laboratory (ASL)/USGS (1992): New China Digital Seismograph Network. International Federation of Digital Seismograph Networks. Other/Seismic Network. doi:10.7914/SN/IC
- Scripps Institution of Oceanography (1986): IRIS/IDA Seismic Network. International Federation of Digital Seismograph Networks. Other/Seismic Network. doi:10.7914/SN/II
- Albuquerque Seismological Laboratory (ASL)/USGS (1988): Global Seismograph Network (GSN - IRIS/USGS). International Federation of Digital Seismograph Networks. Other/Seismic Network. doi:10.7914/SN/IU
- Australian National Seismograph Network (<http://www.fdsn.org/networks/detail/AU/>)
- Caribbean Network (<http://www.fdsn.org/networks/detail/CU/>)

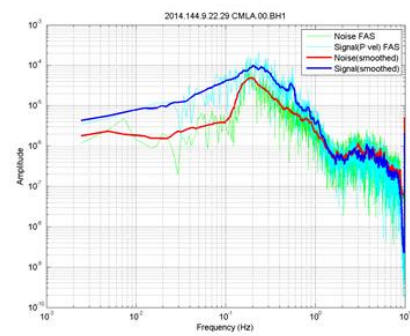
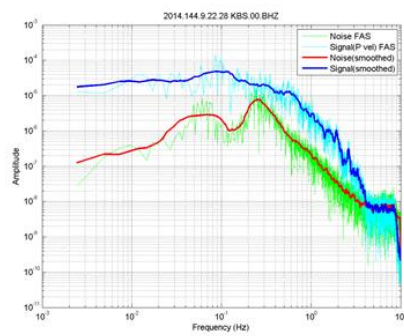
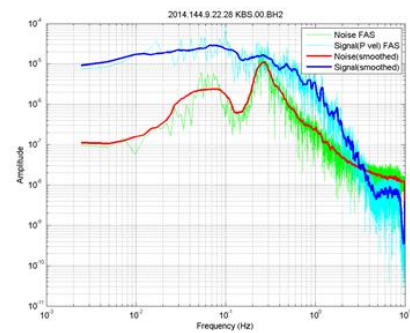
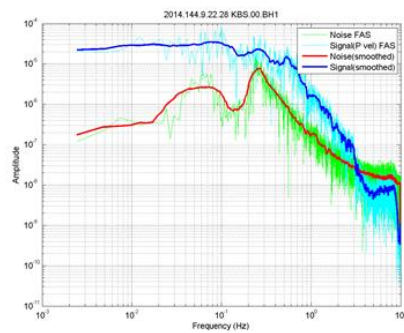
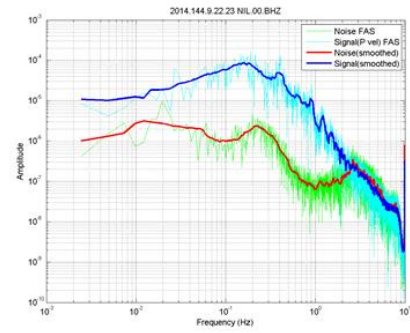
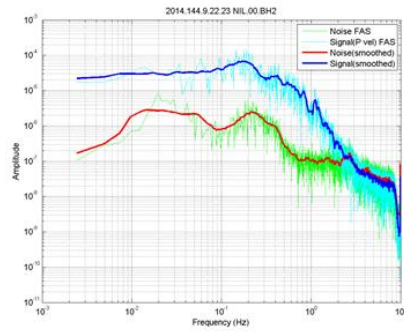
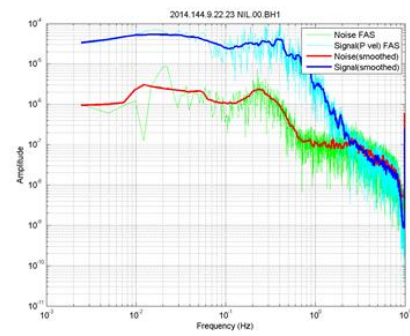
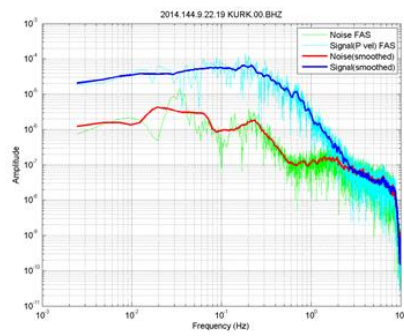
- Hong Kong Seismograph Network
(<http://www.fdsn.org/networks/detail/HK/>)
- International Miscellaneous Stations
(<http://www.fdsn.org/networks/detail/IM/>)
- Singapore Seismological Station
(<http://www.fdsn.org/networks/detail/MS/>)

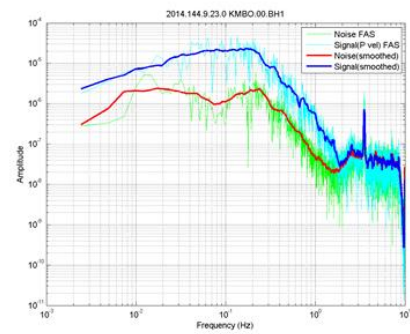
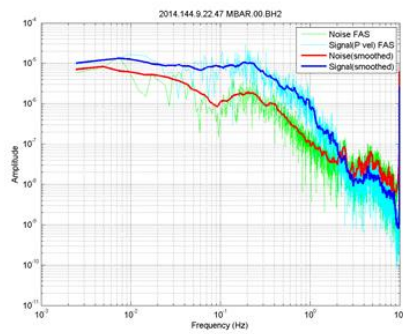
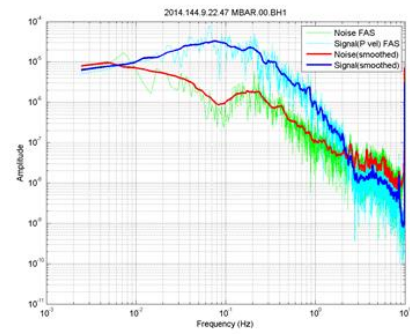
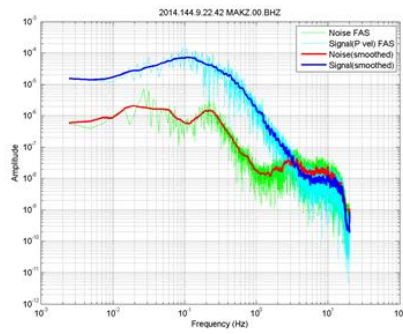
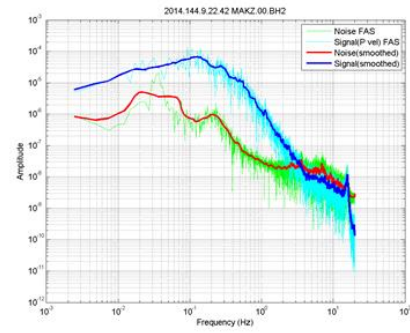
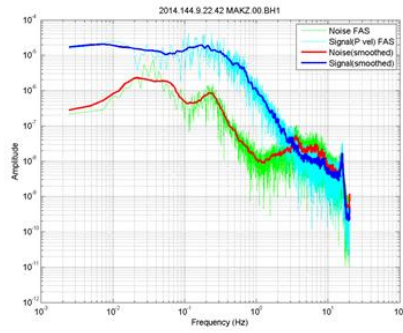
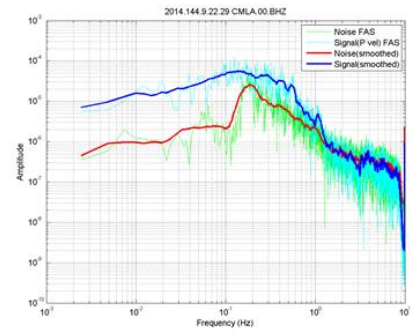
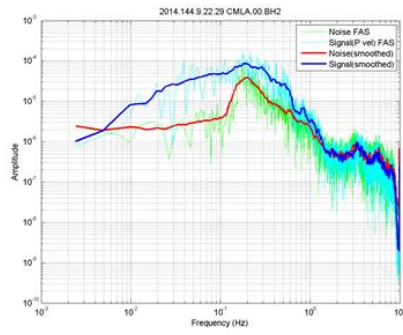
The data preparation was carried out in SAC- Seismic Analysis Code (Goldstein et al., 2003; Goldstein and Snoke, 2005). The teleseismic body wave modeling was performed with the program MT5 (Zwick et al., 1995), which is an advanced version of SYN3 and SYN4 software created by McCaffrey and Abbers (1998) and McCaffrey et al. (1991). Teleseismic moment tensor and slip inversions were accomplished by the software of Kikuchi and Kanamori (M. Kikuchi and H. Kanamori, Note on Teleseismic Body-Wave Inversion Program, <http://www.eri.u-tokyo.ac.jp/ETAL/KIKUCHI/>). Data from the Geophysics Department of the Aristotle University of Thessaloniki (<http://geophysics.geo.auth.gr>) were also retrieved. Matlab® (release R2010b), as well as the Generic Mapping Tools - version 5.1.1 (Wessel and Smith, 1998, <http://gmt.soest.hawaii.edu/>) were used in this study.

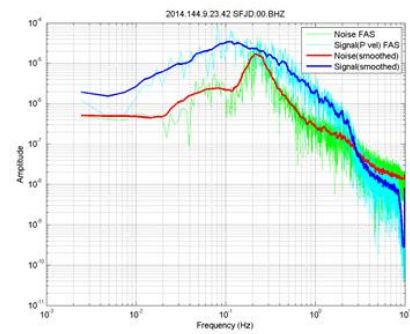
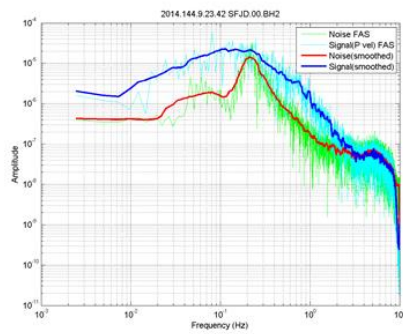
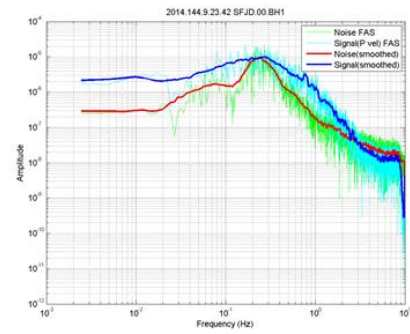
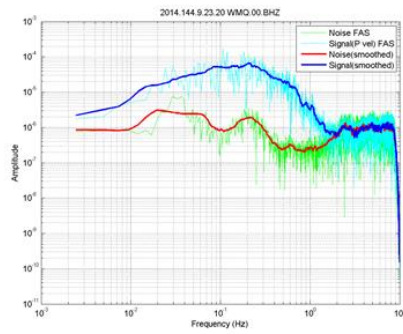
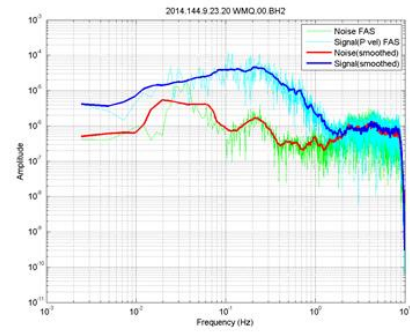
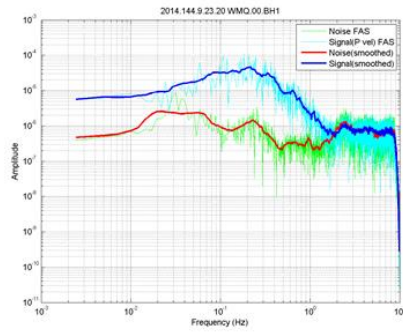
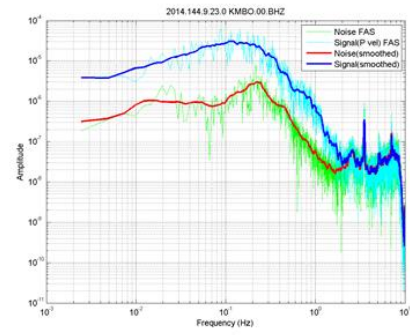
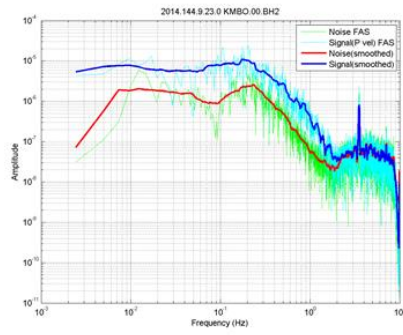
Appendix A: Signal-to-noise Fourier spectrums

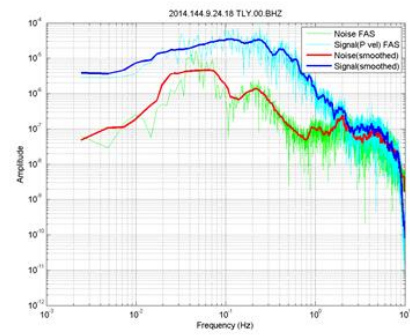
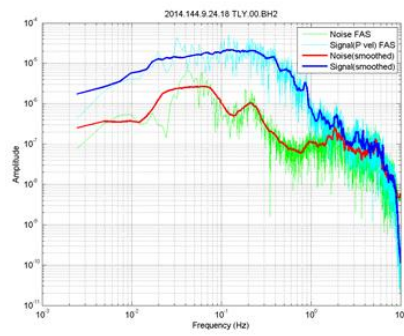
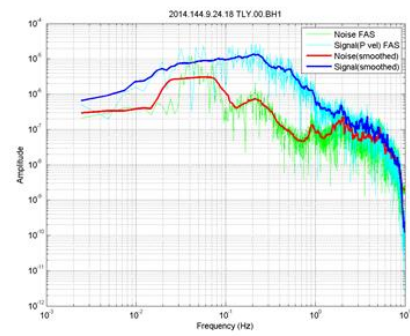
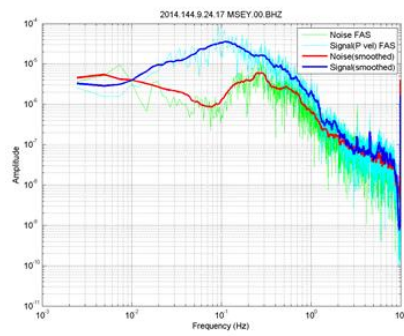
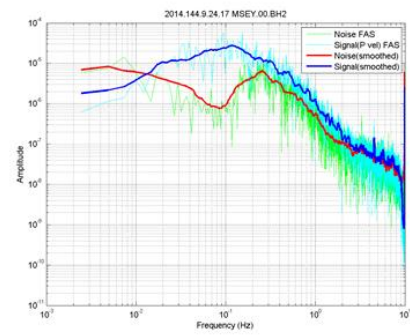
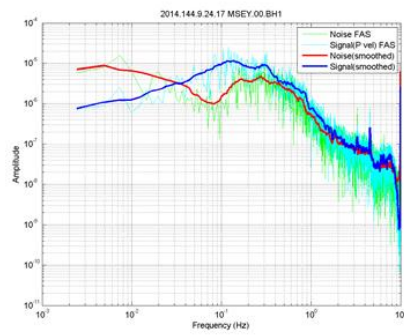
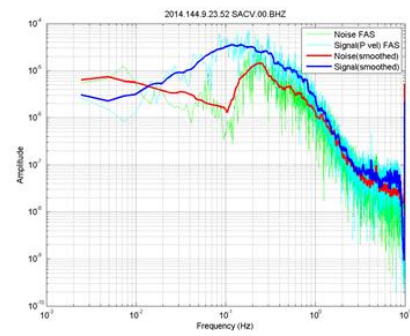
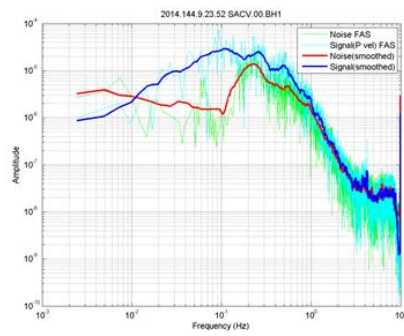


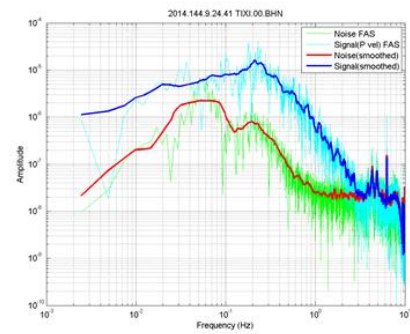
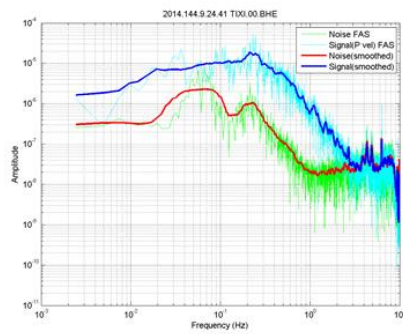
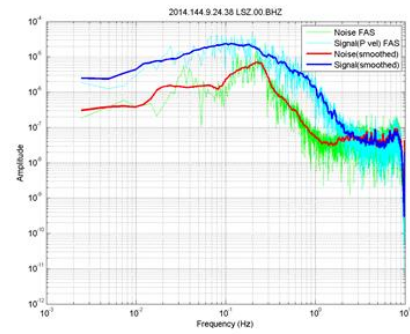
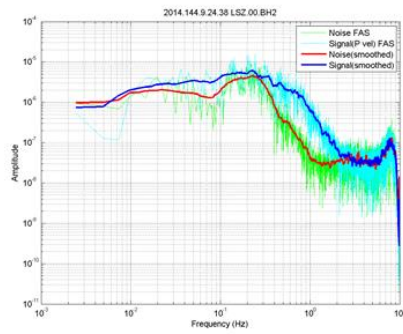
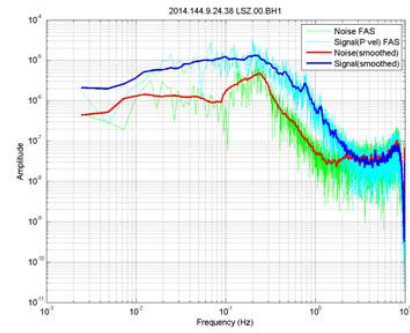
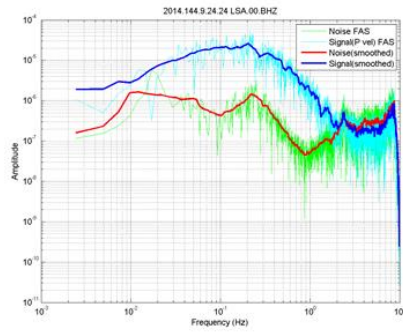
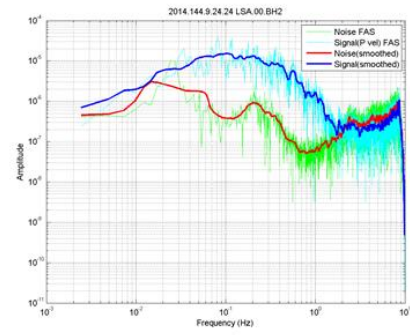
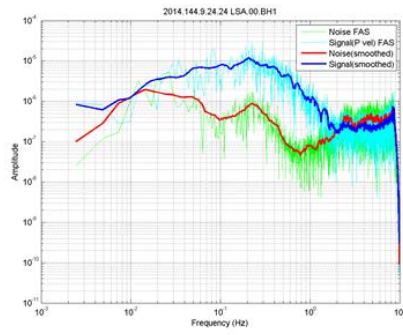


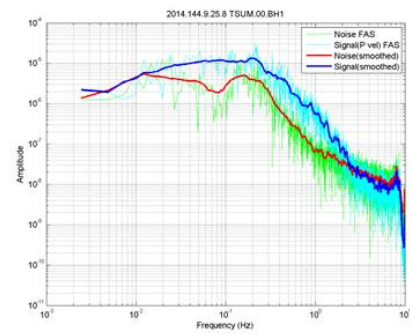
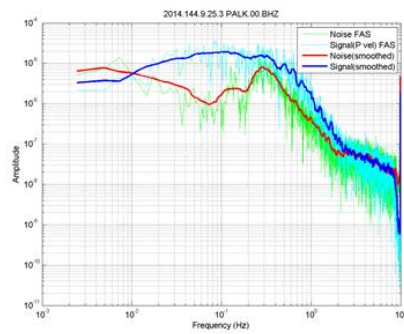
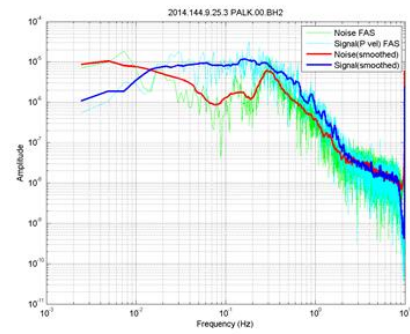
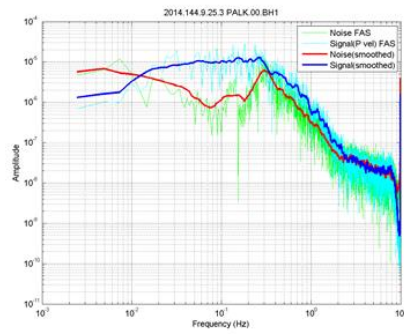
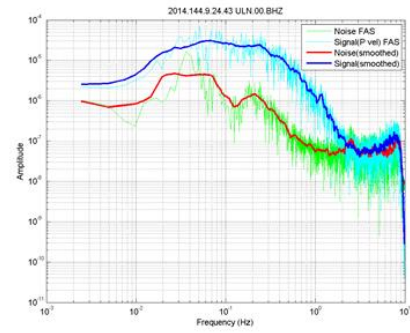
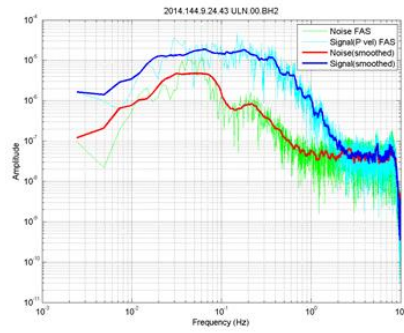
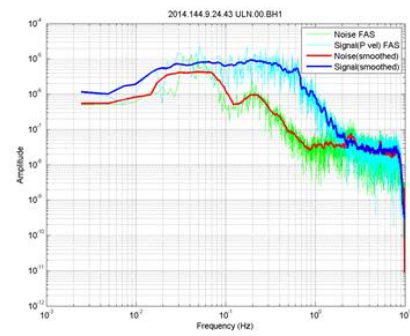
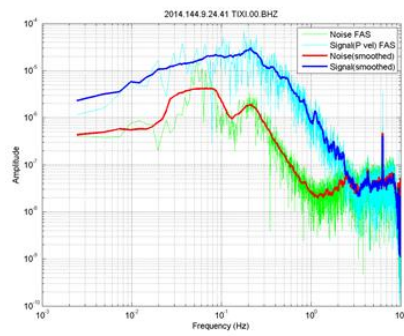


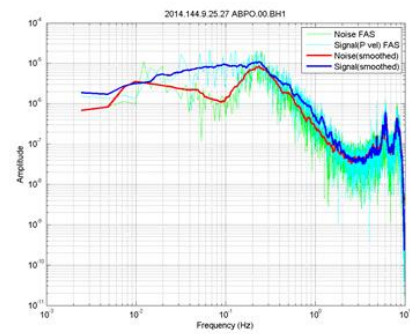
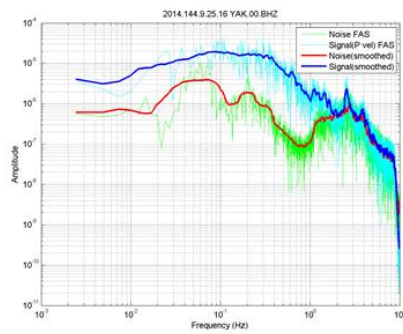
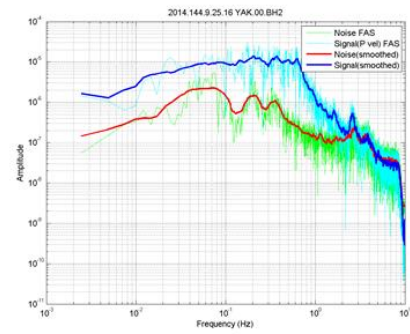
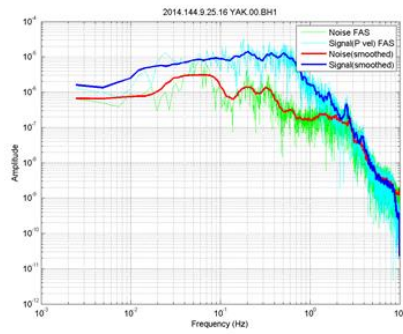
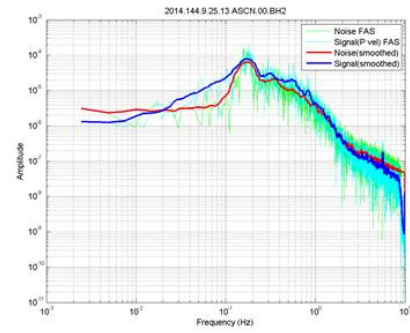
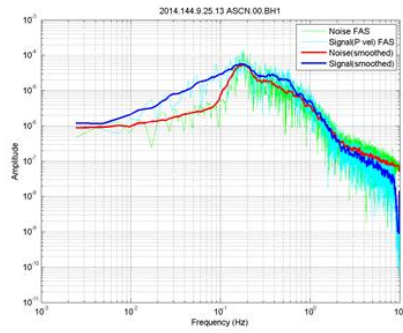
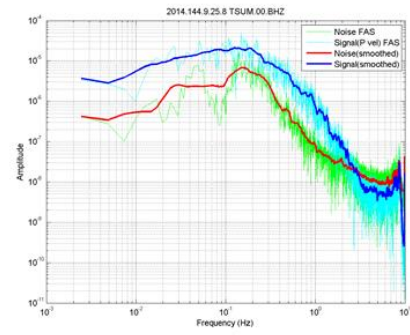
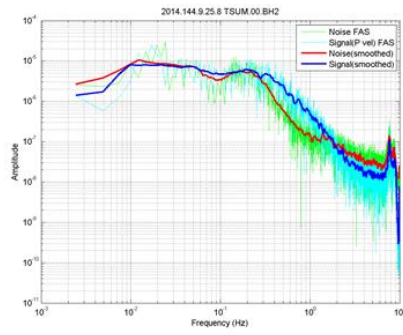


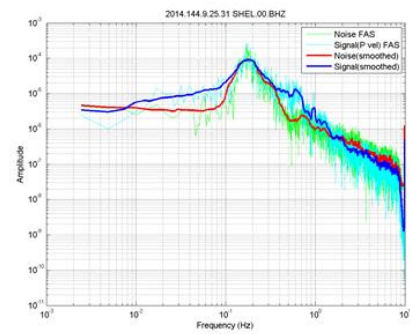
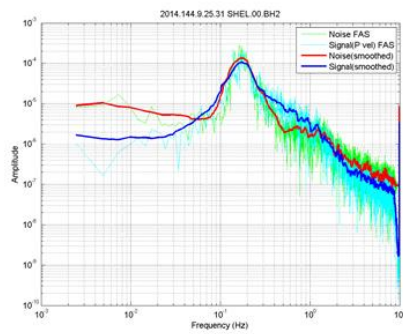
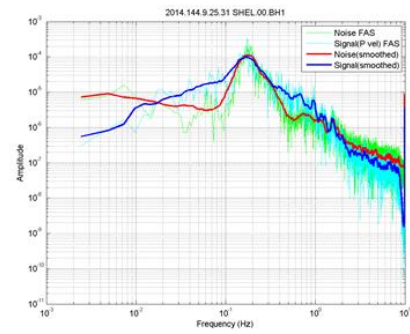
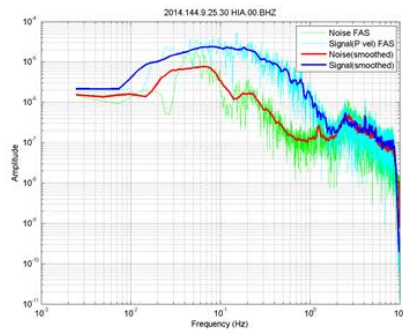
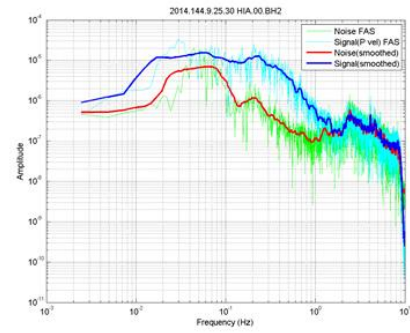
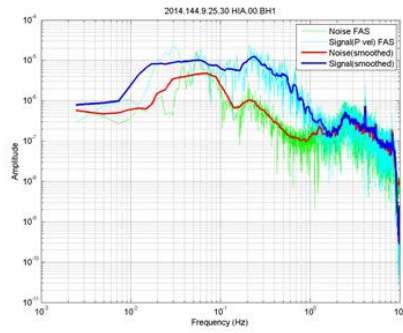
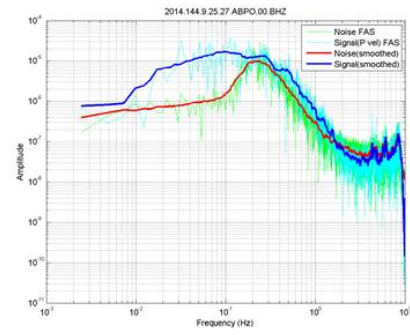
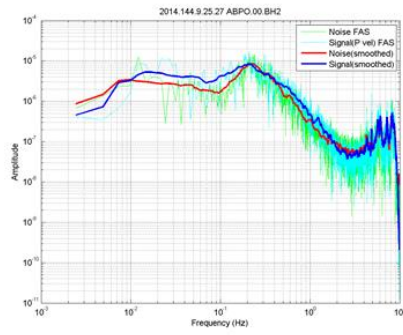


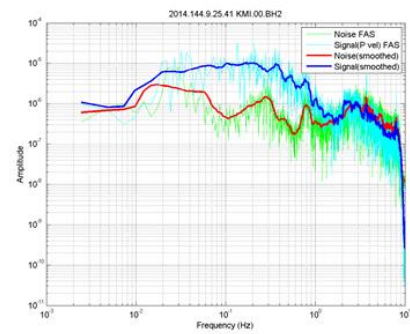
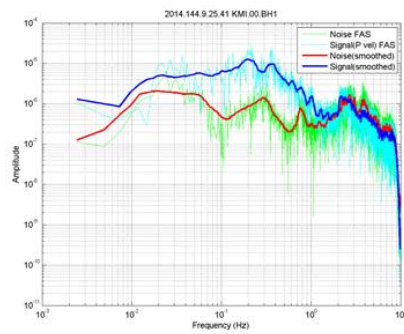
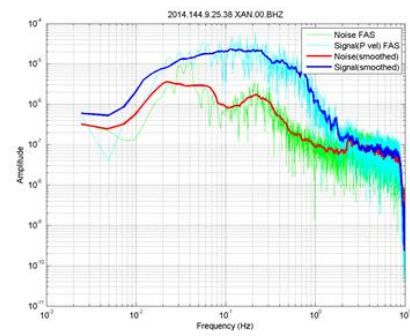
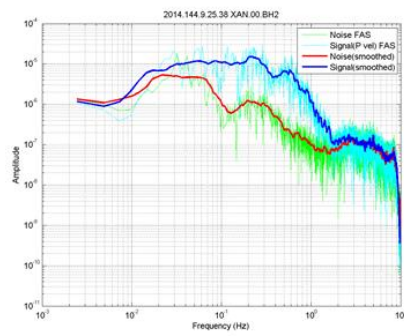
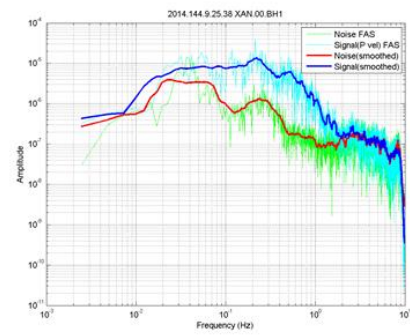
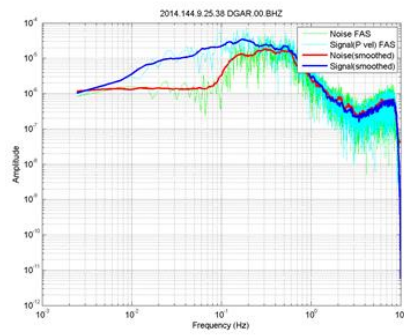
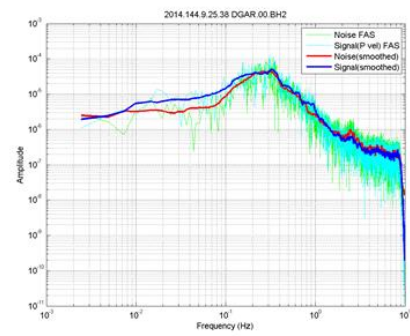
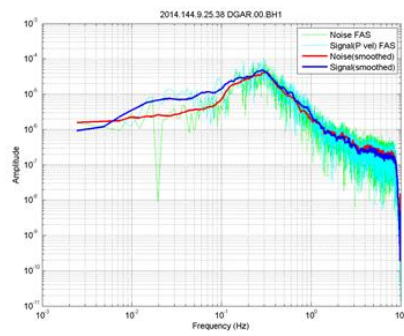


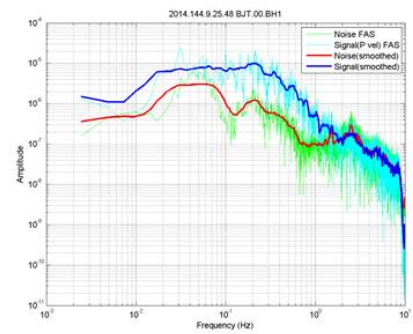
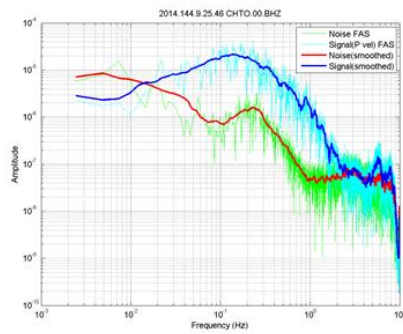
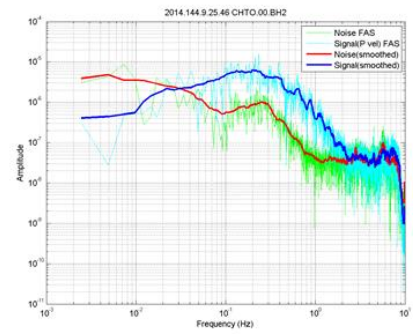
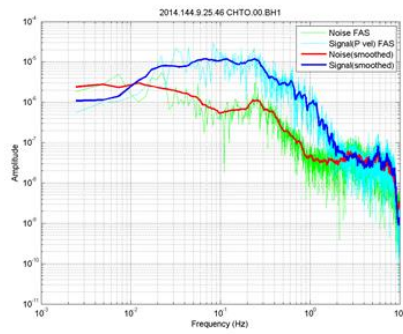
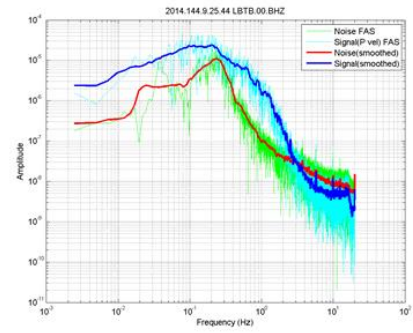
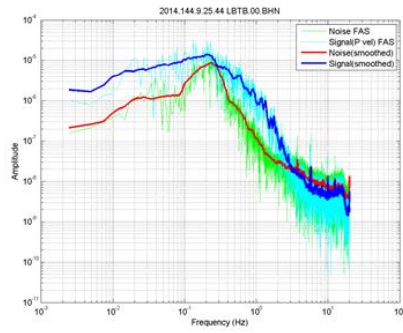
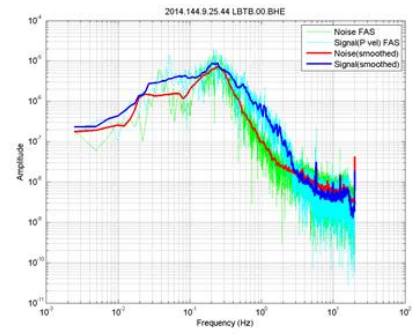
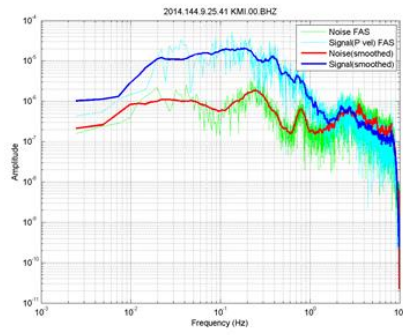


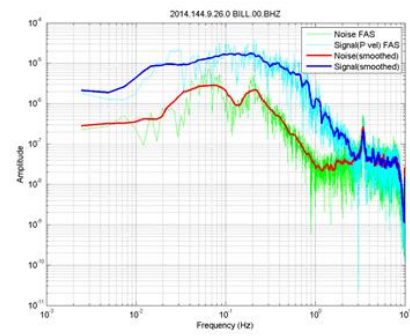
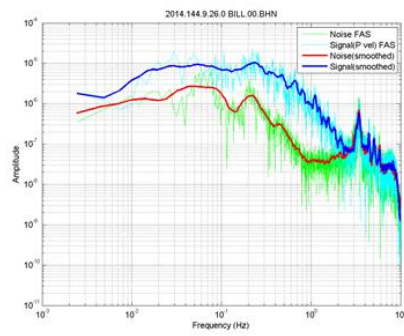
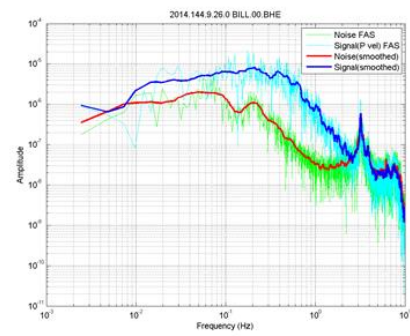
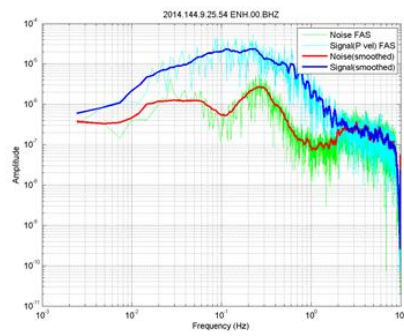
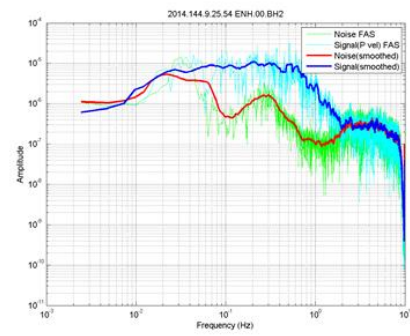
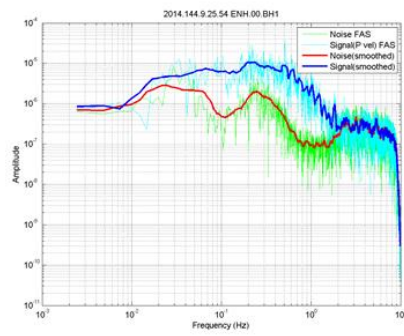
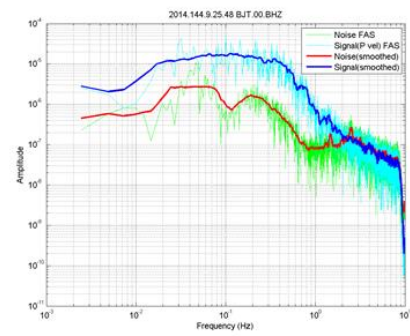
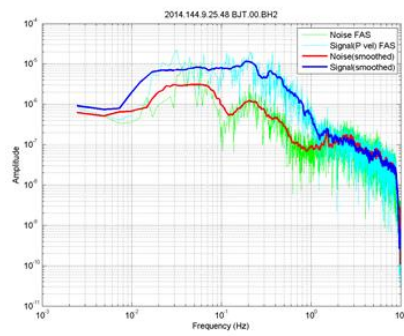


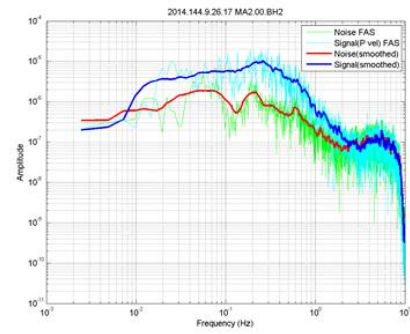
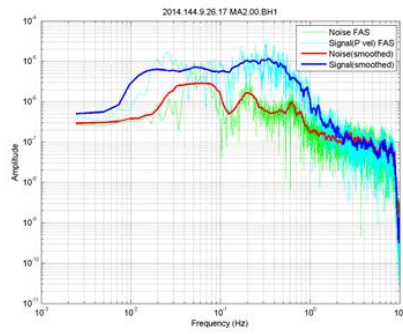
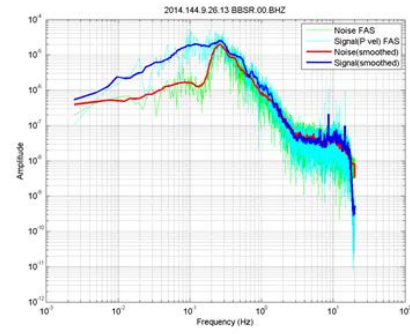
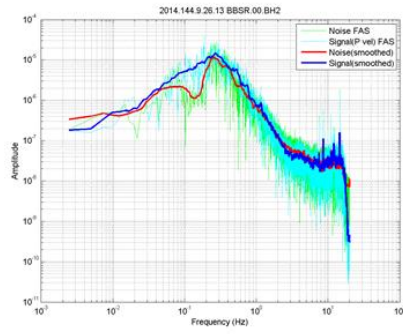
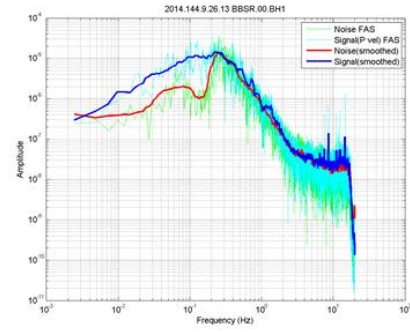
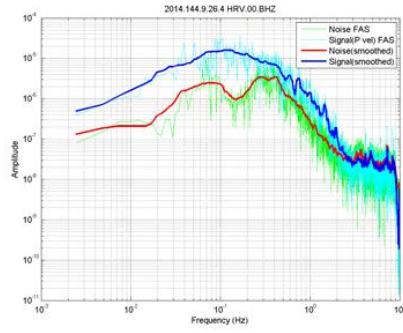
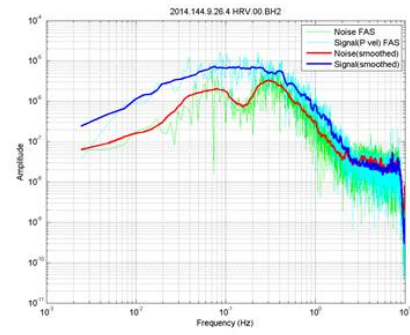
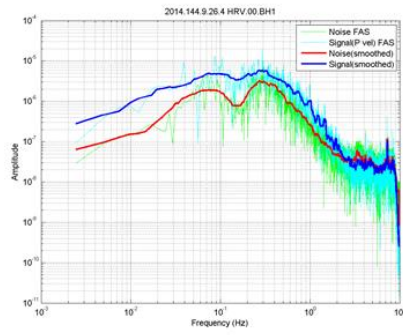


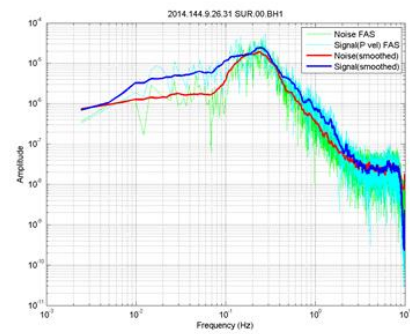
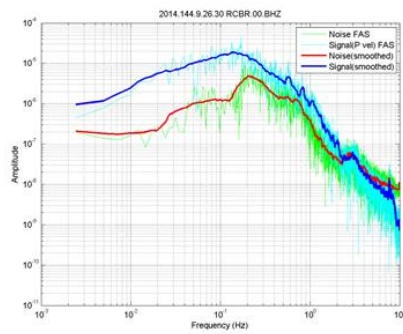
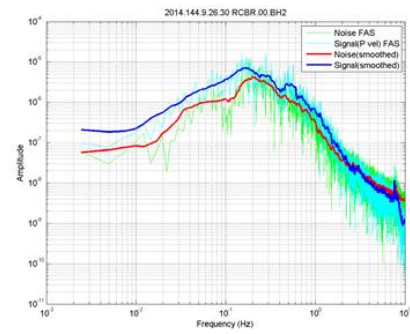
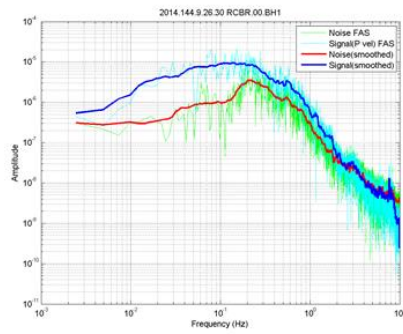
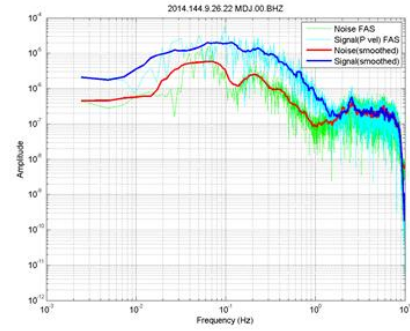
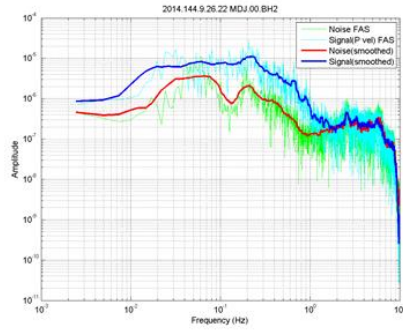
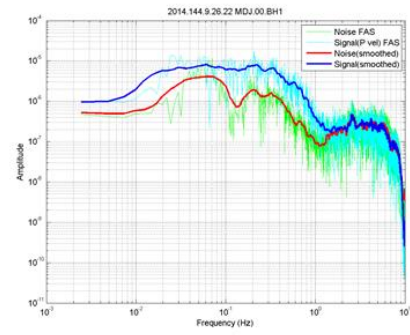
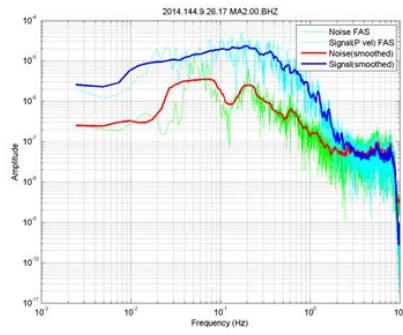


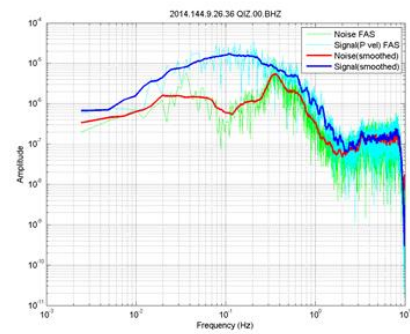
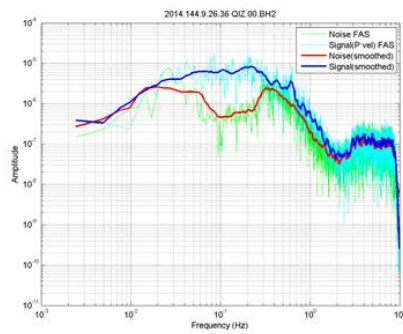
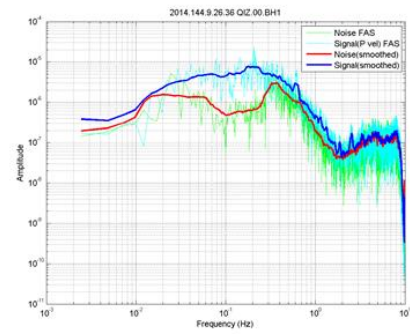
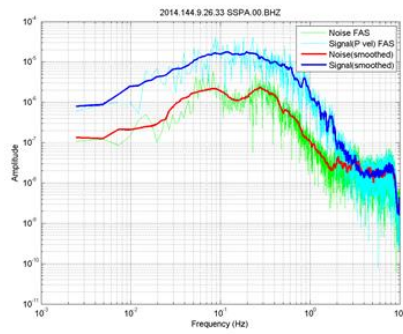
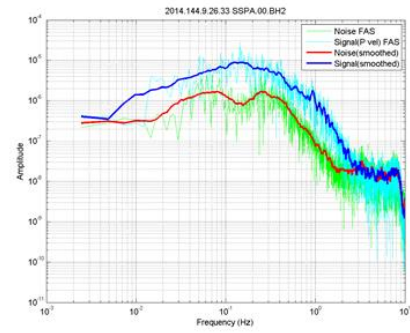
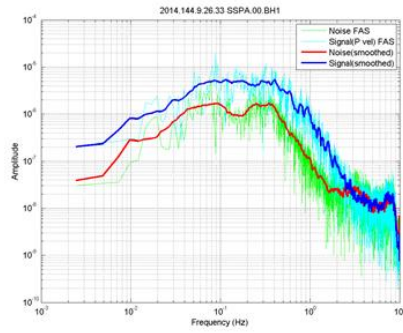
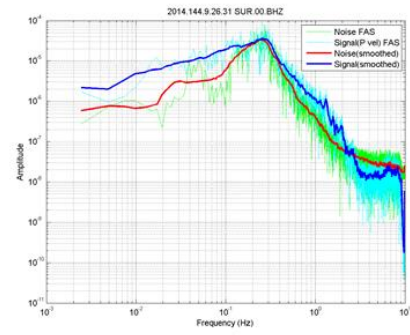
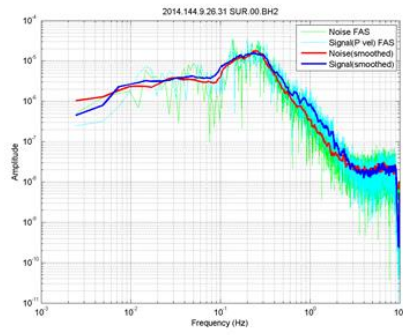


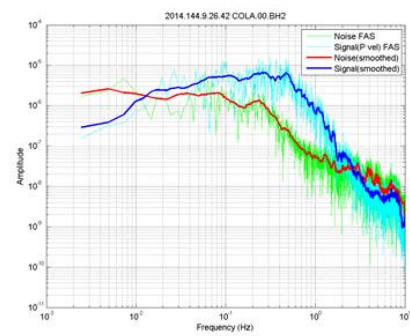
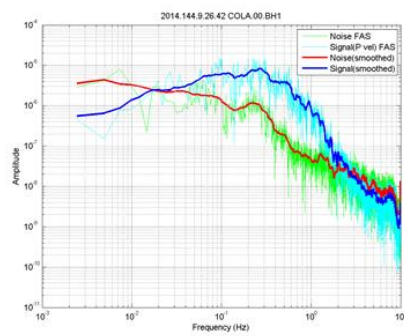
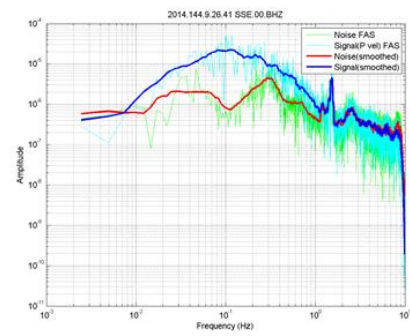
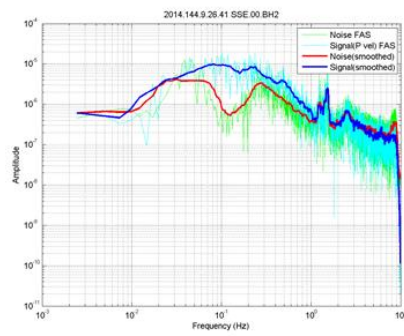
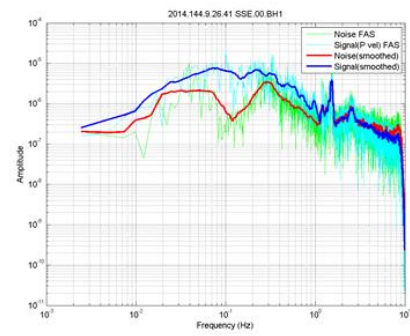
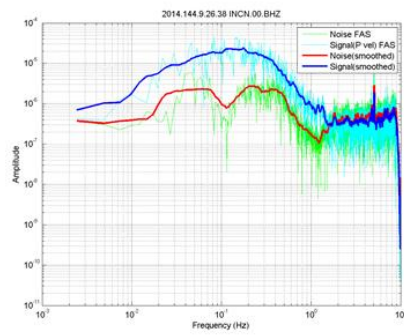
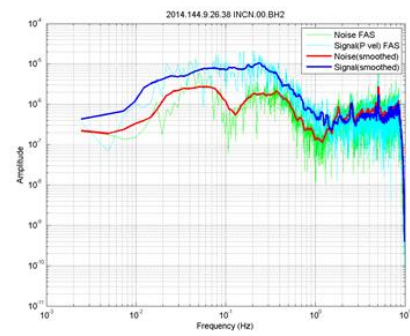
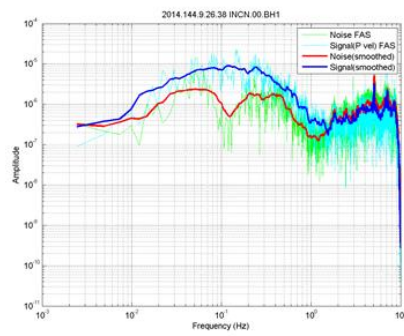


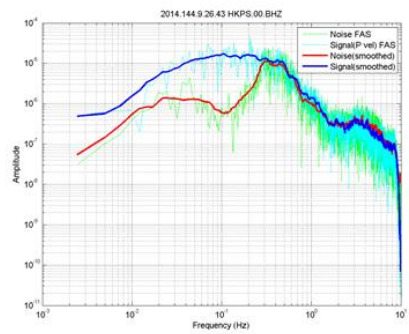
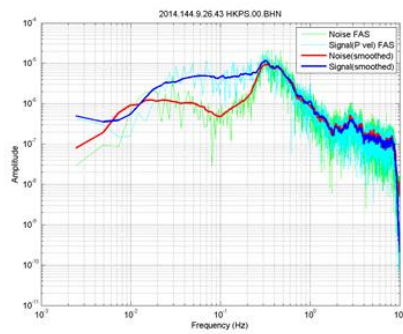
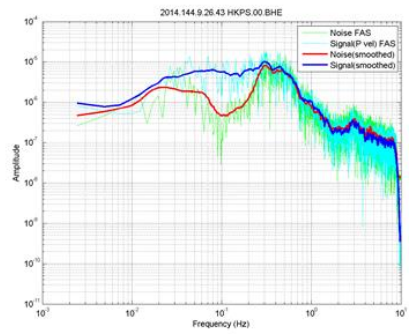
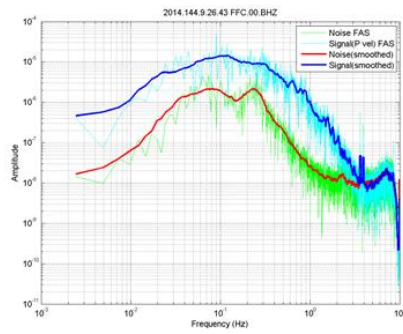
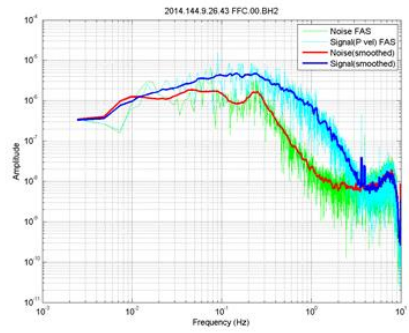
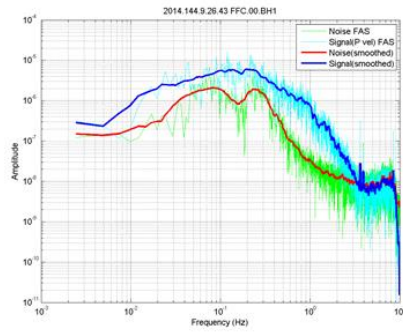
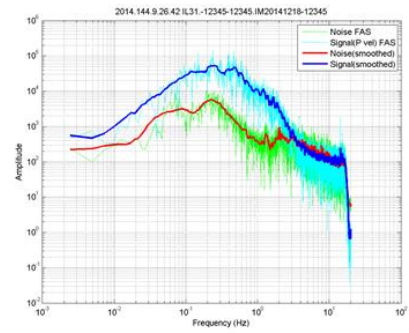
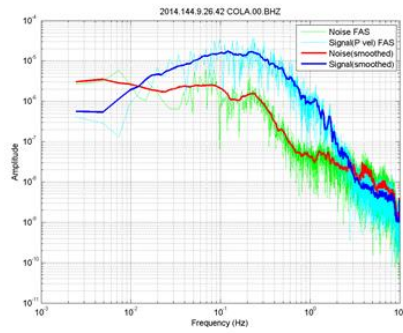


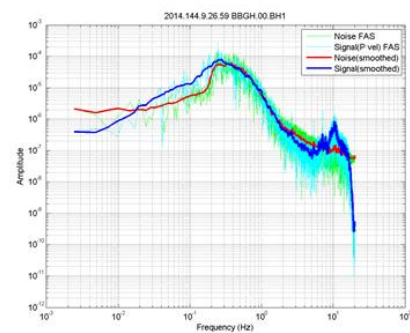
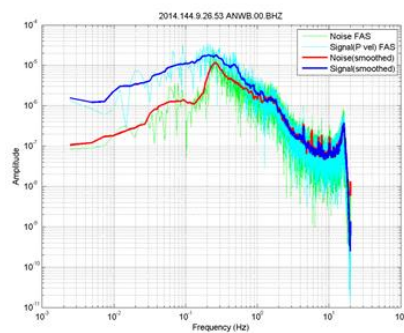
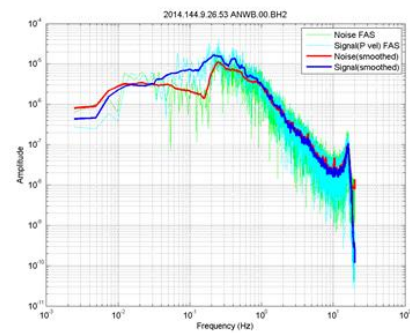
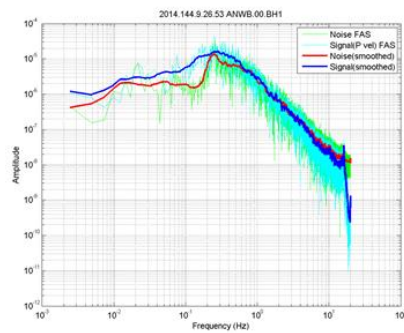
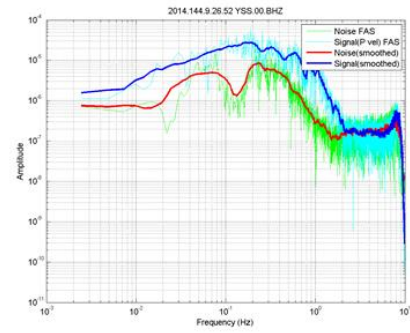
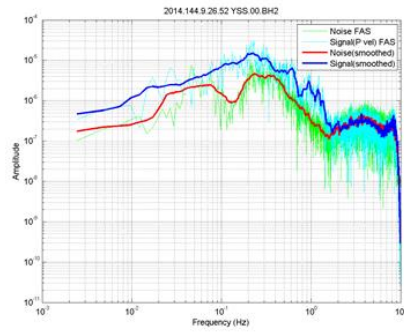
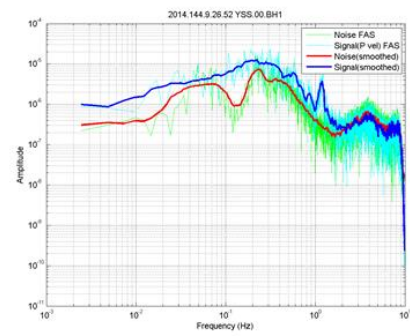
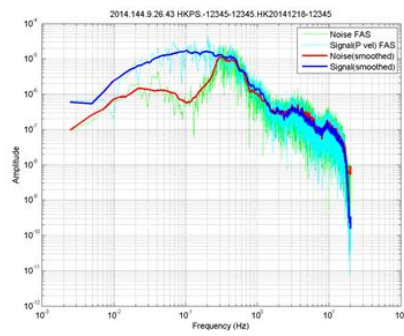


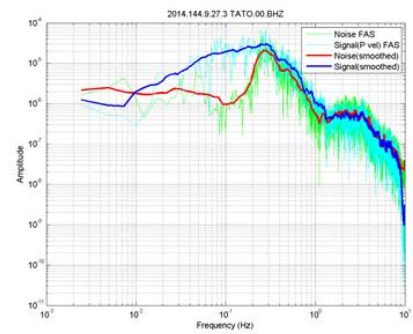
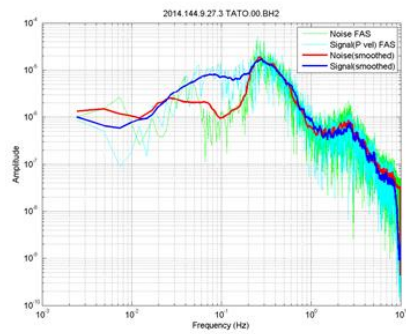
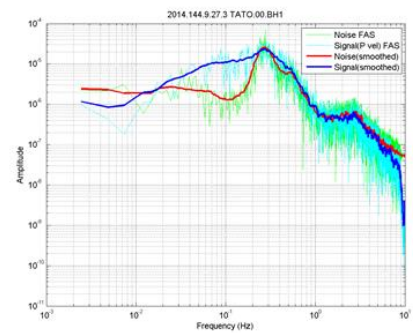
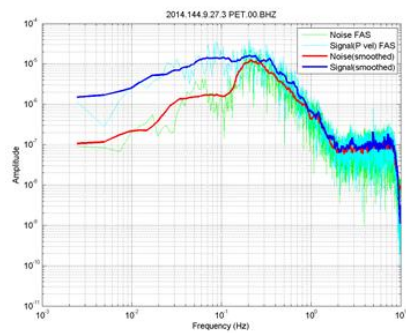
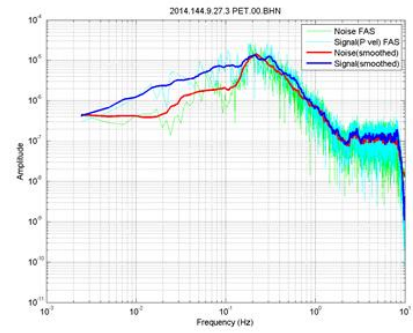
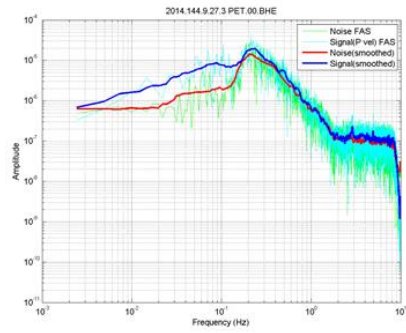
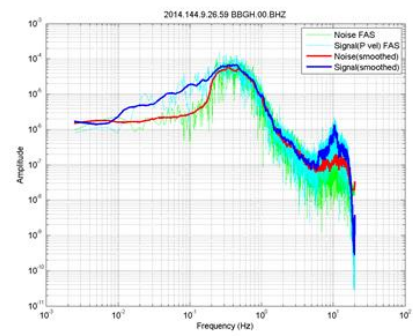
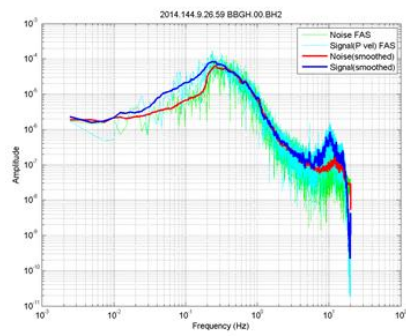


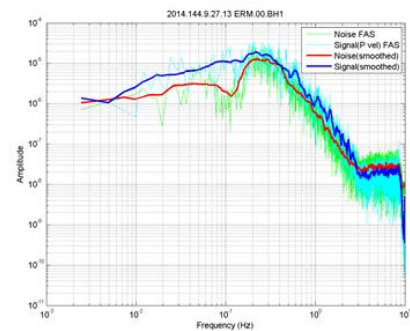
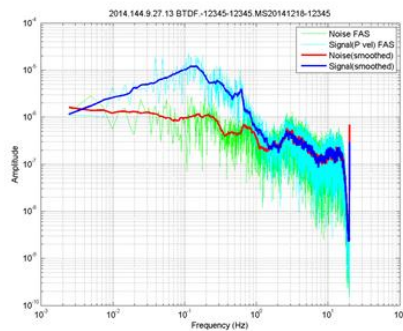
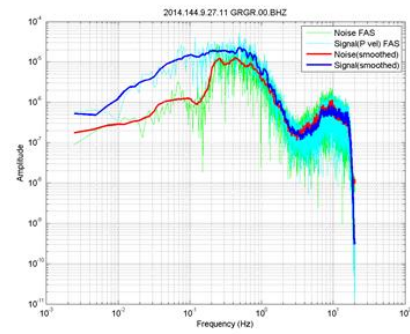
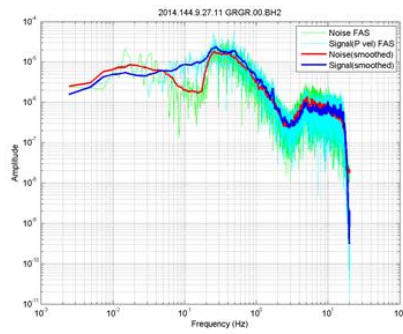
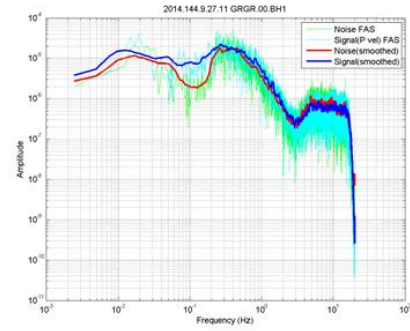
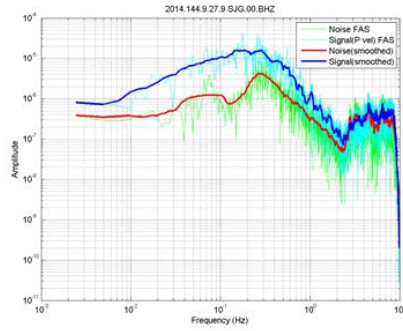
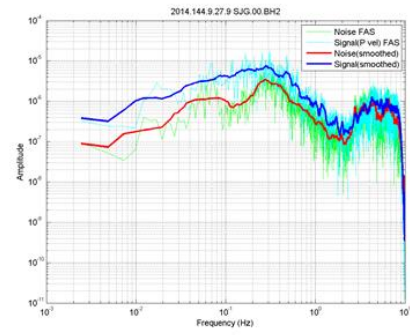
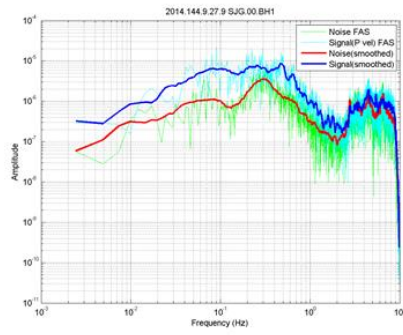


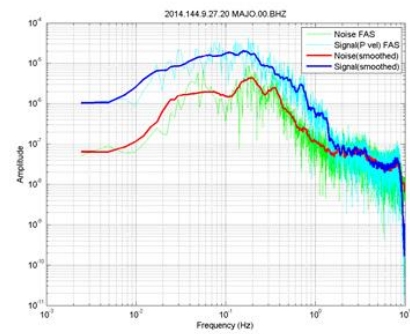
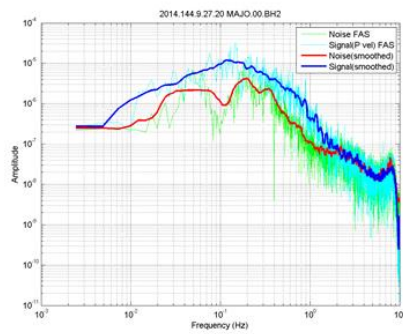
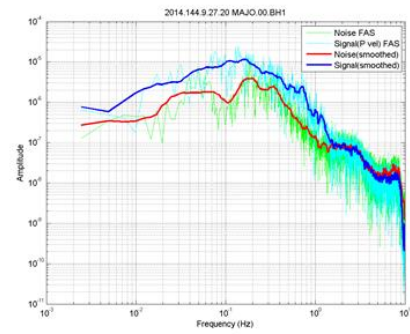
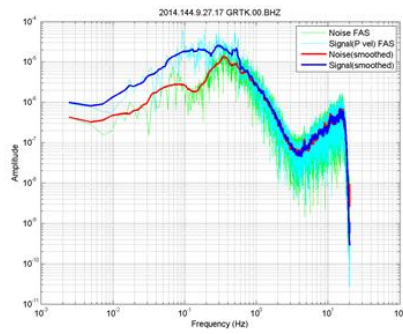
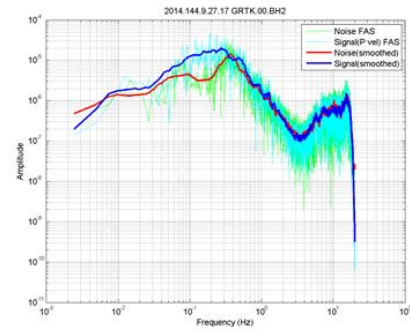
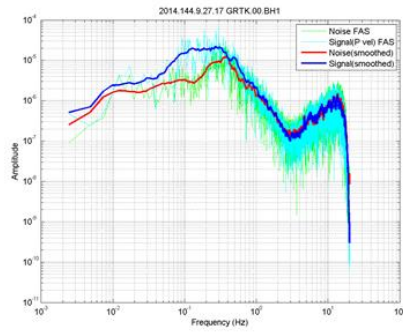
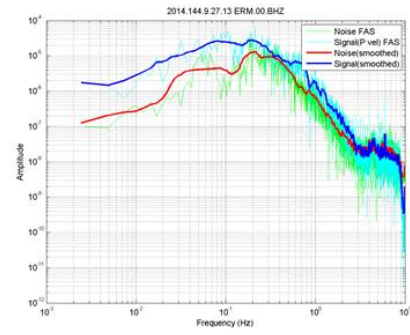
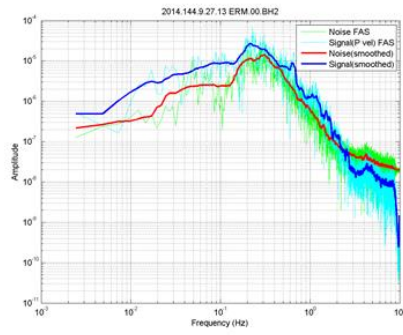


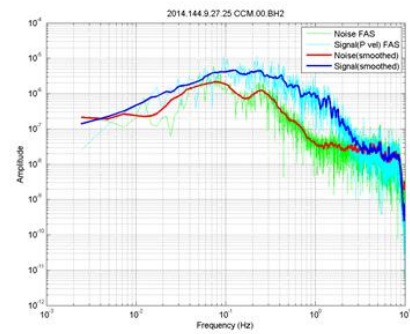
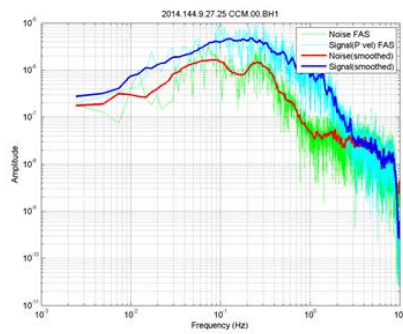
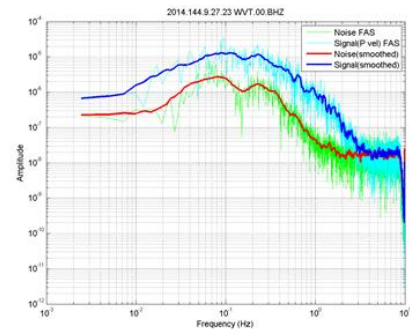
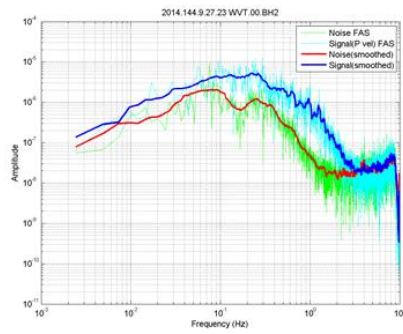
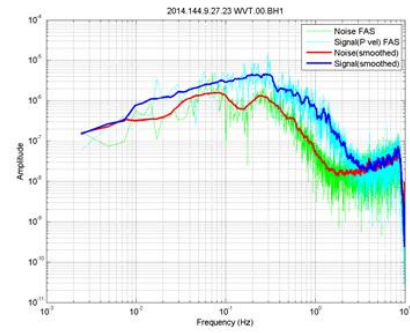
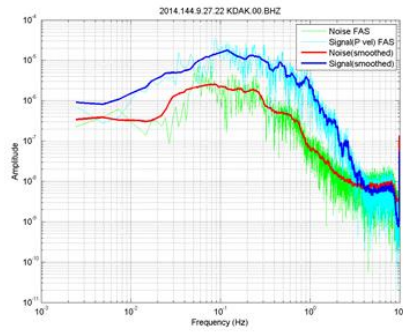
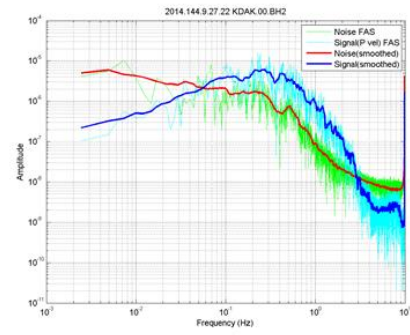
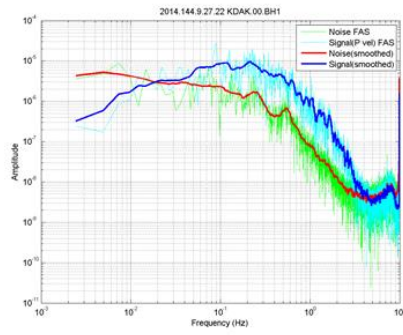


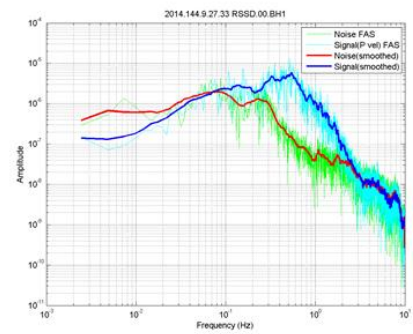
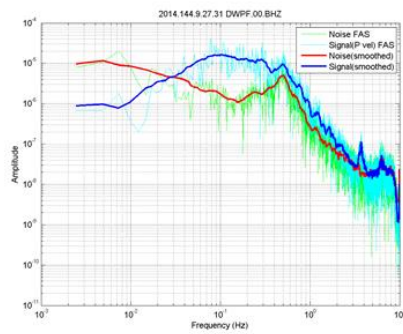
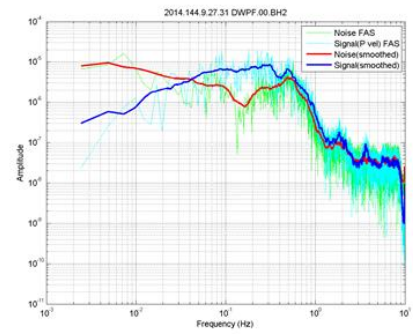
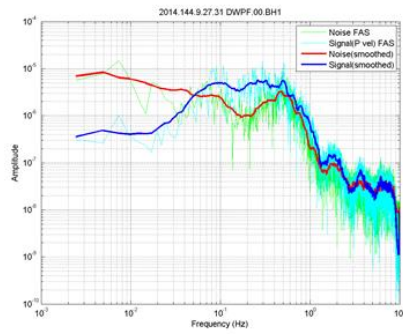
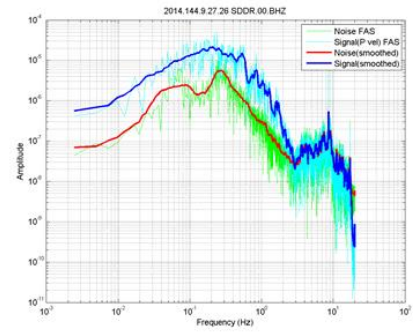
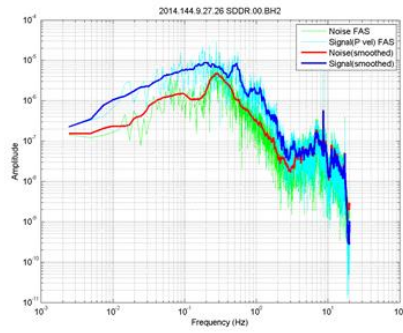
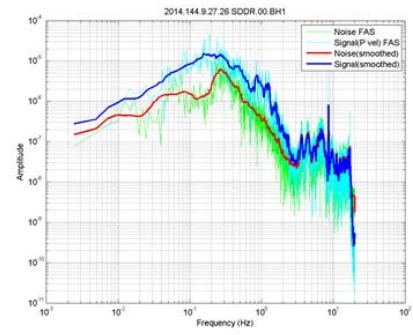
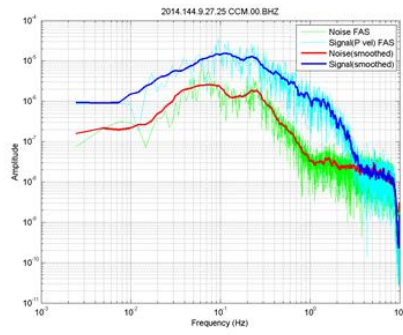


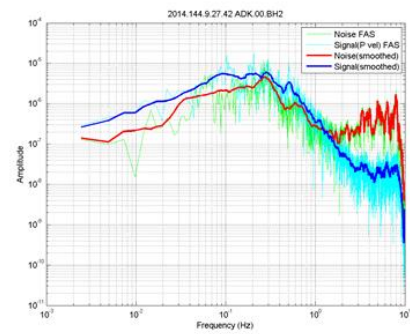
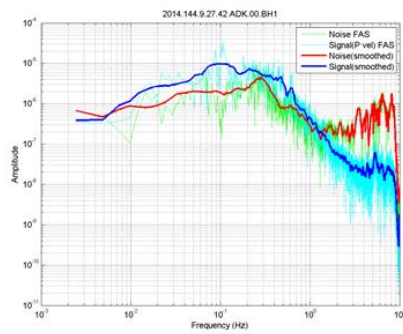
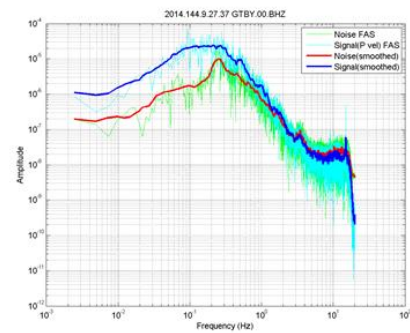
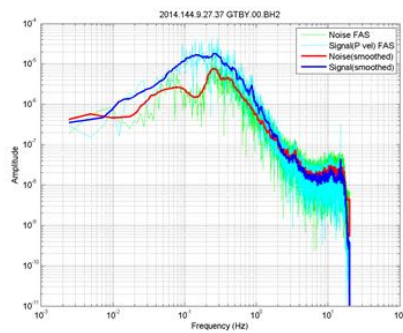
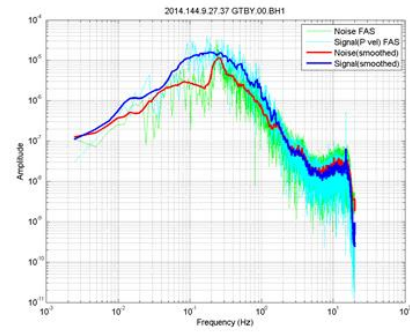
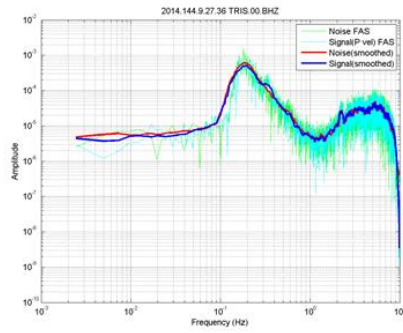
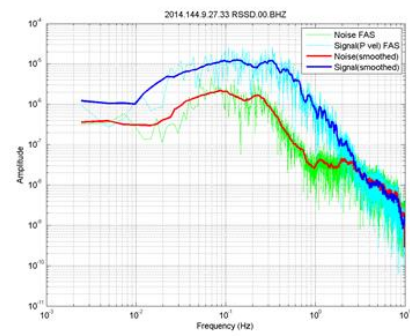
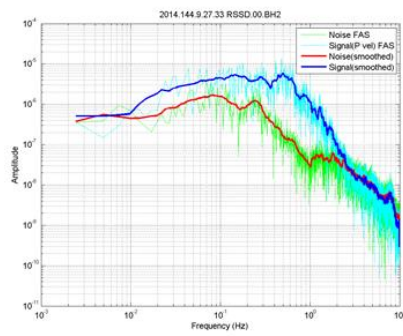


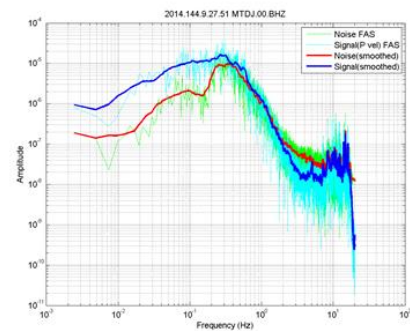
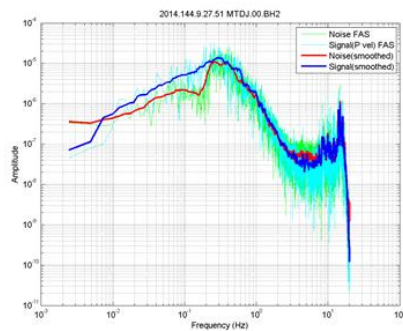
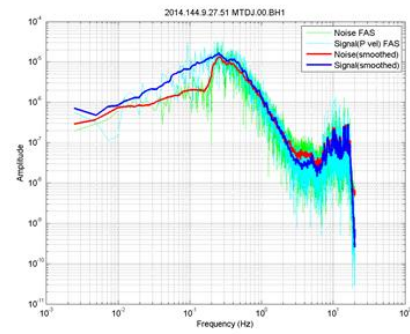
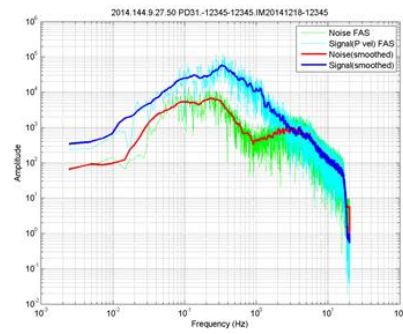
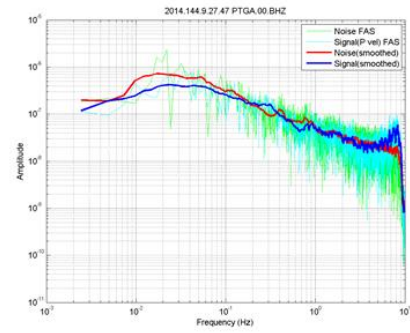
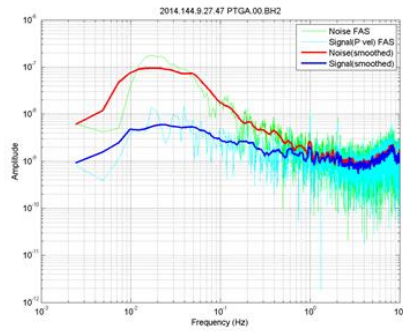
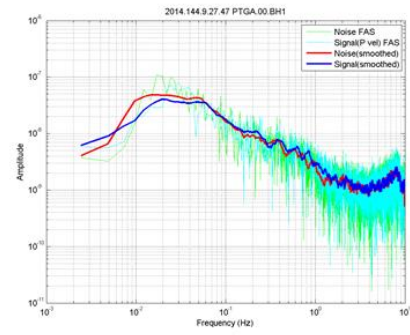
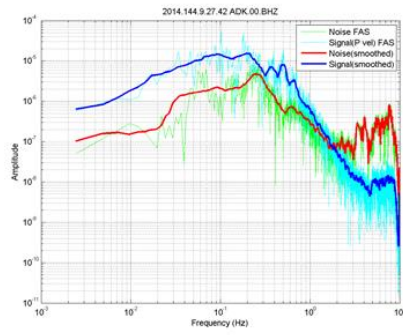


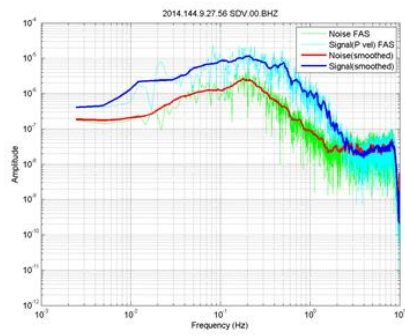
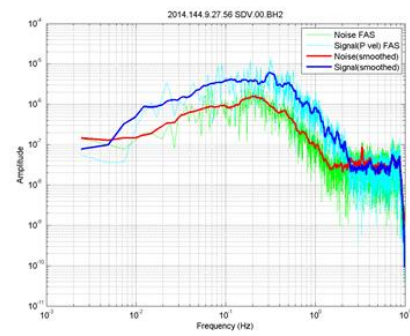
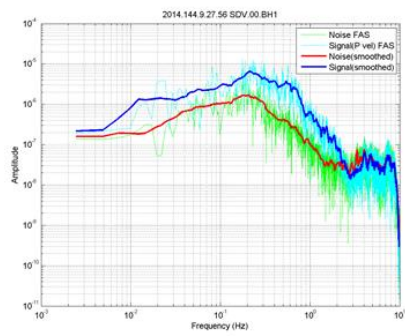






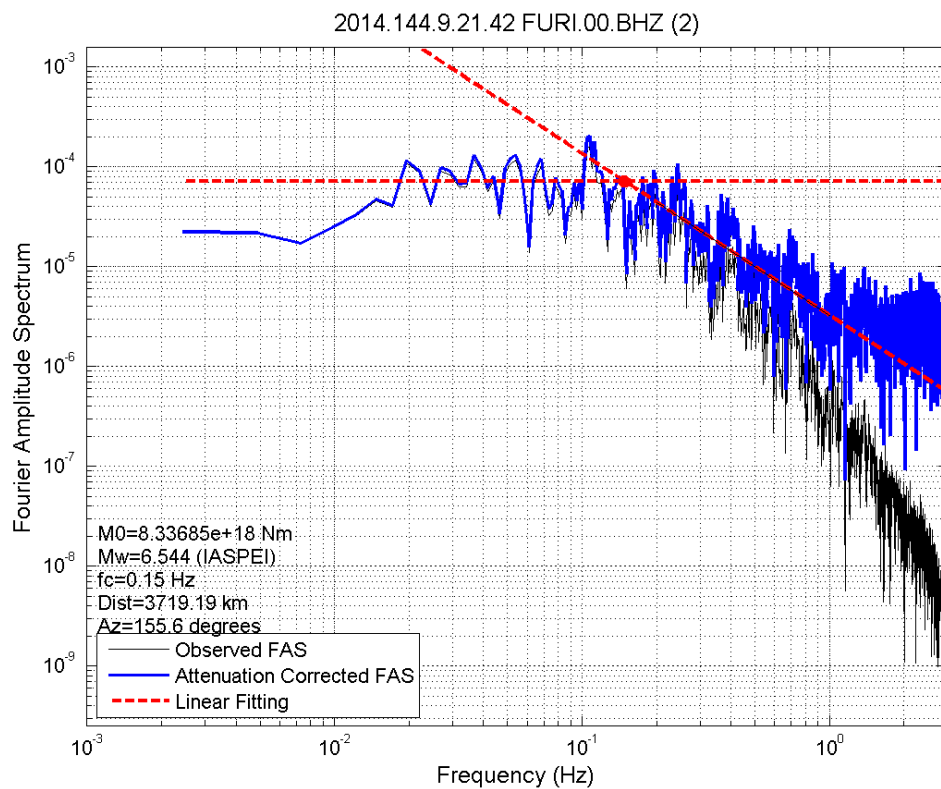
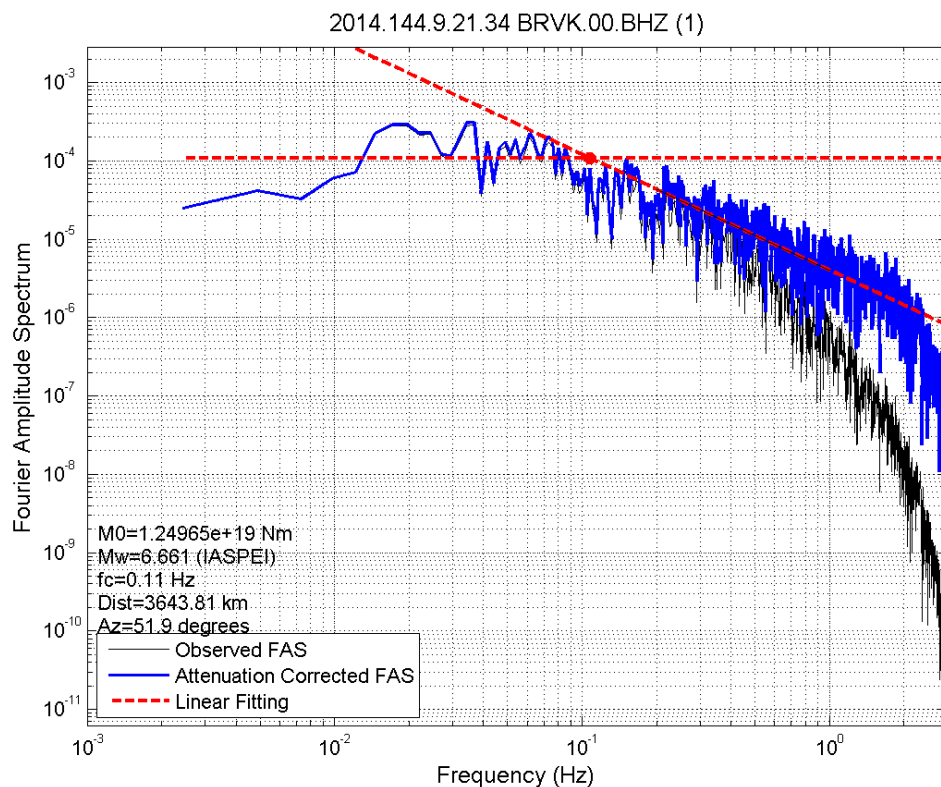


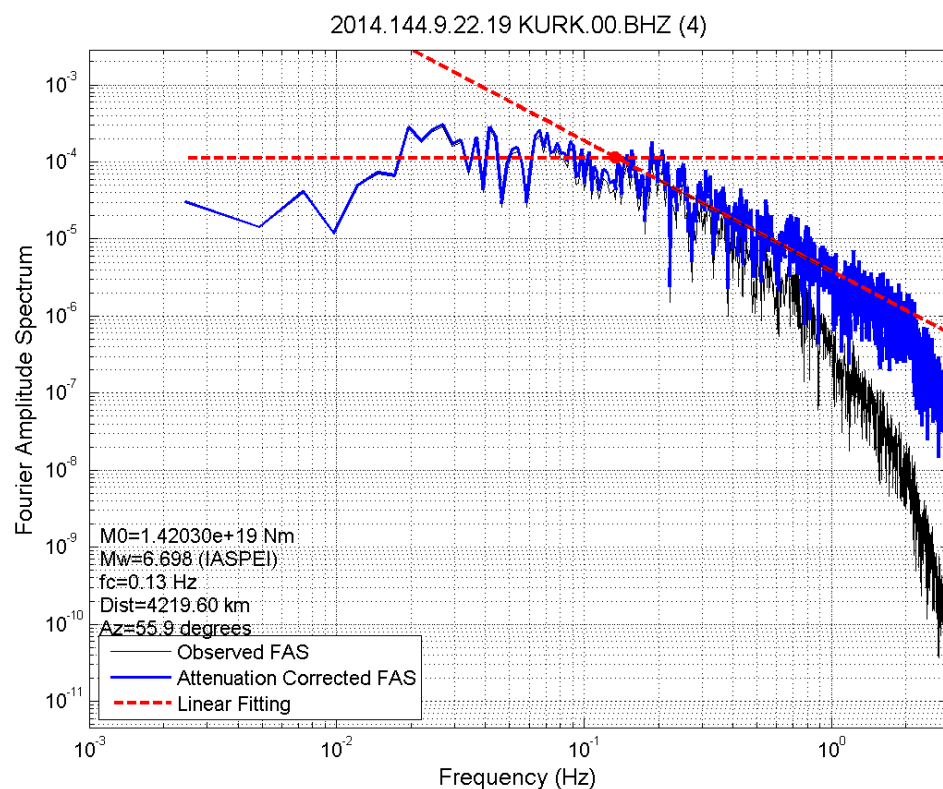
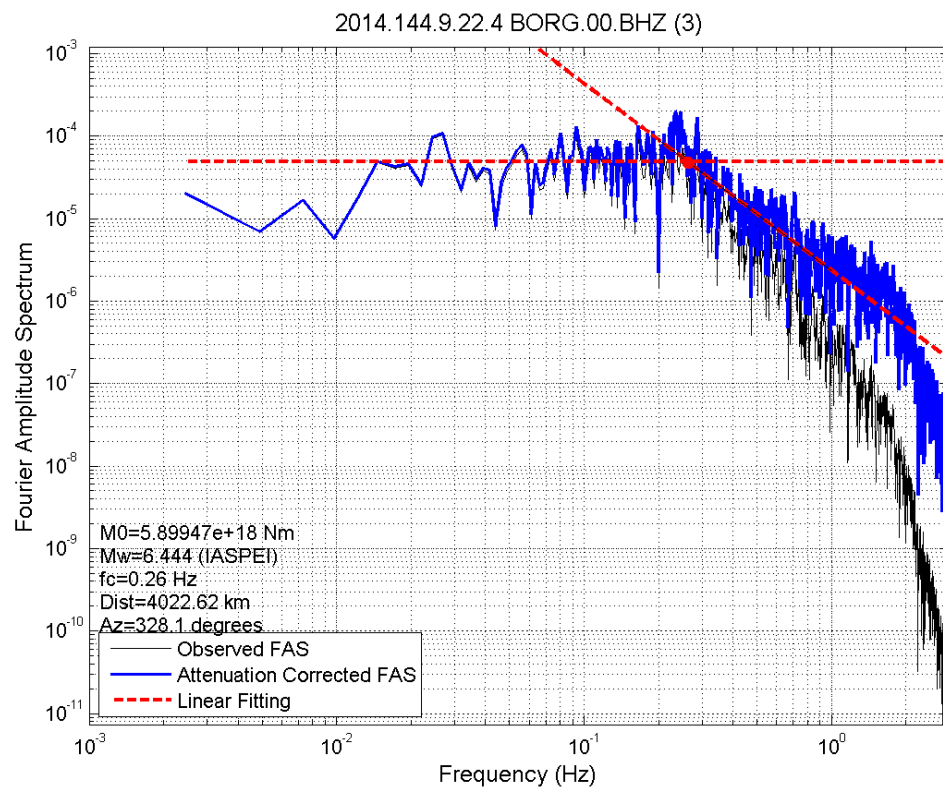


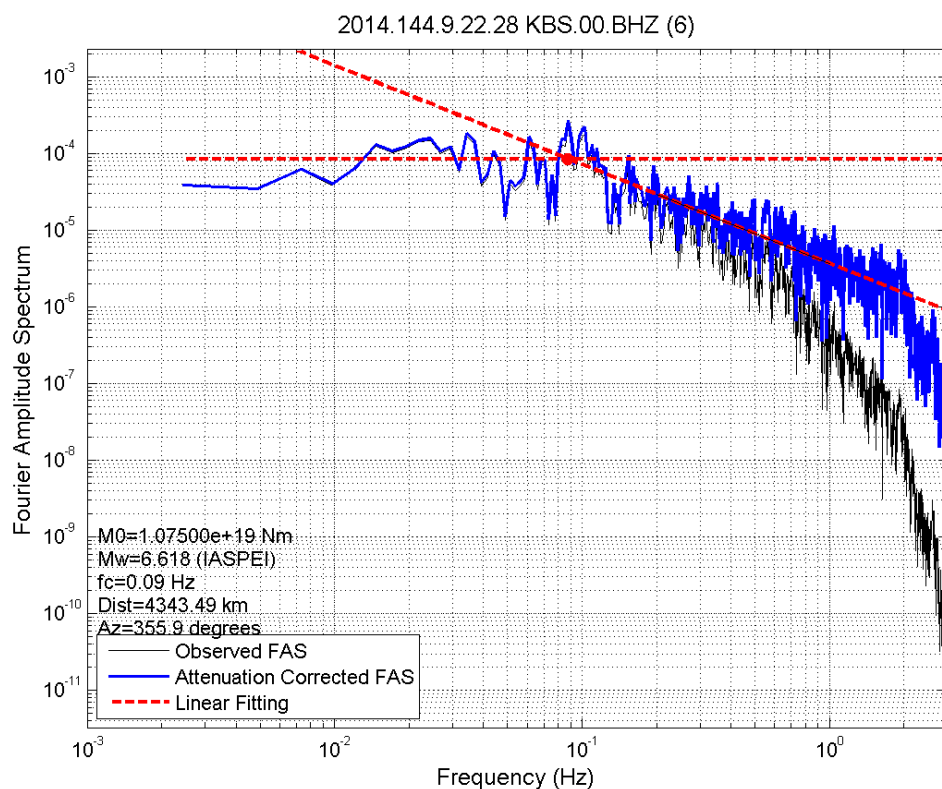
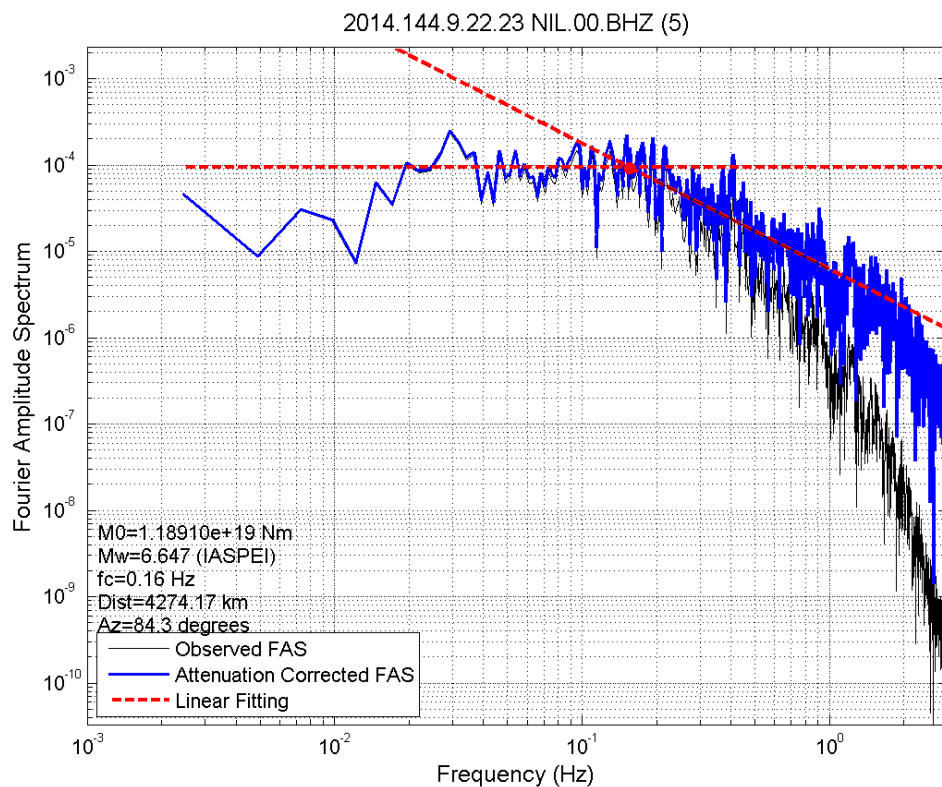


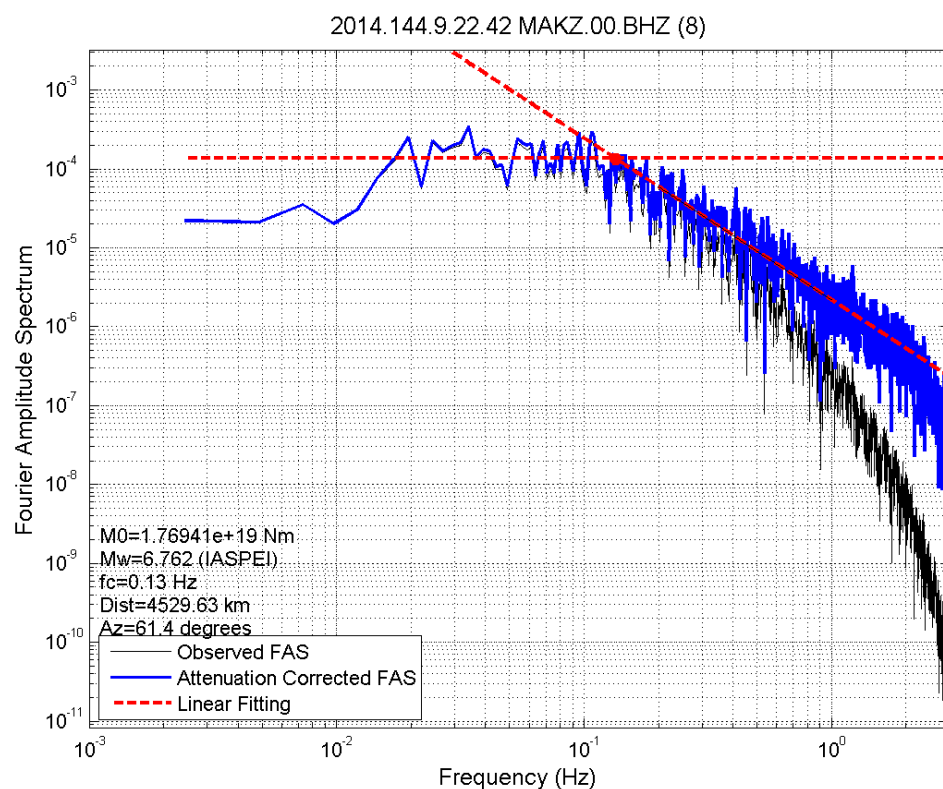
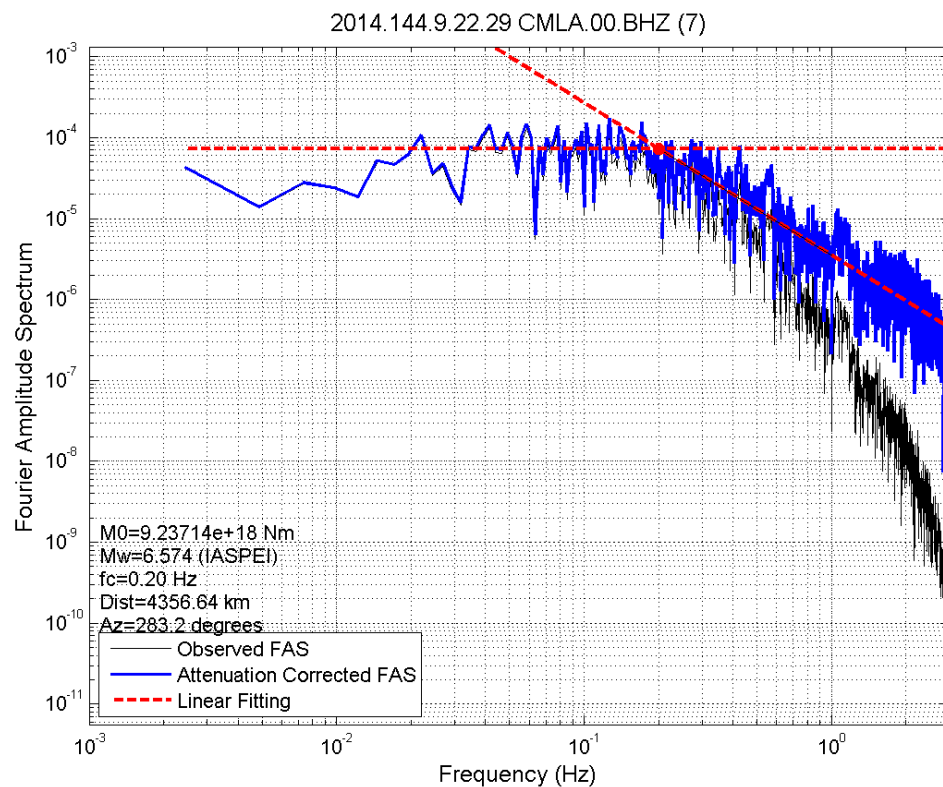
Appendix B: Fourier spectrums of vertical and horizontal components

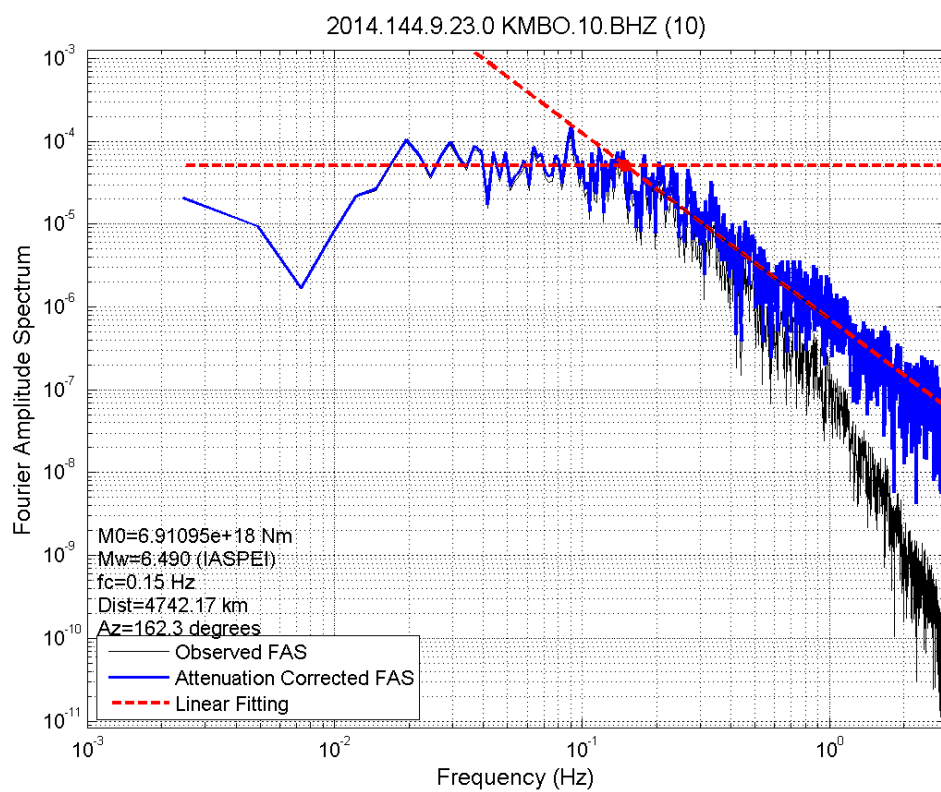
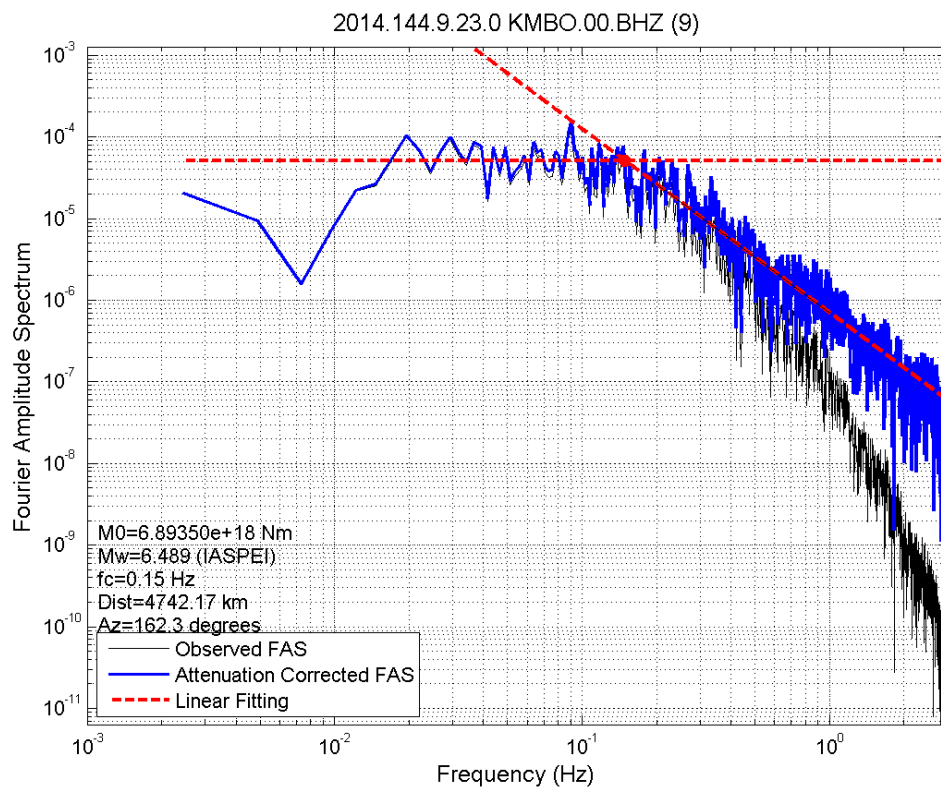
BHZ(vertical) component:

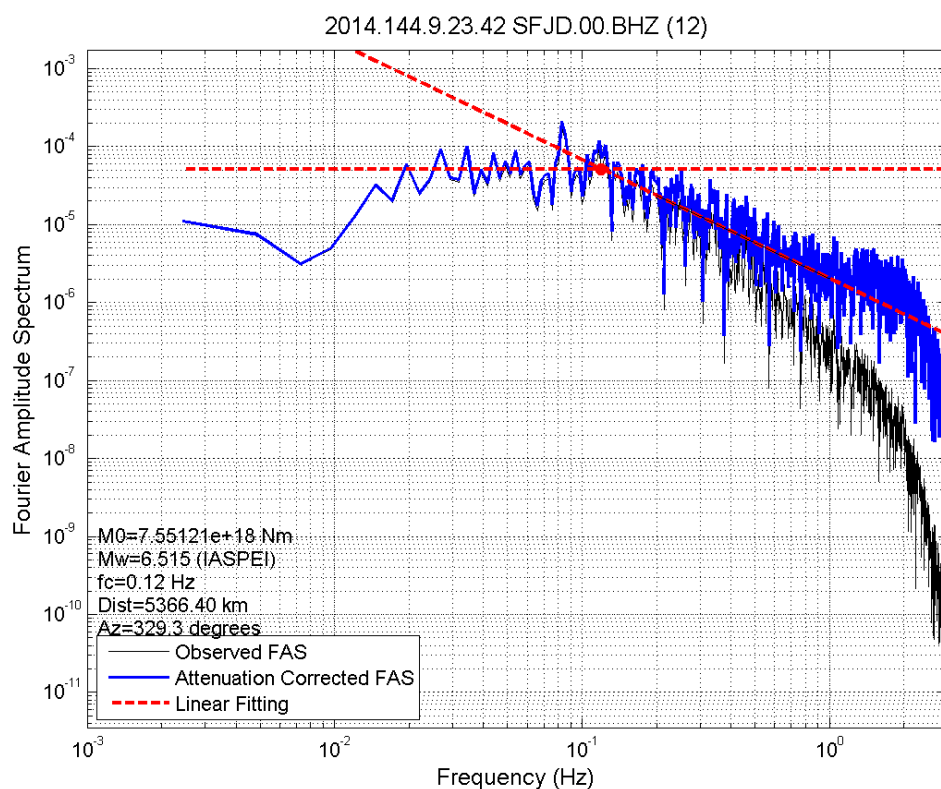
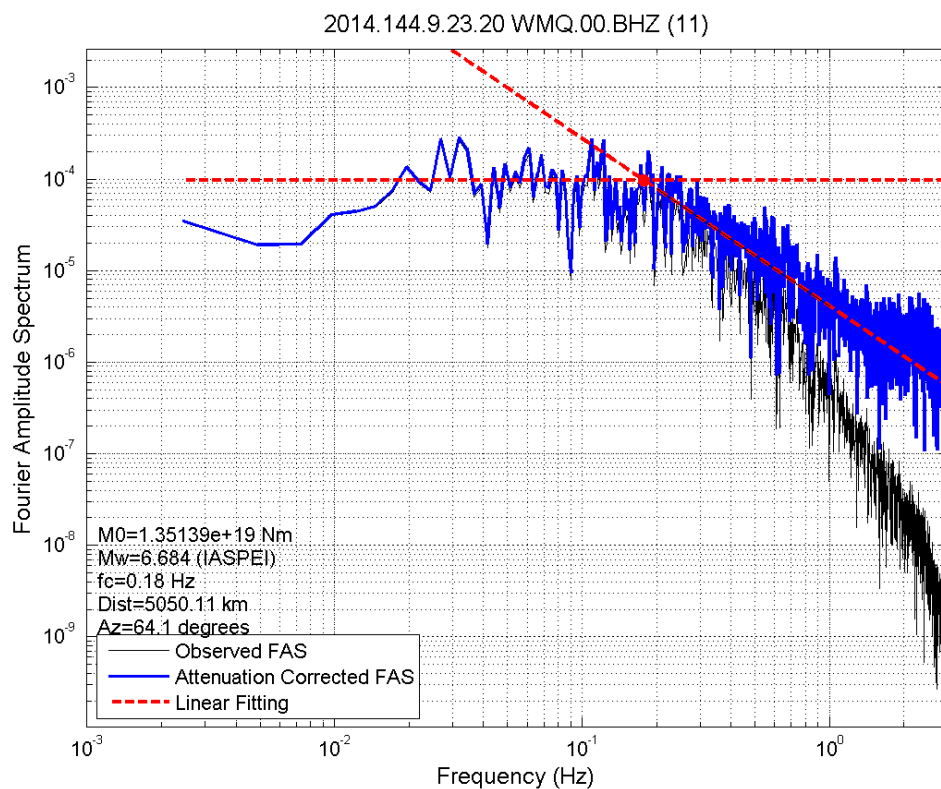


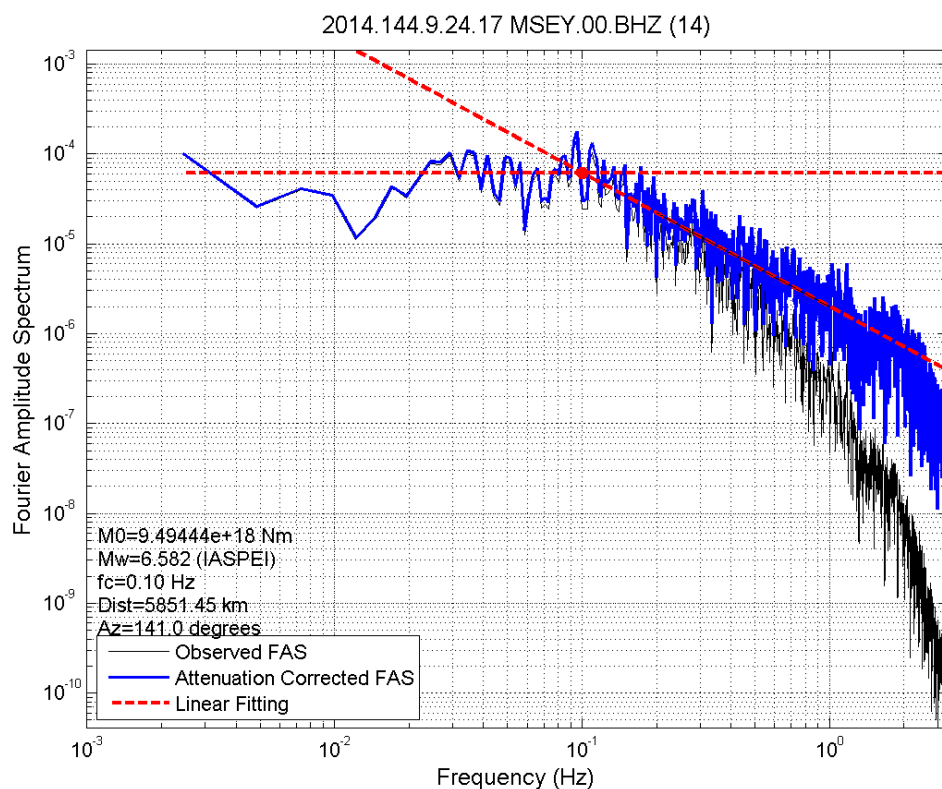
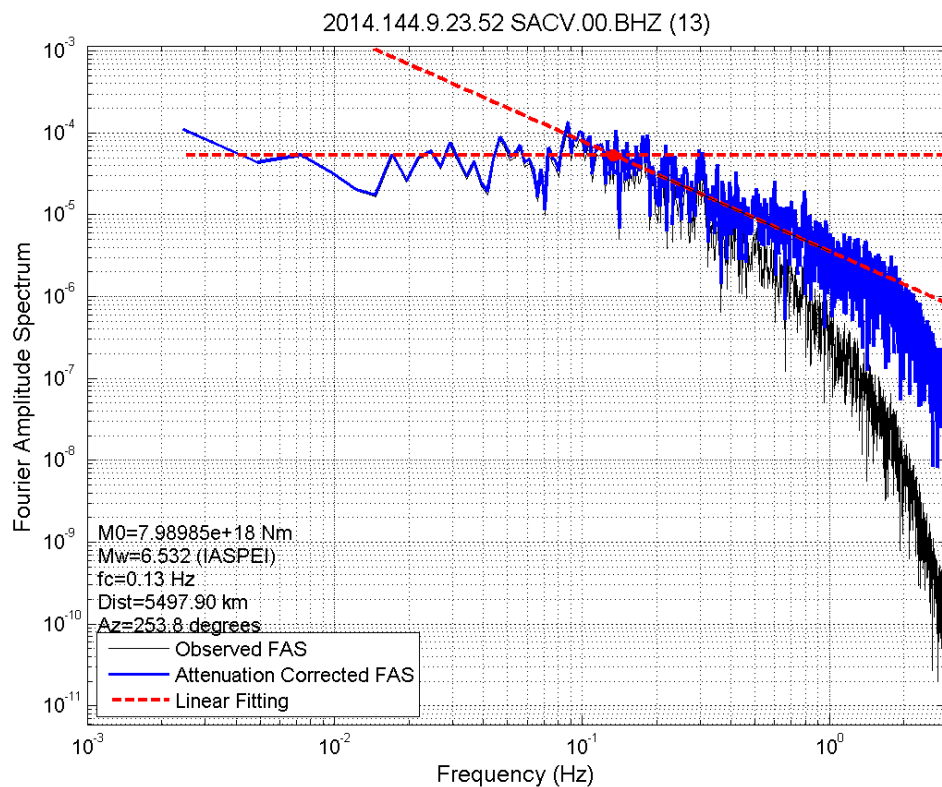


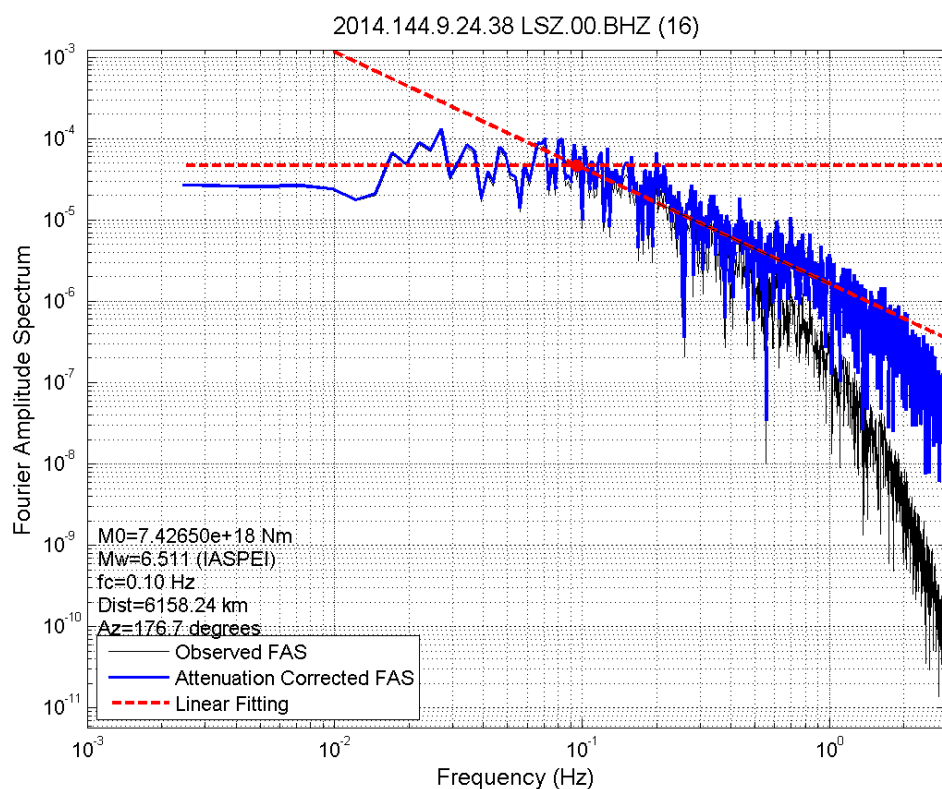
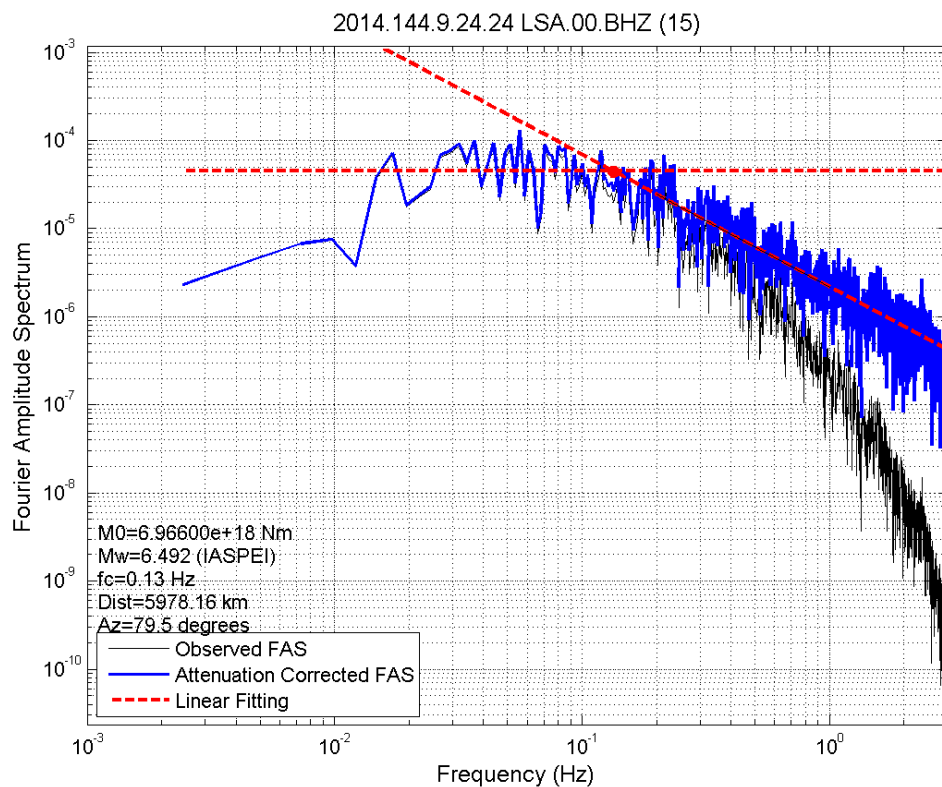


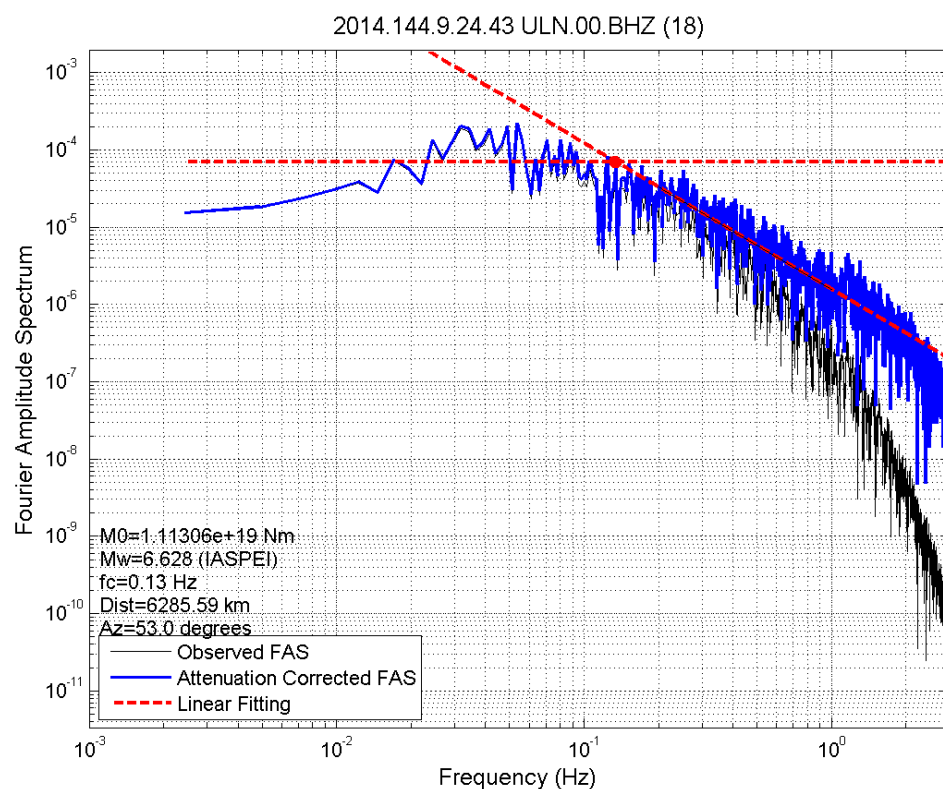
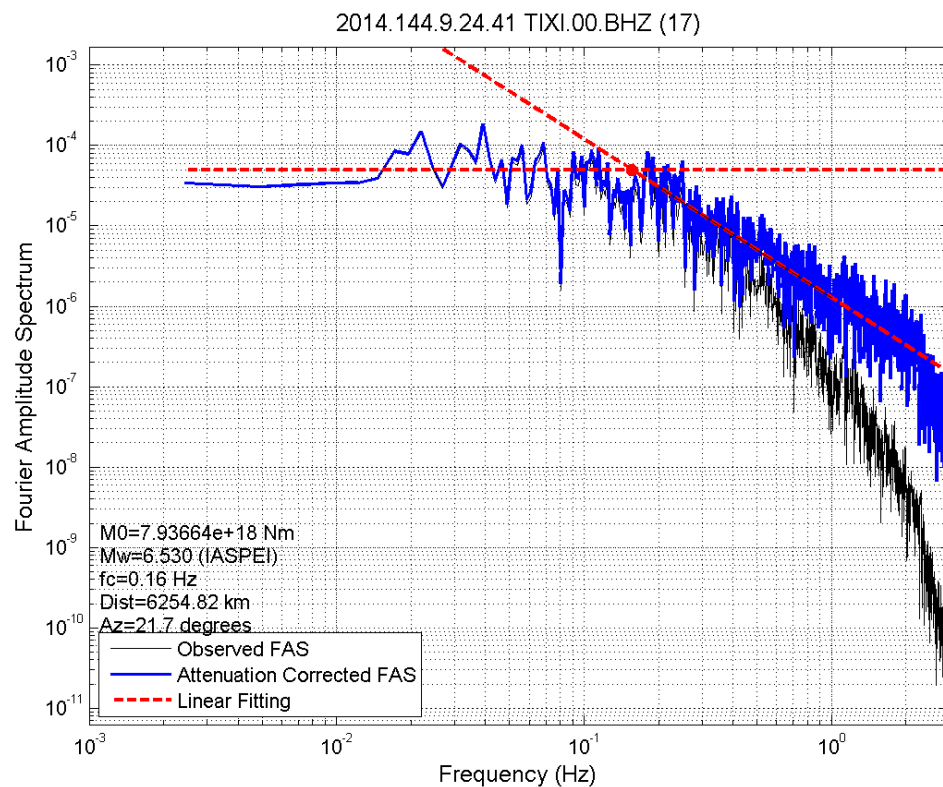


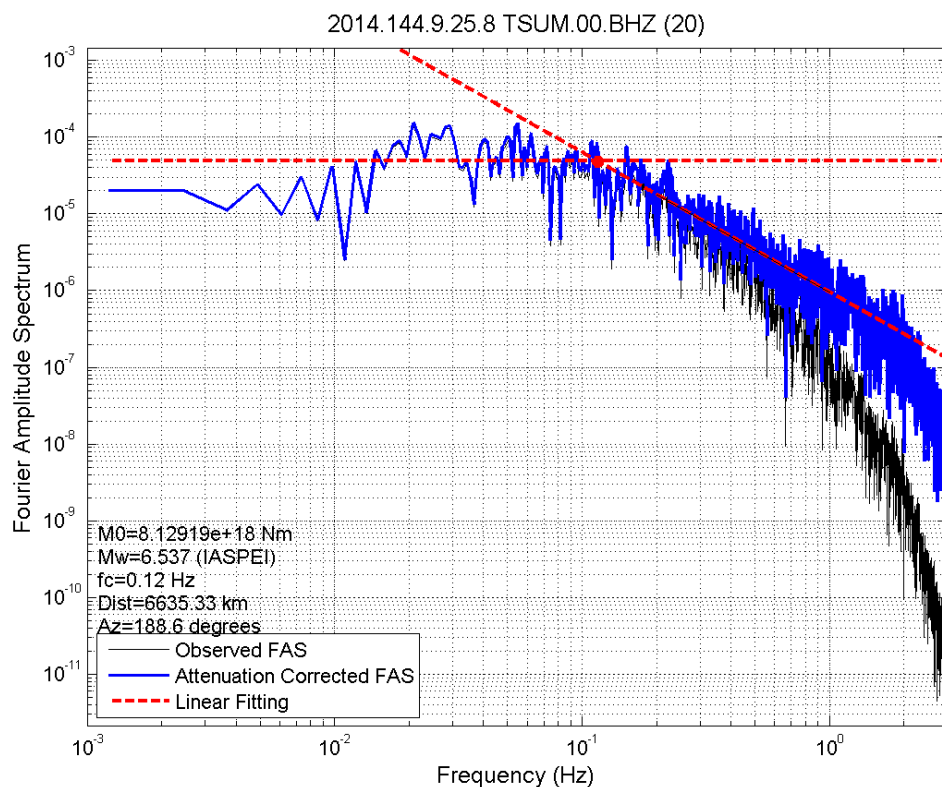
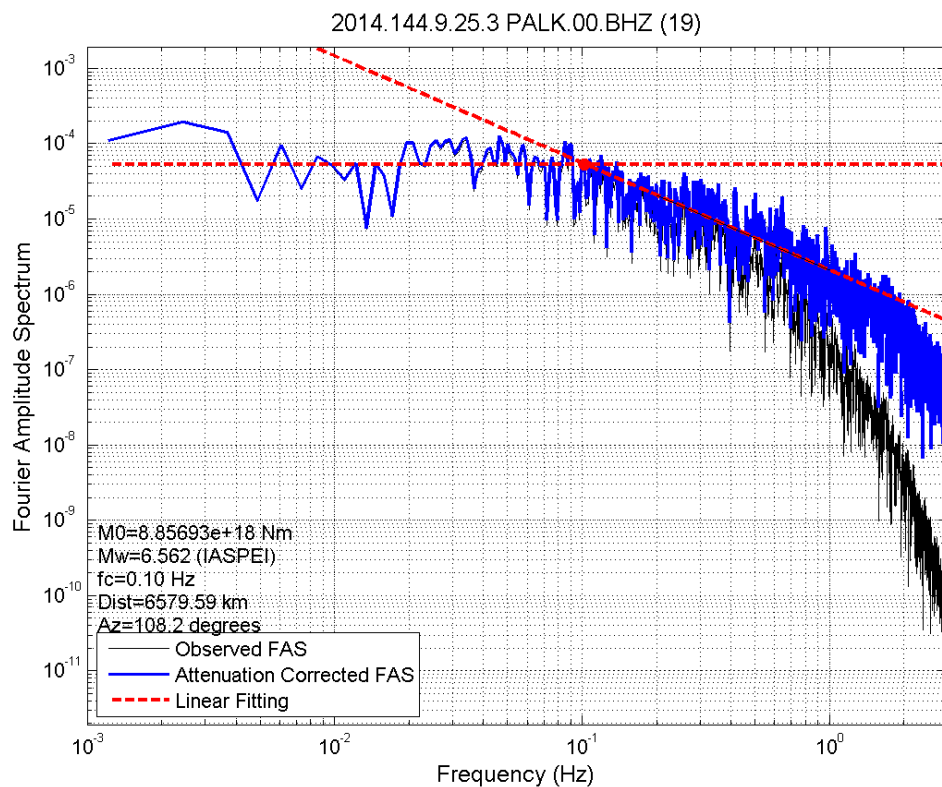


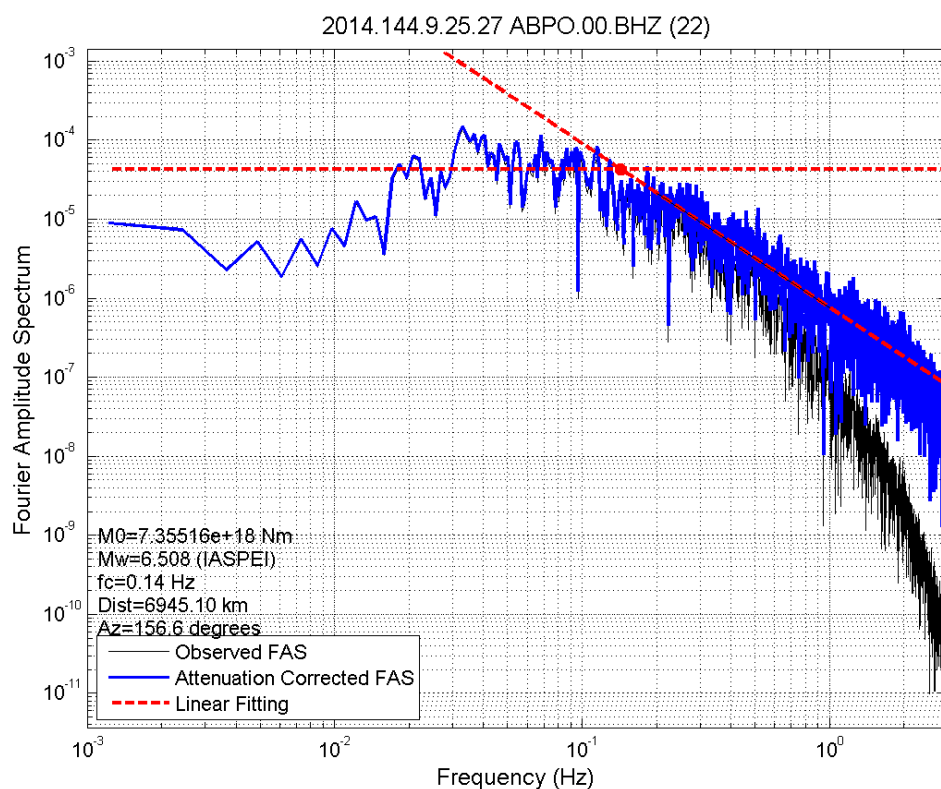
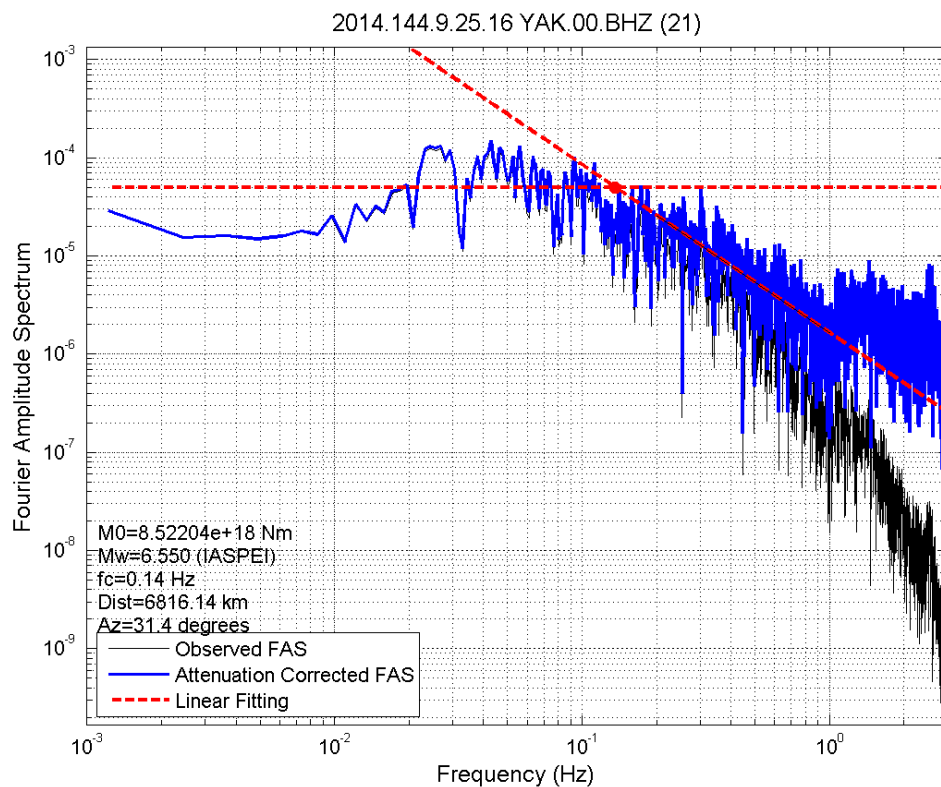


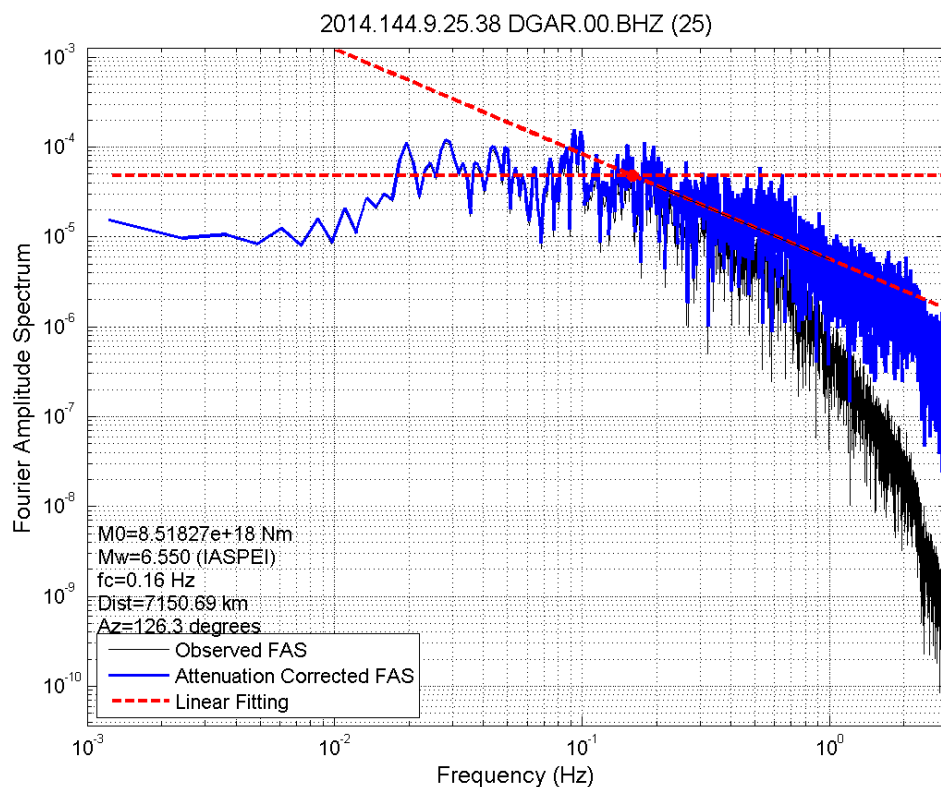
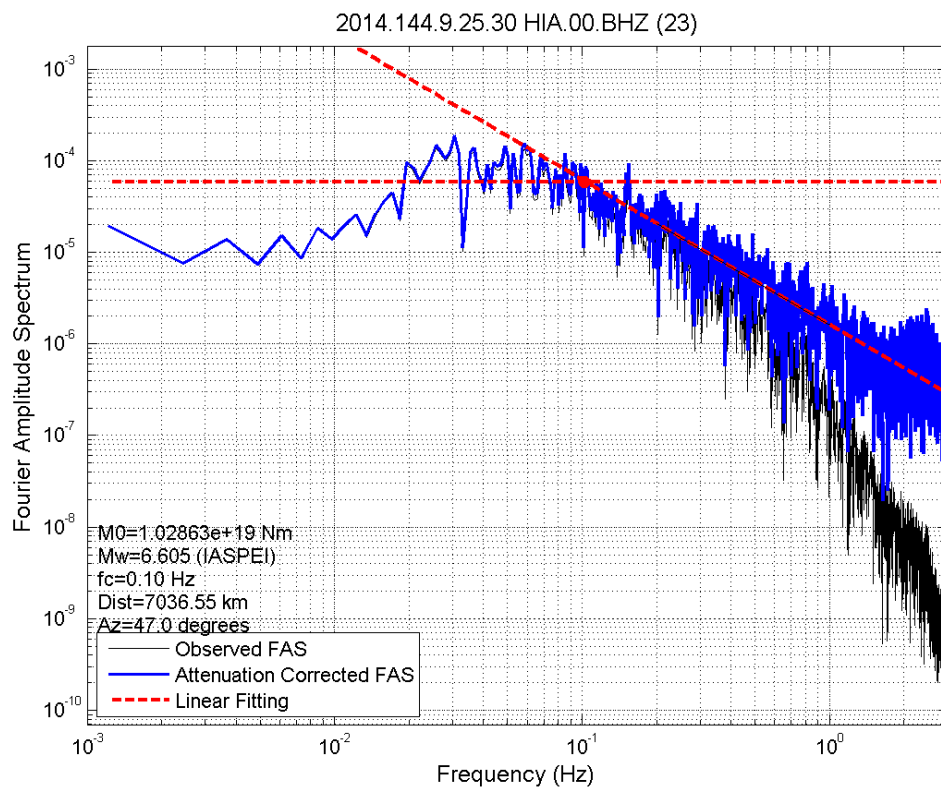


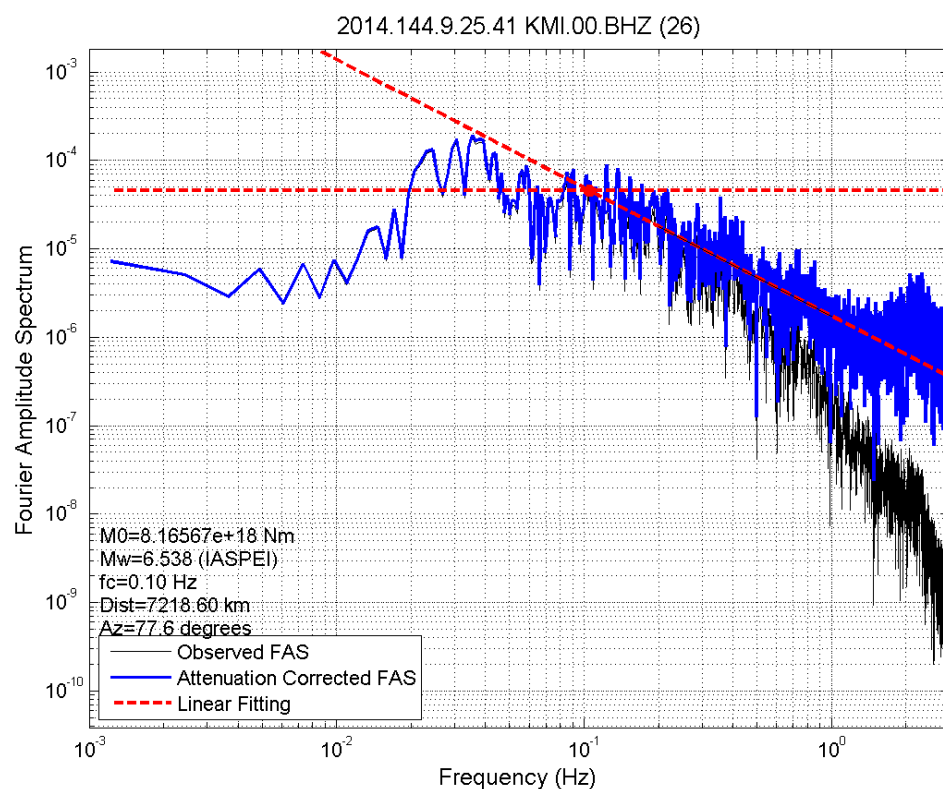
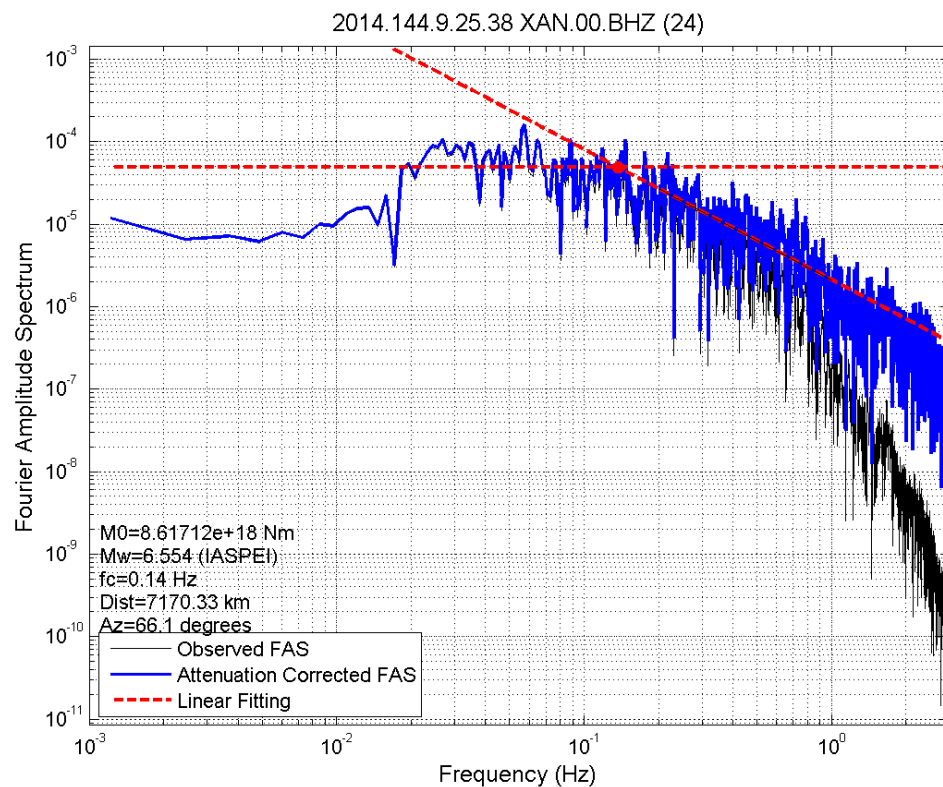


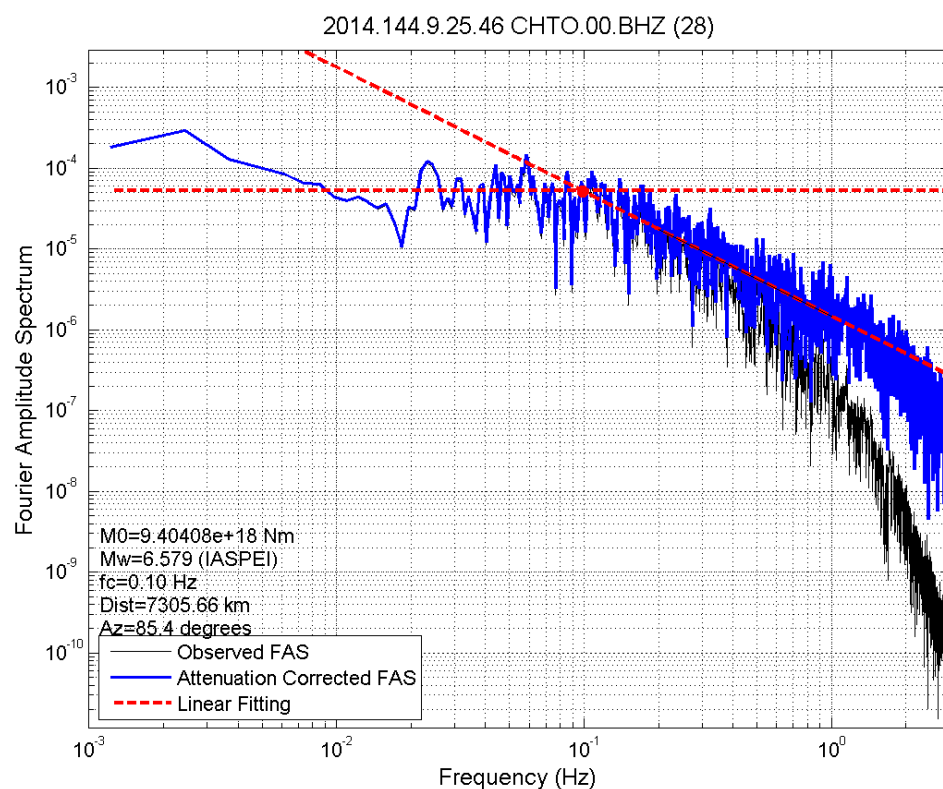
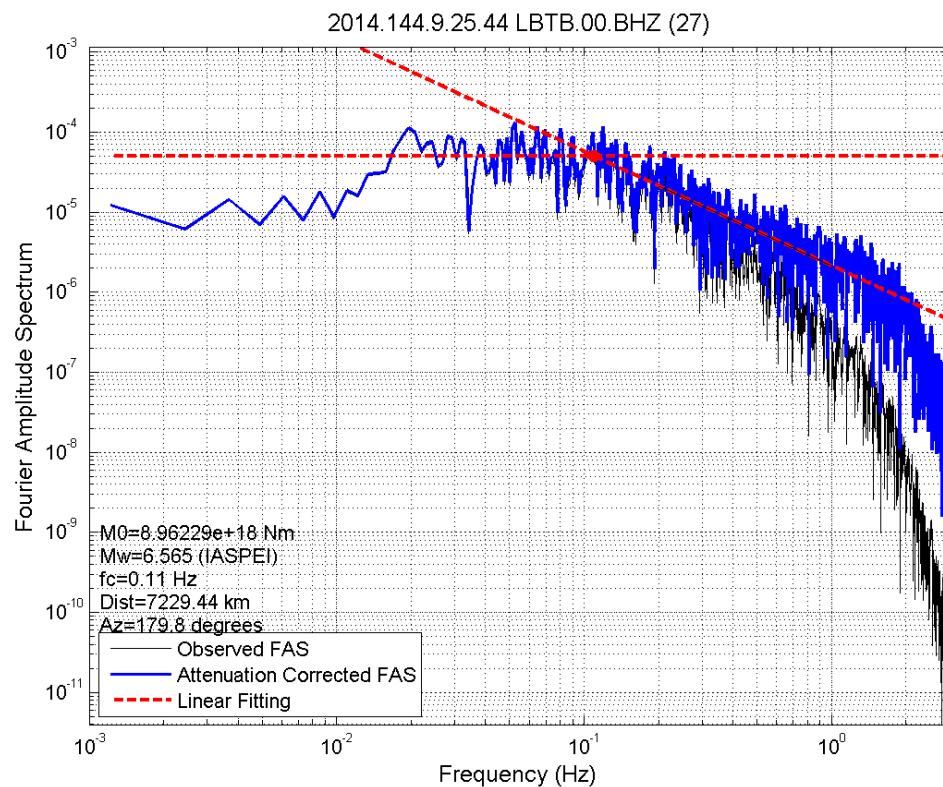


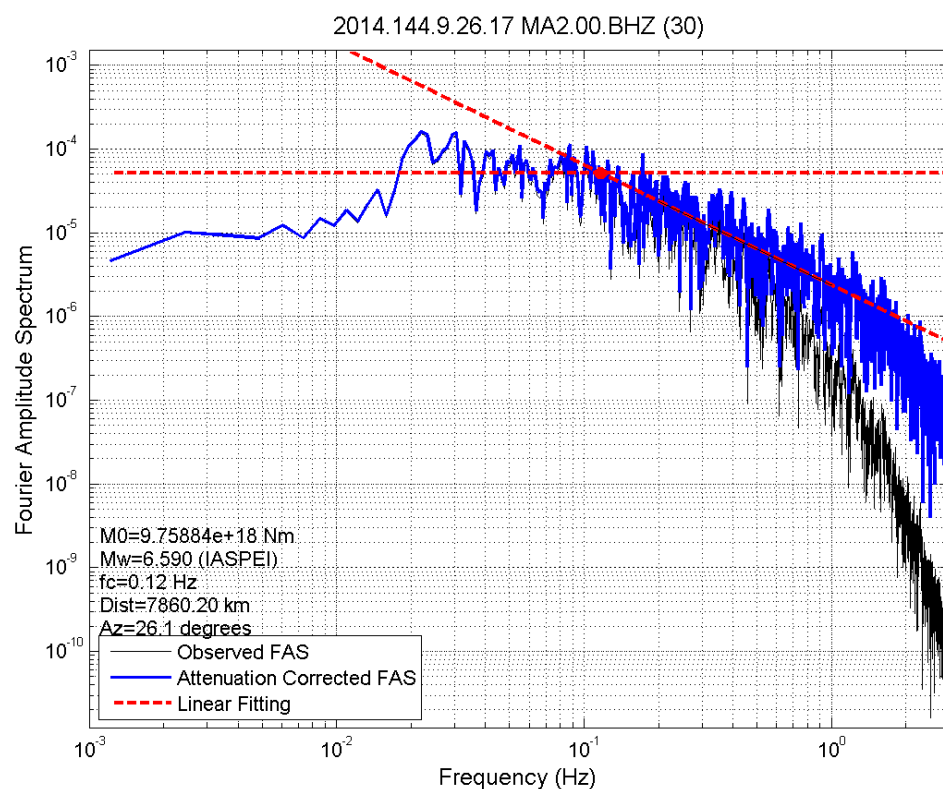
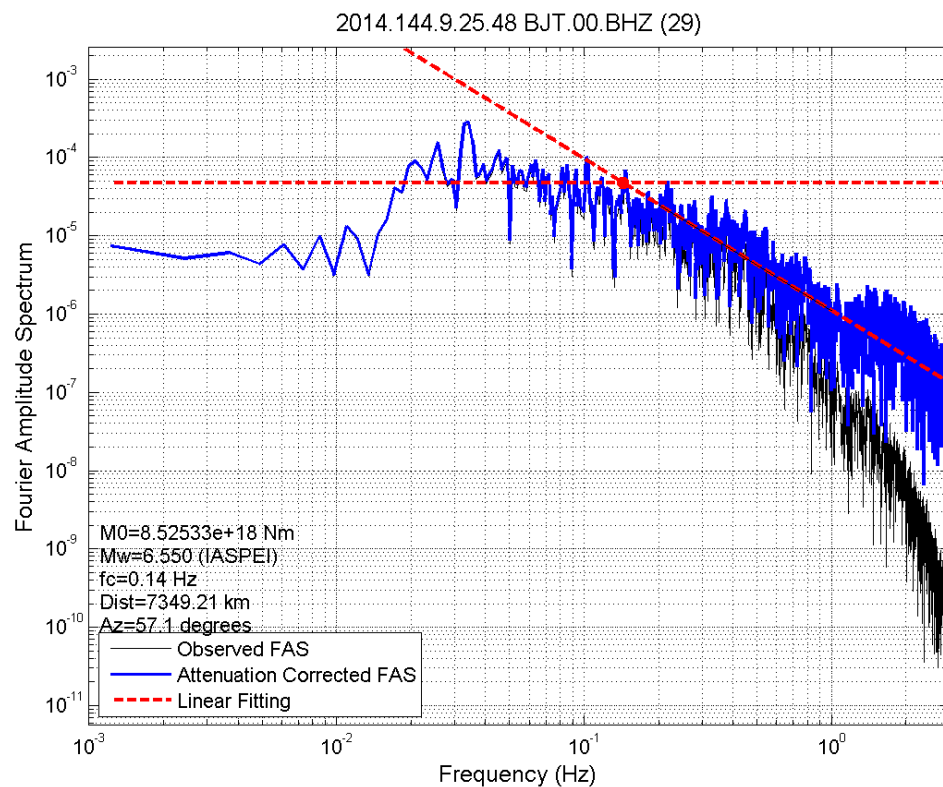


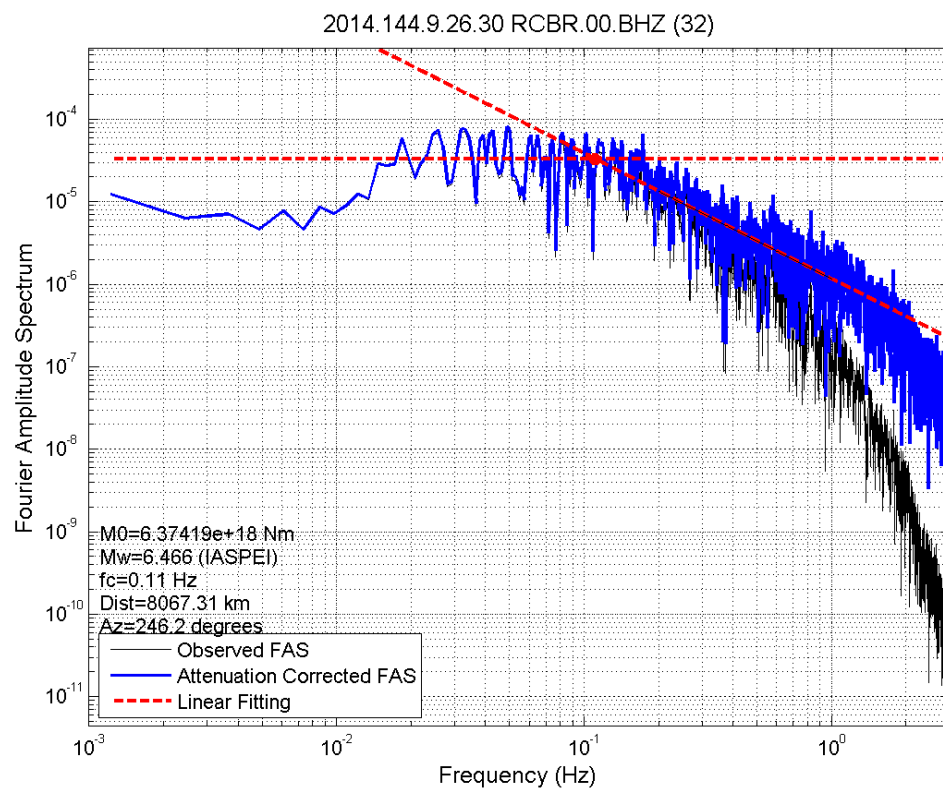
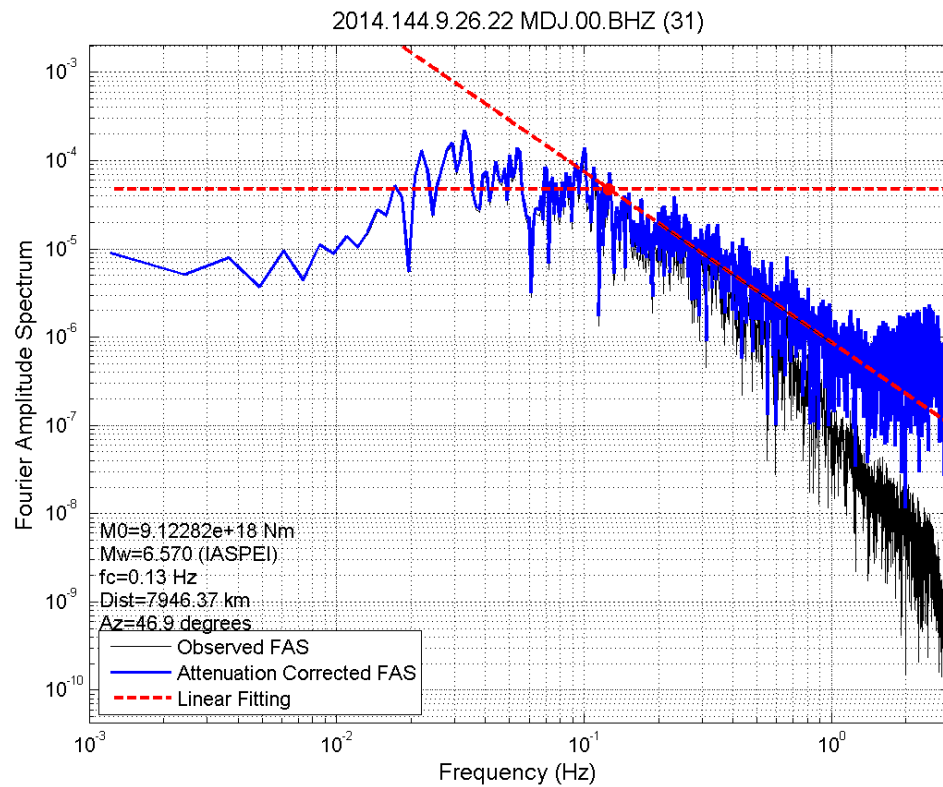


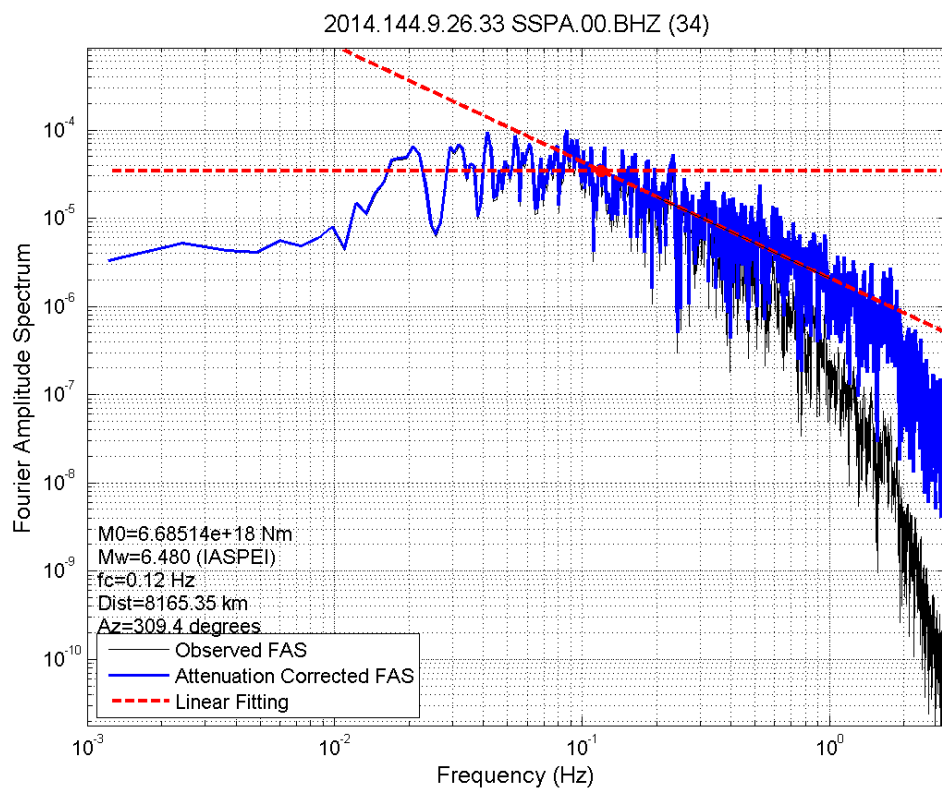
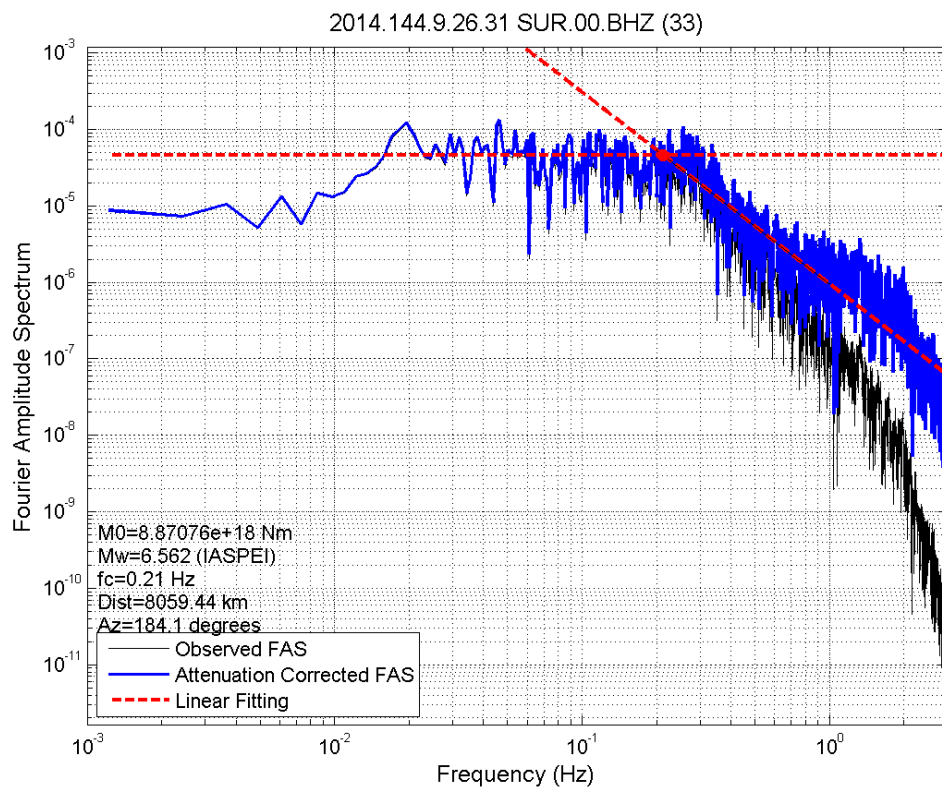


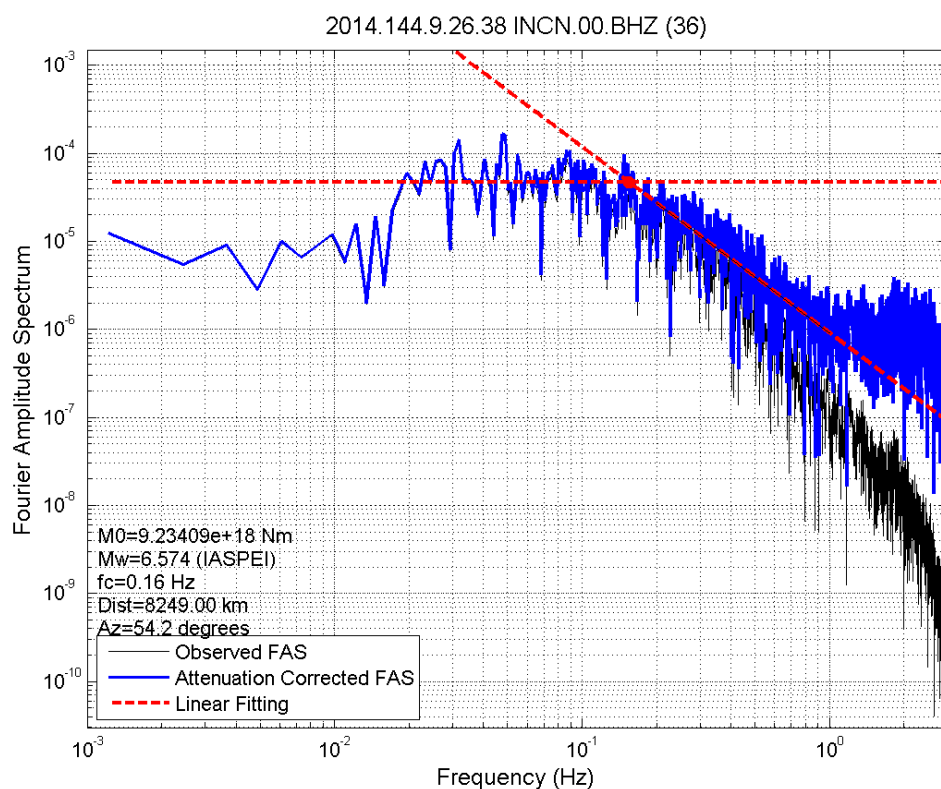
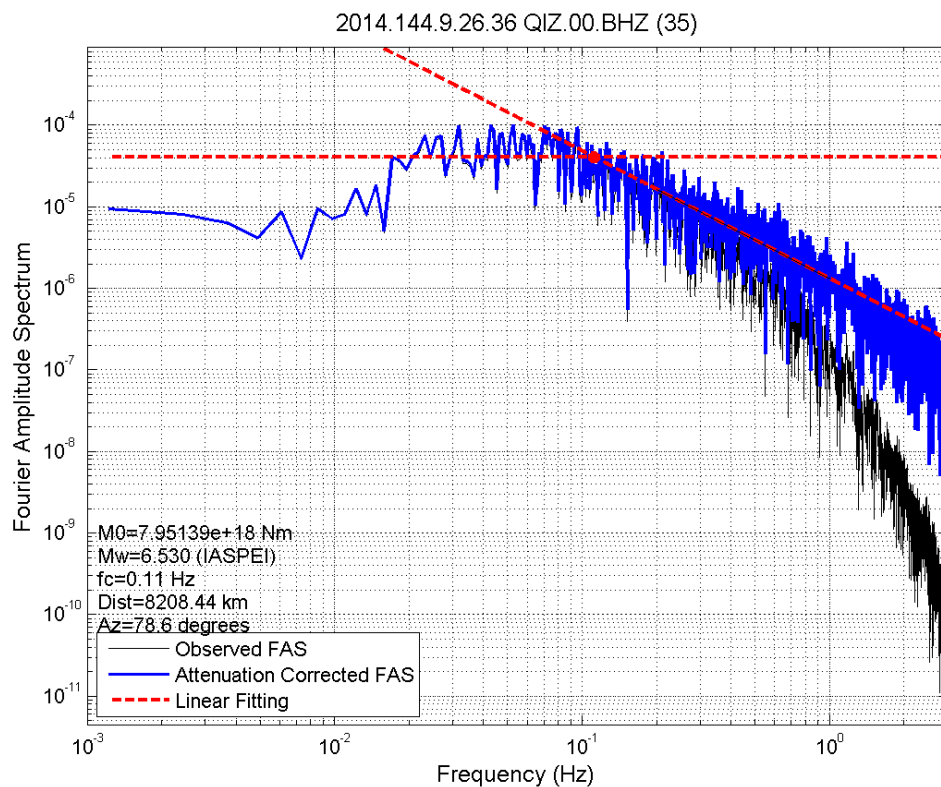


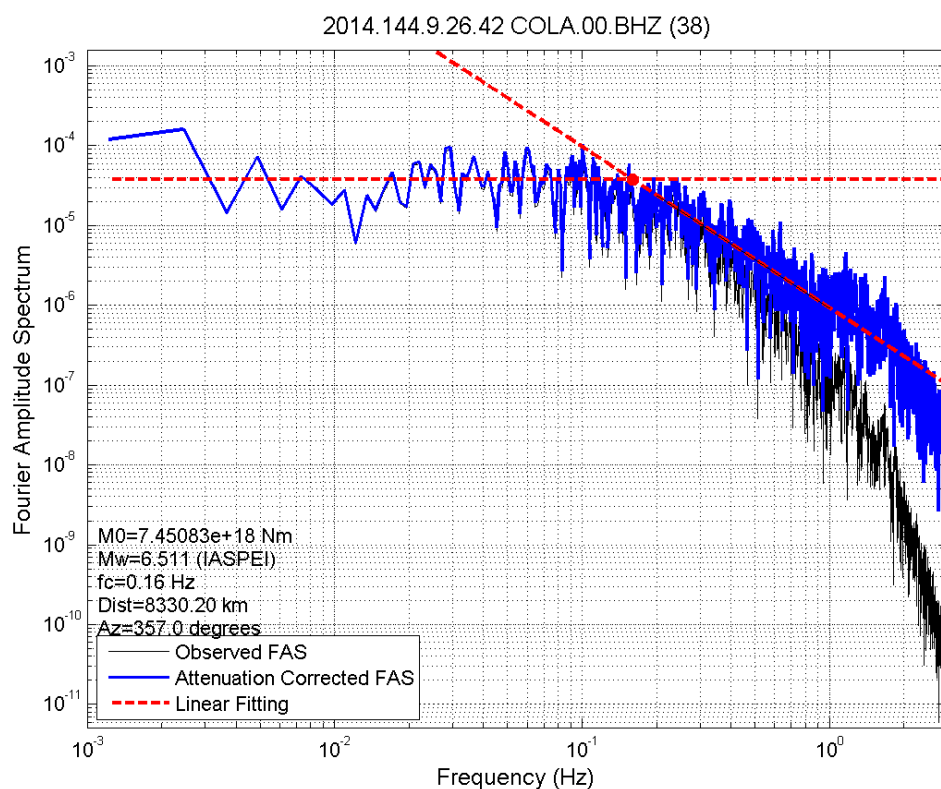
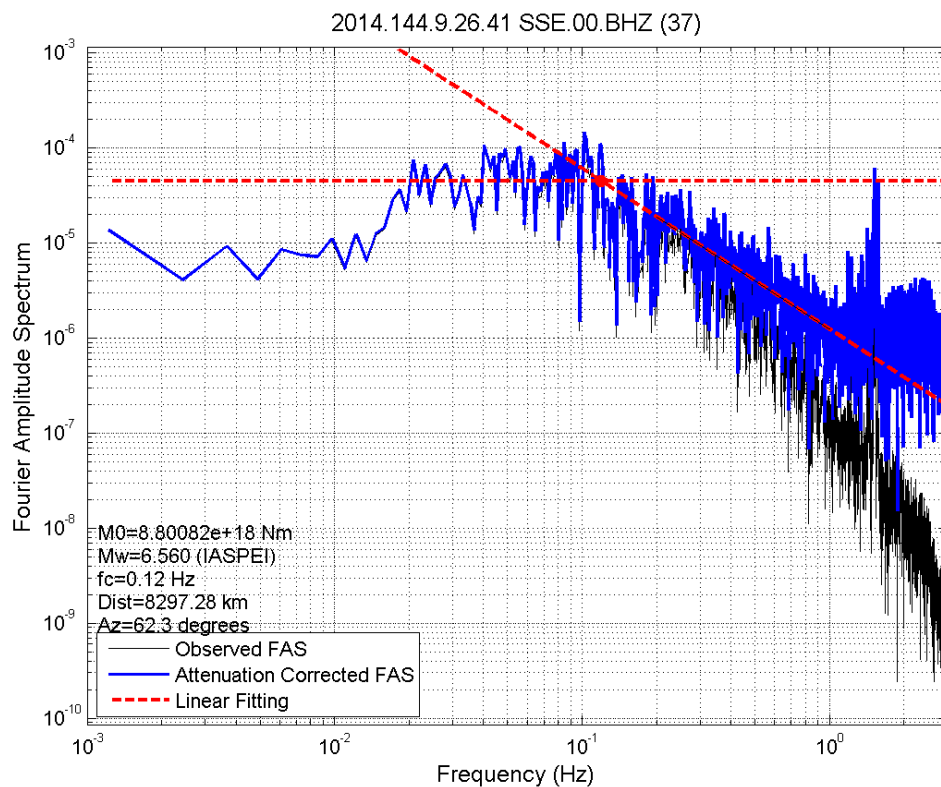


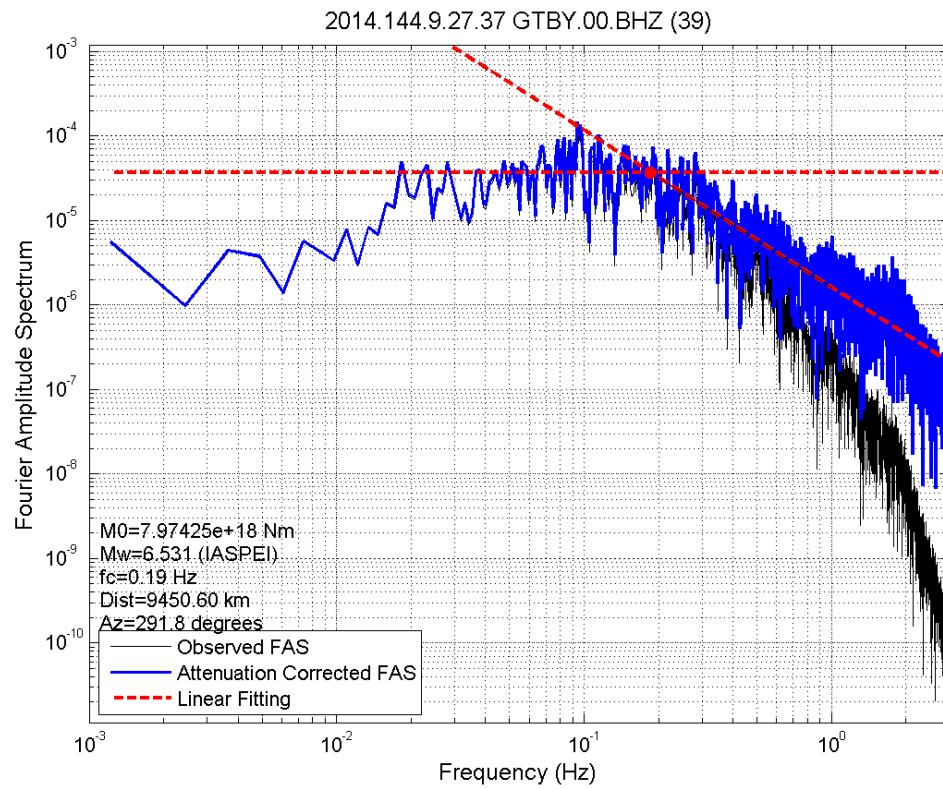




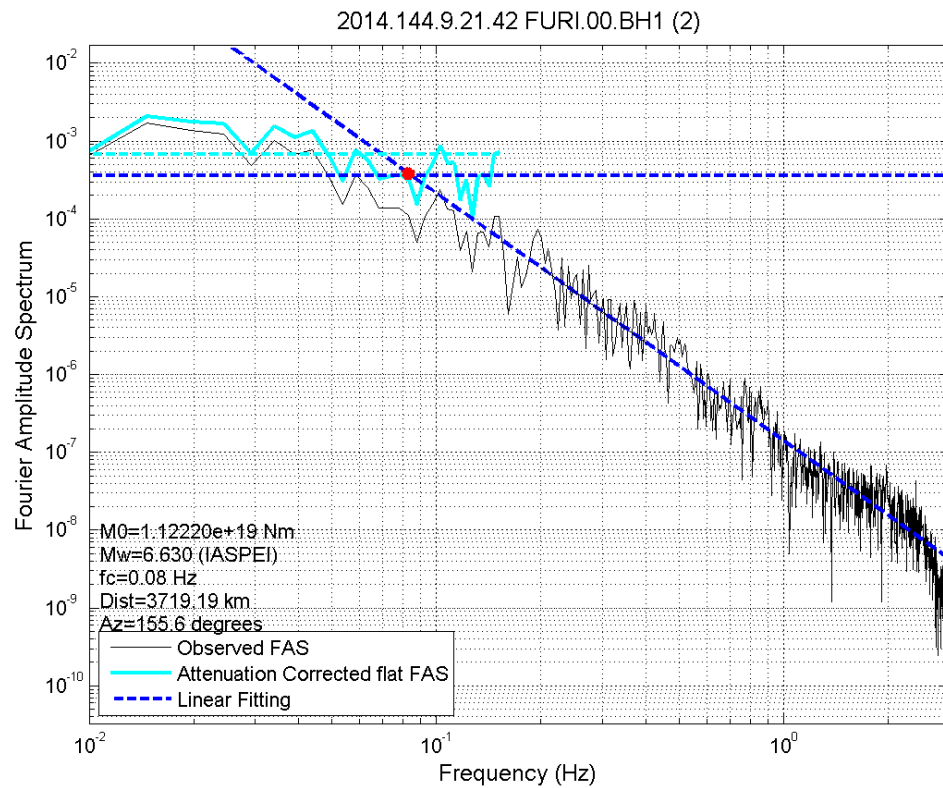
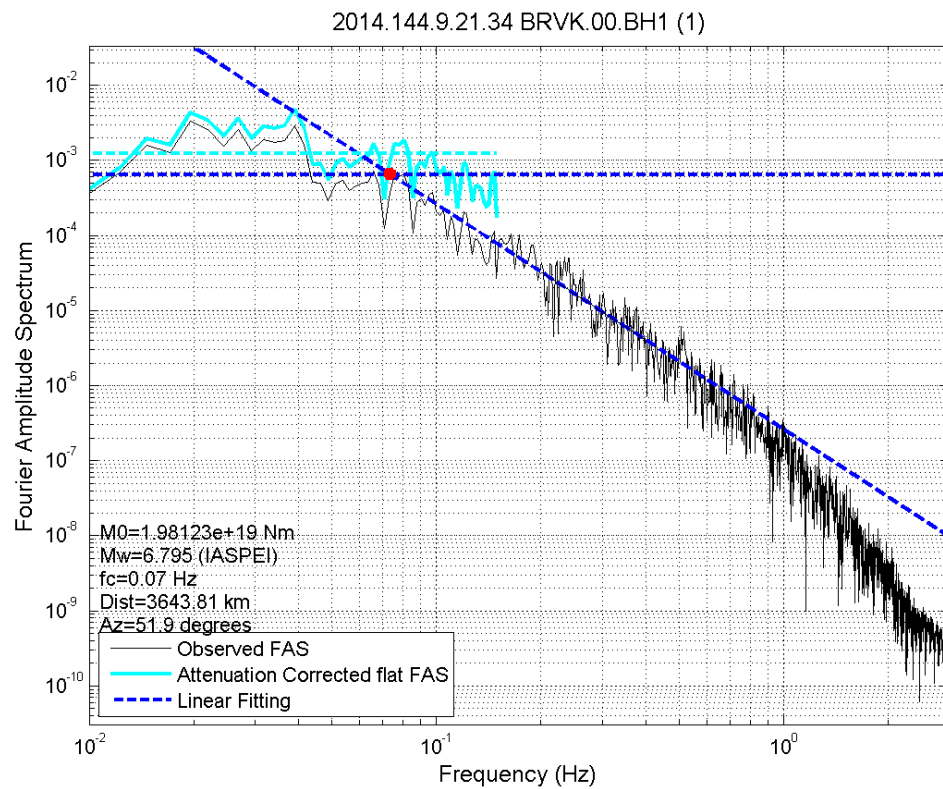


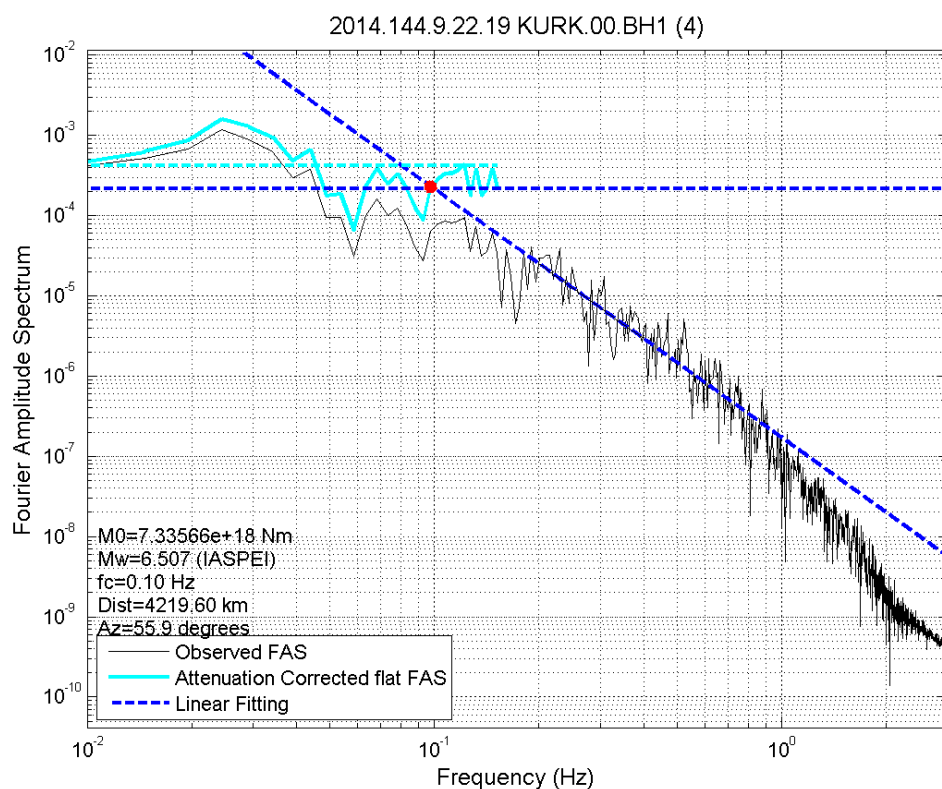
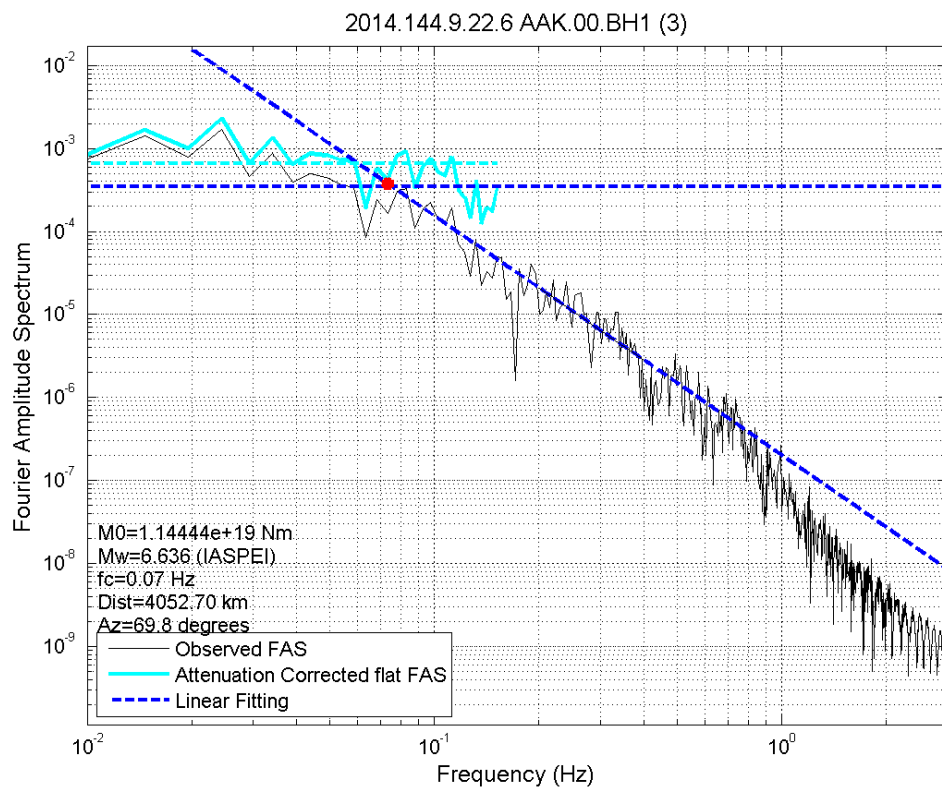


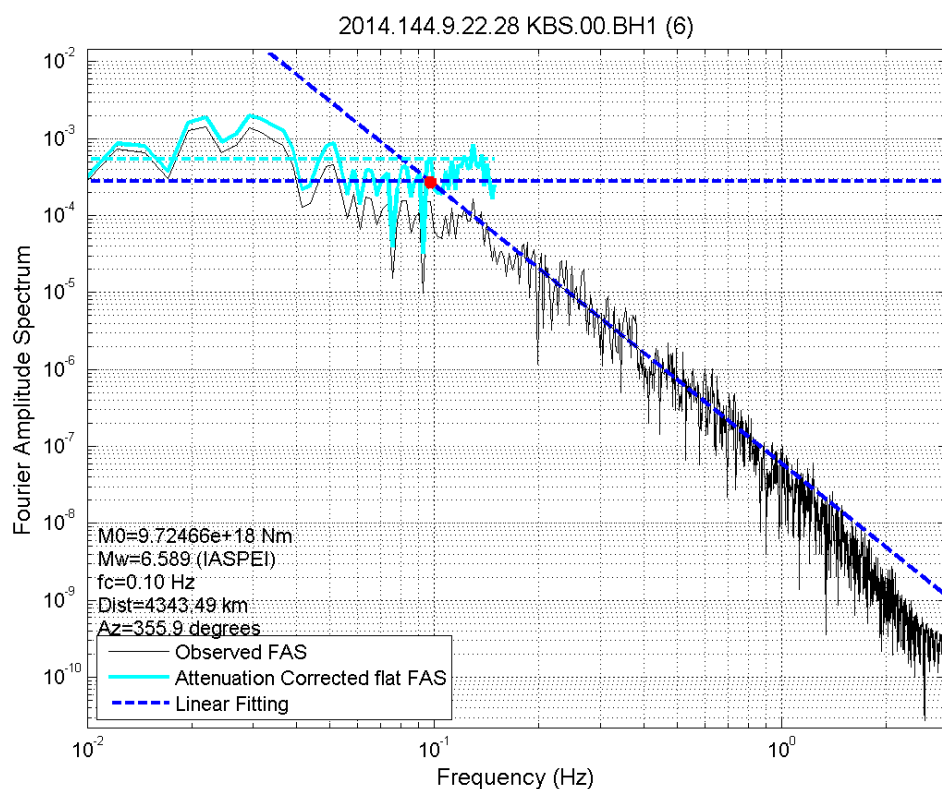
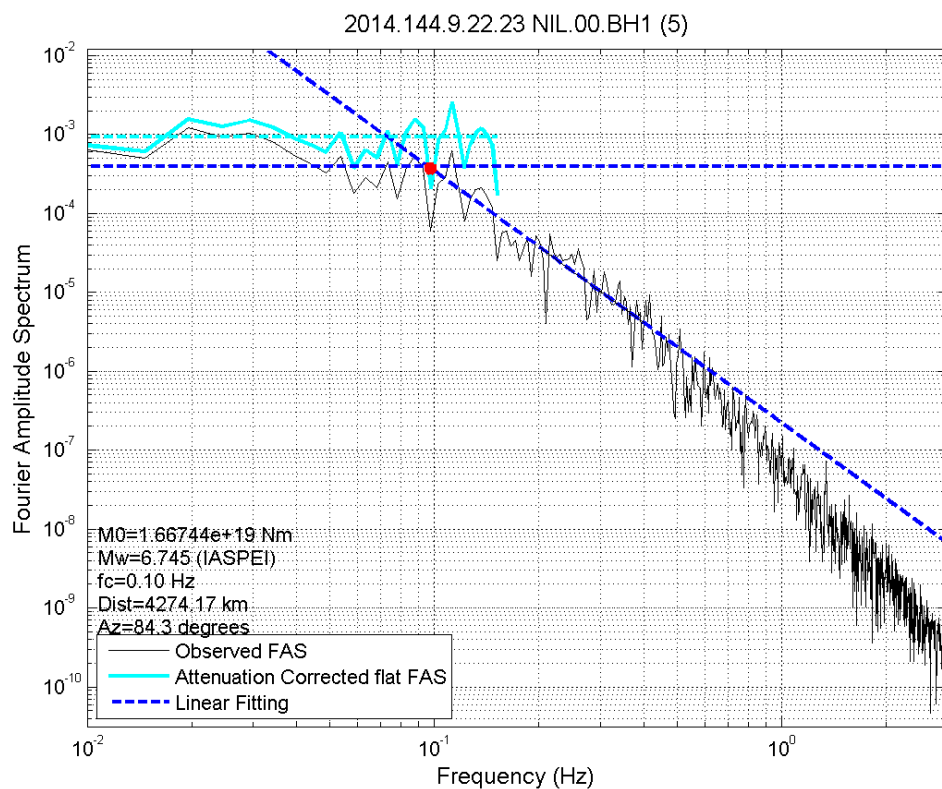


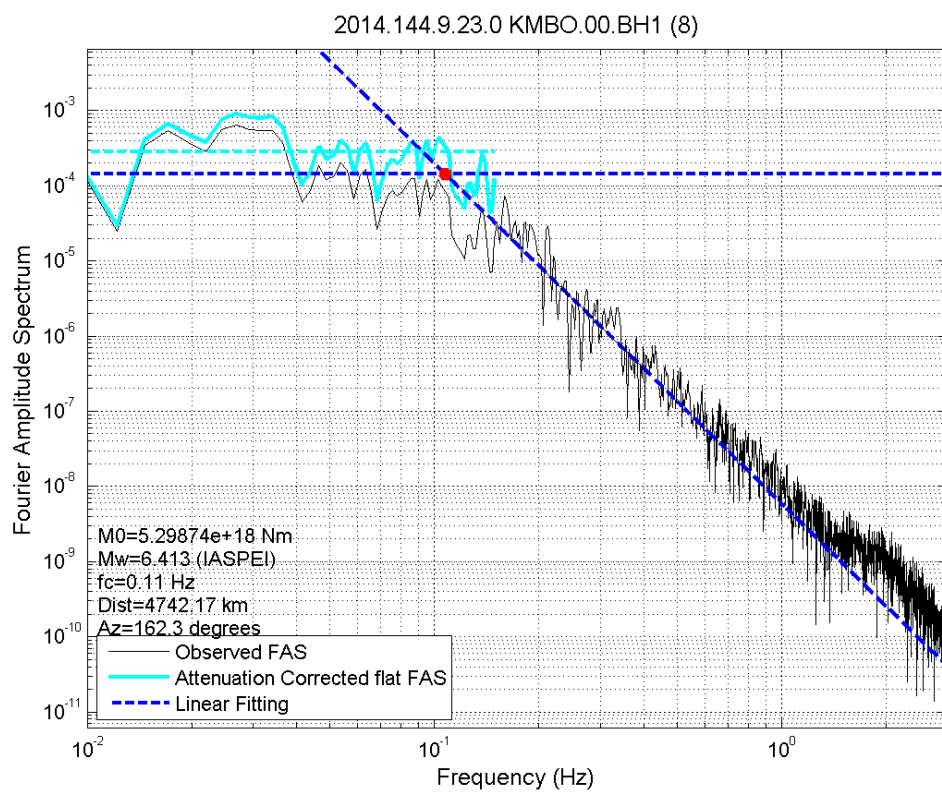
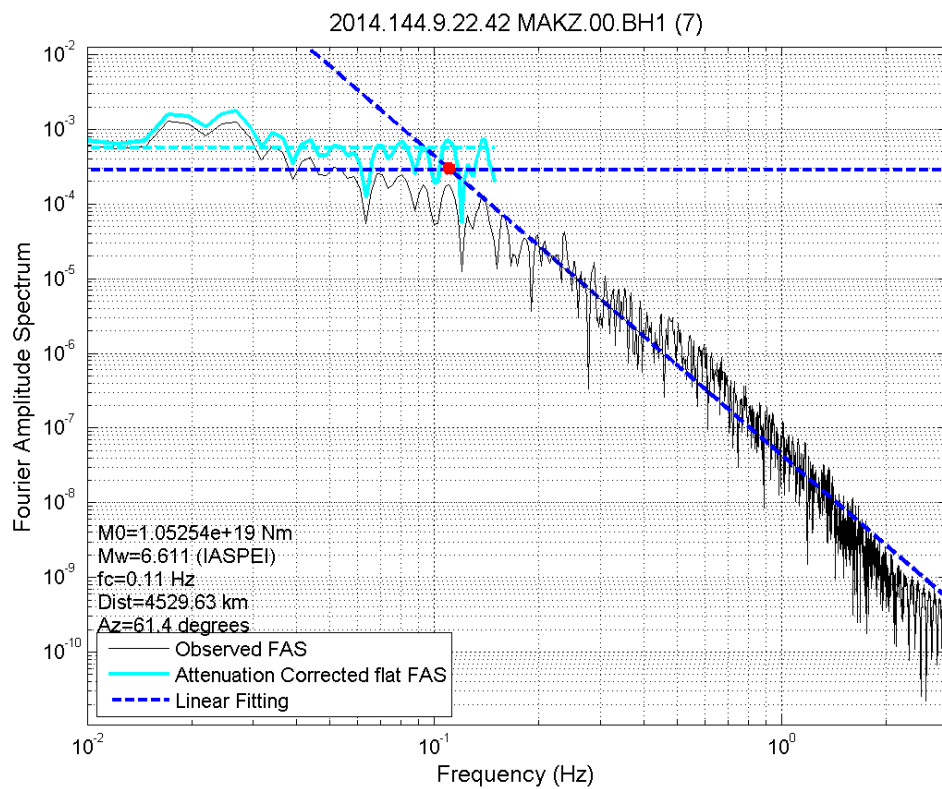


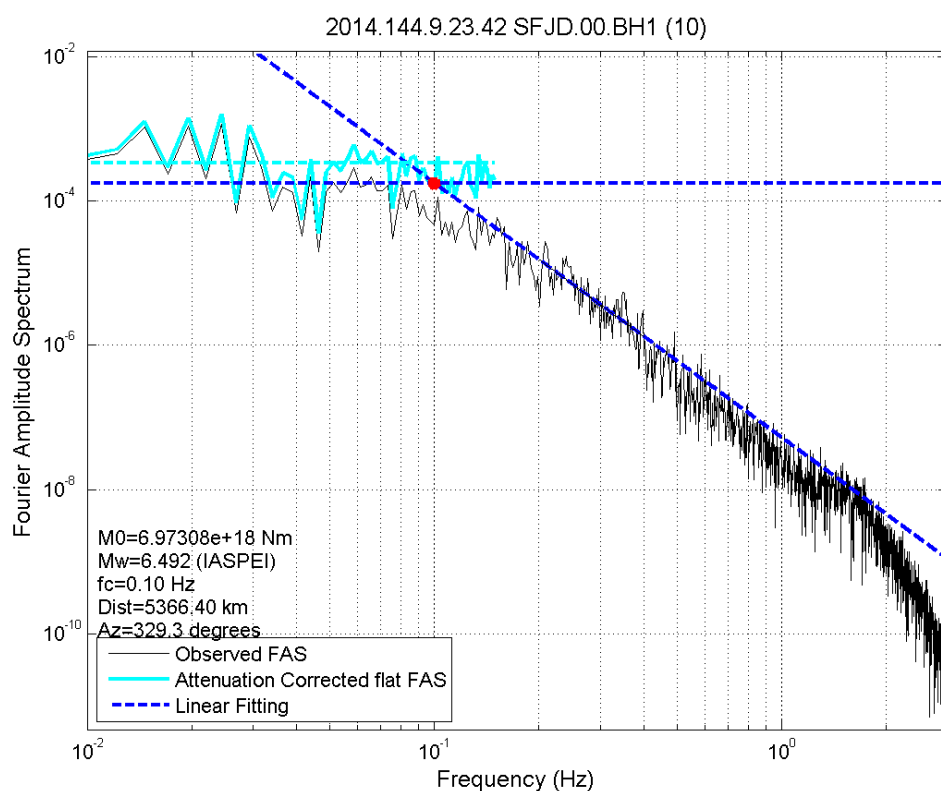
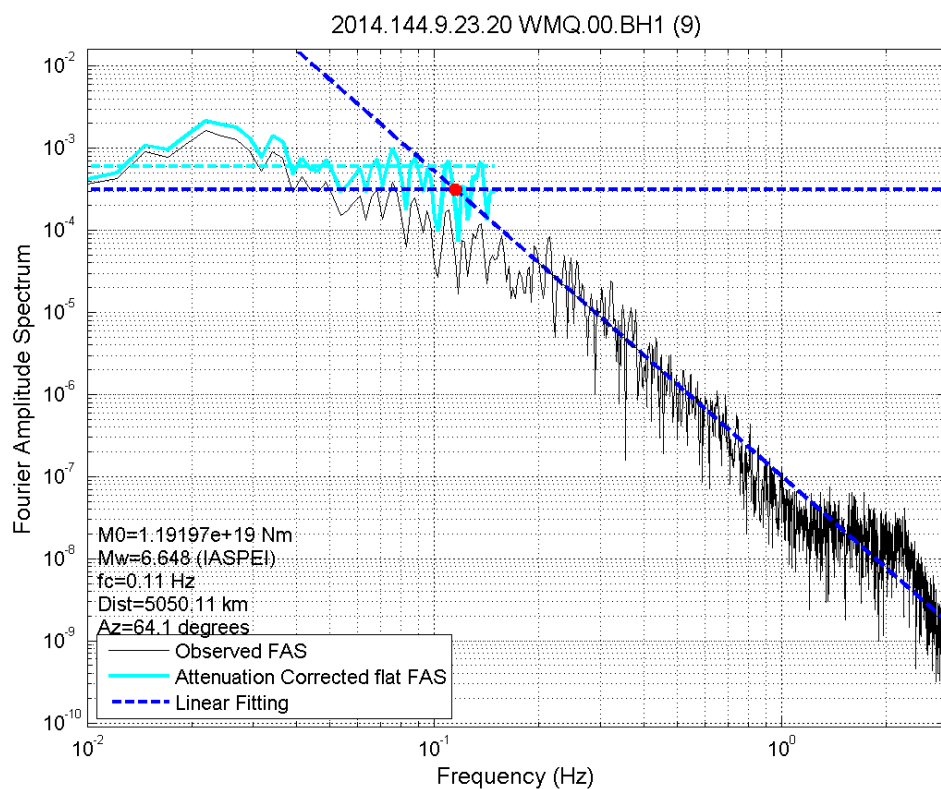
BH1 (E-W horizontal) component:

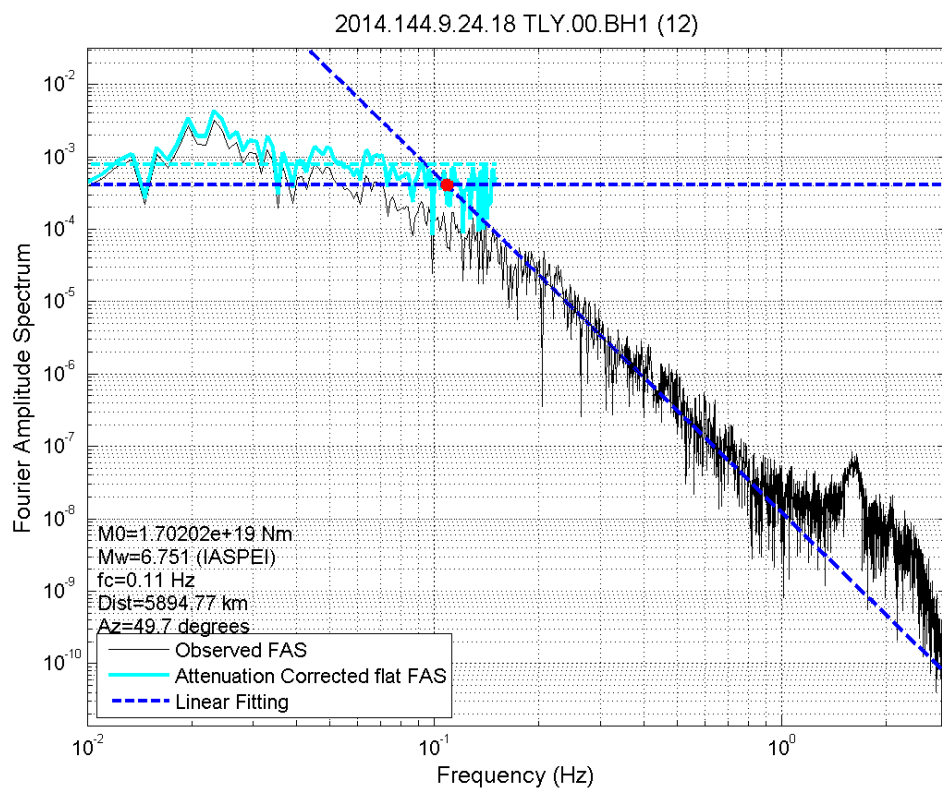
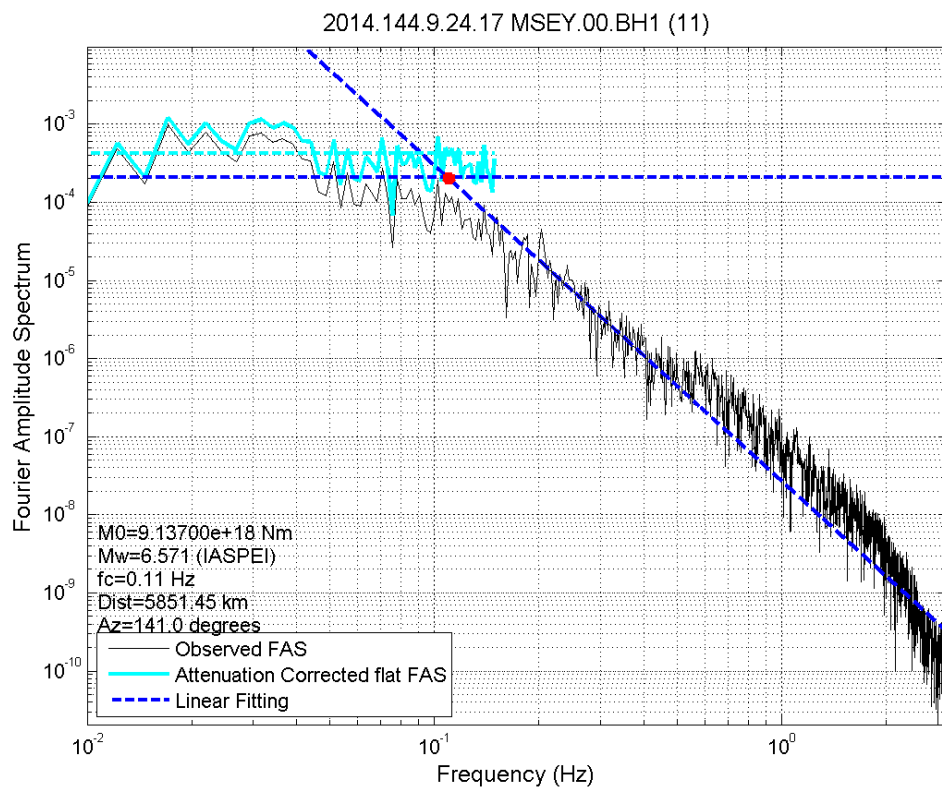


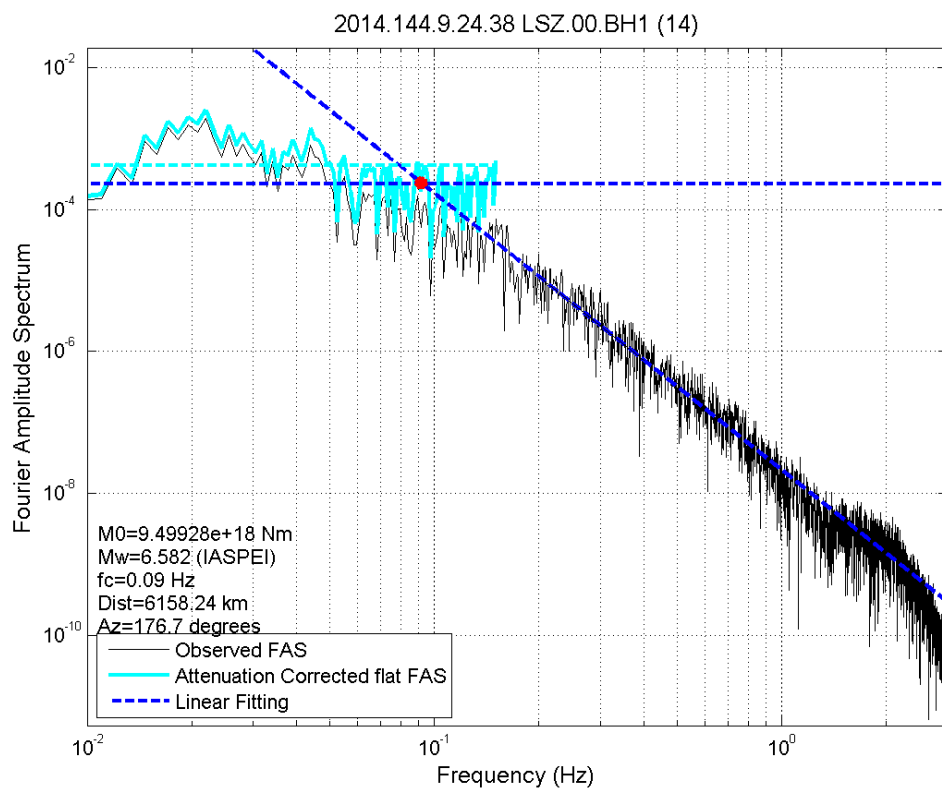
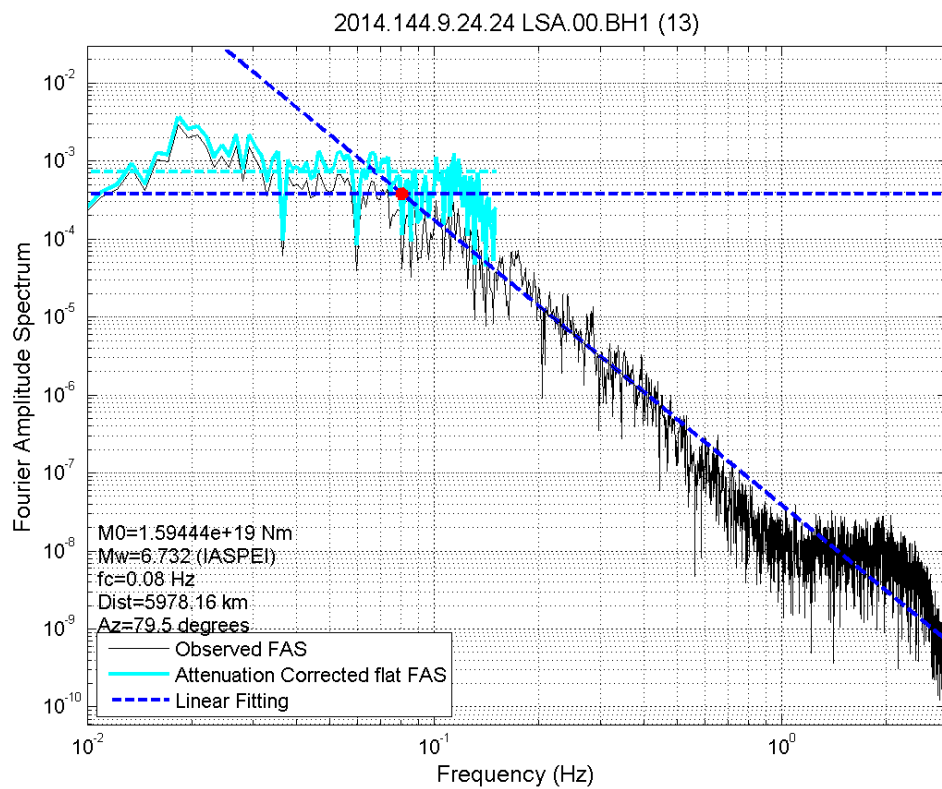


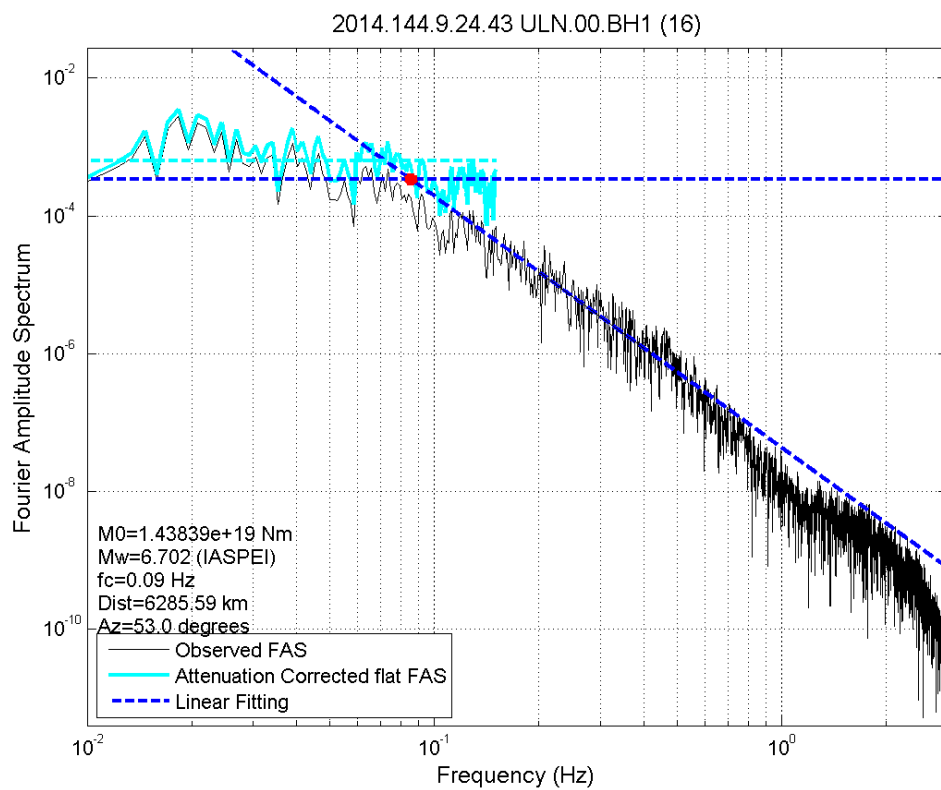
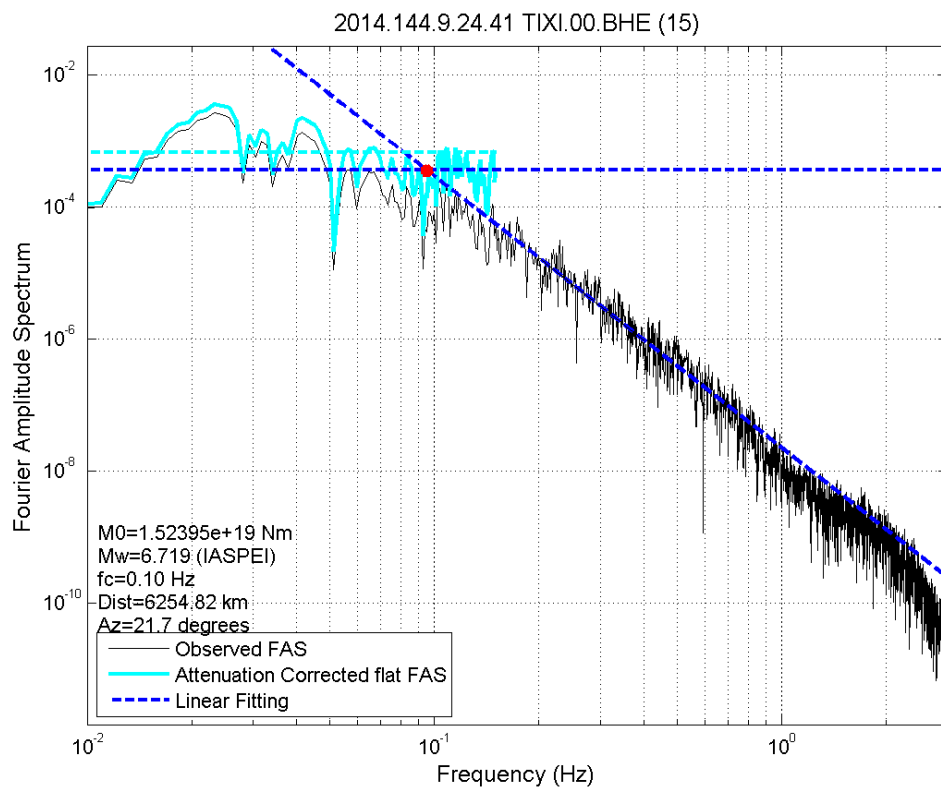


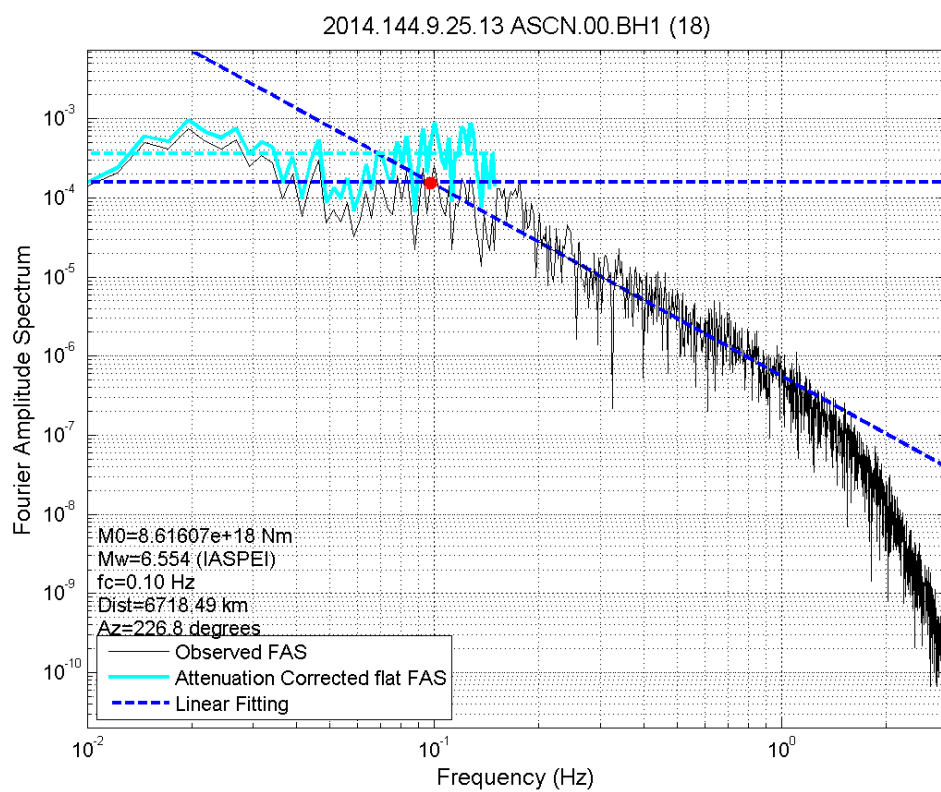
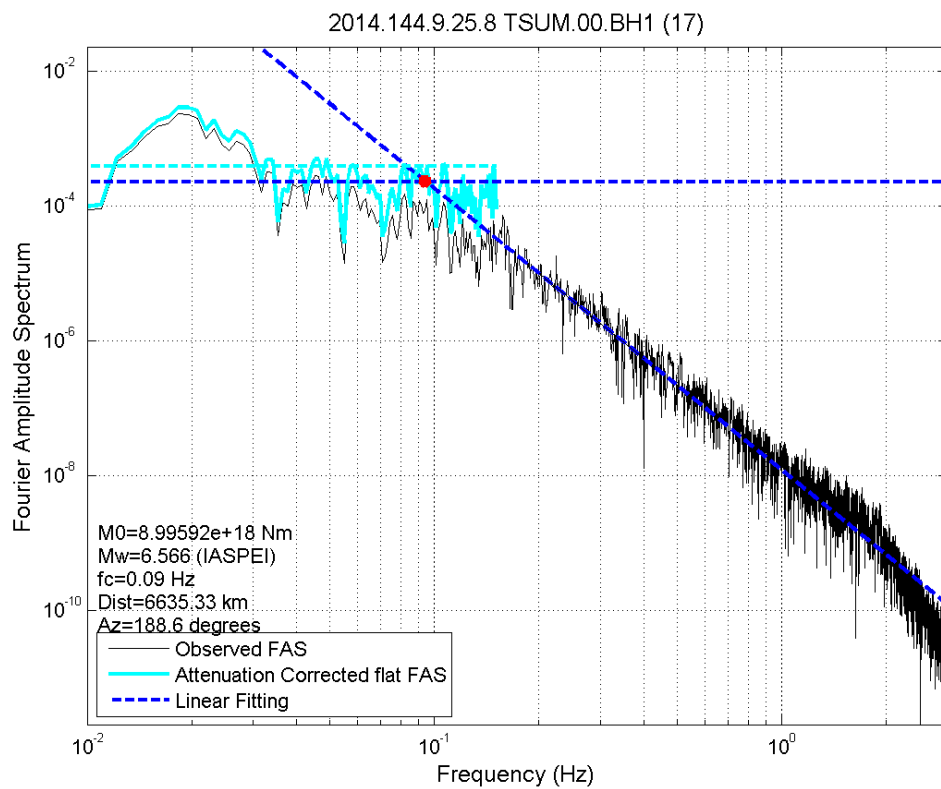


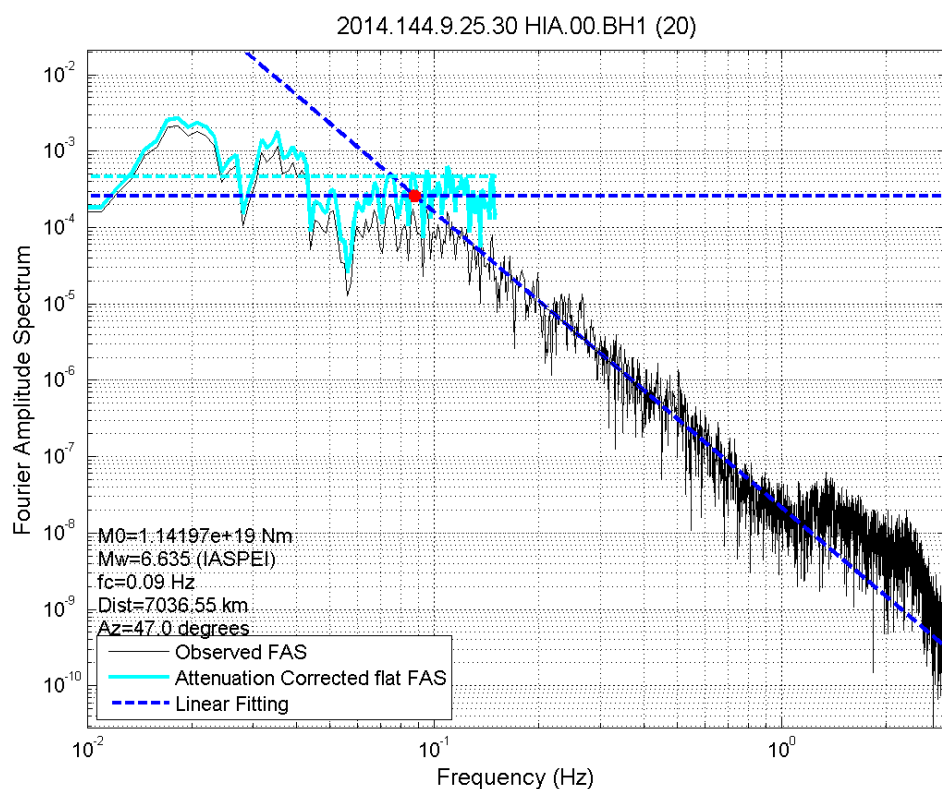
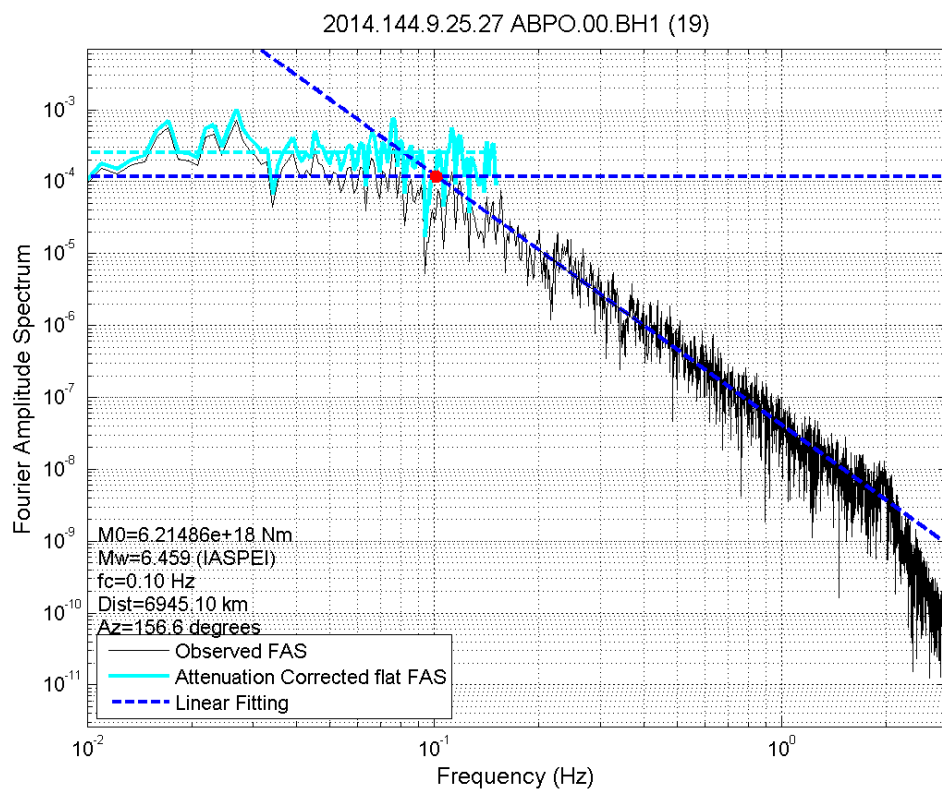


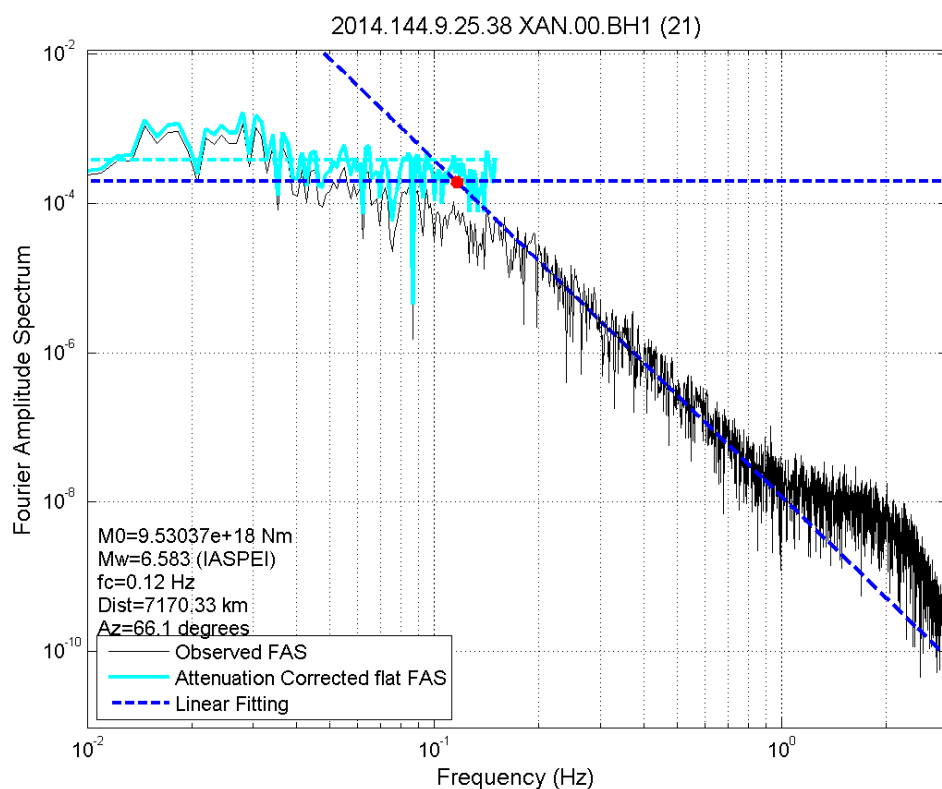
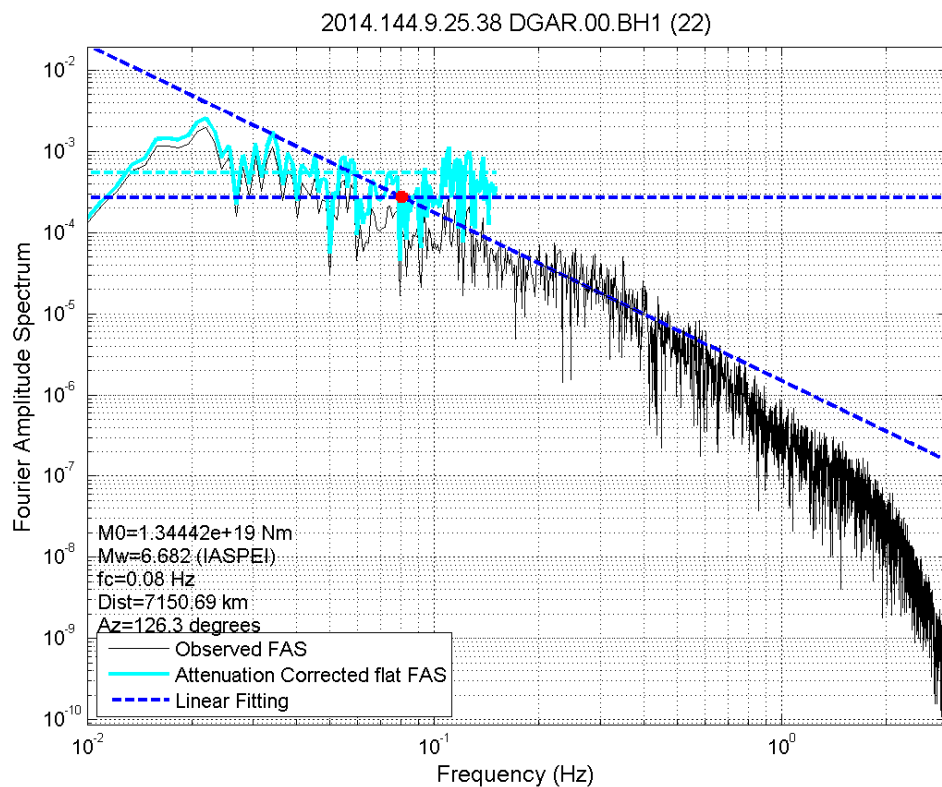


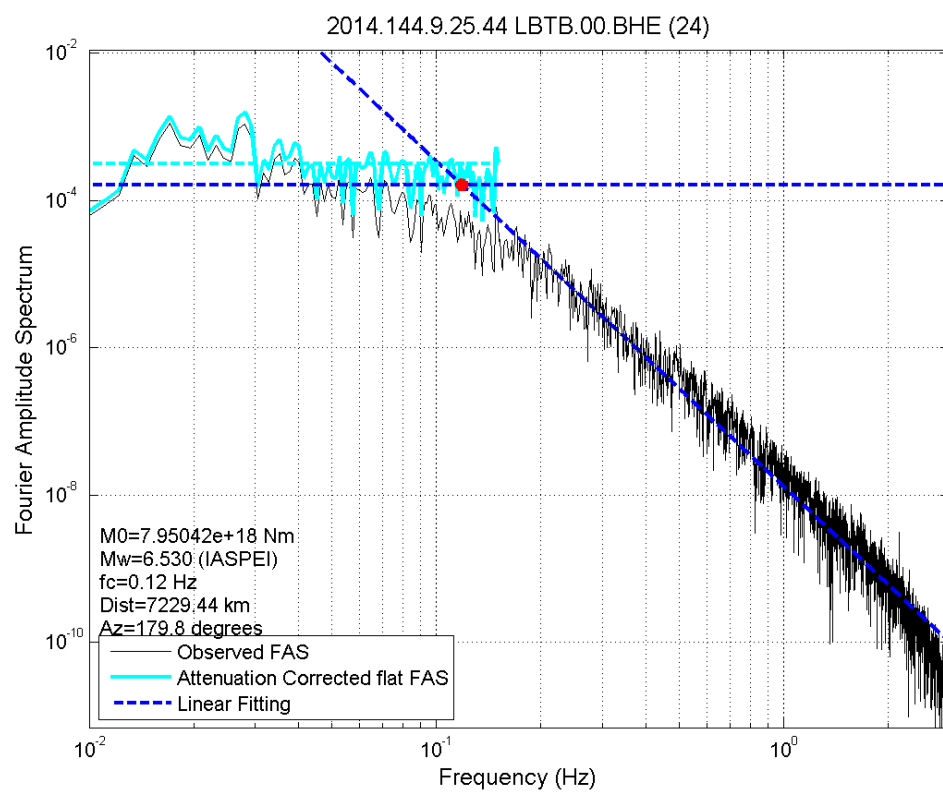
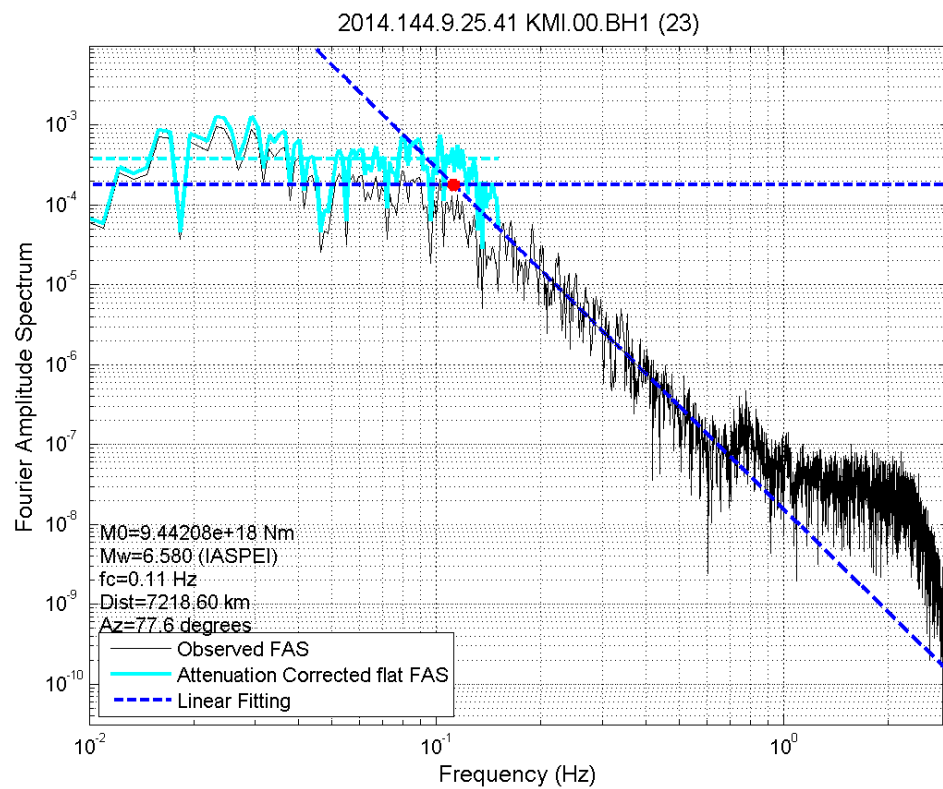


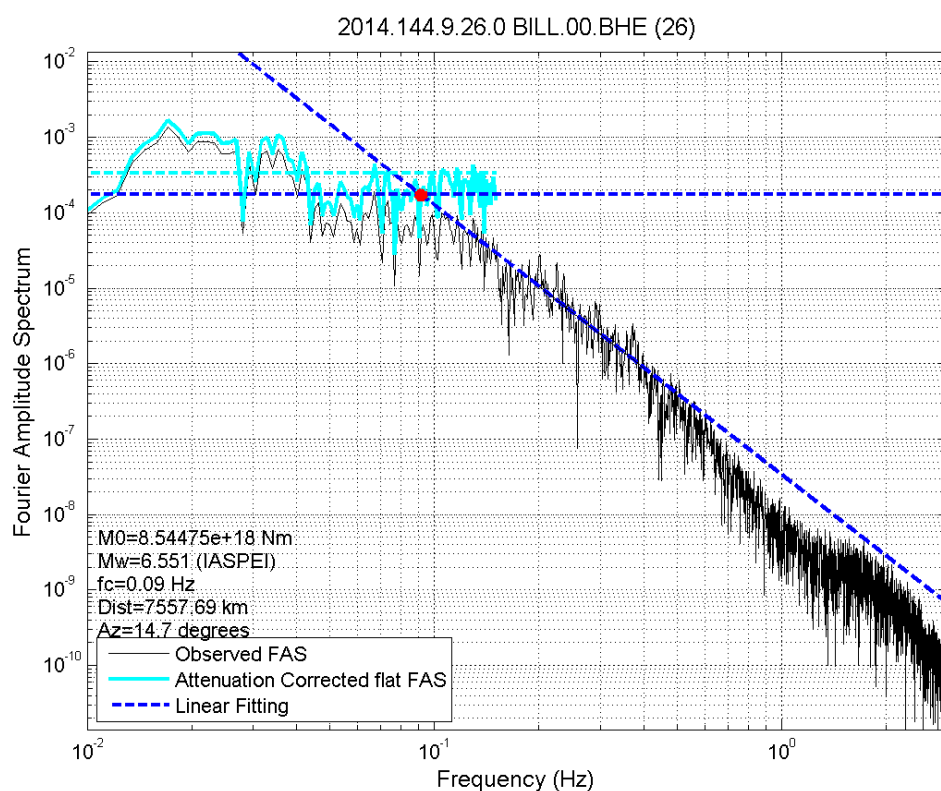
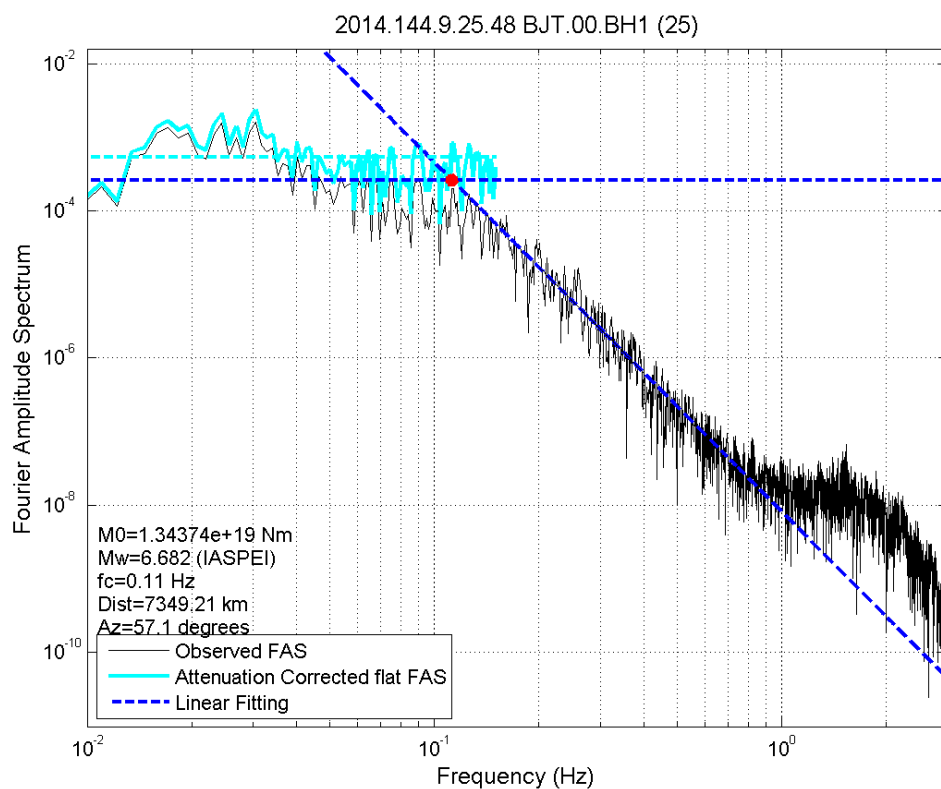


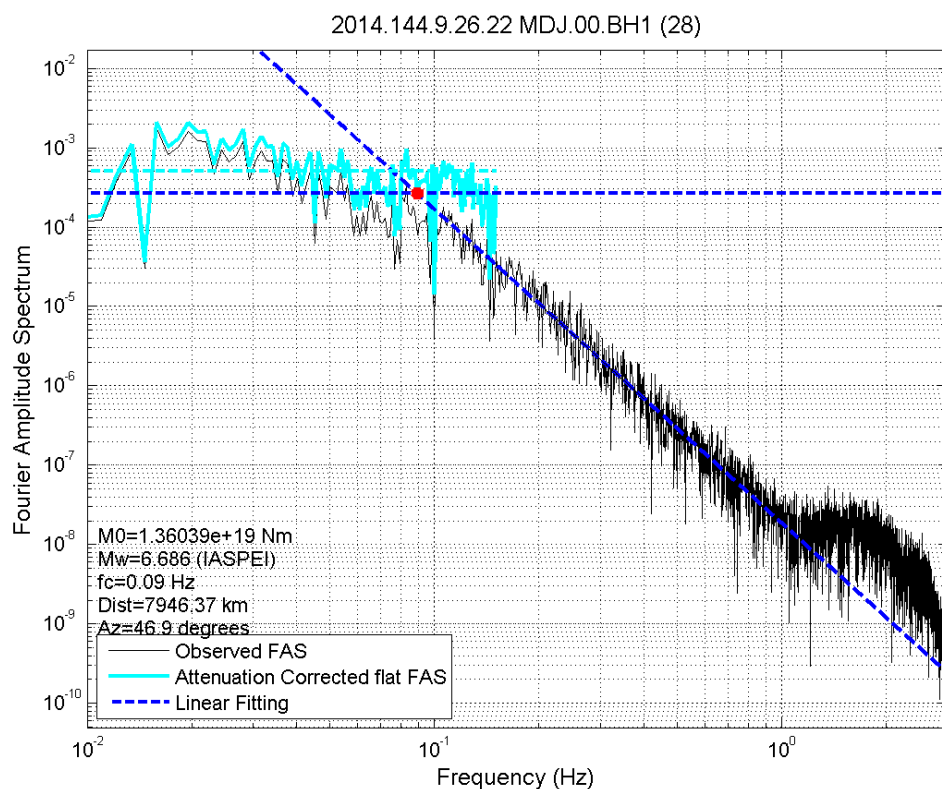
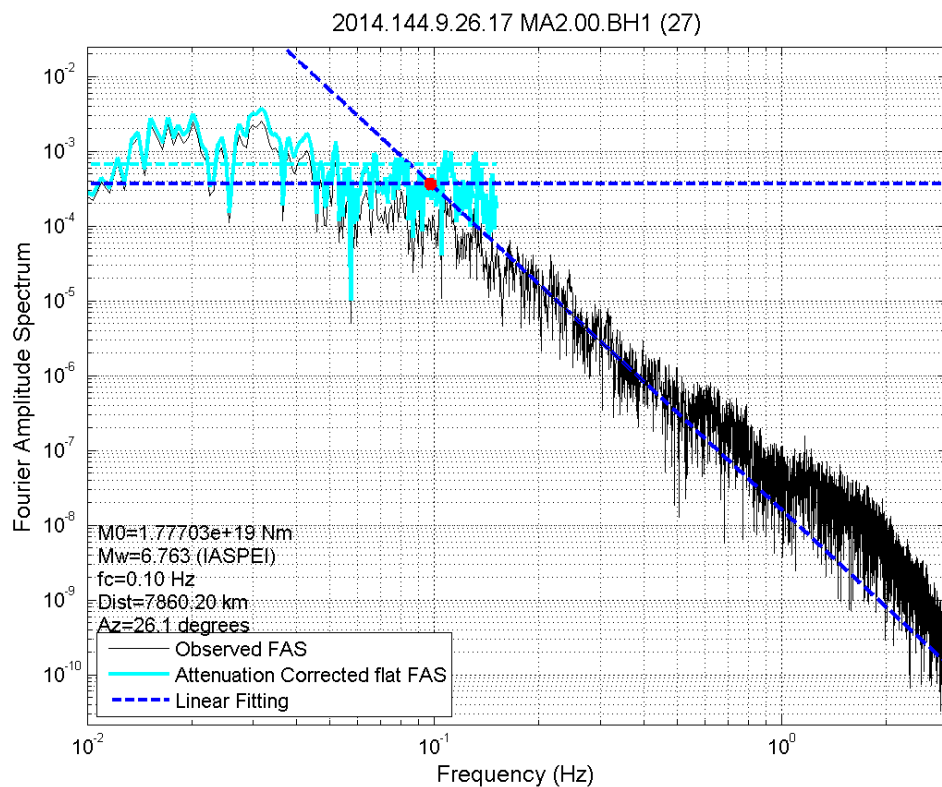


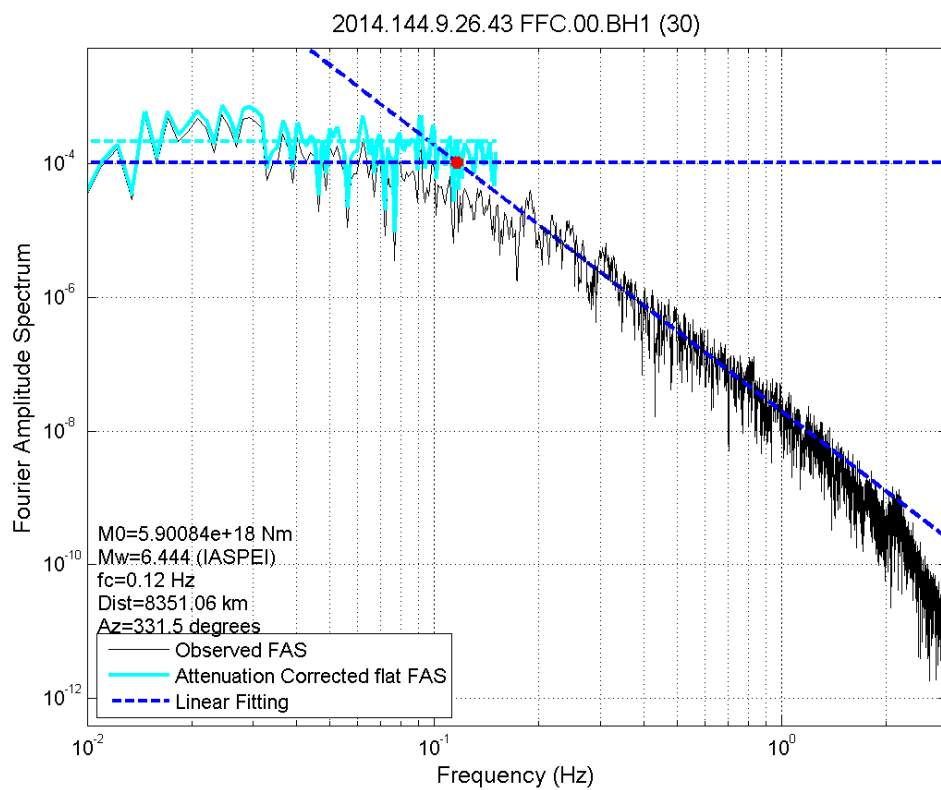
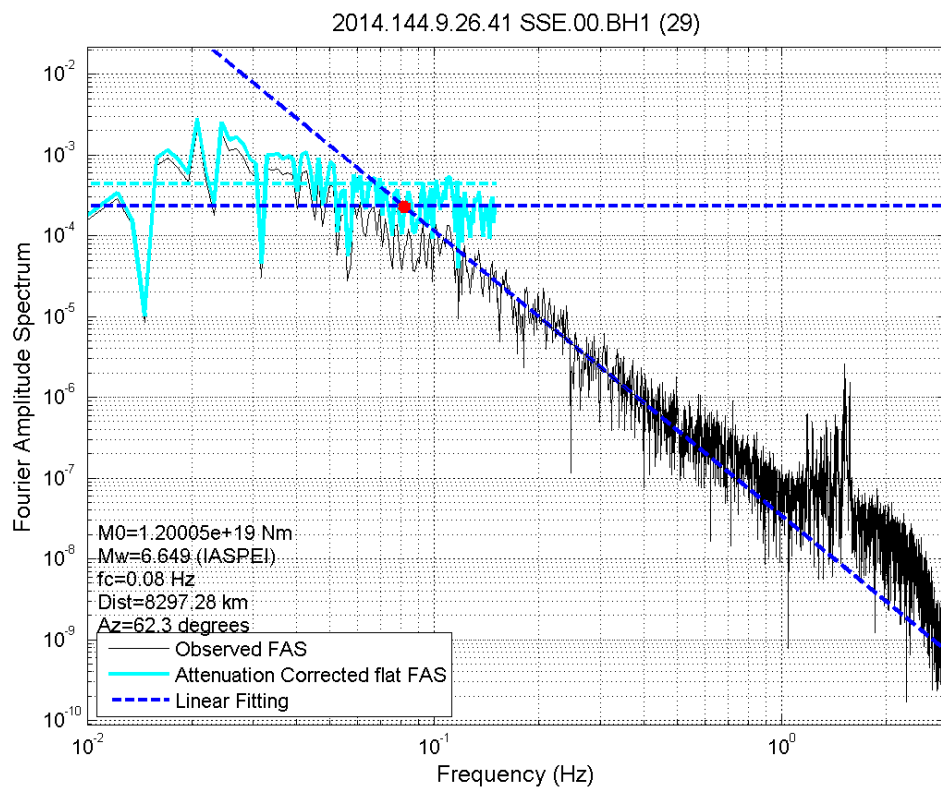


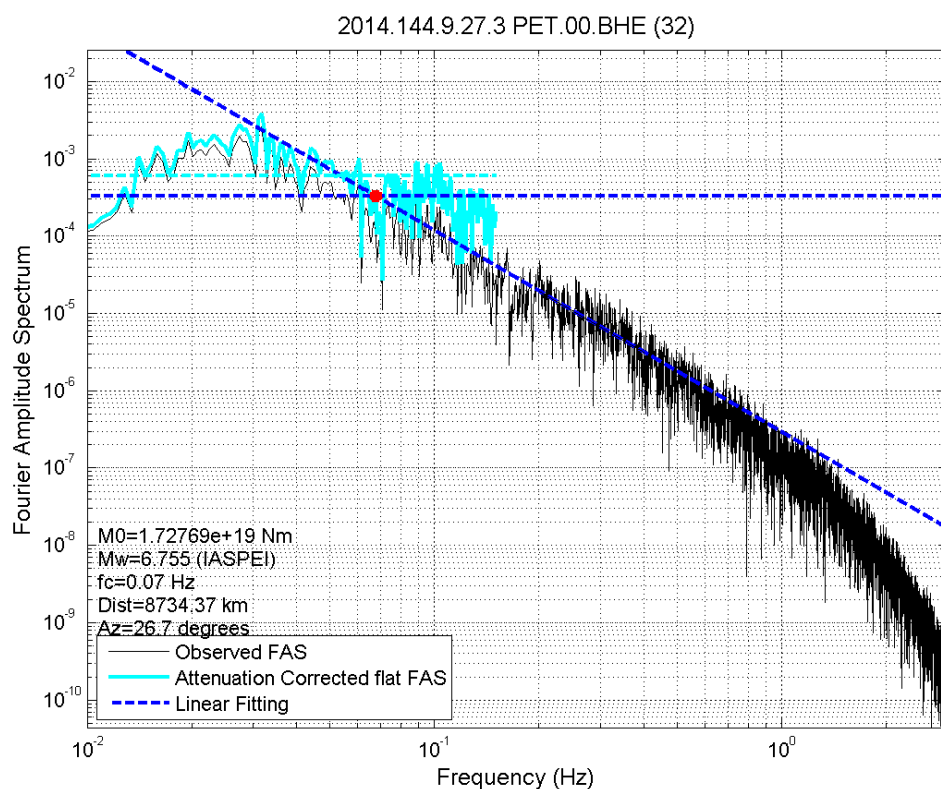
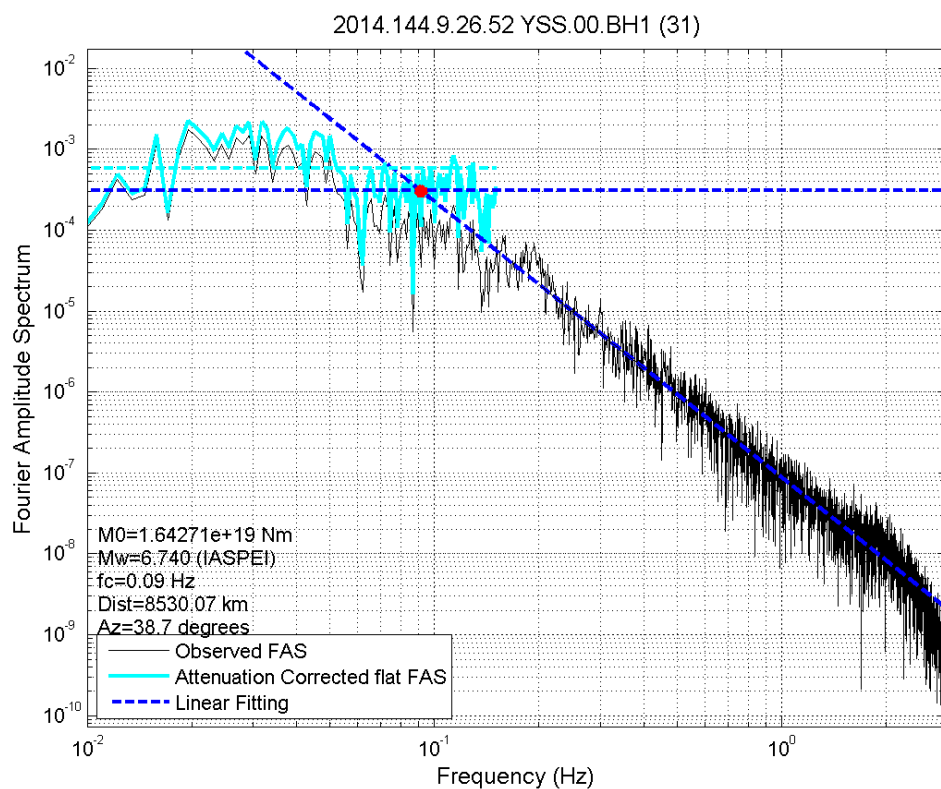


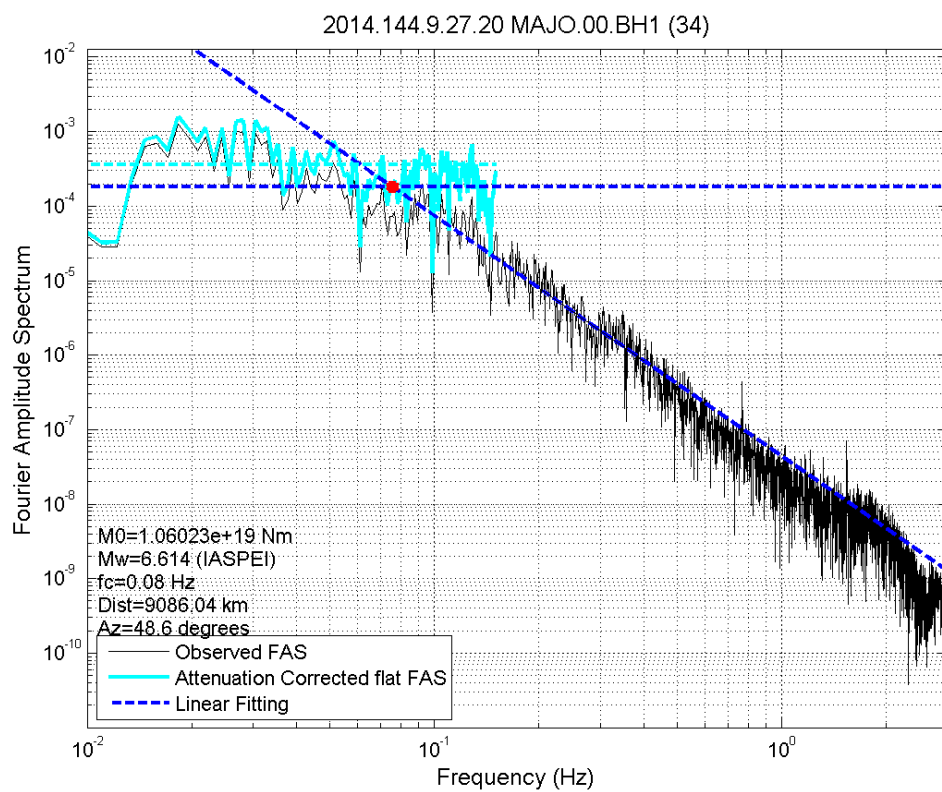
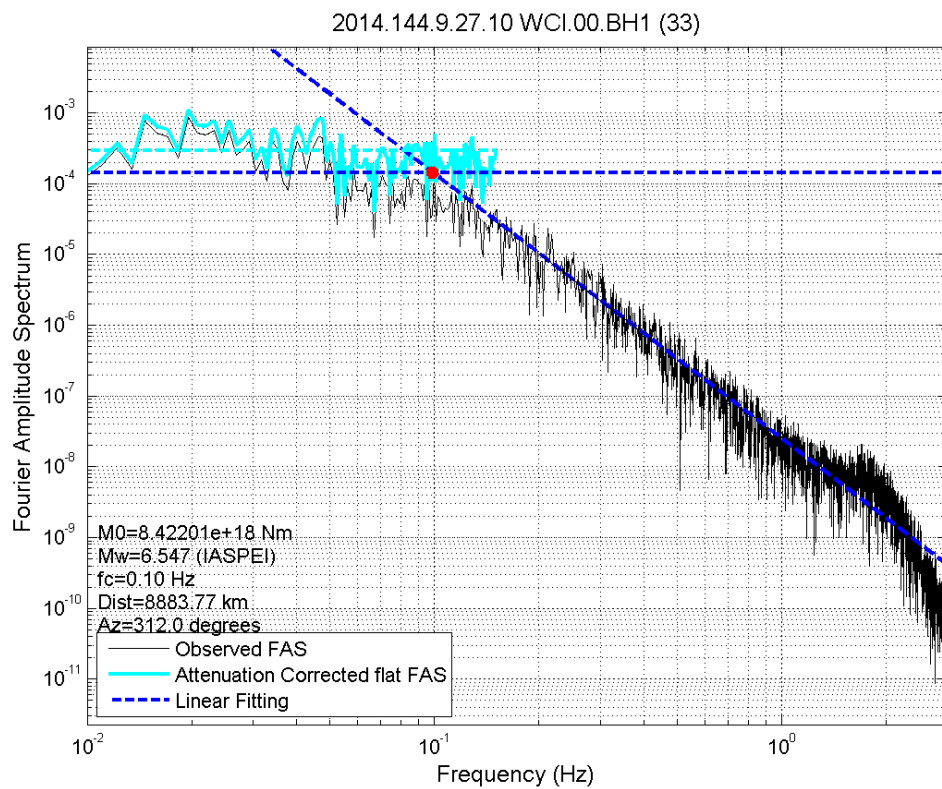


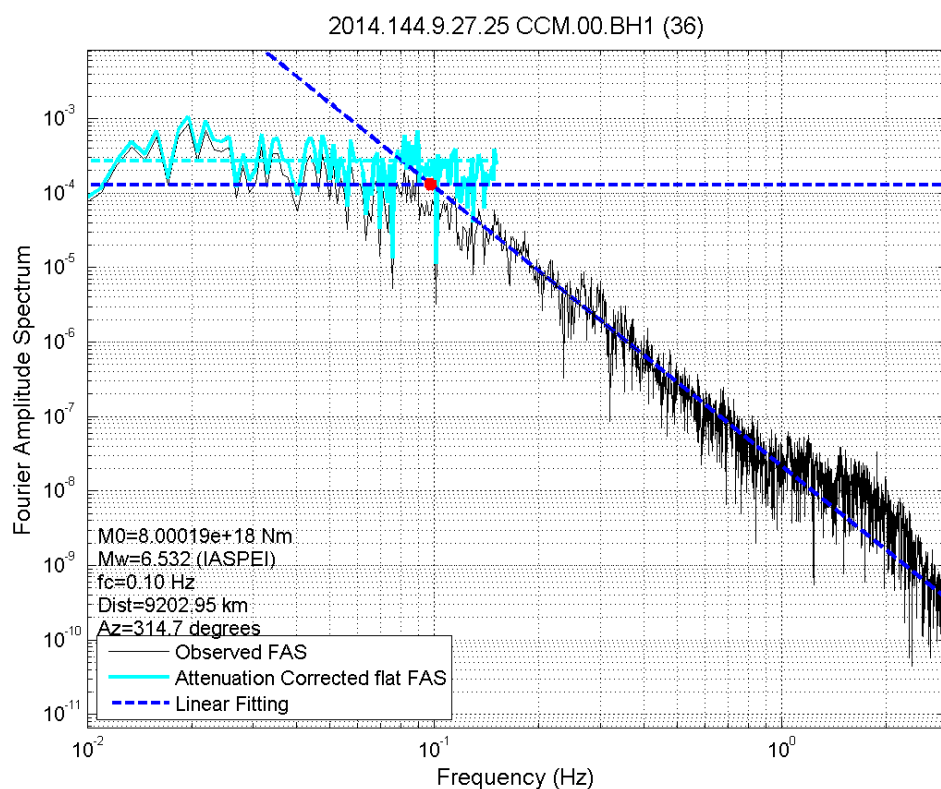
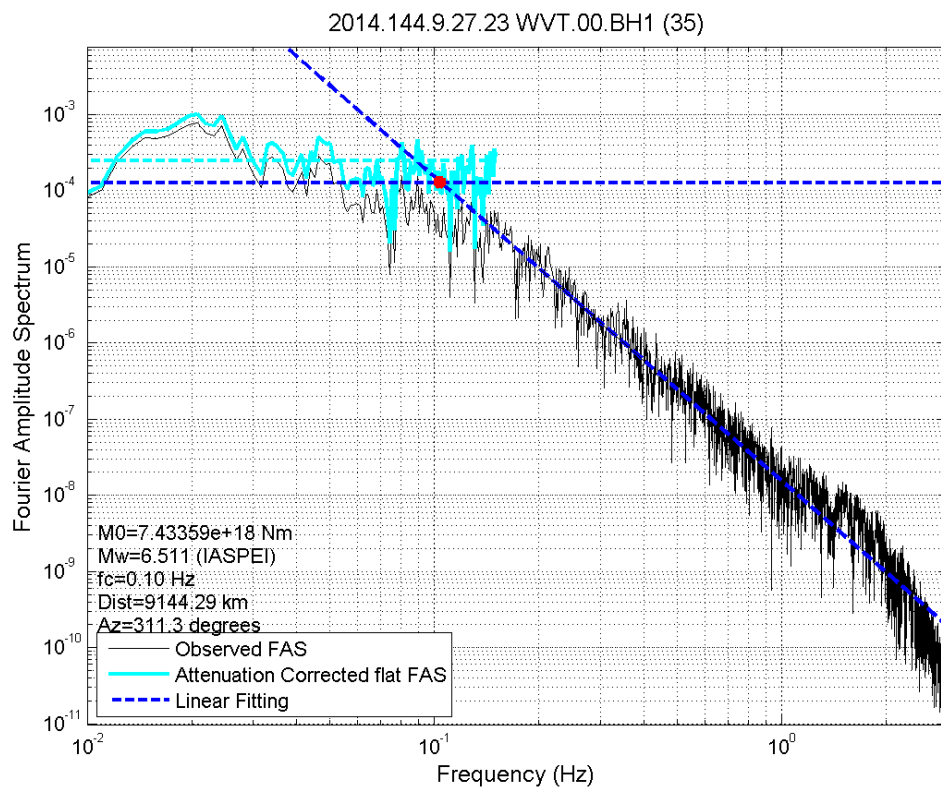


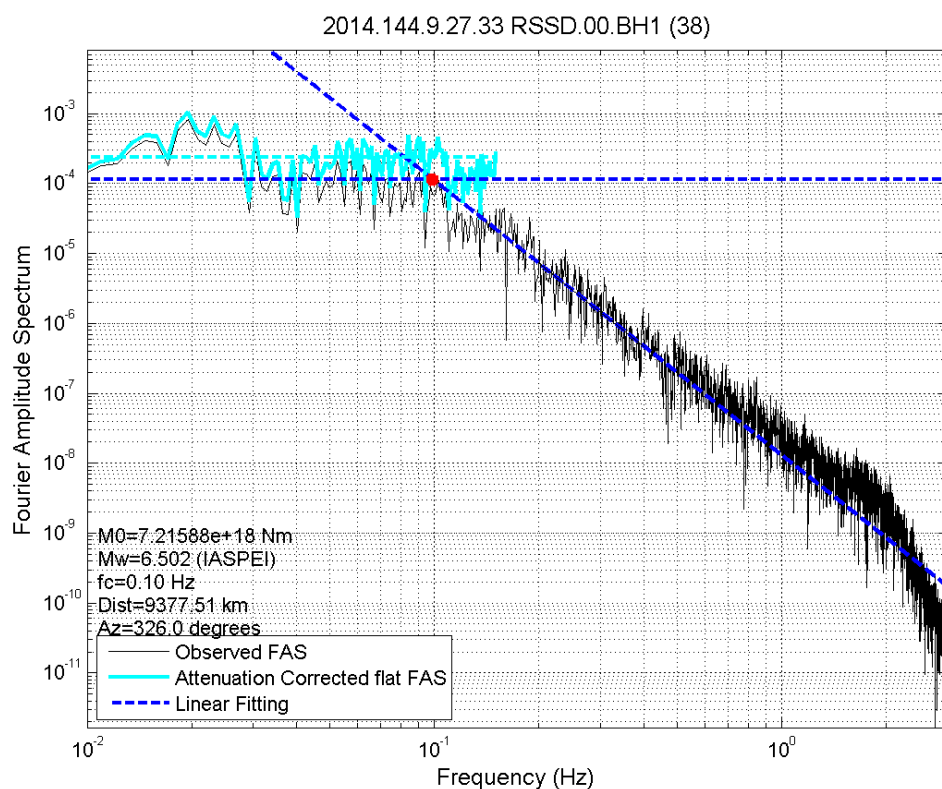
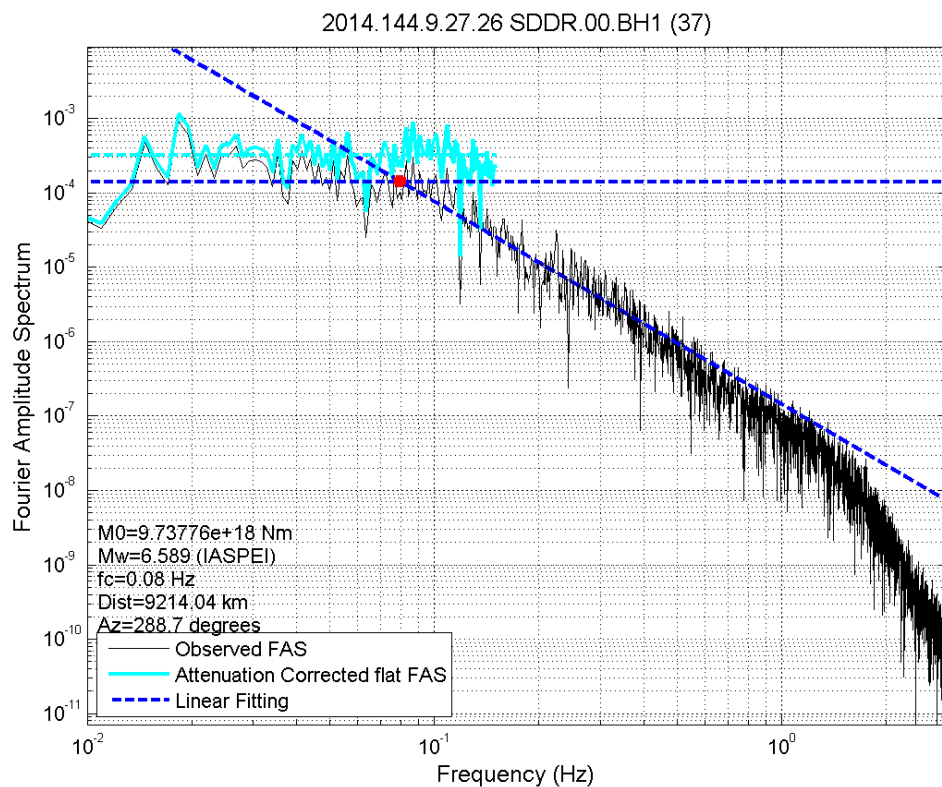












BH2 (N-S horizontal) component:

